Award Number: W81XWH-20-1-0117

TITLE: The Use of High-Quality Chemical Tools to Rescue TBK1 Function and Identify Novel ATP-Competitive Targets in ALS

PRINCIPAL INVESTIGATOR: Dr. Alison Axtman, Ph.D.

CONTRACTING ORGANIZATION: University of North Carolina at Chapel Hill

REPORT DATE: SEPTEMBER 2023

TYPE OF REPORT: Final Report

PREPARED FOR: U.S. Army Medical Research and Development Command
Fort Detrick, Maryland 21702-5012

DISTRIBUTION STATEMENT: Approved for Public Release;
Distribution Unlimited

The views, opinions and/or findings contained in this report are those of the author(s) and should not be construed as an official Department of the Army position, policy or decision unless so designated by other documentation.

REPORT DOCUMENTATION PAGE

Form Approved
OMB No. 0704-0188

Public reporting burden for this collection of information is estimated to average 1 hour per response, including the time for reviewing instructions, searching existing data sources, gathering and maintaining the data needed, and completing and reviewing this collection of information. Send comments regarding this burden estimate or any other aspect of this collection of information, including suggestions for reducing this burden to Department of Defense, Washington Headquarters Services, Directorate for Information Operations and Reports (0704-0188), 1215 Jefferson Davis Highway, Suite 1204, Arlington, VA 22202-4302. Respondents should be aware that notwithstanding any other provision of law, no person shall be subject to any penalty for failing to comply with a collection of information if it does not display a currently valid OMB control number. **PLEASE DO NOT RETURN YOUR FORM TO THE ABOVE ADDRESS.**

1. REPORT DATE	**2. REPORT TYPE**	**3. DATES COVERED**
SEPTEMBER 2023	Final Report	1 April 2020 – 31 May 2023

4. TITLE AND SUBTITLE

The Use of High-Quality Chemical Tools to Rescue TBK1 Function and Identify Novel ATP-Competitive Targets in ALS

5a. CONTRACT NUMBER
W81XWH-20-1-0117

5b. GRANT NUMBER
W81XWH-20-1-0117

5c. PROGRAM ELEMENT NUMBER

6. AUTHOR(S)
Alison Axtman, Thomas Durcan

E-Mail: alison.axtman@unc.edu

5d. PROJECT NUMBER

5e. TASK NUMBER

5f. WORK UNIT NUMBER

7. PERFORMING ORGANIZATION NAME(S) AND ADDRESS(ES)

University of North Carolina at Chapel Hill
Chapel Hill, NC 27599-5023

McGill University
Montreal, Quebec, Canada H3A 0G4

8. PERFORMING ORGANIZATION REPORT NUMBER

9. SPONSORING / MONITORING AGENCY NAME(S) AND ADDRESS(ES)

U.S. Army Medical Research and Development Command
Fort Detrick, Maryland 21702-5012

10. SPONSOR/MONITOR'S ACRONYM(S)

11. SPONSOR/MONITOR'S REPORT NUMBER(S)

12. DISTRIBUTION / AVAILABILITY STATEMENT
Approved for Public Release; Distribution Unlimited

13. SUPPLEMENTARY NOTES

14. ABSTRACT
We are developing chemical tools and biological reagents to interrogate the regulation of kinase-mediated biological pathways as new avenues to reduce the accumulation of toxic protein aggregates in ALS. TDP-43 is the most commonly misfolded and deposited protein in ALS. Failure of the autophagy system is one mechanism that allows proteins like TDP-43 to accrue in aggregates. TBK1 is a human protein kinase that plays an essential role in autophagy and which, through multiple genetic studies, has been confirmed as a protein that exhibits inactivating mutations in ALS patients. We have identified linkable compounds that potently engage TBK1 in cells and several putative TRAF3-recruiting ligands. These are currently being covalently linked to produce the first TBK1-activating activation-targeting chimera (ATTACs). As an alternative approach, we have identified the chemical probes from two distinct chemical series that inhibit casein kinase 2 (CK2), which indirectly activates TBK1. We have and will continue to improve the physical properties of SGC-CK2-1 (from series 1) to make it suitable for *in vivo* use. In parallel, we have designed and are preparing a CK2 degrader based on these two scaffolds. Furthermore, through development of a novel TDP-43 aggregation assay in stem cell-derived motor neurons, we aim to identify protein kinases that, when modulated, reduce the deposition and/or promote the clearance of misfolded proteins. We have generated motor neurons harboring ALS-relevant mutant TDP-43 and characterized expression of mutant versus wild-type (WT) TDP-43 during differentiation as well as viability of these cells. We have also developed a methodology to quantify the nuclear to cytoplasmic translocation of TDP-43. We have confirmed that mutations in TDP-43 elicit subtle changes in its translocation propensity and phosphorylation.

15. SUBJECT TERMS
ALS, TDP-43, iPSC, TRAF3, TBK1, ATTAC, CK2, chemical probe, CX-4945, pyrazolopyrimidine, naphthyridine

16. SECURITY CLASSIFICATION OF:			**17. LIMITATION OF ABSTRACT**	**18. NUMBER OF PAGES**	**19a. NAME OF RESPONSIBLE PERSON**
a. REPORT	**b. ABSTRACT**	**c. THIS PAGE**			USAMRDC
U	U	U	UU	131	**19b. TELEPHONE NUMBER** *(include area code)*

Table of Contents

Page

Introduction……..……..…...…...4

Body……..…...5

Key Research Accomplishments…….……16

Reportable Outcomes…….……18

Conclusion…….21

References…….22

Appendices…….……...24

1, INTRODUCTION

Accumulation of protein and RNA aggregates is a pathological hallmark in amyotrophic lateral sclerosis (ALS) patients. Misfolded wild-type (WT) and mutant proteins deposit and form aggregates that are toxic to motor neurons (MNs), contributing to their degeneration in ALS patients. The protein most commonly found within cytoplasmic inclusions in MNs from ALS patients is transactive response DNA-binding protein 43 (TDP-43).[1] While only 2% of familial ALS cases are linked to mutations in the TDP-43 gene (TARDBP), TDP-43-positive inclusions have been identified in nearly 97% of ALS patients, irrespective of whether they suffer from familial or sporadic disease.[2] Protein aggregation in ALS is exacerbated by failure of the autophagy system, which permits accumulation rather than clearance of aggregates. That impaired autophagy exacerbates ALS pathology and drives its progression supports that identification of target proteins that regulate autophagy is of therapeutic interest. Loss-of-function mutations in TANK-binding kinase (TBK1), an autophagy regulator, are genetically linked with ALS.[1, 3] TBK1 is highly expressed in neurons and plays essential roles in both innate immunity and autophagy. Studies that explore TBK1 function, pathological findings, and known ALS pathogenic mechanisms support that autophagy is the major pathway impacted by TBK1 mutations and that targeting this kinase could slow or halt ALS progression.[3] High-quality chemical tools that rescue or activate TBK1 function, either through directly acting on TBK1 or indirectly modulating TBK1 via inhibition of casein kinase 2 (CK2), represent a novel ALS therapeutic strategy. In tandem, pursuit of an unbiased strategy to identify a small molecule that reduces translocation and/or seeding of TDP-43 in MNs could pinpoint essential aggregation regulators. Targeting protein aggregation and/or autophagy has not been pursued as a clinical strategy for ALS. If successful, this approach would modify the course of disease and slow its progression, giving patients a much more effective therapeutic option than they currently have.

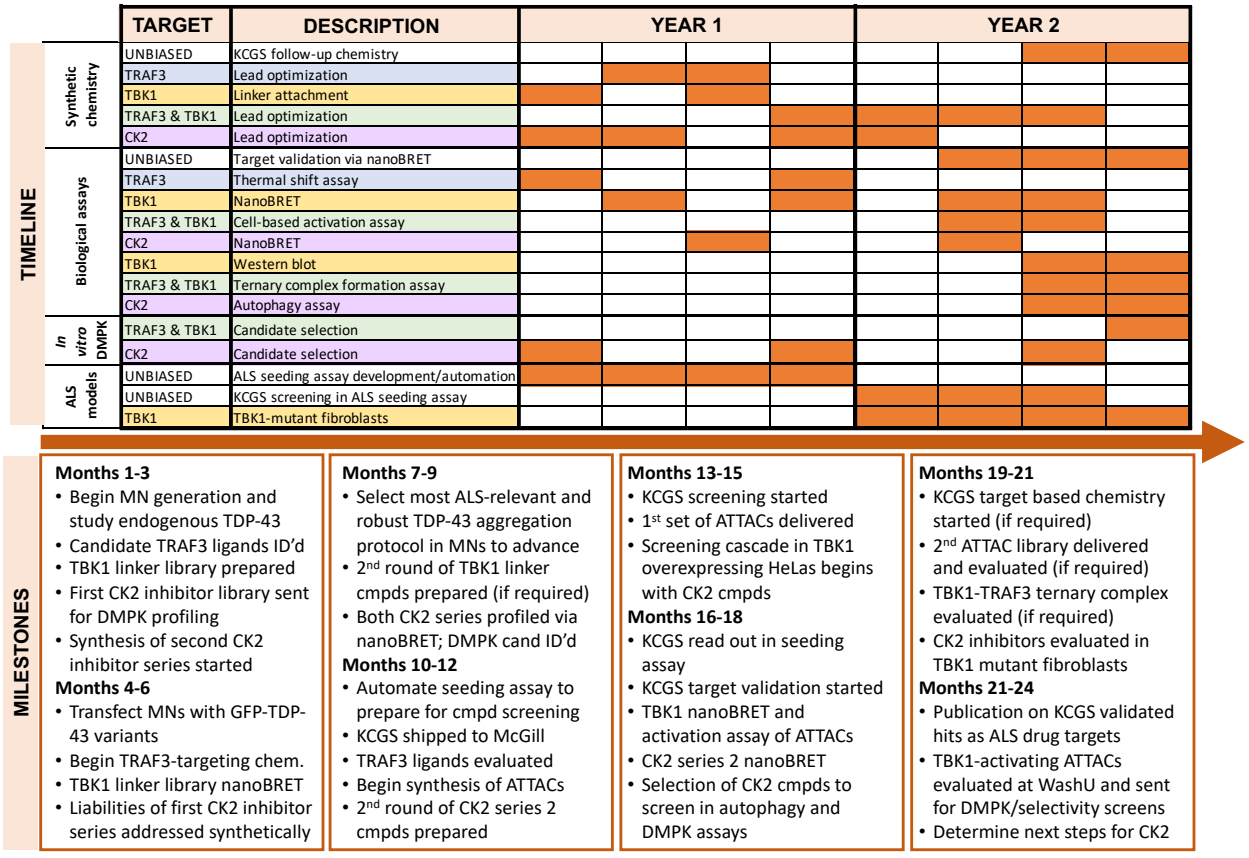

Figure 1. Timelines and milestones for entire award period from original grant proposal.

2. KEYWORDS: ALS, TDP-43, iPSC, TRAF3, TBK1, ATTAC, CK2, chemical probe, CX-4945, pyrazolopyrimidine, naphthyridine

BODY

3. ACCOMPLISHMENTS, 4. IMPACT, and 5. CHANGES/PROBLEMS:

In our grant proposal we set out to accomplish the following **Hypothesis or Objective:** *Successful completion of this project will yield several key compounds and biological assays that target essential proteins in ALS-propagating pathways. Discovery of previously untapped biological targets as well as pre-clinical candidates that reduce protein aggregation provide potential to offer new ALS treatment options.* We defined specific aims, which are included in the following sections, to enable delivery of specific chemical and biological reagents. Our progress was framed in terms of these aims as well as a defined timeline/milestone Gantt chart provided in the grant proposal (Figure 1).

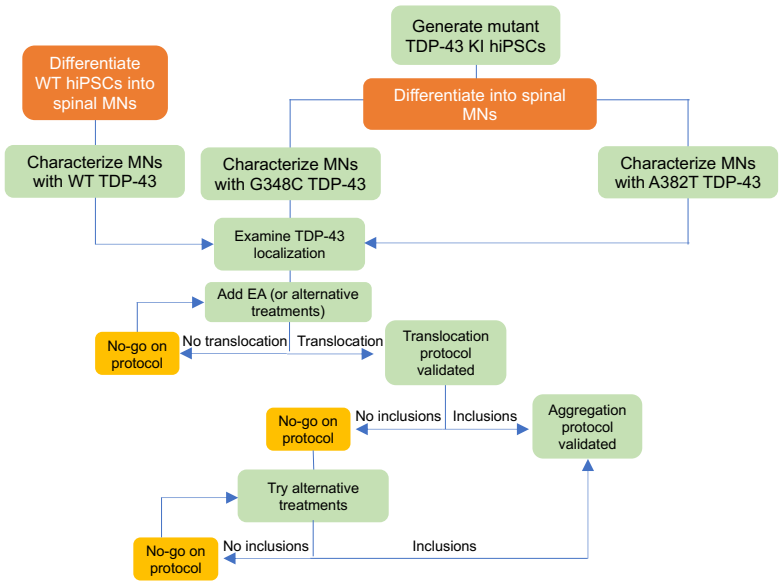

Figure 2. Aim 2 decision tree with edits to the original workflow in light green boxes.

Aim 1. Screen kinase chemogenomic set (KCGS) to identify new ATP-binding protein targets that reduce seeding of protein aggregates. In addition to the design and profiling of targeted small molecules in Aims **2** and **3**, we planned to screen our curated set of 188 potent and narrowly selective kinase inhibitors known as KCGS (Kinase Chemogenomic Set). Details related to the development and kinome coverage of KCGS were published during year one of the award period.[4, 5] Our plan was to screen KCGS in newly developed assays that examined whether TDP-43 translocation and/or aggregation is impacted by small molecule kinase inhibitors. Further development of these assays has been one of the focus areas for the second year of the award period and has continued into the NCE.

As shown in Figure 2, in our workflow that outlined establishment of this TDP-43 aggregation assay, we modified a few steps. Instead of working with artificial GFP-labeled wild-type (WT) or mutant TDP-43, we have opted to use antibodies to visualize unmodified TDP-43. To accomplish this, we knocked-in mutant TDP-43 (two ALS-relevant mutants: G348C and A382T) into human induced pluripotent stem cells (hiPSCs) and differentiated them into spinal motor neurons (MNs), alongside WT, isogenic control hiPSCs. During differentiation, cells were stained and analyzed via qPCR for markers of

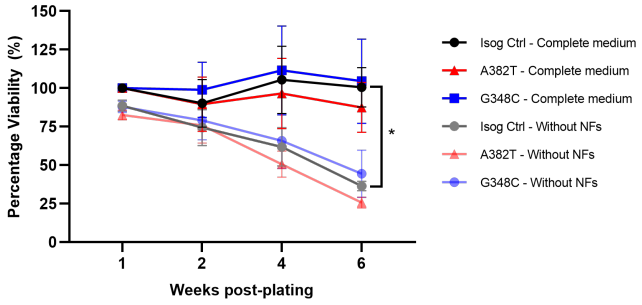

Figure 3. Glutamate-induced excitotoxicity assay results when neuronal viability was assessed in culture with and without growth factors present (n = 4).

differentiation and imaged for their ability to form neuronal networks. TDP-43 transcript and protein levels were analyzed during differentiation and in final MNs, blotting to identify differences, including within the soluble and insoluble fractions. No differences in WT and mutant TDP-43 expression were noted across genotypes and developmental stages. Moreover, no discernible changes in neuronal viability were observed up to six weeks in culture in the presence or absence of growth factors (Figure 3).

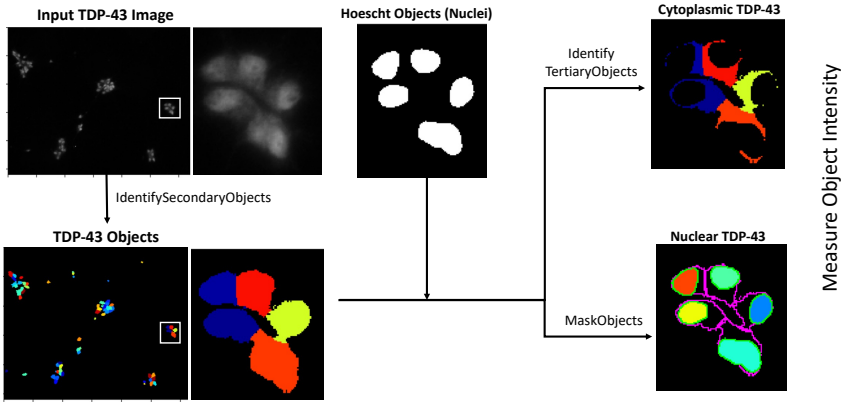

Figure 4. CellProfiler pipeline to quantify TDP-43 translocation.

Next, we monitored localization of TDP-43 in fully differentiated spinal MNs. TDP-43 predominantly resides within the nucleus, binds both DNA and RNA, and plays roles in RNA stabilization, splicing, and translational regulation.[6] In ALS, however, TDP-43 translocates from the nucleus into the cytoplasm where it becomes a major component of ubiquitinated inclusions.[7, 8] Since TDP-43 mutations are rare, mechanisms like oxidative stress have been implicated to drive this nuclear to cytoplasmic translocation.[9] We imaged the localization of WT and mutant TDP-43 using N- and C-terminal antibodies, and found both to be almost exclusively nuclear. In our hands, treatment of MNs with ethacrynic acid (EA) induced a limited amount of TDP-43 translocation (also referred to as mislocalization). No toxicity and some translocation were observed following 5-hour EA treatment at 30, 50, or 70 µM. The observation of diminished bright nuclear staining induced by EA treatment was interpreted as TDP-43 moving into the cytoplasm. We also assessed TDP-43 phosphorylation using antibodies for phosphorylated TDP-43, enabling quantification of phospho-TDP-43 mean intensity and total phospho-TDP-43-positive puncta.

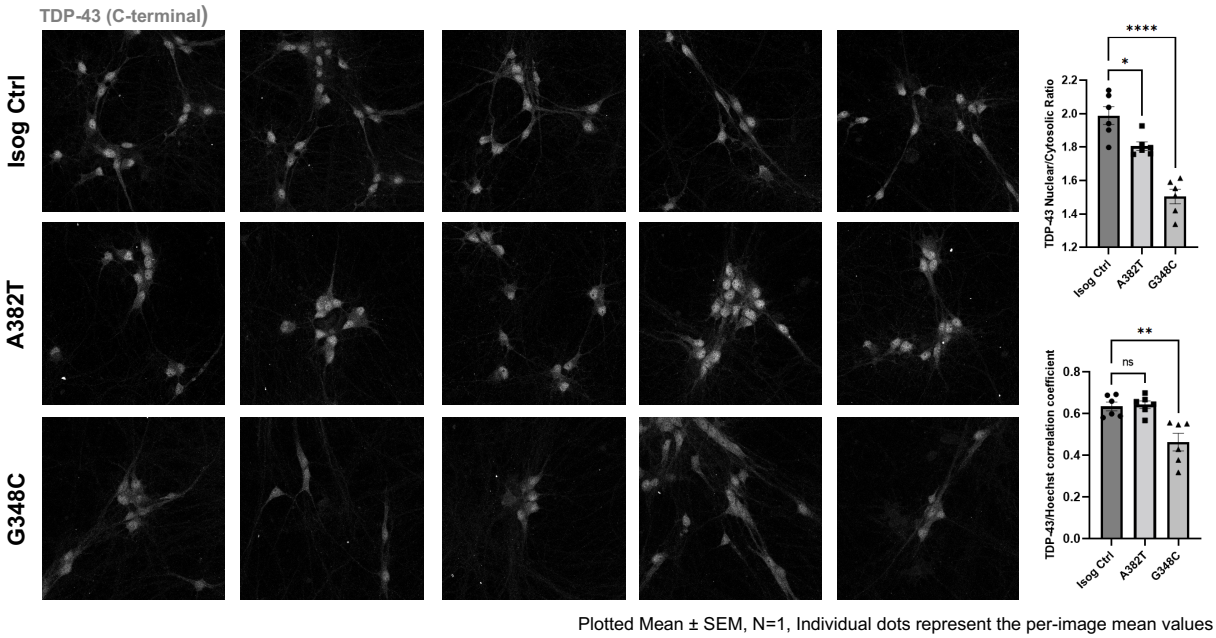

Plotted Mean ± SEM, N=1, Individual dots represent the per-image mean values

Figure 5. Images and quantification of TDP-43 cytoplasmic mislocalization in mutant MNs (six weeks).

We developed a method to quantify TDP-43 translocation using CellProfiler. This method identifies the TDP-43 staining within the image, subtracts out the nucleus (stained with Hoescht), and allows quantification of both cytoplasmic and nuclear TDP-43 (Figure 4). The addition of oxidative/ER stressors (glutamate or cyclopiazonic acid, for example) either alone or in combination with EA did not induce robust TDP-43 relocalization. In parallel, we attempted to identify chemical agents that elicit cytoplasmic TDP-43 aggregation. Based on the hypothesis that phosphorylation of TDP-43 promotes its aggregation, we blotted for the presence of p-TDP-43 to pinpoint aggregates, but did not see observe a significant increase in pharmacologically-induced aggregation.[10-12] Building on these initial findings and using the image analysis pipeline, we matured MNs for up to six weeks and were able to quantify changes in cytoplasmic translocation in MNs harboring G348C TDP-43 (Figure 5) and increased phosphorylation of cytoplasmic TDP-43 in MNs with the other mutant TDP-43 line (A382T) (Figure 6). Finally, the behavior of mutant TDP-43 versus WT MNs was examined. Mutant and WT TDP-43 MNs were found to demonstrate alterations in spontaneous neuronal activity, such that both mutant lines had lower mean firing rates. In addition, MNs harboring mutant TDP-43 exhibited synaptic marker expression abnormalities, which led us investigate and conclude that TDP-43 variants perturb the expression of synapsin I post-transcriptionally.

Since the project inception, we have pivoted our strategy along the way, made improvements to the original proposed workflow, and focused on delivering a more physiologically relevant and robust assay because of these modifications. The discoveries made as a result of the Aim 1 studies have been summarized in a recently submitted pre-print.[13]

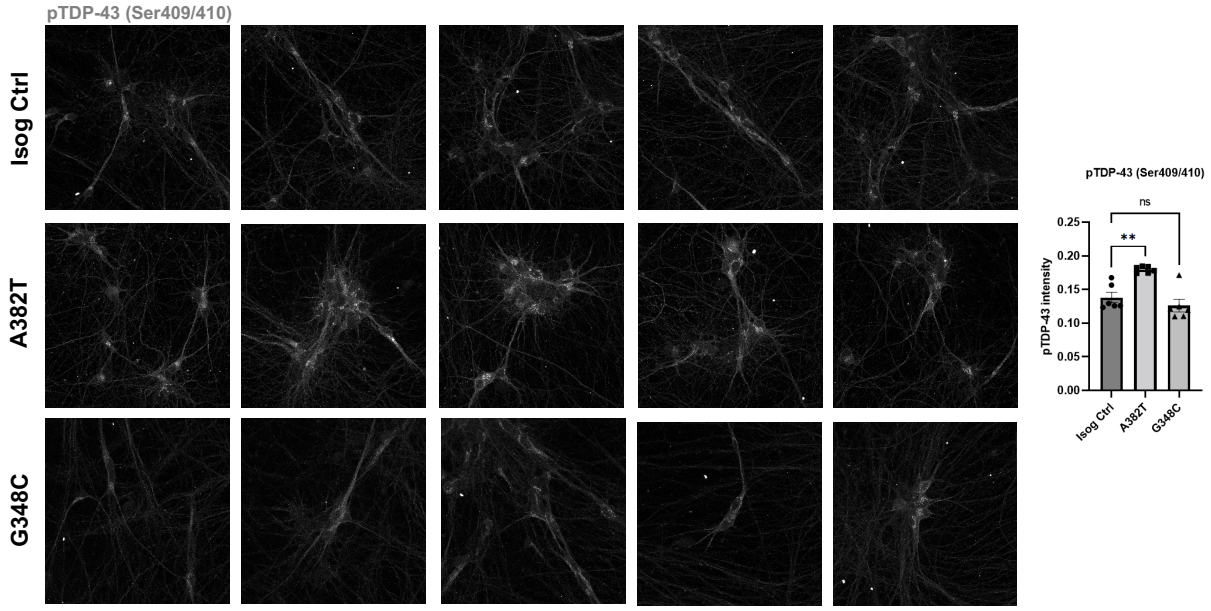

Plotted Mean ± SEM, N=1, Individual dots represent the per-image mean values

Figure 6. Images and quantification illustrate abundant punctate cytosolic phospho-TDP-43 staining in A382T MNs, but not G348C MNs, when compared with isogenic controls.

Aim 2. Develop a TBK1-activating activation-targeting chimera (ATTAC). As a departure from traditional small molecule kinase screening campaigns that aim to identify *inhibitors* of substrate phosphorylation, we aim to develop compounds that *promote* TBK1 auto-phosphorylation and its resultant activation. One type of ubiquitination, K63-linked ubiquitination (UbK63), activates specific protein kinases, including TBK1.[14-16] UbK63 is a known activation step for TBK1, and it triggers TBK1 auto-phosphorylation. Based on this endogenous route of activation, we hypothesize that a heterobifunctional molecule can be designed to recruit an E3 ligase to TBK1 and promote its UbK63, leading to its activation. To explore this hypothesis, we

sought to prepare novel ATTACs that link a potent TBK1-targeting inhibitor and a ligand for an E3 ligase responsible for UbK63 of TBK1 (TRAF3).

As shown in Figure 7, assembly of ATTACs relies both on identification of a warhead that recruits TBK1 and a ligand for TRAF3. During year 1, we worked on a series of cell-active, pyrimidine-based inhibitors of TBK1, which have since been published as a pre-print and in *J*

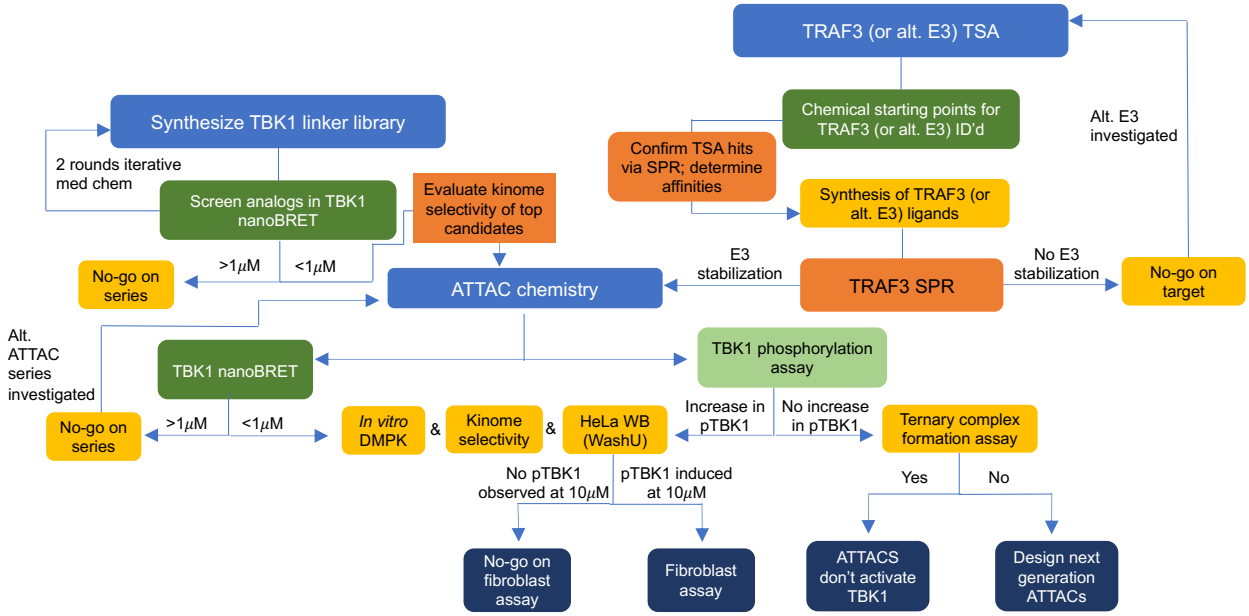

Figure 7. Aim 2 decision tree with an edit to the original workflow in a light green box.

Med Chem.[17, 18] In parallel, potent lead TBK1 inhibitors were modified to probe where a linker could be attached without compromising TBK1 cellular target engagement. Since many exemplars within the resultant library of 33 analogs retained potent TBK1 cellular target engagement, we next profiled the kinome-wide selectivity (screened at 1 μM against 403 human wild-type kinases) of many members. While none of the analogs were found to be exceptionally selective, AA-CS-8-008 and AA-CS-8-010 were more potent and selective analogs than their parent (AA-CS-1-017) and were chosen as the best candidates to move forward (Table 1 and Figure 8). Selectivity data included in Table 1 is expressed as a selectivity score (S_{10}(1 μM)) and the corresponding number of kinases that

Table 1. Kinome-wide screening results of TBK1-targeting compounds.

Compound	Parent compound	S_{10}(1 μM)	Number of kinases with PoC <10
AA-CS-1-005	N/A	0.154	62
AA-CS-1-007	N/A	0.02	8
AA-CS-1-017	N/A	0.223	90
AA-CS-6-003	AA-CS-1-005	0.333	134
AA-CS-6-004	AA-CS-1-005	0.146	59
AA-CS-6-005	AA-CS-1-017	0.273	110
AA-CS-6-016	AA-CS-1-017	0.218	88
AA-CS-6-022	AA-CS-1-017	0.211	85
AA-CS-8-001	AA-CS-1-017	0.226	91
AA-CS-8-002	AA-CS-1-017	0.303	122
AA-CS-8-006	AA-CS-1-017	0.144	58
AA-CS-8-007	AA-CS-1-017	0.164	66
AA-CS-8-008	AA-CS-1-017	0.134	54
AA-CS-8-009	AA-CS-1-005	0.273	110
AA-CS-8-010	AA-CS-1-017	0.154	62

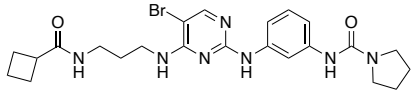

AA-CS-1-017
TBK1 NB IC_{50} = 228 nM
S_{10}(1 μM) = 0.223

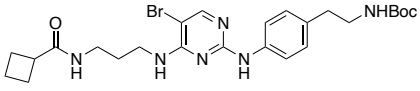

AA-CS-8-010
TBK1 NB IC_{50} = 43.2 nM
S_{10}(1 μM) = 0.154

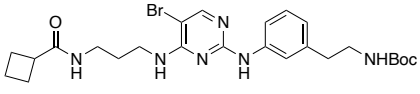

AA-CS-8-008
TBK1 NB IC_{50} = 28.4 nM
S_{10}(1 μM) = 0.134

Figure 8. Structures and associated data for prioritized TBK1 inhibitors selected for ATTAC preparation.

demonstrated <10 PoC (percent of control) when screened. Blue highlighting is used to designate the analogs designed around AA-1-CS-005, while yellow is used for analogs of AA-1-CS-017. AA-CS-8-008 and AA-CS-8-010 were prepared on a larger scale (~150 mg) to enable ATTAC assembly.

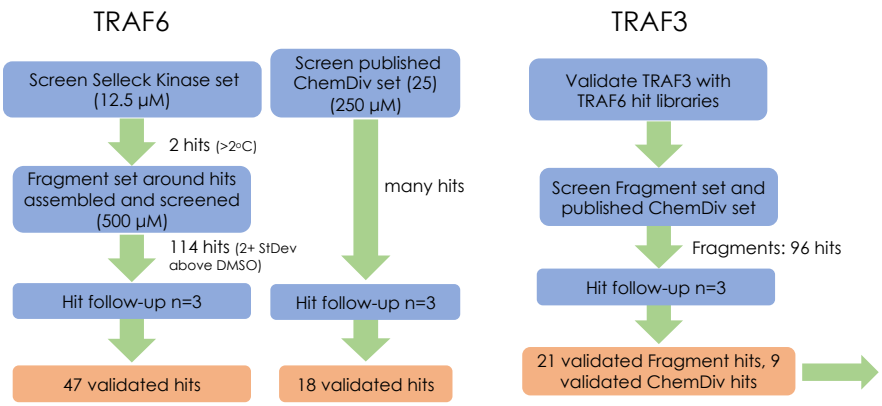

Figure 9. TRAF3 and TRAF6 TSA screening workflow and results.

analysis. First we screened TRAF6 against two libraries in parallel: the Selleck kinase inhibitor set (856 published kinase inhibitors) and a set of analogs (25 in total from ChemDiv) of a putative TRAF6 ligand reported in the literature (C25-140).[20] Screening the Selleck library at 12.5 μM yielded 5 hits that repeated across three runs with average shifts between 1.3–2.5 ºC: AMG900, SLx-2119 (Figure 10), BLU9931, CX6258, and repotrectinib. The C25-140 ChemDiv library was screened at 250 μM to ultimately yield 18 hits that repeated when tested in triplicate. A fragment set of 422 compounds was selected based on substructure and similarity searching around AMG900 and SLx-2119. This set was screened at 500 μM and yielded 47 putative TRAF6 ligands after testing in triplicate. Next, the same workflow and screening concentrations were used to identify putative hits for TRAF3 via TSA. Both the C25-140 ChemDiv library and fragment library of 422 were profiled in parallel. Screening of the ChemDiv library in triplicate yielded 9 hits, while profiling of the fragment library in triplicate resulted in 21 fragment hits. Gratifyingly, there was little overlap in the fragment hits identified for TRAF3 and TRAF6, suggesting that pinpointing selective ligands might be feasible. Our workflow and results are summarized in Figure 9.

To assess whether the binding observed via TSA was recapitulated in an orthogonal assay, we worked with a reputable SPR vendor who assessed binding to our TRAF3 truncate versus to BRD4, another E3 ligase. This SPR screening effort identified compound **87189** (Figure 10), which binds dose-dependently to TRAF3 with an apparent K_D = 19 μM and more weakly to BRD4 (K_D ~120 μM). Next, to determine whether this compound is a promiscuous compound that binds many proteins, we screened **87189** via SPR against two additional proteins from diverse classes. The results indicated that **87189** could bind somewhat indiscriminately to many proteins but did not deter our interest in its use for TRAF3. We revisited our 422-member fragment library

For the TRAF3-targeting warhead, during year 1 we began with thermal shift assay (TSA) screening to identify a possible ligand.[19] We synthesized the RZ3 domain of both TRAF3 and TRAF6 to screen them in parallel and allow for an initial selectivity

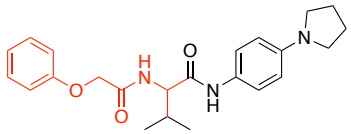

87189
TRAF3 K_D = 19, 67 μM
BRD4 = 120, 185 μM

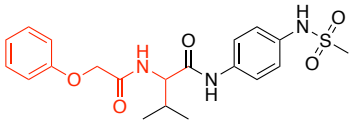

1638
TRAF3 K_D >200 μM
BRD4 NB

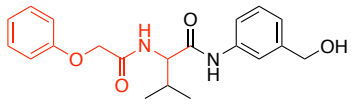

3278
TRAF3 K_D >200 μM
BRD4 NB

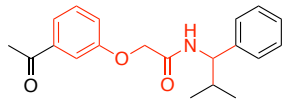

7058
TRAF3 K_D >200 μM
BRD4 NB

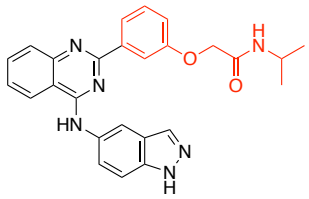

SLx-2119

Figure 10. Structures and associated data for TRAF3 ligands after second round of SPR studies and SLx-2119.

and identified 15 structurally similar analogs of **87189** that had not been screened via SPR. These 15 analogs and 6 analogs that are structurally less similar but still related were screened via SPR to generate structure–activity relationships. In this second study, **87189** was found to bind dose-dependently to TRAF3 with an apparent K_D = 67 μM and with weaker affinity to BRD4 (K_D = 185 μM). Three additional analogs (**1638**, **3278**, and **7058**) bound weakly to TRAF3 with K_D values outside the assay range (>200 μM) and no apparent affinity for BRD4 (Figure 10). The remaining 18 compounds were either found to bind weakly to both TRAF3 and BRD4 (8 analogs, K_D values >200 μM) or not bind either protein (10 analogs). Figure 10 shows the structures of the potential lead series as well as SLx-2119 and highlights in red that these compounds share structurally similarity.

Based on the promising results observed for **87189**, we prepared a small library of ligands based on **87189** to be used in pulldown (PD) experiments and help confirm the SPR results via an orthogonal method. PD experiments were attempted initially using biotinylated **87189** analogs (Figure 11), SH-SY5Y cell lysate (30 μg), streptavidin-conjugated dynabeads, and TRAF3 antibody (CST #4729), but no TRAF3 was identified in the lysate or pulled down by the ligands. Based on its reported enhanced expression of TRAF3, we pivoted to U87MG cell lysate and attempted a titration experiment with a new TRAF3 antibody (CST #61095). As shown in Figure 10, this new antibody was able to detect TRAF3 (~60 kDa), validating our TRAF3 antibody.

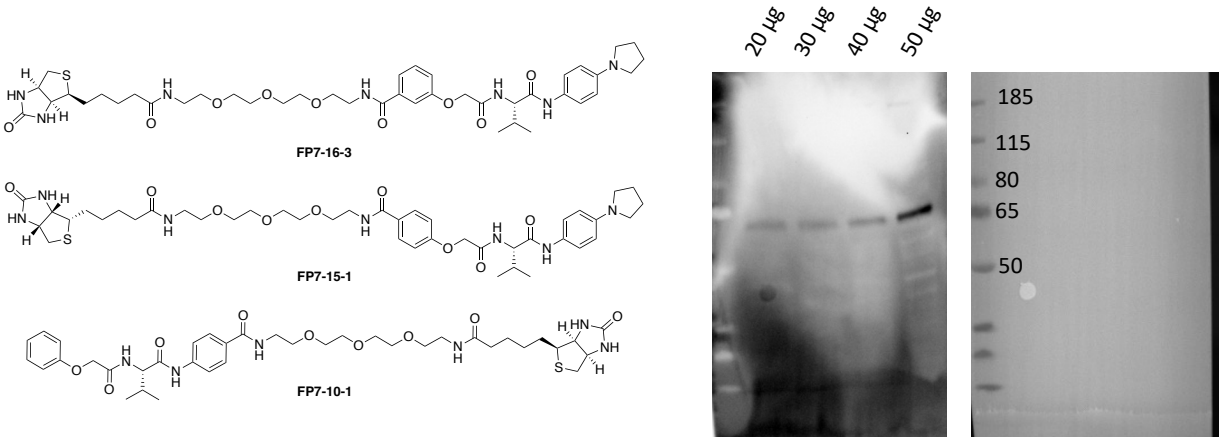

Figure 11. Structures of TRAF3 PD ligands and TRAF3 antibody titration results carried out in U87MG cells.

To build on the results in Figure 10, we synthesized a final library of close analogs of **87189** that included 24 novel analogs and a fresh stock of **87189**. Sixteen of these analogs were modified at a single position, while the remaining eight analogs were prepared with a fixed chiral center at the carbon bearing the isopropyl group. SPR analysis revealed that three analogs (**8512**, **9524**, and **3585**) bind weakly to TRAF3 with fast "on-off" kinetics and do not bind to BRD4 (Figure 12) and two analogs (**3592** and **3587**) bind to both TRAF3 and BRD4 with K_D values within the assay range. **3592** and **3587** were found to bind non-specifically to protein surfaces (Figure 12). Unfortunately, both the previous stock and resynthesized **87189** demonstrated binding to the BRD4 surface only, while the remainder of compounds did not bind to either protein surface. It was suggested by the SPR vendor that the seemingly aberrant result for **87189** in this round was due to a low Rmax value, and that the values obtained in the first round of screening were optimal. Based on the K_D values in the combined results, we scaled up analogs of **87189** and **3592** with pendant carboxylic acids (2 analogs of each TRAF3 ligand, 20–60 mg of each) for easy attachment of a linker to covalently attach them to the TBK1-targeting warheads (Figure 8) and prepare ATTACs.

During the NCE we decided to pivot in approach slightly. A discussion with an E3 ligase expert surfaced that ligands that bind to the RZ3 domain of TRAF3 would not orient TRAF3

properly to ubiquitinate TBK1. The scaled up TRAF3 ligands were repurposed for the preparation of TRAF3 bifunctional molecules (degraders). Degradation of TRAF3 by final degraders will be analyzed via Western blot using the validated TRAF3 antibody (CST #61095).

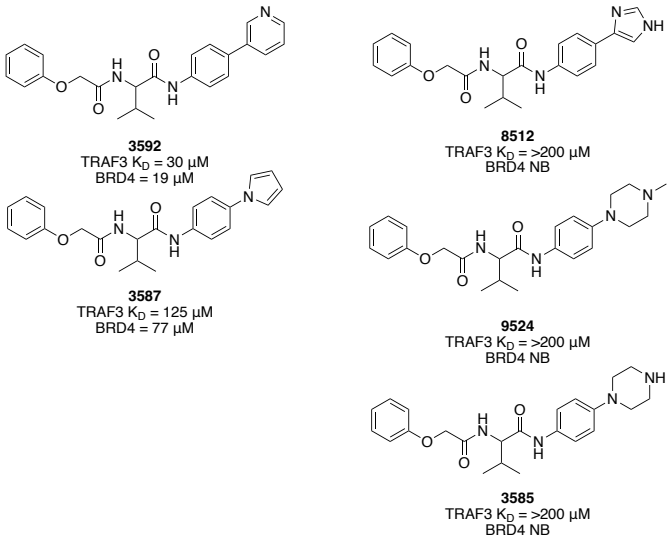

Figure 12. Structures and accompanying data for TRAF3 ligands after third round of SPR studies.

We decided that we should not be so focused on TRAF3 as the E3 ligase to accomplish TBK1 activation. Instead, we have plans to work with the UNC CRISPR Screening Facility to run an arrayed screen to identify E3 ligases capable of eliciting K63-linked ubiquitination of TBK1. Immunoprecipitation experiments using transfected cells will be run to confirm CRISPR screening results. If an E3 ligase ligand is available, we can then design and synthesize bifunctional molecules that promote K63-linked ubiquitination of TBK1 by bringing TBK1 and the E3 ligase in proximity to one another.

Relative to our initial proposed timeline and milestones, the delays posed by COVID-19 set us back slightly. While we intended to begin ATTAC synthesis before the end of year 1, changes in personnel, including loss of two funded scientists from UNC slowed us down. In year two, we were delayed by slow turnaround on SPR studies as well as supply chain shortages and late delivery of custom synthesis products still due to COVID-19. The Ukraine crisis in 2022 made it impossible to get reagents and final products out of Ukraine, which was problematic for us since we rely heavily on Ukrainian companies such as Enamine and Chemspace for chemistry needs.

Aim 3. Develop CK2 inhibitors that inhibit p62 (nucleoporin 62) phosphorylation and indirectly activate TBK1. Autophagy adapter p62 (nucleoporin 62) is among the most well-

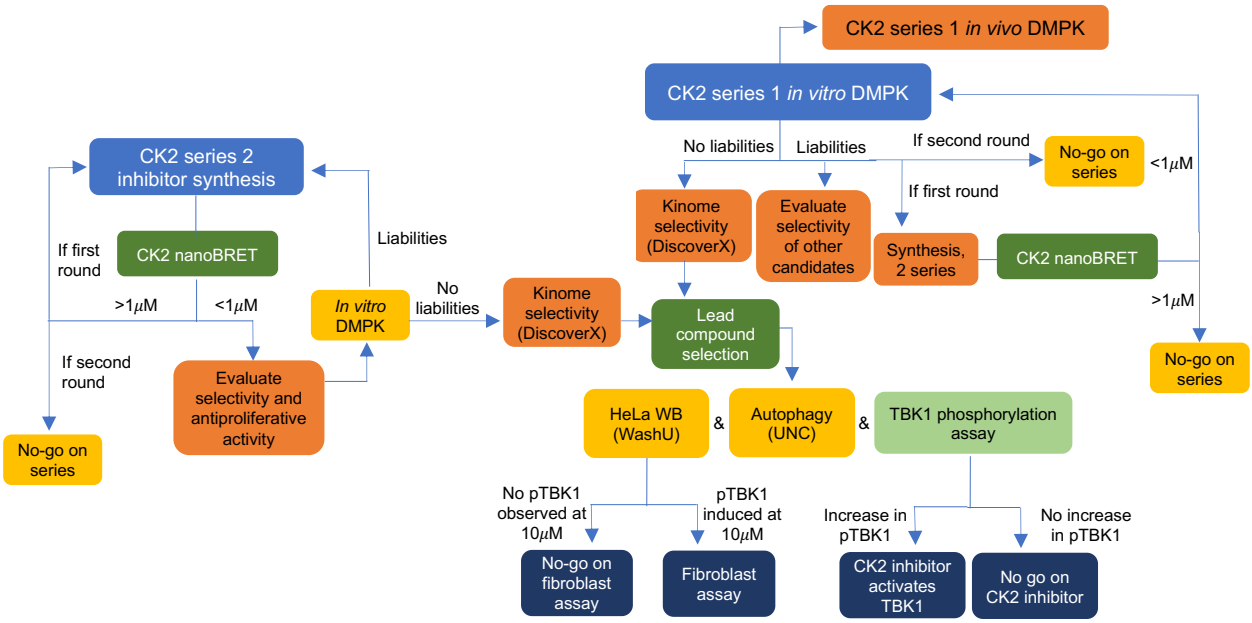

Figure 13. Aim 3 decision tree with edits to the original workflow in light green boxes.

characterized mediators of selective degradation of aggregated protein in mammalian models and its phosphorylation modulates its clearance capabilities.[21] The CK2α catalytic subunit (CSNK2A1) phosphorylates S403 of the p62 ubiquitin-binding domain, leading to enhancement of its ability to form and clear p62 inclusions.[22] In addition, TBK1 phosphorylates p62, leading to amplification of cargo recognition and its degradation.[23] Elevated expression and activity of CK2 have been associated with a plethora of divergent pathways with roles in disease.[24] The known high expression of CK2 in the mammalian brain coupled with its role as a key regulator of neuronal function has resulted in interest in the exploration of CK2 inhibition as a therapeutic option for neurodegenerative diseases, including AD, PD, and ALS.[25-28]

CK2 is an essential regulator of TBK1 activation at steady state and during viral infection. When exposed to virus, knockdown of CK2 (shCK2α) or genetic ablation of its kinase activity leads to TBK1 hyperactivation as well as interferon induction. Regulation of TBK1 by CK2 is indirect, mediated by proteins that have not yet been defined.[29] Since p62 phosphorylation at S403 is essential for autophagy to proceed and is mediated by CK2, it is proposed TBK1 may be recruited to compensate for loss of CK2.[30] When two human cell lines were treated with a small molecule CK2 inhibitor (TBB) *without* co-stimulation or viral infection, time- and dose-dependent TBK1 activation and interferon induction was observed.[29] TBB is not an optimal choice of inhibitor to study CK2 due to its lack of potency (1.6 μM) and limited knowledge surrounding its selectivity and toxicity.[31] We recognized a need for the development of potent and selective chemical probes to study CK2 and synthesized two CK2 chemical probes from structurally distinct chemical series (Figure 13). Among other uses, these probes can be employed to interrogate how CK2 inhibition mediates TBK1 activation and TBK1-mediated autophagy. These studies will help determine whether CK2 inhibitors will be useful as ALS therapeutics. Our first CK2 chemical probe, SGC-CK2-1 (Figure 15), emerged from "series 1" in Figure 13.[32, 33] We demonstrated that this compound blunts a neuroinflammatory response in stem cell derived microglia and outperforms a widely used, clinical phase CK2 inhibitor (CX-4945) when the two were directly compared (Figure 14). This data supports a beneficial outcome of CK2 inhibition to ALS patients since SGC-CK2-1 protected them from an inflammatory insult. We published a paper that captures this work in *Front Mol Neurosci*.[34]

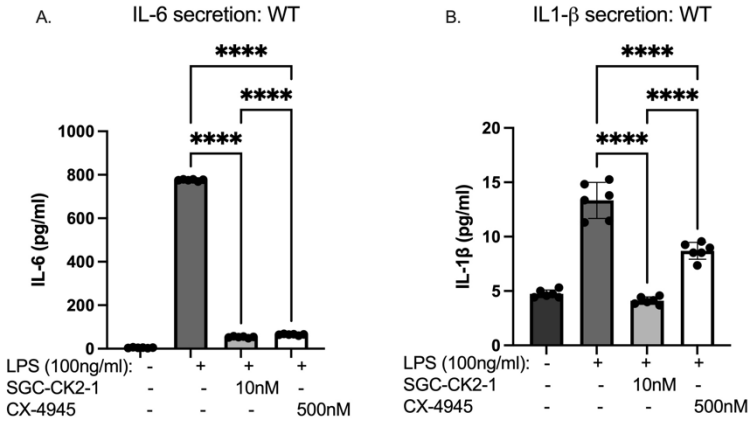

Figure 14. SGC-CK2-1 reduces pro-inflammatory cytokine secretion more effectively than CX-4945 in stem cell-derived microglia (MGLs). MGLs were stimulated with LPS and simultaneously treated with either SCG-CK2-1 or CX-4945 for 24 hours. In all conditions, SGC-CK2-1 more effectively inhibited both IL-6 and IL1-β cytokine secretion into the culture media than CX-4945. These data represent three independent differentiations. **** $p \leq 0.0001$; *** $p = 0.0006$; **$p = 0.0024$. Error bars indicate the mean +/- SD for each treatment.

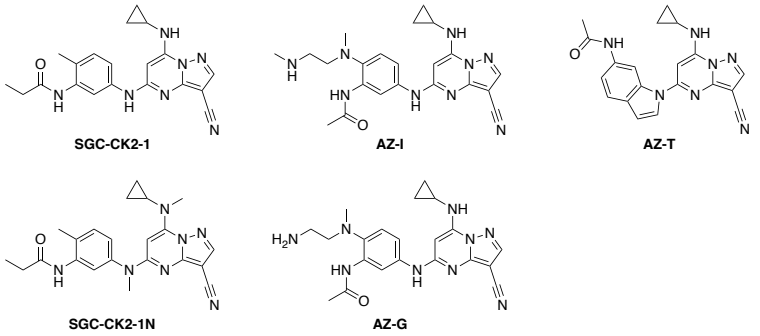

Figure 15. Structures of SGC-CK2-1, negative control (SGC-CK2-1N), and analogs from pyrazolopyrimidine series (series 1 in Figure 13).

We evaluated the developability of SGC-CK2-1, analogs from the library from which it was selected, and its structurally related negative control compound

(SGC-CK2-1N, Figure 15) during year one. We identified that this series demonstrates suboptimal logD values, kinetic solubility in aqueous buffer, and mouse liver microsomal stability. Evaluation of *in vivo* pharmacokinetic (PK) properties when male CD-1 mice were dosed at 10 mg/kg IP confirmed that our chemical probe as well as analogs from the same chemical series were too quickly metabolized for *in vivo* use. We modified in parallel both the Aniline (SGC-CK2-1, AZ-G, and AZ-I in Figure 15) and Indole (AZ-T in Figure 15) scaffolds (Figure 16) to improve the *in vivo* stability of the pyrazolopyrimidines while maintaining structural moieties that make essential interactions with CK2. We employed two computational models to predict that the 7-position cyclopropyl amine was a site of P450 metabolism and thus could be modified to remove a potential site of metabolic liability (Figure 16).[35, 36] The metabolic issues of SGC-CK2-1 and related pyrazolopyrimidines have been summarized in a recent pre-print that is also in press at *ACS Omega*.[37, 38]

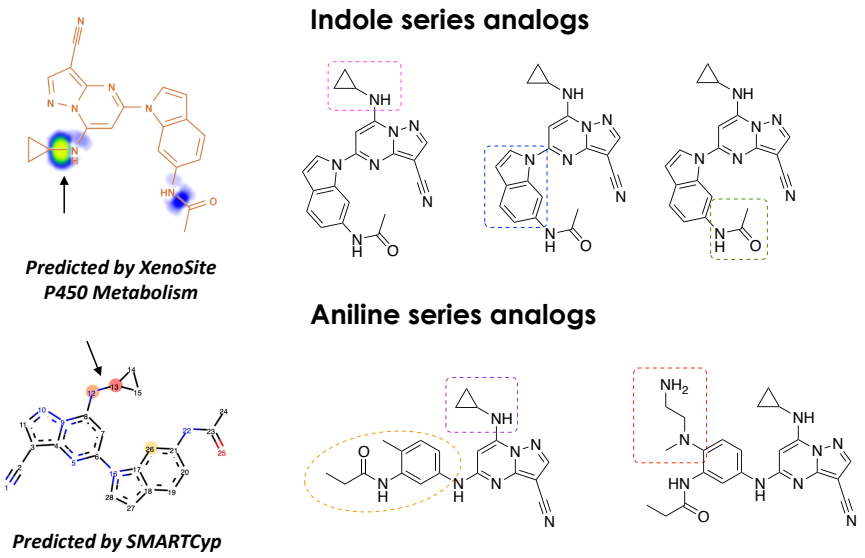

Figure 16. Sites of metabolism and analog design strategy.

More than 150 analogs have been synthesized with structural modifications that address potential sites of metabolic liability. Five promising analogs from this library with structural modifications aimed at addressing liabilities colored pink or blue are included in Figure 17. These analogs are potent in the CK2α' NanoBRET assay (IC_{50} values <400 nM) and exhibit good kinome-wide selectivity scores (S_{10}(1 μM) <0.02). Importantly, they also demonstrate improved kinetic solubility and mouse liver microsomal stability when compared with SGC-CK2-1 (Figure 17). Members of this pyrazolopyrimidine library with promising microsomal stability have been advanced to *in vivo* PK studies in mice. A collaboration with scientists at Takeda is facilitating conversation around these compounds. Informed by data collected to data, synthetic efforts are ongoing to further improve this series and deliver a suitable compound for *in vivo* use. In parallel, efforts are currently underway to convert SGC-CK2-1 into a CK2 degrader. Such a molecule will provide a method via which we can further probe the role of CK2 in driving ALS pathology.

For our orthogonal chemical series (series 2 in Figure 13), we prepared some

Compound	CK2α' NB IC_{50} (nM)	Kinome-wide selectivity score: S_{10}(1 μM)	Mouse Liver Microsomal Stability (% remaining, T=30 min)	Kinetic Solubility (μg/mL)
A	17	0.017 (7)	86.2	55.19
B	216	0.007 (3)	88.5	87.64
C	16	0.01 (4)	83.2	95.71
D	382	0.02 (8)	100.8	1.71
E	104	0.017 (7)	77.7	1.36
SGC-CK2-1	16	0.007 (3)	40.5	1.37

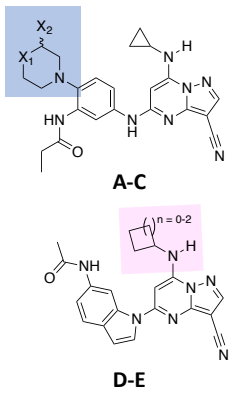

Figure 17. Promising analogs from pyrazolopyrimidine series (series 1) and associated developability data.

exemplified and non-exemplified analogs around the CX-4945 and CX-5011 scaffolds to yield 23 compounds in total. Final compounds were evaluated in the CK2α' and CK2α NanoBRET assays. While a few analogs exhibited solubility problems in 100% DMSO, all demonstrated good to excellent aqueous solubility (Table 2). We initially explored their selectivity for CK2 through profiling the entire library against highly homologous CMGC kinases from the DYRK and HIPK sub-families at 1 μM in corresponding enzymatic assays. Naphthyridine analogs proved to be less selective than pyrazolopyrimidine leads and it was proposed that they likely would inhibit many kinases if broadly profiled. To evaluate this hypothesis and based on the enzymatic panel results, we selected ten analogs from series 2 to send for kinome-wide profiling via DiscoverX *scan*MAX profiling (Table 2). The kinome-wide profiling data, which is captured in the S_{10}(1 μM) column of Table 2, shows the trend of overall selectivity improvements for the Y = N versus Y = CH analogs. With the exception of CX-5033, all compounds demonstrated an improved selectivity score over CX-4945. Compound **2** was found to be the most promising compound when considering its kinome-wide selectivity (S_{10}(1 μM) = 0.007) and was nominated as an orthogonal CK2 chemical probe: SGC-CK2-2 (Figure 18). A co-crystal structure was solved that helps explains its enhanced selectively versus other naphthyridines. To support nomination of SGC-CK2-2, a suitable negative control was prepared (compound 7 in Table 2).

Table 2. Potency and selectivity data for naphthyridine analogs from series 2.

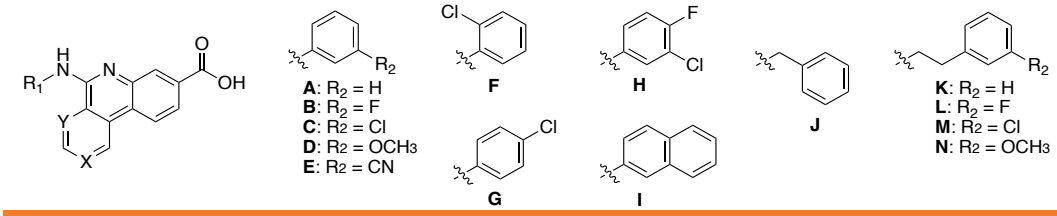

				NanoBRET data		Selectivity data		Solubility data
Compound	**X**	**Y**	**R_1**	**CK2α IC_{50} (nM)**	**CK2α' IC_{50} (nM)**	**S_{10}(1 μM) score[a]**	**# Kinases with PoC <10[b]**	**Kinetic solubility (μM)**
2	N	N	J	920	200	0.007	3	210.8
8	N	N	N	570	93	0.017	7	151.7
9	N	N	M	830	140	0.02	8	109.1
10	N	N	L	930	270	0.022	9	147.0
11	N	N	I	21	6.0	0.025	10	54.3[c]
12	N	N	G	240	25	0.032	13	209.1
13	N	N	B	350	51	0.042	17	192.0
14	N	N	H	110	19			49.1
15	N	N	F	300	42			121.8[c]
16	N	N	A	740	63			168.2
17	N	N	K	550	110			146.4
CX-5011	N	N	E	350	66			66.7
18	N	CH	M	230	17	0.035	14	184.0
19	N	CH	G	430	130	0.05	20	25.3
CX-5033	N	CH	E	4300	1900	0.079	32	131.7
20	N	CH	I	100	22			32.8
21	N	CH	J	1100	450			202.4
22	N	CH	L	300	62			187.7
23	N	CH	B	680	180			236.7
24	N	CH	N	150	19			180.4
25	N	CH	A	1400	420			184.1
26	N	CH	H	220	43			148.4
27	N	CH	K	260	34			171.4
28	N	CH	D	1200	340			190.4
CX-4945	N	CH	C	240	180	0.069	28	277.1
7	CH	N	J	>10000	>10000	0	0	80.4

SGC-CK2-1	NA	NA	NA	36	19	0.007	3	3.7

[a] S_{10}(1 μM): percentage of screened kinases with PoC <10 at 1 μM; [b] PoC: percent of control values determined at 1 μM via DiscoverX *scan*MAX profiling; [c] Insoluble residue noted during solubility assessment.

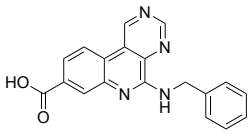

2

S_{10}(1 μM) = 0.007
3 kinases <10 PoC at 1 μM
S_{35}(1 μM) = 0.032
13 kinases <35 PoC at 1 μM

Kinase	DiscoverX PoC value	Assay format	IC_{50} value (nM)
CK2α	0.1	Enzymatic and NB	3.0 and 920
CK2α'	0.2	Enzymatic and NB	<1.0 and 200
DAPK3	6.5	Enzymatic	1500
HIPK1	10	Enzymatic	1800
DAPK2	11	Enzymatic	1500
HIPK3	16	Enzymatic	900
MYLK4	20	Enzymatic	>10000
PIK3CG	23	Enzymatic	5300
PIK3C2G	25	Enzymatic	4500
DYRK1A	28	Enzymatic	760
HIPK2	30	Enzymatic	600
DRAK2	30	Enzymatic	1800
YSK4	34	Enzymatic	3700

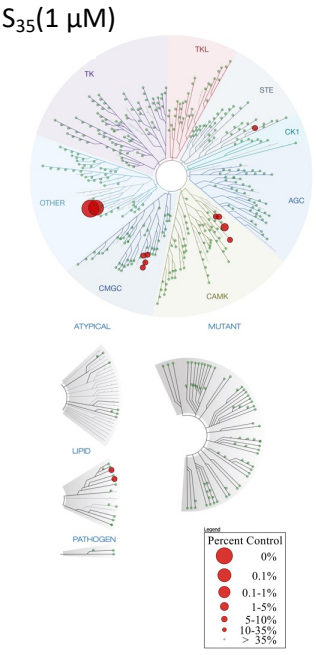

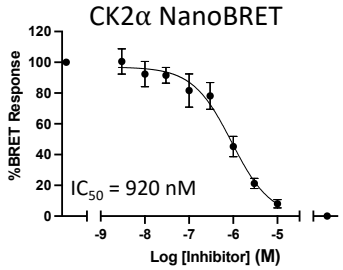

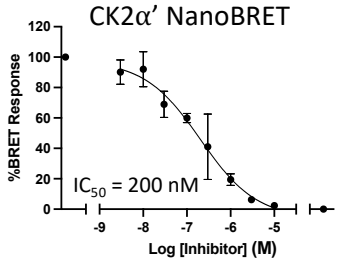

Figure 18. Structure, potency, and selectivity data related to CK2 chemical probe SGC-CK2-2 from series 2. Kinome dendrogram illustrates kinases that bind with PoC <35 when this compound was screened at 1 μM. Assay format used to generate data in the last column of nested table is listed in the preceding column. CK2 NanoBRET assays were run in triplicate (n = 3) with error bars representing standard deviation. PoC = percent of control; NB =

Based on published antiproliferative activity of CX-4945, we collaboratively profiled the entire naphthyridine library as well as CX-4945 and CX-5011 (25 compounds in total) against a panel of Ewing's sarcoma, multiple myeloma, and chordoma cell lines after 5 days treatment at 1 μM. We found that these compounds were not broadly antiproliferative. The STA-ET-1 Ewing's sarcoma cell line was found to be the most sensitive of the cell lines tested. Of the multiple myeloma cell lines evaluated, only two (AMO-1 and L363) of the six cell lines tested were responsive to the series 2 naphthyridines. A summary of the data for the parent naphthyridine inhibitors, SGC-CK2-2 (compound 2), and SGC-CK2-1 are included in Figure 19.

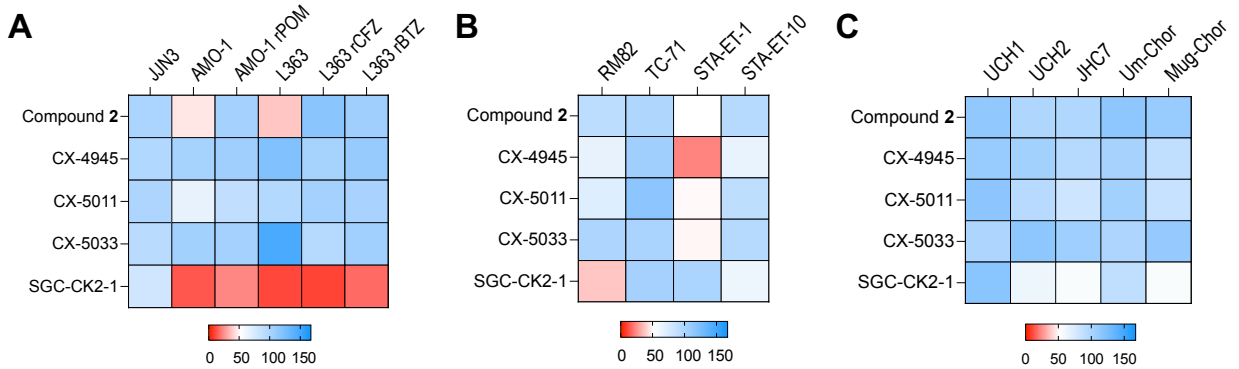

Figure 19. Analysis of impact of naphthyridine and CK2 chemical probes on viability of (A) multiple myeloma, (B) Ewings sarcoma, and (C) chordoma cell lines when dosed at 1 μM. Scale bar defines the color gradient that corresponds with percent viability in the various assays.

A pre-print and publication in *ACS Med Chem Lett* have summarized our work around this scaffold and second CK2 chemical probe.[39, 40] Work is ongoing to improve on the potency of SGC-CK2-2 without compromising its selectivity through continued analog synthesis. In tandem, we have designed a degrader based on SGC-CK2-2 that is being synthesized to support studies aimed at discerning the roles of CK2 in ALS pathology.

We have delivered on most items in our initially proposed timeline and reached nearly all milestones with respect to this Aim (Figure 13). The delays posed by COVID-19 set back advancement of compounds to WUSTL and their ability to evaluate the compounds that we made. Upon completion of degraders based on series 1 and 2, these bifunctional molecules will also be shared with the scientific community.

Key Research Accomplishments

Aim 1

- Published pre-print and peer-reviewed publication in *Int J Mol Sci* about KCGS
- Generated human induced pluripotent stem cells with two ALS-relevant mutant forms of TDP-43 incorporated: G348C and A382T that were successfully used to generate spinal motor neurons
- Characterized transcript and protein levels of mutant versus WT TDP-43 during differentiation, with RNAseq analysis of five replicates across both mutant and control MNs completed, leading to the identification of a number of genes altered across mutant and control lines
- Characterized localization of mutant versus WT TDP-43 in spinal motor neurons without and with treatment with ethacrynic acid
- Demonstrated translocation and phosphorylation is associated with mutations in TDP-43 with maturation of MN cultures
- No changes in MN viability observed with TDP-43 mutations
- Developed methodology to allow quantification of TDP-43 translocation
- Identified alterations in spontaneous neuronal activity of mutant and WT TDP-43 MNs, including lower mean firing rates
- Found that MNs harboring mutant TDP-43 exhibited synaptic marker expression abnormalities
- Concluded that TDP-43 variants perturb the expression of synapsin I post-transcriptionally
- Published pre-print summarizing our observed results in MNs

Aim 2

- Identified several potent TBK1 inhibitors that permeate cells and engage TBK1 in a cellular target engagement assay
- Published pre-print and peer-reviewed publication in *J Med Chem* about this series
- Confirmed GSK8612 to be the best available TBK1 inhibitor in terms of cellular potency and kinome-wide selectivity
- Found that GSK8612 was not tolerant of incorporation of a linker without significant losses in TBK1 cellular target engagement potency
- Prioritized several analogs with linkers attached that maintain potent TBK1 cellular target engagement and demonstrated improved kinome-wide selectivity versus the corresponding parent compound
- Selected and scaled up two TBK1-targeting warheads with linker attached (AA-CS-8-008 and AA-CS-8-010) to enable ATTAC assembly
- Identified several putative TRAF6 ligands via thermal shift assay
- Identified several putative TRAF3 ligands via thermal shift assay

- Confirmed dose-dependent binding of a small molecule ligand (**87189**) to TRAF3 with an apparent K_D = 19/67 μM and some demonstrated binding selectivity over E3 ligase BRD4 (n = 2)
- Identified a ligand (**3592**) that binds TRAF3 with an apparent K_D = 30 μM but also binds to BRD4
- Identified several additional weakly binding TRAF3 ligands that show some selectivity for TRAF3 versus BRD4 via SPR
- Validated a commercially available TRAF3 antibody
- Designed linkable versions of **87189** and **3592** that were scaled-up and repurposed for TRAF3 degraders
- Developed plans to run an arrayed CRISPR screen to identify E3 ligases capable of eliciting K63-linked ubiquitination of TBK1

Aim 3

- Delivered best available chemical probe targeting CK2 from series one: SGC-CK2-1
- Published pre-print and publication in *Cell Chem Biol* about SGC-CK2-1
- Validated that selective CK2 inhibition is not toxic to the majority of cancer cell lines or primary cells
- Demonstrated that SGC-CK2-1 blunts a neuroinflammatory response in stem cell derived microglia and outperforms clinical CK2 agent CX-4945
- Published microglial neuroinflammation results in *Front Cell Neurosci*
- Determined that SGC-CK2-1 has sub-optimal developability properties and requires improvement to be a useful *in vivo* tool compound
- Confirmed that, while it demonstrates improved mouse liver microsomal stability versus SGC-CK2-1, Aniline I suffers from poor kinome-wide selectivity that precludes its use as a high-quality CK2 tool compound
- Prepared more than 150 pyrazolopyrimidine analogs (series 1) to address metabolic liabilities and improve *in vivo* stability
- Delivered several potent CK2 inhibitors that engage CK2 in cells, retain excellent kinome-wide selectivity, and demonstrate improved mouse liver microsomal stability and kinetic solubility versus SGC-CK2-1
- Selected a subset of pyrazolopyrimidine-based CK2 inhibitors for evaluation of *in vivo* mouse PK
- Designed a CK2 degrader based on SGC-CK2-1 (in progress)
- Delivered a series of 23 naphthyridine analogs based on CX-4945 and CX-5011
- Determined that naphthyridines based on CX-4945 (series 2) suffer from poor solubility in DMSO, but good aqueous solubility
- Confirmed that naphthyridine analogs designed around CX-4945 and CX-5011 demonstrate potent engagement of CK2 in cells, but suffer from sub-optimal selectivity when profiled against highly homologous CMGC kinase families
- Showed overall selectivity improvements for the CX-5011 versus CX-4945 naphthyridine analogs
- Demonstrated that series 2 naphthyridines are not broadly antiproliferative when tested against Ewing's sarcoma, multiple myeloma, and chordoma cell lines
- Selected a chemical probe from the naphthyridine series: SGC-CK2-2
- Designed a suitable negative control compound to be offered with this chemical probe
- Co-crystalized SGC-CK2-2 with human CK2α that helps explain its enhanced selectivity
- Demonstrated that SGC-CK2-2 inhibits downstream phosphorylation mediated by CK2
- Designed a CK2 degrader based on SGC-CK2-2 (in progress)

- Published a pre-print and peer-reviewed paper in *ACS Med Chem Lett* to summarize work on naphthyridine series
- Designed and synthesized analogs of SGC-CK2-2 to improve on its CK2 potency (in progress)
- Designed a CK2 degrader based on SGC-CK2-2 (in progress)

6. PRODUCTS:

Reportable Outcomes

Manuscripts, abstractions, presentations

A. Manuscripts and published abstracts

1. Yang, X.; Ong, H. W.; Dickmander, R. J.; Smith, J. L.; Brown, J. W.; Tao, W.; Chang, E.; Moorman, N. J.; Axtman, A. D.; Willson, T. M. Optimization of 3-cyano-7-cyclopropylamino-pyrazolo[1,5-a]pyrimidines toward the development of an in vivo chemical probe for CSNK2. *ACS Omega* **2023**, *In Press*.
2. Durcan, T. M.; Axtman, A. D. Editorial: The next generation of tools and technologies for studying human neurons in a dish. *Front Cell Neurosci* **2023**, *17*, 1196543; doi: 10.3389/fncel.2023.1196543.
3. Davis-Gilbert, Z. W.; Krämer, A.; Dunford, J. E.; Howell, S.; Senbabaoglu, F.; Wells, C. I.; Bashore, F. M.; Havener, T. M.; Smith, J. L.; Hossain, M. A.; Oppermann, U.; Drewry, D. H.; Axtman, A. D. Discovery of a potent and selective naphthyridine-based chemical probe for casein kinase 2. *ACS Med Chem Lett* **2023**, *14*, 432–441; doi: 10.1021/acsmedchemlett.2c00530.
4. Mishra, S.; Kinoshita, C.; Axtman, A. D.*; Young, J. E.* Evaluation of a selective chemical probe validates that CK2 mediates neuroinflammation in an hiPSC-derived microglial model. *Front Mol Neurosci* **2022**, *15*, 824956; doi: 10.3389/fnmol.2022.824956.
5. Drewry, D. H.; Annor-Gyamfi, J. K.; Wells, C. I.; Pickett, J. E.; Dederer, V.; Preuss, F.; Mathea, S.; Axtman, A. D. Identification of pyrimidine-based lead compounds for understudied kinases implicated in driving neurodegeneration. *J Med Chem* **2022**, *65*, 2, 1313–1328; doi: 10.1021/acs.jmedchem.1c00440.
6. Axtman, A. D. Characterizing the role of the dark kinome in neurodegenerative disease – A mini review. *Biochim Biophys Acta Gen Subj* **2021**, *1865*, 130014; doi: 10.1016/j.bbagen.2021.130014.
7. Wells, C.; Drewry, D. H.; Pickett, J. E.; Tjaden, A.; Krämer, A.; Müller, S.; Gyenis, L.; Menyhart, D.; Litchfield, D. W.; Knapp, S.; Axtman, A. D. Development of a potent and selective chemical probe for the pleiotropic kinase CK2. *Cell Chem Biol* **2021**, *28*, 546-558.e10; doi.org/10.1016/j.chembiol.2020.12.013.
8. Wells, C. I.; Al-Ali, H.; Andrews, D. M.; Asquith, C. R. M.; Axtman, A. D.; Dikic, I.; Ebner, D.; Elkins, J.; Ettmayer, P.; Fischer, C.; Frederiksen, M.; Futrell, R. E.; Gray, N. S.; Hatch, S. B.; Knapp, S.; Lücking, U.; Michaelides, M.; Mills, C. E.; Müller, S.; Owen, D.; Picado, A.; Saikatendu, K. S.; Schröder, M.; Stolz, A.; Tellechea, M.; Turunen, B. J.; Vilar, S.; Wang, J.; Zuercher, W. J.; Willson, T. M.; Drewry, D. H. The Kinase Chemogenomic Set (KCGS): An open science resource for kinase vulnerability identification. *Int J Mol Sci* **2020**, *22*, 566; doi: 10.3390/ijms22020566.
9. Wells, C.; Drewry, D. H.; Pickett, J. E.; Tjaden, A.; Krämer, A.; Knapp, S.; Menyhart, D.; Gyenis, L.; Litchfield, D. W.; Axtman, A. D. Development of the first selective chemical probe for the pleiotropic kinase CK2, an emerging target in neurodegenerative disease. *Alzheimer's Dement* **2020**, 16, e12278; doi: 10.1002/alz.12278.
10. Lindsley, C. W.; Axtman, A. D. NeuroChat with Research Assistant Professor Alison Axtman. *ACS Chem Neurosci* **2020**, *11*, 2783–2785; doi: 10.1021/acschemneuro.0c00548.

11. Krahn, A. I.; Wells, C.; Drewry, D. H.; Beitel, L. K.; Durcan, T. M.; Axtman, A. D. Defining the neural kinome: strategies and opportunities for small molecule drug discovery to target neurodegenerative diseases. *ACS Chem Neurosci* **2020**, *11*, 1871–1886; doi: 10.1021/acschemneuro.0c00176.

B. Preprints

1. Lépine, S.; Nauleau-Javaudin, A.; Deneault, E.; Chen, C. X.-Q.; Abdian, N.; Franco-Flores, A. K.; Haghi, G.; Castellanos-Montiel, M. J.; Maussion, G.; Chaineau, M.; Durcan, T. M. Homozygous ALS-linked mutations in TARDBP/TDP-43 lead to progressive synaptic dysfunction in human iPSC-derived motor neurons. *BioRxiv* **2023**, 2023.2003.2022.533562, doi: 10.1101/2023.03.22.533562.
2. Yang, X.; Ong, H. W.; Dickmander, R. J.; Smith, J. L.; Brown, J. W.; Tao, W.; Chang, E.; Moorman, N. J.; Axtman, A. D.; Willson, T. M. Optimization of 3-cyano-7-cyclopropylamino-pyrazolo[1,5-a]pyrimidines toward the development of an in vivo chemical probe for CSNK2. *BioRxiv* **2023**, doi: 10.1101/2023.05.15.540828.
3. Davis-Gilbert, Z. W.; Krämer, A.; Dunford, J. E.; Howell, S.; Senbabaoglu, F.; Wells, C. I.; Havener, T. M.; Smith, J. L.; Hossain, M. A.; Oppermann, U.; Drewry, D. H.; Axtman, A. D. Discovery of a potent and selective naphthyridine-based chemical probe for casein kinase 2. *ChemRxiv* **2022**, doi: 10.26434/chemrxiv-2022-05jcz.
4. Drewry, D.; Annor-Gyamfi, J. K.; Wells, C.; Pickett, J. E.; Axtman, A. Strategy for Lead Identification for Understudied Kinases. *ChemRxiv* **2021**, *14195207*; doi: 10.26434/chemrxiv.14195207.v1.
5. Wells, C.; Drewry, D. H.; Pickett, J. E.; Tjaden, A.; Krämer, A.; Müller, S.; Gyenis, L.; Menyhart, D.; Litchfield, D. W.; Knapp, S.; Axtman, A. D. Development of a potent and selective chemical probe for the pleiotropic kinase CK2. *Cell Press Sneak Peek* **2020**; doi: https://ssrn.com/abstract=3732376.
6. Wells, C.; Drewry, D. H.; Pickett, J. E.; Axtman, A. D. SGC-CK2-1: the first selective chemical probe for the pleiotropic kinase CK2. *ChemRxiv* **2020**, *12296180*; doi: 10.26434/chemrxiv.12296180.
7. Krahn, A. I.; Wells, C.; Drewry, D. H.; Beitel, L. K.; Durcan, T. M.; Axtman, A. D. Defining the neural kinome: strategies and opportunities for small molecule drug discovery to target neurodegenerative diseases. *BioRxiv* **2020**, doi: 10.1101/2020.04.01.020206.
8. Wells, C.; Al-Ali, H.; Andrews, D. M.; Asquith, C. R. M.; Axtman, A. D.; Chung, M.; Dikic, I.; Ebner, D.; Elkins, J.; Ettmayer, P.; Fischer, C.; Frederiksen, M.; Gray, N. S.; Hatch, S.; Knapp, S.; Lee, S.; Lücking, U.; Michaelides, M.; Mills, C. E.; Müller, S.; Owen, D.; Picado, A.; Ramadan, K.; Saikatendu, K. S.; Schröder, M.; Stolz, A.; Tellechea, M.; Treiber, D. K.; Turunen, B. J.; Vilar, S.; Wang, J.; Zuercher, W. J.; Willson, T. M.; Drewry, D. H. The Kinase Chemogenomic Set (KCGS): An open science resource for kinase vulnerability identification. *BioRxiv* **2019**, *886523;* doi: 10.1101/886523.

C. Oral presentations

March 2023:	"Using kinase chemical probes to elucidate disease-propagating pathways in the brain" 265th ACS National Meeting, Indianapolis, IN
March 2023:	"Using kinase chemical probes to elucidate disease-propagating pathways in the brain" University of Miami, Miami, FL
March 2022:	"Casein kinase 2: Not understudied, but still dark" St. Jude Children's Research Hospital, virtual
February 2022:	"Development of a chemical probe for CK2 enables illumination of its function"

Emory University, virtual

July 2021: "Development of Chemical Probes for Kinases Implicated in Neurodegeneration"
Innovations and Transformation in Pharmaceutical Sciences 2021, virtual

March 2021: "Characterizing the Role of the Dark Proteome in Neurodegenerative Disease" SGC Board Meeting, virtual

November 2020: "Design of the first selective chemical probe for the pleiotropic kinase CK2" Target 2035 kick-off webinar, virtual

November 2020: "Casein kinase 2 (CK2): Not understudied but still dark"
CBMC Faculty Research Update Meeting, virtual

October 2020: "Progress on Chemical Tools and Role of IDG Dark Kinases in Neurodegeneration" Kinase-DRGC meeting, virtual

October 2020: "Opportunities for Small Molecule Drug Discovery within the Neural Kinome" ATOM-IDG symposium, virtual

April 2020: "CSNK2A1/2 (CK2) probe"
SGC Chemical Probes Joint Management Committee meeting, virtual

D. Poster presentations

February 2021: "Illumination of CK2 uncovers new roles in cell biology"
IDG Face-to-Face Annual Meeting, virtual

December 2020: "Development of the first selective chemical probe for the pleiotropic kinase CK2, an emerging target in neurodegenerative disease"
CSHL Neurodegenerative Diseases: Biology & Therapeutics, virtual

November 2020: "Development of the first selective chemical probe for the pleiotropic kinase CK2, an emerging target in neurodegenerative disease"
Alzheimer's Association International Conference Neuroscience Next, virtual

September 2020: "Identification of novel kinase targets in ALS"
19th Annual NEALS Meeting, virtual

Funding applied for based on work supported by this training grant

A. Received

1. Clinical NIH Loan Repayment Program award through the National Institute on Aging: 2020–2022 (Axtman)
2. Renewal of clinical NIH Loan Repayment Program award through the National Institute on Aging: 2022–2024 (Axtman)

B. Applied for

1. "TBK1 activation as a therapeutic strategy for lowering soluble huntingtin protein and preventing its aggregation" Novartis Institutes for Biomedical Research Global Scholars Program- pre-proposal due May 5, 2023
2. "Manipulation of TBK1 ubiquitination using small molecules to rescue TBK1 function" Pershing Square Foundation Mind Prize- LOI due December 12, 2022
3. Optimization of a potent and cell active CK2 chemical probe for use in Alzheimer's disease" NIH PAR-21-029 Discovery of in vivo Chemical Probes for the Nervous System (R01 Clinical Trial Not Allowed)- due February 5, 2023
4. Resubmission of "Optimization of a potent and cell active CK2 chemical probe for use in Alzheimer's disease" NIH PAR-21-029 Discovery of in vivo Chemical Probes for the Nervous System (R01 Clinical Trial Not Allowed)- due July 5, 2022

5. “Use of iPSC-based model systems to interrogate novel protein targets that drive neurodegeneration” 2021 NYSCF- Robertson Neuroscience Investigator Award- due February 17, 2021
6. “Optimization of a potent and cell active CK2 chemical probe for use in Alzheimer’s disease” NIH PAR-21-029 Discovery of in vivo Chemical Probes for the Nervous System (R01 Clinical Trial Not Allowed)- due February 5, 2021
7. “Design and evaluation of first-in-class chimeric molecules in 3D ALS co-culture models” NIH Director’s Transformative Research Awards (R01); NOSI: Common Fund ALS-related Transformative Research Award- due September 30, 2020
8. “Strategies to activate kinases in pursuit of novel small molecule therapeutics for neurodegenerative diseases” New Innovator Award (DP2)- due August 21, 2020

Employment or research opportunities applied for and/or received based on experience/training supported by this grant

1. Promotion to Assistant Professor (tenure-track), effective January 18, 2024 (Axtman)
2. Promotion to Research Associate Professor, effective April 1, 2021 (Axtman)
3. Promotion to Associate Professor, effective February 14, 2021 (Durcan)
4. Guest Associate Editors for a co-listed special topic in *Front Cell Neurosci* and *Front Mol Neurosci*: “The Next Generation of Tools and Technologies for Studying Human Neurons in a Dish” (Axtman and Durcan)
5. Promoted to Medicinal Chemistry Core Lead Principal Investigator for NIA-funded TREAT-AD program, effective January 2022 (Axtman)

7. PARTICIPANTS & OTHER COLLABORATING ORGANIZATIONS

Personnel receiving pay from the research effort

Alison Axtman (UNC)- PI
Carrow Wells (UNC)- Research Associate
Jeffery Smith (UNC)- Research Associate
Anna Franco (McGill)- Research Associate
Mathilde Chaineau (McGill)- Research Associate
Andrea Krahn (McGill)- Research Associate
Timothy Miller (WUSTL)- co-I
Cindy Ly (WUSTL)- co-PI

Personnel working on the project but not receiving pay from the research effort

Thomas Durcan (McGill)- co-PI
Sarah Lépine (McGill)- Graduate Student

Conclusions

Despite setbacks incurred due circumstances out of our control, including COVID-19 and the crisis in Ukraine, we have delivered on many of our original milestones. We have pivoted our strategy where necessary to produce the most robust and biologically relevant portfolio of deliverables. The long list of significant research accomplishments as well as notable reportable outcomes highlights our measurable and impactful progress. We have continued to work together collaboratively and be productive beyond the award period and NCE. We aim to provide the research community with useful chemical and biological tools for use in their studies in hopes that better therapies for ALS patients will be realized through their use.

References

(1) Freischmidt, A.; Wieland, T.; Richter, B.; Ruf, W.; Schaeffer, V.; Muller, K.; Marroquin, N.; Nordin, F.; Hubers, A.; Weydt, P.; et al. Haploinsufficiency of TBK1 causes familial ALS and fronto-temporal dementia. *Nat Neurosci* **2015**, *18*, 631–636. DOI: 10.1038/nn.4000.
(2) Chen-Plotkin, A. S.; Lee, V. M.; Trojanowski, J. Q. TAR DNA-binding protein 43 in neurodegenerative disease. *Nat Rev Neurol* **2010**, *6*, 211–220. DOI: 10.1038/nrneurol.2010.18.
(3) Oakes, J. A.; Davies, M. C.; Collins, M. O. TBK1: a new player in ALS linking autophagy and neuroinflammation. *Mol Brain* **2017**, *10*, 5. DOI: 10.1186/s13041-017-0287-x.
(4) Wells, C. I.; Al-Ali, H.; Andrews, D. M.; Asquith, C. R. M.; Axtman, A. D.; Dikic, I.; Ebner, D.; Ettmayer, P.; Fischer, C.; Frederiksen, M.; et al. The Kinase Chemogenomic Set (KCGS): An open science resource for kinase vulnerability identification. *Int J Mol Sci* **2021**, *22*, 566. DOI: 10.3390/ijms22020566.
(5) Wells, C. I.; Hassan, A.-A.; Andrews, D. M.; Asquith, C. R. M.; Axtman, A. D.; Chung, M.; Dikic, I.; Ebner, D.; Elkins, J. M.; Ettmayer, P.; et al. The Kinase Chemogenomic Set (KCGS): An open science resource for kinase vulnerability identification. *BioRxiv* **2019**, 10.1101/2019.1112.1122.886523. DOI: 10.1101/2019.12.22.886523.
(6) Buratti, E.; Baralle, F. E. Multiple roles of TDP-43 in gene expression, splicing regulation, and human disease. *Front Biosci* **2008**, *13*, 867–878. DOI: 10.2741/2727.
(7) Arai, T.; Hasegawa, M.; Akiyama, H.; Ikeda, K.; Nonaka, T.; Mori, H.; Mann, D.; Tsuchiya, K.; Yoshida, M.; Hashizume, Y.; et al. TDP-43 is a component of ubiquitin-positive tau-negative inclusions in frontotemporal lobar degeneration and amyotrophic lateral sclerosis. *Biochem Biophys Res Commun* **2006**, *351*, 602–611. DOI: 10.1016/j.bbrc.2006.10.093.
(8) Neumann, M.; Sampathu, D. M.; Kwong, L. K.; Truax, A. C.; Micsenyi, M. C.; Chou, T. T.; Bruce, J.; Schuck, T.; Grossman, M.; Clark, C. M.; et al. Ubiquitinated TDP-43 in frontotemporal lobar degeneration and amyotrophic lateral sclerosis. *Science* **2006**, *314*, 130–133. DOI: 10.1126/science.1134108.
(9) Iguchi, Y.; Katsuno, M.; Takagi, S.; Ishigaki, S.; Niwa, J.; Hasegawa, M.; Tanaka, F.; Sobue, G. Oxidative stress induced by glutathione depletion reproduces pathological modifications of TDP-43 linked to TDP-43 proteinopathies. *Neurobiol Dis* **2012**, *45*, 862–870. DOI: 10.1016/j.nbd.2011.12.002.
(10) Choksi, D. K.; Roy, B.; Chatterjee, S.; Yusuff, T.; Bakhoum, M. F.; Sengupta, U.; Ambegaokar, S.; Kayed, R.; Jackson, G. R. TDP-43 Phosphorylation by casein kinase Iε promotes oligomerization and enhances toxicity in vivo. *Hum Mol Genet* **2013**, *23*, 1025–1035. DOI: 10.1093/hmg/ddt498.
(11) Nonaka, T.; Suzuki, G.; Tanaka, Y.; Kametani, F.; Hirai, S.; Okado, H.; Miyashita, T.; Saitoe, M.; Akiyama, H.; Masai, H.; et al. Phosphorylation of TAR DNA-binding Protein of 43 kDa (TDP-43) by truncated casein kinase 1delta triggers mislocalization and accumulation of TDP-43. *J Biol Chem* **2016**, *291*, 5473–5483. DOI: 10.1074/jbc.M115.695379.
(12) Hasegawa, M.; Arai, T.; Nonaka, T.; Kametani, F.; Yoshida, M.; Hashizume, Y.; Beach, T. G.; Buratti, E.; Baralle, F.; Morita, M.; et al. Phosphorylated TDP-43 in frontotemporal lobar degeneration and amyotrophic lateral sclerosis. *Ann Neurol* **2008**, *64*, 60–70. DOI: 10.1002/ana.21425.
(13) Lépine, S.; Nauleau-Javaudin, A.; Deneault, E.; Chen, C. X.-Q.; Abdian, N.; Franco-Flores, A. K.; Haghi, G.; Castellanos-Montiel, M. J.; Maussion, G.; Chaineau, M.; et al. Homozygous ALS-linked mutations in TARDBP/TDP-43 lead to progressive synaptic dysfunction in human iPSC-derived motor neurons. *BioRxiv* **2023**, 2023.2003.2022.533562. DOI: 10.1101/2023.03.22.533562.
(14) Mohapatra, B.; Ahmad, G.; Nadeau, S.; Zutshi, N.; An, W.; Scheffe, S.; Dong, L.; Feng, D.; Goetz, B.; Arya, P.; et al. Protein tyrosine kinase regulation by ubiquitination: critical roles of Cbl-family ubiquitin ligases. *Biochim Biophys Acta* **2013**, *1833*, 122–139. DOI: 10.1016/j.bbamcr.2012.10.010.

(15) Nazio, F.; Carinci, M.; Cecconi, F. ULK1 ubiquitylation is regulated by phosphorylation on its carboxy terminus. *Cell Cycle* **2017**, *16*, 1744–1747. DOI: 10.1080/15384101.2017.1361063.
(16) Nguyen, L. K.; Kolch, W.; Kholodenko, B. N. When ubiquitination meets phosphorylation: a systems biology perspective of EGFR/MAPK signalling. *Cell Commun Signal* **2013**, *11*, 52. DOI: 10.1186/1478-811x-11-52.
(17) Drewry, D. H.; Annor-Gyamfi, J. K.; Wells, C. I.; Pickett, J. E.; Dederer, V.; Preuss, F.; Mathea, S.; Axtman, A. D. Identification of pyrimidine-based lead compounds for understudied kinases implicated in driving neurodegeneration. *J Med Chem* **2022**, *65*, 1313–1328. DOI: 10.1021/acs.jmedchem.1c00440.
(18) Drewry, D.; Annor-Gyamfi, J. K.; Wells, C.; Pickett, J. E.; Axtman, A. D. Strategy for lead identification for understudied kinases. *ChemRxiv* **2021**, 14195207. DOI: 10.26434/chemrxiv.14195207.v1.
(19) Fedorov, O.; Niesen, F. H.; Knapp, S. Kinase inhibitor selectivity profiling using differential scanning fluorimetry. In *Kinase Inhibitors. Methods in Molecular Biology (Methods and Protocols)*, B, K. Ed.; Vol. 795; Humana Press, 2012.
(20) Brenke, J. K.; Popowicz, G. M.; Schorpp, K.; Rothenaigner, I.; Roesner, M.; Meininger, I.; Kalinski, C.; Ringelstetter, L.; R'kyek, O.; Jürjens, G.; et al. Targeting TRAF6 E3 ligase activity with a small-molecule inhibitor combats autoimmunity. *J Biol Chem* **2018**, *293*, 13191–13203. DOI: 10.1074/jbc.RA118.002649.
(21) Lamark, T.; Kirkin, V.; Dikic, I.; Johansen, T. NBR1 and p62 as cargo receptors for selective autophagy of ubiquitinated targets. *Cell Cycle* **2009**, *8*, 1986–1990. DOI: 10.4161/cc.8.13.8892.
(22) Matsumoto, G.; Wada, K.; Okuno, M.; Kurosawa, M.; Nukina, N. Serine 403 phosphorylation of p62/SQSTM1 regulates selective autophagic clearance of ubiquitinated proteins. *Mol Cell* **2011**, *44*, 279–289. DOI: 10.1016/j.molcel.2011.07.039.
(23) Herhaus, L.; Dikic, I. Expanding the ubiquitin code through post-translational modification. *EMBO Rep* **2015**, *16*, 1071–1083. DOI: 10.15252/embr.201540891.
(24) Pierre, F.; Chua, P. C.; O'Brien, S. E.; Siddiqui-Jain, A.; Bourbon, P.; Haddach, M.; Michaux, J.; Nagasawa, J.; Schwaebe, M. K.; Stefan, E.; et al. Discovery and SAR of 5-(3-chlorophenylamino)benzo[c][2,6]naphthyridine-8-carboxylic acid (CX-4945), the first clinical stage inhibitor of protein kinase CK2 for the treatment of cancer. *J Med Chem* **2011**, *54*, 635–654. DOI: 10.1021/jm101251q.
(25) Perez, D. I.; Gil, C.; Martinez, A. Protein kinases CK1 and CK2 as new targets for neurodegenerative diseases. *Med Res Rev* **2011**, *31* (6), 924–954. DOI: 10.1002/med.20207.
(26) Castello, J.; Ragnauth, A.; Friedman, E.; Rebholz, H. CK2—An emerging target for neurological and psychiatric disorders. *Pharmaceuticals* **2017**, *10*, 7. DOI: 10.3390/ph10010007.
(27) Cozza, G.; Pinna, L. A.; Moro, S. Kinase CK2 inhibition: an update. *Curr Med Chem* **2013**, *20*, 671–693. DOI: 10.2174/092986713804999312.
(28) Guerra, B.; Issinger, O. G. Protein kinase CK2 in human diseases. *Curr Med Chem* **2008**, *15*, 1870–1886. DOI: 10.2174/092986708785132933.
(29) Du, M.; Liu, J.; Chen, X.; Xie, Y.; Yuan, C.; Xiang, Y.; Sun, B.; Lan, K.; Chen, M.; James, S. J.; et al. Casein kinase II controls TBK1/IRF3 activation in IFN response against viral infection. *J Immunol* **2015**, *194*, 4477–4488. DOI: 10.4049/jimmunol.1402777.
(30) Matsumoto, G.; Shimogori, T.; Hattori, N.; Nukina, N. TBK1 controls autophagosomal engulfment of polyubiquitinated mitochondria through p62/SQSTM1 phosphorylation. *Hum Mol Genet* **2015**, *24*, 4429–4442. DOI: 10.1093/hmg/ddv179.
(31) Sarno, S.; Reddy, H.; Meggio, F.; Ruzzene, M.; Davies, S. P.; Donella-Deana, A.; Shugar, D.; Pinna, L. A. Selectivity of 4,5,6,7-tetrabromobenzotriazole, an ATP site-directed inhibitor of protein kinase CK2 ('casein kinase-2'). *FEBS Lett* **2001**, *496*, 44–48. DOI: 10.1016/S0014-5793(01)02404-8.

(32) Wells, C. I.; Drewry, D. H.; Pickett, J. E.; Tjaden, A.; Krämer, A.; Müller, S.; Gyenis, L.; Menyhart, D.; Litchfield, D. W.; Knapp, S.; et al. Development of a potent and selective chemical probe for the pleiotropic kinase CK2. *Cell Chem Biol* **2021**, *28*, 546–558.e510. DOI: 10.1016/j.chembiol.2020.12.013.
(33) Wells, C.; Drewry, D. H.; Pickett, J. E.; Axtman, A. D. SGC-CK2-1: the first selective chemical probe for the pleiotropic kinase CK2. *ChemRxiv* **2020**, 12296180, DOI: 10.26434/chemrxiv.12296180.v12296181.
(34) Mishra, S.; Kinoshita, C.; Axtman, A. D.; Young, J. E. Evaluation of a selective chemical probe validates that CK2 mediates neuroinflammation in an hiPSC-derived microglial model. *Front Mol Neurosci* **2022**, *15*, 824956. DOI: 10.3389/fnmol.2022.824956.
(35) Matlock, M. K.; Hughes, T. B.; Swamidass, S. J. XenoSite server: a web-available site of metabolism prediction tool. *Bioinformatics* **2014**, *31*, 1136–1137. DOI: 10.1093/bioinformatics/btu761.
(36) Rydberg, P.; Gloriam, D. E.; Zaretzki, J.; Breneman, C.; Olsen, L. SMARTCyp: A 2D method for prediction of cytochrome P450-mediated drug metabolism. *ACS Med Chem Lett* **2010**, *1*, 96–100. DOI: 10.1021/ml100016x.
(37) Yang, X.; Ong, H. W.; Dickmander, R. J.; Smith, J. L.; Brown, J. W.; Tao, W.; Chang, E.; Moorman, N. J.; Axtman, A. D.; Willson, T. M. Optimization of 3-cyano-7-cyclopropylamino-pyrazolo[1,5-a]pyrimidines toward the development of an in vivo chemical probe for CSNK2A. *BioRxiv* **2023**, 2023.2005.2015.540828. DOI: 10.1101/2023.05.15.540828.
(38) Yang, X.; Ong, H. W.; Dickmander, R. J.; Smith, J. L.; Brown, J. R.; Tao, W.; Chang, E. F.; Moorman, N. J.; Axtman, A. D.; Willson, T. M. Optimization of 3-cyano-7-cyclopropylamino-pyrazolo[1,5-a]pyrimidines toward the development of an in vivo chemical probe for CSNK2A. *ACS Omega* **2023**, *In Press*.
(39) Davis-Gilbert, Z. W.; Krämer, A.; Dunford, J. E.; Howell, S.; Senbabaoglu, F.; Wells, C. I.; Bashore, F. M.; Havener, T. M.; Smith, J. L.; Hossain, M. A.; et al. Discovery of a ootent and selective naphthyridine-based chemical probe for casein kinase 2. *ACS Med Chem Lett* **2023**, *14*, 432–441. DOI: 10.1021/acsmedchemlett.2c00530.
(40) Davis-Gilbert, Z. W.; Krämer, A.; Dunford, J. E.; Howell, S.; Senbabaoglu, F.; Wells, C. I.; Havener, T. M.; Smith, J. L.; Hossain, M. A.; Oppermann, U.; et al. Discovery of a ootent and selective naphthyridine-based chemical probe for casein kinase 2. *ChemRxiv* **2022**, DOI: 10.26434/chemrxiv-2022-05jcz.

8. SPECIAL REPORTING REQUIREMENTS: not applicable

9. APPENDICES

Attached are copies of the following:

1. Yang, X.; Ong, H. W.; Dickmander, R. J.; Smith, J. L.; Brown, J. W.; Tao, W.; Chang, E.; Moorman, N. J.; Axtman, A. D.; Willson, T. M. Optimization of 3-cyano-7-cyclopropylamino-pyrazolo[1,5-a]pyrimidines toward the development of an in vivo chemical probe for CSNK2. *BioRxiv* **2023**, 2023.2005.2015.540828. DOI: 10.1101/2023.05.15.540828.

2. Davis-Gilbert, Z. W.; Krämer, A.; Dunford, J. E.; Howell, S.; Senbabaoglu, F.; Wells, C. I.; Bashore, F. M.; Havener, T. M.; Smith, J. L.; Hossain, M. A.; Oppermann, U.; Drewry, D. H.; Axtman, A. D. Discovery of a potent and selective naphthyridine-based chemical probe for casein kinase 2. *ACS Med Chem Lett* **2023**, *14*, 432–441. doi: 10.1021/acsmedchemlett.2c00530.

3. Mishra, S.; Kinoshita, C.; Axtman, A. D.*; Young, J. E.* Evaluation of a selective chemical probe validates that CK2 mediates neuroinflammation in an hiPSC-derived microglial model. *Front Mol Neurosci* **2022**, *15*, 824956. doi: 10.3389/fnmol.2022.824956.

4. Lépine, S.; Nauleau-Javaudin, A.; Deneault, E.; Chen, C. X.-Q.; Abdian, N.; Franco-Flores, A. K.; Haghi, G.; Castellanos-Montiel, M. J.; Maussion, G.; Chaineau, M.; Durcan, T. M. Homozygous ALS-linked mutations in TARDBP/TDP-43 lead to progressive synaptic dysfunction in human iPSC-derived motor neurons. *BioRxiv* **2023**, 2023.2003.2022.533562, doi: 10.1101/2023.03.22.533562.

bioRxiv preprint doi: https://doi.org/10.1101/2023.05.15.540828; this version posted July 23, 2023. The copyright holder for this preprint (which was not certified by peer review) is the author/funder, who has granted bioRxiv a license to display the preprint in perpetuity. It is made available under aCC-BY 4.0 International license.

Optimization of 3-Cyano-7-cyclopropylamino-pyrazolo[1,5-a]pyrimidines Toward the Development of an In Vivo Chemical Probe for CSNK2A

Xuan Yang,[a,b] Han Wee Ong,[a,b] Rebekah J. Dickmander,[b.c.d.e] Jeffery L. Smith,[a] Jason W. Brown,[f] William Tao,[f] Edcon Chang,[f] Nathaniel J. Moorman,[b,c,d] Alison D. Axtman,[a,b] and Timothy M. Willson[a,b,*]

[a] *Structural Genomics Consortium, UNC Eshelman School of Pharmacy, University of North Carolina at Chapel Hill, Chapel Hill, NC 27599, United States*

[b] *Rapidly Emerging Antiviral Drug Development Initiative (READDI), Chapel Hill, NC 27599, United States*

[c] *Department of Microbiology & Immunology, University of North Carolina at Chapel Hill, Chapel Hill, NC 27599, United States*

[d] *Lineberger Comprehensive Cancer Center, University of North Carolina at Chapel Hill, Chapel Hill, NC 27599, United States*

[e] *Department of Chemistry, University of North Carolina at Chapel Hill, Chapel Hill, NC 27599, United States*

[f] *Takeda San Diego, San Diego, CA 92121, United States*

* E-mail: tim.willson@unc.edu

bioRxiv preprint doi: https://doi.org/10.1101/2023.05.15.540828; this version posted July 23, 2023. The copyright holder for this preprint (which was not certified by peer review) is the author/funder, who has granted bioRxiv a license to display the preprint in perpetuity. It is made available under aCC-BY 4.0 International license.

Abstract: 3-cyano-7-cyclopropylamino-pyrazolo[1,5-a]pyrimidines, including the chemical probe SGC-CK2-1, are potent and selective inhibitors of CSNK2A in cells but have limited utility in animal models due to their poor pharmacokinetic properties. While developing analogs with reduced intrinsic clearance and the potential for sustained exposure in mice, we discovered that Phase II conjugation by GST enzymes was a major metabolic transformation in hepatocytes. A protocol for co-dosing with ethacrynic acid, a covalent reversible GST inhibitor, was developed to improve the exposure of analog **2h** in mice. A double co-dosing protocol, using a combination of ethacrynic acid and irreversible P450 inhibitor 1-aminobenzotriazole increased the blood level of **2h** by 40-fold at a 5 h time point.

Graphical Abstract

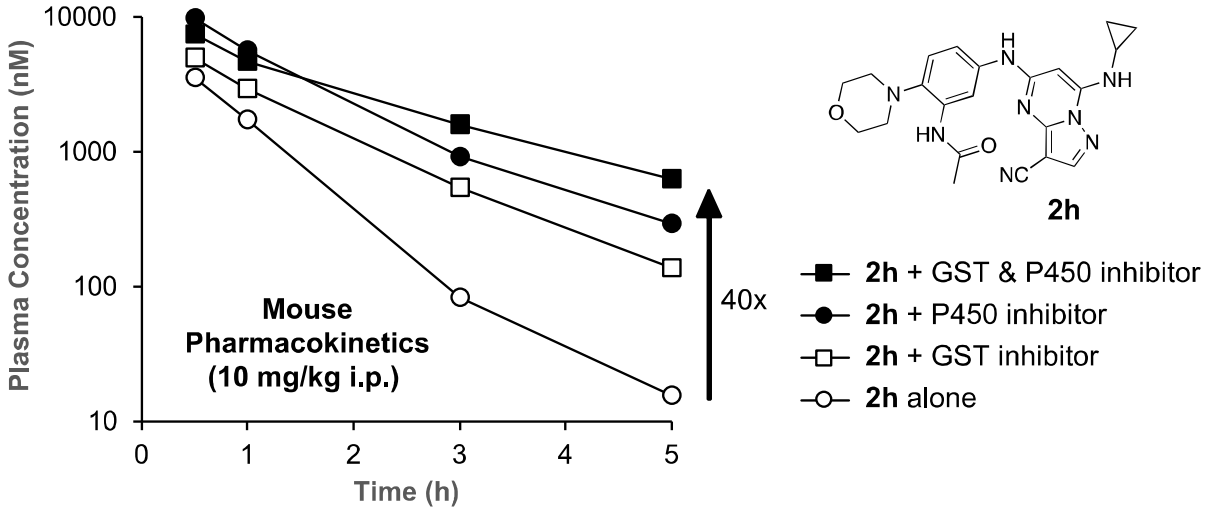

bioRxiv preprint doi: https://doi.org/10.1101/2023.05.15.540828; this version posted July 23, 2023. The copyright holder for this preprint (which was not certified by peer review) is the author/funder, who has granted bioRxiv a license to display the preprint in perpetuity. It is made available under aCC-BY 4.0 International license.

Introduction

The appearance of a novel coronavirus SARS-CoV-2 and the resulting pandemic have highlighted the need for effective treatments against COVID-19.[1] Host-directed therapies that target cellular pathways required for virus replication have emerged as a promising approach to combat viral infections.[2] Protein kinases have been proposed as potential targets for development of antiviral drugs.[3] Among these kinases, Casein Kinase 2α (CSNK2A) has been shown to play a role in the replication of β-coronaviruses (β-CoV), including SARS-CoV-2.[4-6]. Recent studies have demonstrated the efficacy of CSNK2A inhibitors in reducing the replication of β-CoV in vitro.[6] However, there has yet to be a demonstration of anti-COVID-19 efficacy in vivo.

3-cyano-7-cyclopropylamino-pyrazolo[1,5-a]pyrimidine (PZP) is a promising chemotype of CSNK2A inhibitor that has demonstrated potent activity in vitro.[7] PZPs possess good selectivity for CSNK2A over other kinases and display unique chemical features that contribute to their potent inhibitory activity (Figure 1). Specifically, X-ray crystallography studies (Figure 1A) revealed that the 4'-methyl substituent of the chemical probe SGC-CK2-1 (**1a**) enforces an s-cis (*E*)-conformation of the propionamide, allowing it to coordinate with a bound water molecule, which also interacts with the cyano group of the PZP core (Figure 1B). Notably, the alkyl group

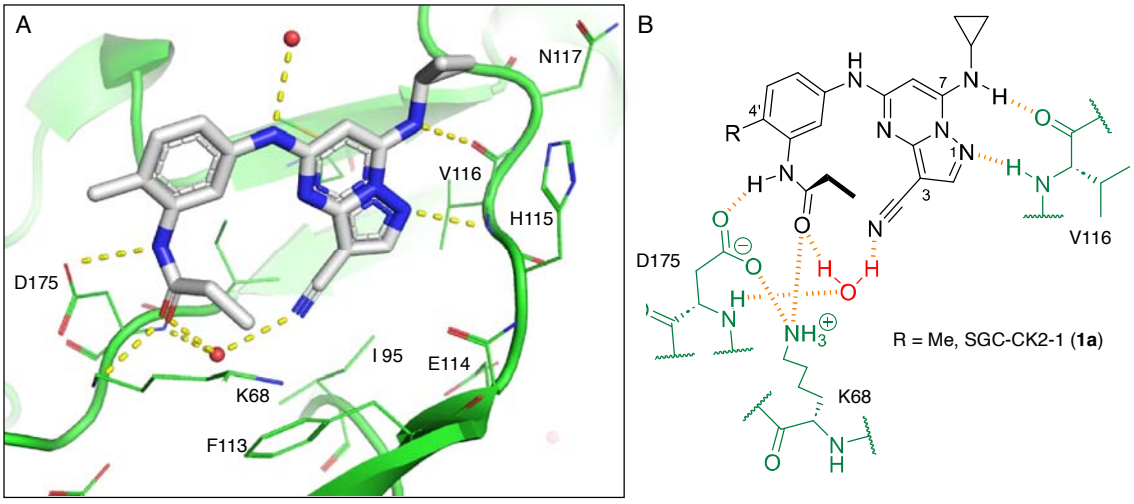

Figure 1. A. X-ray cocrystal structure of SGC-CK2-1 (**1a**) bound to CSNK2A1 (PDB: 6Z83). Image created in PyMOL 2.4.0 with the CSNK2A1 protein shown as a green ribbon and **1a** shown as sticks colored by atom type. Bound water molecules are shown as red spheres. Intermolecular hydrogen bonds are shown as yellow dashed lines. B. Illustration of the key interactions observed in the X-ray structure. The 7-cyclopropylamine and N-1 of the PZP form H-bond interactions with V116 in the hinge region. The 4'-substiuent (Me for **1a**) causes the amide to adopt an s-cis conformation that allows the carbonyl group to interact with K68 and a bound water molecule. The ethyl group of the amide is placed in a pocket that increases selectivity over other kinases. The cyano group of the PZP also interacts with the bound water molecule, which is further coordinated through interaction with the backbone NH of D175.

bioRxiv preprint doi: https://doi.org/10.1101/2023.05.15.540828; this version posted July 23, 2023. The copyright holder for this preprint (which was not certified by peer review) is the author/funder, who has granted bioRxiv a license to display the preprint in perpetuity. It is made available under aCC-BY 4.0 International license.

of the propionamide contributes to the exquisite selectivity of the PZP-based CSNK2A inhibitors over other kinases.[8] However, despite their promising in vitro activity, PZPs have shown limited bioavailability in rodents by oral dosing due to their low to moderate aqueous solubility, high first-pass metabolism, and rapid clearance.[9, 10]

In this paper, we report our initial studies to identify a PZP-based CSNK2A inhibitor with potent antiviral activity and high sustained blood levels for use in mouse-adapted model of COVID-19 developed for preclinical evaluation of potential drug therapies.[11, 12] We discovered that the rapid clearance of PZPs in mice was due to pathways of both Phase I and Phase II metabolism. Co-dosing with a glutathione S-transferase (GST) enzyme inhibitor and an irreversible cytochrome P450 inhibitor greatly reduced intrinsic clearance of a PZP analog in mice and may be a viable approach to increase in vivo exposure for preclinical pharmacology studies.

bioRxiv preprint doi: https://doi.org/10.1101/2023.05.15.540828; this version posted July 23, 2023. The copyright holder for this preprint (which was not certified by peer review) is the author/funder, who has granted bioRxiv a license to display the preprint in perpetuity. It is made available under aCC-BY 4.0 International license.

Results

Antiviral PZPs with Reduced Phase I Metabolism. All compounds were screened for CSNK2A1 and CSNK2A2 activity using a NanoBRET assay in HEK293 cells and for inhibition of mouse β-CoV replication using an MHV-nLuc assay in DBT cells.[6] Kinetic solubility was determined using a miniaturized shake flask method. The stability of compounds to Phase I metabolism was determined by incubation with mouse liver microsome for 30 min. SGC-CK2-1 (**1a**) demonstrated low aqueous solubility and rapid metabolism in primary mouse liver microsomes (MLM), with only 40% of the parent compound remaining after 30 min (Table 1). Since hepatic metabolism of **1a** would likely lead to rapid in vivo clearance, we decided to focus

Table 1: Modification of the 4'-position group of the propionamide series

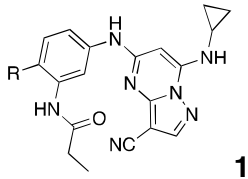

1a-i

Compound	R	CSNK2A1 pIC_{50} [a]	CSNK2A2 pIC_{50} [a]	MHV pIC_{50} [b]	cLogP[c]	Kinetic solubility (μg/mL)[d]	MLM metabolism @ 30 min (%)[e]
1a[f]	Me	7.4	7.4	6.9	0.38	1.4	60
1b[f]	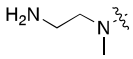	8.6	8.7	6.8	0.03	66	38
1c[f]	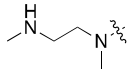	8.2	8.3	7.1	0.33	78	34
1d[f]	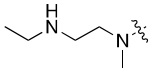	7.4	7.6	6.6	0.86	81	38
1e[f]	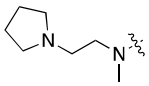	7.4	6.8	6.2	1.58	77	94
1f[f]	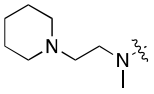	7.0	6.6	5.9	2.15	69	99
1g[f]	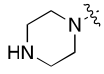	6.7	6.7	5.8	-0.03	88	12
1h	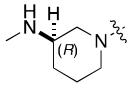	7.1	7.2	6.3	0.40	65	11
1i	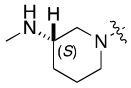	7.6	7.7	6.9	0.40	71	10

[a]In-cell target engagement by NanoBRET assay, n = 1. [b]Inhibition of MHV-nLuc replication, n = 3 with SE ± 0.1. [c]Values from ChemDraw Professional v16.0. [d]Miniaturized shake flask using CLND detection, n = 1; [e]Metabolism of compound in primary mouse liver microsomes (MLM) calculated as 100 – (% remaining), n = 1. [f]Compound previously reported in reference 6.

bioRxiv preprint doi: https://doi.org/10.1101/2023.05.15.540828; this version posted July 23, 2023. The copyright holder for this preprint (which was not certified by peer review) is the author/funder, who has granted bioRxiv a license to display the preprint in perpetuity. It is made available under aCC-BY 4.0 International license.

initially on increasing its stability in MLM. SMARTCyp,[13, 14] a web-based predictor of metabolic hot spots, analyzes sites of metabolism using a ligand-based approach from a library of molecular fragments that can be applied across multiple species and isoforms of CYPs.[15] SMARTCyp suggested that that the cyclopropylamine and the 4'-methyl group might be sites of P450 oxidation (Figure S1). As modification of the cyclopropylamine, which forms part of the hinge-binding motif (Figure 1B), resulted in a large decrease in CSNK2A potency[6, 8] we opted to study analogs with modification of the 4'-methyl group in order to lower logD, improve aqueous solubility, and possibly reduce P450 metabolism.[16] Analogs **1b–g** with substituted ethylenediamines replacing the 4'-methyl group demonstrated good CSNK2A potency and retained antiviral activity, as previously reported.[6] Analogs **1b–g** had ~50–60-fold improved aqueous solubility. The ethylenediamines **1b–d** also had reduced metabolism in MLM compared to **1a** (Table 1). In contrast the pyrrolidine (**1e**) and piperidine (**1f**) containing diamines were highly metabolized despite their improved aqueous solubility, possibly due to their increased lipophilicity. The piperazine (**1g**) had greatly improved metabolic stability, but at a cost of lower CSNK2A potency and antiviral IC_{50} >1 μM. From this initial series of analogs of **1a** we found that addition of ethylenediamines at the 4' position resulted in PZPs with good antiviral activity and reduced P450 metabolism in MLM. Although the piperazine **1g** had the best metabolic stability, it showed reduced potency in both CSNK2A and antiviral assays.

Scheme 1[a]

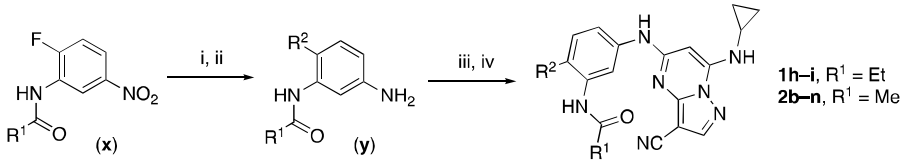

[a]Reagents and conditions: (i) R_2-H, K_2CO_3, MeCN. (ii) H_2, Pd-C, MeOH. (iii) 5-chloro-7-(cyclopropyl-amino)pyrazolo[1,5-*a*]pyrimidine-3-carbonitrile, BINAP, $Pd(OAc)_2$, Cs_2CO_3, dioxane, μW, 130°C. (iv) TFA, CH_2Cl_2.

To build on these results we designed new analogs with 3-aminomethyl piperidine substituents at the 4'-position to combine the features of both the cyclic and linear diamines. The synthesis employed the methods previously developed for analogs **1b–g** (Scheme 1). Addition of the (*R*) or (*S*)-enantiomer of the *N*-Boc-protected 3-aminomethyl piperidine to the acyl-2-fluoro-5-nitroaniline (**x**, R^1 = Et) followed by reduction of the nitro group yielded the aniline intermediate (**y**, R^1 = Et). Palladium-catalyzed Buchwald-Hartwig cross coupling with the 5-chloro-pyrazolo[1,5-a]pyrimidine core followed by *N*-Boc deprotection yielded the 3*R*-isomer (**1h**) and the 3*S*-isomer (**1i**). Both isomers, **1h** and **1i**, demonstrated good aqueous solubility and low metabolism in mouse liver microsomes compared to **1a** (Table 1). The 3*S*-isomer (**1i**)

bioRxiv preprint doi: https://doi.org/10.1101/2023.05.15.540828; this version posted July 23, 2023. The copyright holder for this preprint (which was not certified by peer review) is the author/funder, who has granted bioRxiv a license to display the preprint in perpetuity. It is made available under aCC-BY 4.0 International license.

Table 2: Modification of the 4'-position group of the acetamide series

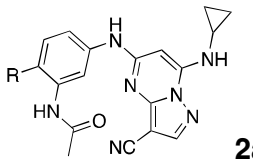

2a-n

Compound	R	CSNK2A1 pIC_{50}[a]	CSNK2A2 pIC_{50}[a]	MHV pIC_{50}[b]	cLogP[c]	Kinetic solubility (μg/mL)[d]	MLM metabolism @ 30 min (%)[e]
2a[f]	Me	9.3	9.2	7.1	-0.15	2.9	52
2b	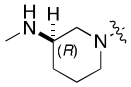	7.8	8.0	7.0	-0.13	52	14
2c	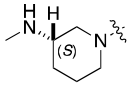	8.3	8.4	7.9	-0.13	54	14
2d	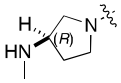	8.6	8.8	7.5	-0.69	64	8
2e	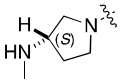	8.3	8.4	7.7	-0.69	49	16
2f	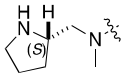	8.4	8.5	7.9	0.50	68	24
2g	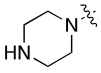	7.1	7.6	5.6	-0.56	52	18
2h[f]		7.5	7.7	7.1	-0.54	1.0	30
2i	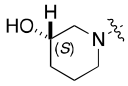	7.5	7.7	7.0	-0.50	37	55
2j	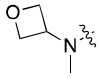	7.6	7.7	6.8	0.00	0.9	92
2k	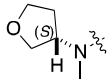	6.9	7.0	6.5	0.03	21	97
2l	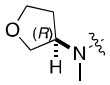	6.9	7.1	6.3	0.03	25	100
2m	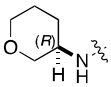	8.0	8.1	6.4	-0.23	2.4	76
2n	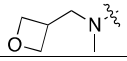	7.0	7.5	6.4	-0.70	0.2	100

[a]In-cell target engagement by NanoBRET assay, n = 1. [b]Inhibition of MHV-nLuc replication, n = 3 with SE ± 0.1. [c]Values from ChemDraw Professional v16.0. [d]Miniaturized shake flask using CLND detection, n = 1; [e]Metabolism of compound in primary mouse liver microsomes (MLM) calculated as 100 – (% remaining), n = 1. [f]Compound previously reported in reference 6.

was more potent than the 3*R*-isomer (**1h**) in both the CSNK2A assay and the antiviral assay. Overall, **1i** had comparable potency to **1a** but with improved solubility and metabolic stability.

bioRxiv preprint doi: https://doi.org/10.1101/2023.05.15.540828; this version posted July 23, 2023. The copyright holder for this preprint (which was not certified by peer review) is the author/funder, who has granted bioRxiv a license to display the preprint in perpetuity. It is made available under aCC-BY 4.0 International license.

To further improve the potency, we synthesized 4'-substituted analogs in the acetamide series of PZPs (Table 2). The compounds were synthesized by the established route from the acyl-2-fluoro-5-nitroaniline (**x**, R^1 = Me) and the appropriate secondary amine for the R^2-substituent (Scheme 1). For those R^2-substituents with chiral centers, the enantiomerically-pure amine was utilized as a building block. The 4'-methyl analog (**2a**) had shown sub-nanomolar activity on CSNK2A and good activity in the antiviral assay.[6] **2a** had a lower cLogP and slightly improved solubility and metabolic stability compared to the corresponding propionamide (**1a**) (Table 2). Synthesis of the 3*R*-isomer (**2b**) and 3*S*-isomer (**2c**) of the 3-aminomethyl piperidine gave analogs with 10-fold improved potency in the CSNK2A and the antiviral assays while maintaining good metabolic stability. The 3*S*-isomer (**2c**) was again the more potent of the two enantiomers. Additional 4'-substituted analogs were synthesized in the acetamide series. The 3*R*-isomer (**2d**) and 3*S*-isomer (**2e**) of the 3-aminomethyl pyrrolidine also combined potency on CSNK2A and antiviral activity with good metabolic stability. Switching the orientation of the 3-aminomethyl pyrrolidine gave analog **2f** with similar potency but slightly poorer metabolic stability. The piperazine (**2g**) was less potent on CSNK2A and in the antiviral assay, but had good metabolic stability, as had been seen in the corresponding propionamide (**1g**). We had previously prepared and tested morpholine (**2h**),[6] which had improved antiviral activity compared to **2g**. Although the morpholine (**2h**) showed low aqueous solubility its metabolic stability was much better than the parent analog **2a** (Table 2). Introduction of a hydroxy substituent in **2i** maintained activity and improved aqueous solubility but decreased metabolic stability. The oxo-analogs **2j–n** had lower activity in the antiviral assay and poor metabolic stability, despite some analogs (e.g. **2l**) having low cLogP and good solubility.

Pharmacokinetic Profiling of PZPs. Having identified several analogs with improved metabolic stability in MLM and potent activity in the CSNK2A and antiviral assays, we selected three compounds (**1i**, **2c**, and **2e**) for pharmacokinetic studies. These analogs showed only 10–16% metabolism in primary MLM after 30 min incubation. The compounds were dosed at 1.0 mg/kg i.v. and 10 mg/kg i.p. to mice and the level of the parent compound was monitored over 24 h (Table 3). Despite their stability in MLM, all three compounds demonstrated moderate to high clearance following i.v. dosing, with $t_{1/2}$ of 1.2–1.8 h. Similar results were observed following i.p. dosing with $t_{1/2}$ of 1.2–1.5 h. Although the bioavailability by i.p. dosing was good, the rapid clearance resulted in low total exposure and blood levels that fell below the IC_{50} for antiviral activity within 1 h.

bioRxiv preprint doi: https://doi.org/10.1101/2023.05.15.540828; this version posted July 23, 2023. The copyright holder for this preprint (which was not certified by peer review) is the author/funder, who has granted bioRxiv a license to display the preprint in perpetuity. It is made available under aCC-BY 4.0 International license.

Table 3: In vivo mouse pharmacokinetic parameters of 1i, 2c, and 2e[a]

Compound	i.v. (1 mg/kg)					i.p. (10 mg/kg)			
	C_{max} (ng/mL)	AUC_{last} (ng.h/mL)	Vd_{ss} (L/kg)	$t_{1/2}$ (h)	CL_{int} (mL/min/kg)	C_{max} (ng/mL)	AUC_{last} (ng.h/mL)	$t_{1/2}$ (h)	*F* (%)
1i	1100	670	2.60	1.3	36	4700	7010	1.2	100
2c	350	200	5.07	1.8	84	670	770	1.5	40
2e	810	250	2.67	1.2	69	1500	1300	1.4	53

[a]Mice dosed by i.v. or i.p. route of administration, n = 3. Compounds quantified by LC/MS.

Phase II Metabolism of PZPs. To further explore the reason for the rapid in vivo clearance of the PZPs (**1i**, **2c**, and **2e**), we performed time course studies to measure their rate of intrinsic clearance using in vitro systems of hepatic metabolism (Table 4). In mouse primary liver microsomes the three compounds showed low intrinsic clearance consistent with the single time point measurements (Tables 1 and 2). Repeating the experiment with primary liver microsomes that included the S9 fraction resulted in a decrease in clearance indicating that metabolic stability was unaffected by inclusion of the cytosolic enzymes. However, when incubated with primary mouse hepatocytes, all three compounds were rapidly metabolized with high rates of intrinsic clearance (Table 4). The results suggested that a non-P450 metabolic pathway could be responsible for the rapid hepatic clearance of the PZPs in hepatocytes and in mice in vivo.[17]

Table 4: In vitro mouse metabolism of 1i, 2c, and 2e[a]

Compound	Liver Microsomes CL_{int} (mL/min/kg)	S9 fraction CL_{int} (mL/min/kg)	Hepatocytes CL_{int} (mL/min/kg)
1i	<24	0	143
2c	<24	1	132
2e	27	4	69

[a]Compounds quantified by LC/MS at 5 time points over 5h, n = 1.

Metabolite ID Study of 1i. To identify the metabolic pathway responsible for the rapid clearance in mouse hepatocytes, we performed a metabolite ID study using the 3*S*-aminomethyl piperidine (**1i**). Incubation of **1i** for 4 h in primary cultures of mouse hepatocytes resulted in the appearance of 12 metabolites by ultrahigh performance liquid chromatography (Figure 2A). Analysis of the metabolites by mass spectroscopy and quantification by UV absorbance enabled the assignment of the primary pathways of metabolic transformation (Table 4, Figures 2B and S2). Six of the metabolites (M1–4, M10–11) resulted from GSH conjugation of the PZPs (Figure 2B), a Phase II metabolic transformation that could only occur in whole hepatocytes that contain the active GST enzymes. GSH conjugation was observed in the major fraction of the total metabolites as quantified by UV absorbance (Table 5) and is likely to be an important pathway

bioRxiv preprint doi: https://doi.org/10.1101/2023.05.15.540828; this version posted July 23, 2023. The copyright holder for this preprint (which was not certified by peer review) is the author/funder, who has granted bioRxiv a license to display the preprint in perpetuity. It is made available under aCC-BY 4.0 International license.

Table 5: Metabolites of 1i in Mouse Hepatocytes

Peak[a]	Time (min)	Mass (m/z)	Transformation									Rel. (%)
			-Alkyl	+GSH	$-CH_3$	$-H_2$	Hydrol.	$-NH_2$	[O]	[H]	Acyl.	
M1	5.67	370.16[b]	X	X								<1
M2	6.03	370.16[b]	X	X								3
M3	6.89	390.17[b]		X								9
M4	7.10	390.17[b]		X								9
M5	7.34	390.17[b]		X								<1
M6	7.59	230.63[b]			X							<1
M7	7.70	472.26				X						<1
M8	7.79	418.25					X					<1
M9	7.80	417.18				X	X	X	X			2
M10	7.91	342.12[b]	X	X					X			5
M11	8.47	230.63[b]			X							10
Parent	8.58	474.27										53
M12	8.90	463.21					X	X	X	X	X	<1
Total Rel. (%)[c]			**9**	**27**	**11**	**3**	**4**	**3**	**8**	**1**	**1**	

[a] See Figure 2 for structural assignments. [b] $[M+2H]^{2+}$, z=2. [c] Sum of metabolites with the transformation, using <1 = 1.

of clearance of the PZP **1i** (Figure 2B). In addition to GSH conjugation, demethylation of the secondary amine on the piperidine and dealkylation of the 7-amino group on the PZP were found among the metabolites (Table 4 and Figure 2B). Notably, dealkylation was often found in combination with GSH conjugation. P450 oxidation of electron-rich aromatic rings to an epoxide intermediate is well known activation step in GST-catalyzed GSH conjugation,[18] making the electron-rich amino-substituted phenyl ring the most likely site of Phase II metabolism (Figure 2C). Although we initially considered the nitrile as a potential site of conjugation, since it can undergo a Pinner reaction with free GSH,[19] there is no evidence that the reaction is catalyzed by GST enzymes.[20, 21] The metabolite ID study implicated both cytochrome P450 and GST enzymes as likely to be responsible for the rapid clearance of the PZPs in mouse hepatocytes through a combination of demethylation, dealkylation, and GSH conjugation (Figure 2C).

Hepatocyte Metabolism of Antiviral PZPs. Eight acetamide PZPs (**2a–f,h–i**) with IC_{50} ≤100 nM in the antiviral assay were selected for time course metabolic stability profiling in mouse and human and primary hepatocytes (Table 6). Unfortunately, all acetamide PZPs (**2a–f,h–i**) showed high intrinsic clearance in mouse hepatocytes, independent of their stability in liver microsomes (Table 2), suggesting that they were substrates for the Phase II GST enzymes in the hepatocytes. These in vitro metabolism data in mouse hepatocytes predicted that acetamide PZPs with potent antiviral activity would be likely to have rapid in vivo clearance in mice. In contrast, the compounds had much lower intrinsic clearance in human primary hepatocytes, with only **2h** and **2i** showing moderate and high rates of clearance, respectively. These results demonstrated that the metabolism of the PZPs in primary hepatocytes was

bioRxiv preprint doi: https://doi.org/10.1101/2023.05.15.540828; this version posted July 23, 2023. The copyright holder for this preprint (which was not certified by peer review) is the author/funder, who has granted bioRxiv a license to display the preprint in perpetuity. It is made available under aCC-BY 4.0 International license.

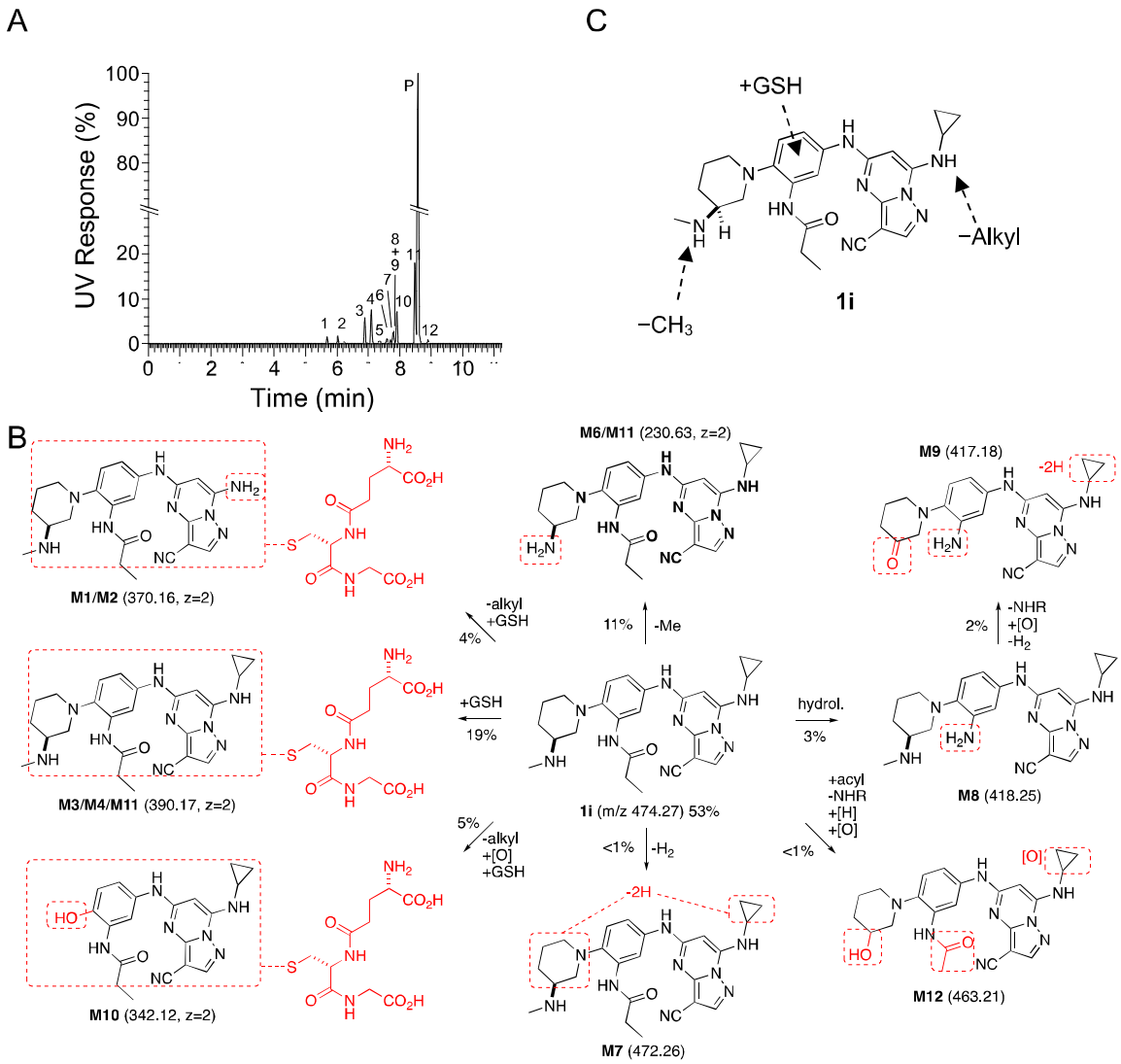

Figure 2. A. Identification of 12 metabolites of **1i** (Parent, P) after incubation in mouse primary hepatocytes for 4 h. The relative quantity of each metabolite was determined by UV. B. Structural assignment of the metabolites (**M1**–**M12**) from MS fragmentation (see Figure S2). Molecular ions shown in parentheses. Doubly charged ions are indicated as z=2. The relative percent contribution of each metabolite taken from Table 5. C. Summary of the major sites of metabolism of **1i** in mouse primary hepatocytes.

a predominantly a species-specific issue, with intrinsic clearance always much higher in mouse than human hepatocytes. Although this was a promising result for the future development of PZPs as therapeutic drugs for use in humans, it still limited their utility as pharmacological tools for studies in mice.

Inhibition of GSH Conjugation in Hepatocytes. Given our long-term objective to identify a potent CSNK2A inhibitor for use in an in vivo mouse COVID-19 efficacy model in vivo to

bioRxiv preprint doi: https://doi.org/10.1101/2023.05.15.540828; this version posted July 23, 2023. The copyright holder for this preprint (which was not certified by peer review) is the author/funder, who has granted bioRxiv a license to display the preprint in perpetuity. It is made available under aCC-BY 4.0 International license.

validate the host kinase as a potential antiviral drug target, we opted to explore the effect of inhibition of the Phase II GST enzyme on intrinsic clearance. Ethacrynic acid (EA) is an

Table 6: Mouse and human hepatocyte clearance[a]

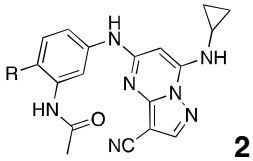

2

Compound	R	Mouse Hepatocyte CL_{int} (mL/min/kg)	Human Hepatocyte CL_{int} (mL/min/kg)
2a	Me	173	8
2b	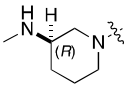	162	0
2c	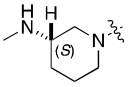	132	0
2d	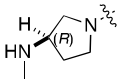	126	0
2e	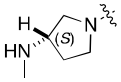	69	0
2f	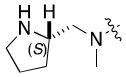	171	0.8
2h		279	23
2i	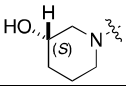	511	73

[a]Compounds quantified by LC/MS at 5 time points over 5 h, n = 1.

FDA-approved loop diuretic that is also a potent covalent, but reversible, inhibitor of GST enzymes [22]. EA has demonstrated potent inhibition of GST enzymes in perfused rat liver and human cancer cell lines,[22] but although it has been used in human clinical studies to block GSH conjugation[23] there are only a few reports of its use in rodents as a GST inhibitor.[24-26] To determine if EA could improve the metabolic stability of a PZP in primary mouse hepatocytes we tested the effect of co-dosing on the stability of **2h**, which was one of the analogs with the highest intrinsic clearance (Table 6). The intrinsic clearance of **2h** in primary mouse hepatocytes was determined by measuring the decrease in the level of the parent compound over 2 h (Figure 3). Parallel sets of incubations were performed in the presence of increasing doses of EA from 0–400 μM. In the absence of EA intrinsic clearance was >250 mL/min/kg. However, in

bioRxiv preprint doi: https://doi.org/10.1101/2023.05.15.540828; this version posted July 23, 2023. The copyright holder for this preprint (which was not certified by peer review) is the author/funder, who has granted bioRxiv a license to display the preprint in perpetuity. It is made available under aCC-BY 4.0 International license.

the presence of doses of EA from 10–50 μM the intrinsic clearance was decreased by >50% (Figure 3). At doses of EA above 100 μM, the intrinsic clearance of **2h** was further decreased to <50 mL/min/kg. The co-dosing mouse experiments in primary mouse hepatocytes demonstrated that EA was effective at increasing the metabolic stability of PZP **2h**, presumably by blocking its GSH conjugation.

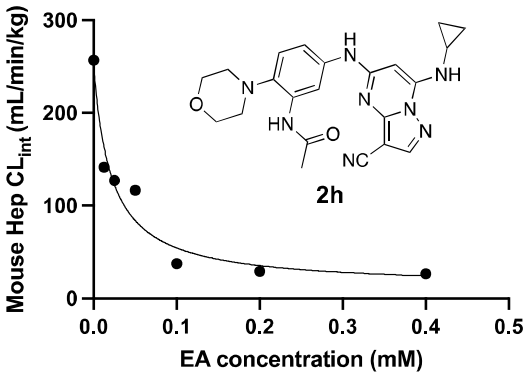

Figure 3. Mouse hepatocyte clearance of **2h** in the presence of GST inhibitor EA.

Co-dosing of 2h with Inhibitors of Metabolic Enzymes In Vivo. To determine if inhibition of GSH conjugation could also be an effective strategy to increase the bioavailability of **2h** in vivo, we performed a series of co-dosing studies in mice of **2h** with either EA or 1-aminobenzotriaole (1-ABT), a widely used broad-spectrum inhibitor of mouse cytochrome P450s[27] (Figure 4). When dosed alone to mice at 10 mg/kg i.p., **2h** was rapidly cleared from the circulation with a $t_{1/2}$ ~35 min and AUC ~4000 h•nM. A 6-hour pre-treatment and co-dosing with 10 mg/kg i.p. EA resulted in a small increase in $t_{1/2}$ and AUC. Increasing the dose to 30 mg/kg i.p. EA resulted in an additional increase in both parameters, demonstrating that inhibition of GST enzymes could reduce the intrinsic clearance of **2h**. The 30 mg/kg i.p. dose of EA increased the $t_{1/2}$ 1.5-fold and AUC 1.8-fold. Unfortunately, we were unable to further increase the dose of EA to 100 mg/kg i.p. due to the observation of toxicity in mice on repeat dosing (Table S1). Since GSH conjugation of electron-rich aromatic groups requires a prior cytochrome P450 oxidation, we also evaluated the in vivo pharmacokinetics of **2h** in mice pretreated with 1-ABT for 2 h. 1-ABT was able to block the metabolism of **2h** in primary mouse hepatocytes (Figure S2). A decrease in the clearance of **2h** was observed in mice pretreated with 1-ABT at 100 mg/kg p.o. with an increase in $t_{1/2}$ and AUC of 1.6-fold and 3.5-fold, respectively, compared to dosing of **2h** alone. The larger increase in AUC with 1-ABT compared to EA may be due to both inhibition of Phase I P450 metabolism and indirect inhibition of Phase II GSH conjugation.

bioRxiv preprint doi: https://doi.org/10.1101/2023.05.15.540828; this version posted July 23, 2023. The copyright holder for this preprint (which was not certified by peer review) is the author/funder, who has granted bioRxiv a license to display the preprint in perpetuity. It is made available under aCC-BY 4.0 International license.

Importantly, the results demonstrate that it is possible to increase the circulating levels of the PZP CSNK2A inhibitor **2h** by co-dosing with either a GST inhibitor or a P450 inhibitor. Finally, to

A

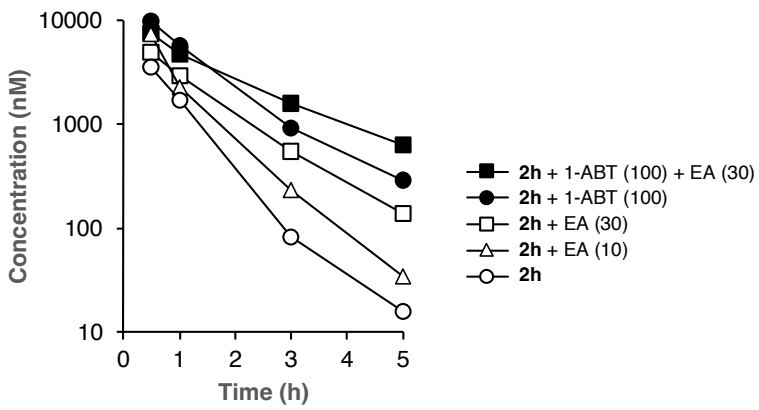

B

	2h i.p. (10)				
		+EA (10)	+EA (30)	+1-ABT (100)	+EA (30) +1-ABT (100)
$t_{1/2}$ (h)	0.59	0.66	0.90	0.93	1.4
C_{max} (nM)	3520	7350	4970	9730	7500
AUC_{last} (h*nM)	4090	7010	7410	14100	13400

Figure 4. In vivo clearance of **2h** in mice in the presence of a GST inhibitor (EA) or a P450 inhibitor (1-ABT). A. Blood levels of **2h** over 5 h following a 10 mg/kg dose i.p. All data is the average from 3 mice. The dose of EA or 1-ABT is indicated in mg/kg. EA was administered i.p. as a 6 h pre-treatment and again co-dosed with **2h**. 1-ABT was administered p.o. as a 2 h pre-treatment. B. Pharmacokinetic parameters.

determine whether combined co-dosing with both EA and 1-ABT could further decrease the clearance of **2h**, we performed a study in the presence of both the GST and P450 inhibitors. A combination of 30 mg/kg i.p. EA (6-hour pre-treatment and co-dosed) with 100 mg/kg p.o. 1-ABT (2-hour pre-treatment) resulted in the highest levels of **2h** at the 3h and 5h time-points (Figure 4), with the $t_{1/2}$ increased by 2.4-fold compared to dosing of **2h** alone.

bioRxiv preprint doi: https://doi.org/10.1101/2023.05.15.540828; this version posted July 23, 2023. The copyright holder for this preprint (which was not certified by peer review) is the author/funder, who has granted bioRxiv a license to display the preprint in perpetuity. It is made available under aCC-BY 4.0 International license.

Discussion and Conclusions

The 3-cyano-7-cyclopropylamino-pyrazolo[1,5-a]pyrimidine (PZP) is the most potent and selective chemotype of ATP-competitive CSNK2A inhibitors,[7] with fewer kinase off-targets than silmitasertib and related compounds.[28] SGC-CK2-1 (**1a**)[8] has been established as high-quality chemical probe for studying CSNK2 signaling in phenotypic assay and human-derived primary cells.[29-31] However, the use of PZP-based CSNK2A inhibitors as chemical probes in rodent pharmacology models has been limited by their generally poor pharmacokinetic properties. Although Dowling and coworkers reported that **2a** had modest oral bioavailability in rats (F = 25%, C_{max} = ~300 nM, $t_{1/2}$ = 2.6 h), **2a** showed in vivo activity only at short time points after dosing.[9] After extensive work on the series, Dowling concluded that an analog with an ethylenediamine substituent at the 4'-position could be used as a pharmacological tool by i.v. or i.p. dosing, despite its rapid clearance in rats.[10] For the studies reported herein, we decided to focus on development of an in vivo pharmacological probe that would maintain high sustained exposure in mice following i.p. dosing, since this route of administration was preferred in many academic laboratories for preclinical target validation studies.[32]

Initially, we examined the potential of the 4'-substitued analogs of SGC-CK2-1 (**1a**) to improve solubility and reduce its rapid metabolism in mouse liver microsomes. Testing several of the previously prepared analogs of **1a**[6, 8] confirmed prior observations[10] of reduced metabolism of linear and cyclic diamine analogs with cLogP <0.5 (Table 1). After synthesizing many new 4'-substituted PZPs in the acetamide (**1**) and propionamide (**2**) series, the chiral 3-methylaminopipiperides **1h–l**, **2b–c** and 3-methylaminopyrollidines **2d–e** were found to have the best balance of reduced MLM metabolism and good cellular potency in the antiviral assay. However, despite their improved stability to Phase I metabolism **1i, 2c,** and **2e** showed rapid clearance in mice following i.v. or i.p. administration (Table 3).

After discovering that **1i**, although stable in MLM, was rapidly metabolized in mouse primary hepatocytes, we performed a metabolic ID study that identified Phase II GSH conjugation as a major metabolic transformation (Table 4 and Figure 2). This result suggested that Phase II metabolism by GST enzymes was a previously underappreciated metabolic liability of PZPs containing electron-rich di- and tri-aniline rings. Unfortunately, all potent antiviral PZPs showed rapid metabolism in mouse primary hepatocytes (Table 6). Although the metabolic instability may be species-specific, since it was not observed in human primary hepatocytes, the rapid clearance in mouse primary hepatocytes predicted that none of the potent antiviral PZP analogs would be suitable for use in the mouse-adapted COVID-19 model.

bioRxiv preprint doi: https://doi.org/10.1101/2023.05.15.540828; this version posted July 23, 2023. The copyright holder for this preprint (which was not certified by peer review) is the author/funder, who has granted bioRxiv a license to display the preprint in perpetuity. It is made available under aCC-BY 4.0 International license.

To explore ways to reduce the Phase II metabolism of a PZP analog, we investigated co-dosing with EA, a well characterized broad-spectrum covalent, but reversible, inhibitor of rodent and human GSTs.[22] The studies were performed with the potent antiviral morpholine analog **2h**, which exhibited very high clearance in primary mouse hepatocytes. Co-dosing of EA with **2h** in primary mouse hepatocytes demonstrated that metabolism could be reduced in a dose dependent manner, with >90% reduction in intrinsic clearance at EA concentrations >100 μM (Figure 3).

Translating the use of EA as a GST inhibitor to an in vivo setting in mice was not straightforward. EA is an inhibitor of NKCC2, a Na-K-Cl transporter, and is approved for use in humans as a loop diuretic for treatment of high blood pressure and edema.[33] At its commonly used 50 mg oral dose, EA does not cause significant drug-drug interactions that might result from GST inhibition. However, in rodents, no dose ranging studies to establish the lowest effective dose for GST inhibition have been reported. Although, doses of 10–20 mg/kg p.o. have been used to boost the activity of oncology drugs in mice.[24-26] Our pharmacokinetic studies in mice revealed that the maximum tolerated dose of EA by i.p. dosing was only 30 mg/kg. Doses of 100 mg/kg and higher resulted in clinical symptoms including death (Table S1). Although the reason for the toxicity of EA by i.p. administration is unclear, the rapid onset suggests that it may be unrelated to inhibition liver metabolism enzymes. Nevertheless, we observed a reduction in the plasma clearance of **2h** at both the 10 and 30 mg/kg i.p. co-doses of EA. Furthermore, the clearance of **2h** was also reduced by a 100 mg/kg p.o. dose of the irreversible cytochrome P450 inhibitor 1-ABT, which would be expected to block direct Phase I and indirect Phase II metabolism. The most effective strategy to decrease the clearance of **2h** was the co-dosing protocol, using a combination of 30 mg/kg i.p. EA and 100 mg/kg p.o 1-ABT. With this approach the blood level of **2h** was boosted ~40-fold at the 5 h time point.

In conclusion, our findings demonstrate that Phase II metabolism limits the in vivo exposure of PZP-based CSNK2A inhibitors in mice, which severely limits their utility as pharmacological probes despite their remarkable potency and selectivity in cells. Although the use of EA as a GST inhibitor provides an effective method to reduce the intrinsic clearance of the current molecules in mice, we are continuing to optimize the series to identify analogs with reduced potential for Phase II metabolism. Our goal is to find in vivo chemical probes for CSNK2A that can be dosed in mice without the additional complication of co-dosing with multiple inhibitors of drug metabolizing enzymes.

bioRxiv preprint doi: https://doi.org/10.1101/2023.05.15.540828; this version posted July 23, 2023. The copyright holder for this preprint (which was not certified by peer review) is the author/funder, who has granted bioRxiv a license to display the preprint in perpetuity. It is made available under aCC-BY 4.0 International license.

Experimental Section.

NanoBRET Assay. Assays were run with a modified version of the previously published protocols.[6, 8] HEK293 cells were cultured at 37 °C, 5% CO_2 in Dulbecco's modified Eagle medium (DMEM; Gibco) supplemented with 10% fetal bovine serum (VWR/Avantor). A transfection complex of DNA at 10 μg/mL was created, consisting of 9 μg/mL of carrier DNA (Promega) and 1 μg/mL of CSNK2A-NLuc fusion DNA in Opti-MEM without serum (Gibco). FuGENE HD (Promega) was added at 30 μl/mL to form a lipid:DNA complex. The solution was then mixed and incubated at room temperature for 20 min. The transition complex was mixed with a 20x volume of HEK293 cells at 20,000 cells per mL in DMEM/FBS and 100 μL per well was added to a 96-well plate that was incubated overnight at 37°C, 5% CO_2. The following day, the media was removed via aspiration and replaced with 85 µL of Opti-MEM without phenol red. A total of 5 µL per well of 20x-NanoBRET Tracer K10 (Promega) at 10 µM for CSNK2A1 or 5 µM for CSNK2A2 in Tracer Dilution Buffer (Promega N291B) was added to all wells, except the "no tracer" control wells. Test compounds (10 mM in DMSO) were diluted 100x in Opti-MEM media to prepare stock solutions and evaluated at eleven concentrations. A total of 10 µL per well of the 10-fold test compound stock solutions (final assay concentration of 0.1% DMSO) were added. For "no compound" and "no tracer" control wells, DMSO in OptiMEM was added for a final concentration of 1.1% across all wells. 96-well plates containing cells with NanoBRET Tracer K10 and test compounds (100 μL total volume per well) were equilibrated (37°C / 5% CO_2) for 2 h. The plates were cooled to room temperature for 15 min. NanoBRET NanoGlo substrate (Promega) at a ratio of 1:166 to Opti-MEM media in combination with extracellular NLuc Inhibitor (Promega) diluted 1:500 (10 µL of 30 mM stock per 5 mL Opti-MEM plus substrate) were combined to create a 3X stock solution. A total of 50 µL of the 3X substrate/extracellular NL inhibitor were added to each well. The plates were read within 30 min on a GloMax Discover luminometer (Promega) equipped with 450 nm BP filter (donor) and 600 nm LP filter (acceptor) using 0.3 s integration time. Raw milliBRET (mBRET) values were obtained by dividing the acceptor emission values (600 nm) by the donor emission values (450 nm) and multiplying by 1000. Averaged control values were used to represent complete inhibition (no tracer control: Opti-MEM + DMSO only) and no inhibition (tracer only control: no compound, Opti-MEM + DMSO + Tracer K10 only) and were plotted alongside the raw mBRET values. The data was first normalized and then fit using Sigmoidal, 4PL binding curve in Prism Software to determine IC_{50} values.

MHV Assay. DBT cells were cultured at 37°C in Dulbecco's modified Eagle medium (DMEM; Sigma) supplemented with 10% fetal bovine serum (Gibco) and penicillin and

bioRxiv preprint doi: https://doi.org/10.1101/2023.05.15.540828; this version posted July 23, 2023. The copyright holder for this preprint (which was not certified by peer review) is the author/funder, who has granted bioRxiv a license to display the preprint in perpetuity. It is made available under aCC-BY 4.0 International license.

streptomycin (Sigma). DBT cells were plated in 96 well plates to be 80% confluent at the start of the assay. Test compounds were diluted to 15 μM in DMEM. Serial 4-fold dilutions were made in DMEM, providing a concentration range of 15 μM to 0.22 μM. Media was aspirated from the DBT cells and 100 µL of the diluted test compounds were added to the cells for 1 h at 37°C. After 1 h, MHV-nLuc[6] was added at an MOI of 0.1 in 50 µL DMEM so that the final concentration of the first dilution of compound was 10 µM (T=0). After 10 h, the media was aspirated, and the cells were washed with PBS and lysed with passive lysis buffer (Promega) for 20 min at room temperature. Relative light units (RLUs) were measured using a luminometer (Promega; GloMax). Triplicate data was analyzed in Prism Graphpad to generate IC_{50} values.

Kinetic Solubility. 50 mL of phosphate buffered saline (PBS, Fisher, pH 7.4) was added to HPLC grade H_2O (450 mL) for a total dilution factor of 1:10 and a final PBS concentration of 1X. 6 µL of the test compound as a 10 mM DMSO stock solutions was combined with the aqueous PBS solution (294 µL) for 50-fold dilution in a Millipore solubility filter plate with 0.45 µM polycarbonate filter membrane using a Hamilton Starlet liquid handler. The final DMSO concentration was 2.0% and maximum theoretical compound concentration was 200 µM. The filter plate was heat sealed for the duration of the 24 h incubation period. The sample was placed on a rotary shaker (200 RPM) for 24 h at ambient temperature (21.6–22.8°C) then vacuum filtered. All filtrates were injected into a chemiluminescence nitrogen detector for quantification. The equimolar nitrogen response of the detector was calibrated using standards which span the dynamic range of the instrument from 0.08 to 4500 µg/mL nitrogen. The filtrates were quantified with respect to this calibration curve. The calculated solubility values were corrected for background nitrogen present in the DMSO and the media used to prepare the samples.

Mouse Liver Microsomal Stability. Compounds as 10 mM DMSO stock solutions were diluted to 2.5 mM with DMSO and again to 0.5 mM with MeCN to give a final solution containing 0.5 mM compound in 1:4 DMSO/MeCN. Liver microsomes from male CD-1 mice were sourced from Xenotech (Kansas City, KS), Lot No. 1710069. A reaction plate was prepared by adding 691.25 µL, pre-warmed (37ºC) microsomal solution (0.63 mg/mL protein in 100 mM KPO_4 with 1.3 mM EDTA) to an empty well of a 96-well plate and maintained at 37ºC. The diluted 0.5 mM compound (8.75 µL) was added to the microsomal solution in the reaction plate and mixed thoroughly by repeated pipetting to give a final assay concentration of 5.0 µM compound. The resulting solutions were pre-incubated for 5 min at 37ºC and then dispensed into T = 0 and incubation plates. For the T = 0 plates, an aliquot (160 µL) of each reaction solution was added to an empty well of a 96-well plate, as an exact replicate of the Reaction Plate. Cold (4ºC)

bioRxiv preprint doi: https://doi.org/10.1101/2023.05.15.540828; this version posted July 23, 2023. The copyright holder for this preprint (which was not certified by peer review) is the author/funder, who has granted bioRxiv a license to display the preprint in perpetuity. It is made available under aCC-BY 4.0 International license.

MeOH (400 µL) was added to each well and mixed thoroughly by repeated pipetting. NADPH regeneration solution (40 µL) was added to each well and mixed thoroughly by repeated pipetting. For the T = 30-min Incubation Plate, NADPH (95 µL) was added to the remaining solution (microsomes + test compound) in each well in the previously prepared reaction plate to initiate the reaction. The plate was sealed and incubated at 37ºC for 30 min. An aliquot (100 µL) was removed from each well at the desired time point and dispensed into a well of a 96-well plate. 200µL of cold (4ºC) MeOH was added to quench the reaction. All plates were sealed, vortex and centrifuged at 3000 RPM, 4ºC for 15 min, and the supernatants were transferred for analysis by LC-TOFMS. The supernatant (20 μL) was injected onto an AQUASIL C18 column and eluted using a fast-generic gradient program. TOFMS Data was acquired using Agilent 6538 Ultra High Accuracy TOF MS in extended dynamic range (m/z 100-1000) using generic MS conditions in positive mode. Following data acquisition, exact mass extraction and peak integration was performed using MassHunter Software (Agilent Technologies). The stability of the compound was calculated as the percent remaining of the unchanged parent at T=30 min relative to the peak area at T=0 min.

To determine CL_{int}, aliquots of 50 μL were taken from the reaction solution at 0, 15, 30, 45 and 60 min. The reaction was stopped by the addition of 4 volumes of cold MeCN with IS (100 nM alprazolam, 200 nM imipramine, 200 nM labetalol and 2 µM ketoprofen). Samples were centrifuged at 3,220 g for 40 min and of 90 μL of the supernatant was mixed with 90 μL of ultra-pure H_2O and then used for LC-MS/MS analysis. Peak areas were determined from extracted ion chromatograms and the slope value, k, was determined by linear regression of the natural logarithm of the remaining percentage of the parent drug vs. incubation time curve. The intrinsic clearance (CL_{int} in μL/min/mg) was calculated using the relationship CL_{int} = kV/N where V = incubation volume and N = amount of protein per well. To measure CL_{int} in the presence of microsomal and cytosolic enzymes, the experiment was repeated using liver S9 fractions microsomes from male CD-1 mice sourced from Xenotech (Kansas City, KS), Lot No. 1510255.

Hepatocyte Stability. Human cryopreserved hepatocytes were supplied by BioIVT (lot QZW, 10 pooled donors). Mouse cryopreserved hepatocytes were supplied by BioIVT (lot ZPG, pooled male CD-1). Vials of cryopreserved hepatocytes were removed from storage and thawed in a 37ºC water bath with gently shaking, and then the contents were poured into a 50 mL thawing medium conical tube. Vials were centrifuged at 100 g for 10 minutes at room temperature. Thawing medium was aspirated and hepatocytes were resuspended with serum-free incubation medium to yield ~1.5 x 10^6 cells/mL. Cell viability and density were counted using AO/PI fluorescence staining, and then cells were diluted with serum-free incubation

bioRxiv preprint doi: https://doi.org/10.1101/2023.05.15.540828; this version posted July 23, 2023. The copyright holder for this preprint (which was not certified by peer review) is the author/funder, who has granted bioRxiv a license to display the preprint in perpetuity. It is made available under aCC-BY 4.0 International license.

medium to a working cell density of 0.5 x 10^6 viable cells/mL. Aliquots of 198 µL hepatocytes were dispensed into each well of a 96-well non-coated plate. The plate was placed in an incubator for approximately 10 min. Aliquots of 2 µL of 100 µM test compound in duplicate and positive control were added into respective wells of the non-coated 96-well plate to start the reaction. The final concentration of test compound was 1 µM. The plate was placed in an incubator for the designed time points. 25 µL of contents were transferred and mixed with 6 volumes (150 µL) of cold MeCN with IS (100 nM alprazolam, 200 nM labetalol, 200 nM caffeine and 200 nM diclofenac) to terminate the reaction at time points of 0, 15, 30, 60, 90 and 120 minutes. Samples were centrifuged for 45 min at 3,220 g and aliquot of 100 μL of the supernatant was diluted with 100 μL of ultra-pure H_2O, and the mixture was used for LC/MS/MS analysis. Peak areas were determined from extracted ion chromatograms and the slope value, k, was determined by linear regression of the natural logarithm of the remaining percentage of the parent drug vs. incubation time curve. The intrinsic clearance (CL_{int} in μL/min/10^6 cells) was calculated using the relationship CL_{int} = kV/N where V = incubation volume (0.2 mL) and N = number of hepatocytes per well (0.1 x 10^6 cells). Scaling factors to convert CL_{int} from μL/min/10^6 cells to mL/min/kg were 2540 (human hepatocytes) and 11800 (mouse hepatocytes).

Pharmacokinetics (PK). Male CD-1 mice (6–8 weeks, 20–30 g) were dosed by intravenous (i.v.) or interperitoneal (i.p.) administration. For i.v. administration a single dose of the compound (1 mg/kg) was administered as a 5 mL/kg volume of a 0.2 mg/mL solution in NMP/Solutol/PEG-400/normal saline (v/v/v/v, 10:5:30:55) to three mice. For i.p. administration a single dose of the compound (10 mg/kg) was administered as a 10 mL/kg volume of a 1.0 mg/mL solution in 0.5% HPMC/0.2% Tween 80/99.3% H_2O or DMSO/PEG-400/saline (v/v/v/v, 10:30:60) to three mice. The mice had free access to water and food. Blood (0.03 mL) was collected from dorsal metatarsal vein at 0.5, 1, 3, and 5 h timepoints (snapshot PK) or at 0.08, 0.25, 0.5, 1, 2, 4, 8, and 24 h (full PK). Blood from each sample was transferred into plastic microcentrifuge tubes containing EDTA-K2 and mixed well, then placed in a cold box prior to centrifugation. Blood samples were centrifuged at 4000 g for 5 min at 4ºC to obtain plasma and then stored at -75ºC prior to analysis. Concentrations of test compound in the plasma samples were determined using a Prominence LC-30AD, AB Sciex Triple Quan 5500 LC/MS/MS instrument fitted with a HALO 160A C18 column (2.7 μm, 2.1 x 50 mm) using a mobile phase of 5–95% MeCN in H_2O with 0.1% formic acid. PK parameters were calculated from the mean plasma concentration versus time by a non-compartmental model using WinNonlin 8.3 (Phoenix) to determine C_{max}, AUC_{last}, $t_{1/2}$, CL_{int}, and *F*.

bioRxiv preprint doi: https://doi.org/10.1101/2023.05.15.540828; this version posted July 23, 2023. The copyright holder for this preprint (which was not certified by peer review) is the author/funder, who has granted bioRxiv a license to display the preprint in perpetuity. It is made available under aCC-BY 4.0 International license.

For co-dosing studies, **2h** (10 mg/kg) was administered i.p. as a 10 mL/kg volume of a 1.0 mg/mL solution in DMSO/PEG-400/saline (v/v/v/v, 10:30:60). EA (10 or 30 mg/kg) was administered i.p. as a 1 mL/kg volume of a 30 mg/mL solution in NMP/PEG-400/Water (v/v/v, 10:60:30) as a 6 h pretreatment and again at time of dosing of **2h**. 1-ABT (100 mg/kg) was administered p.o. as a 10 mL/kg volume of a 10 mg/mL solution in saline as a 2 h pretreatment. Blood (0.03 mL) was collected from dorsal metatarsal vein at 0.5, 1, 3, and 5 h timepoints and the level of **2h** in plasma determined by LC/MS/MS as described above. With this dosing protocol no adverse clinical observations were recorded during the study.

General Synthetic Methods. All chemical reagents were commercially available except those whose synthesis is described below. All reaction mixtures and column eluents were monitored via analytical thin-layer chromatography (TLC) performed on pre-coated fluorescent silica gel plates, 200 μm with an F254 indicator; visualization was accomplished by UV light (254/365 nm). NMR spectra were obtained on a Bruker/AVANCE NEO 400MHz instrument. LCMS measurements were determined on Shimadzu LC-AB+LCMS2020, Shimadzu LC-AD+LCMS2020, Shimadzu LC-AD xR+LCMS2020, or Agilent 1200+ Infinitylab LC/MSD instruments. Purity was determined by HPLC measurement using a Shimadzu LC-20+LCMS-2020 instrument fitted with an Agilent PoroShell 120 EC-C18 column (45°C, 2.7 μm, 3.0*50 mm); 8 min chromatography run 0.037% TFA in water/MeCN (19:1) (solvent A), 0.018% TFA/MeCN (solvent B), gradient 0–60% (solvent B) over 6.0 min, held at 60% for 1.0 min, and returned to 0% (solvent B) for 1.0 min at a flow rate of 1.0 ml/min; 4 min chromatography run 0.037% TFA in water/MeCN (19:1) (solvent A), 0.018% TFA/MeCN (solvent B), gradient 10–80% (solvent B) over 3.0 min, held at 80% for 0.5 min, and returned to 0% (solvent B) for 0.5 min at a flow rate of 1.0 ml/min; which indicated that all final compounds were >95% pure.

General Procedure A. Synthesis of intermediate **y**. To a solution of *N*-(2-fluoro-5-nitrophenyl)propionamide (800 mg, 3.77 mmol) or *N*-(2-fluoro-5-nitrophenyl)acetamide (747 mg, 3.77 mmol) and an amine (3.77 mmol) in MeCN (8 mL) was added K_2CO_3 (1.56 g, 11.3 mmol) at 25°C. The mixture was stirred at 100°C for 10 h. The reaction mixture was concentrated in vacuo. Water (200 mL) was added, and the mixture was extracted with EtOAc (250 mL x 2). The combined organic phase was washed with brine (250 mL), dried over anhydrous Na_2SO_4, filtered, and concentrated in vacuo. To the resulting nitrobenzene (4.67 mmol) in MeOH (3 mL) was added 10% Pd/C (900 mg) under N_2 atmosphere. The suspension was degassed and purged with H_2 three times, and then stirred under H_2 (15 psi) at 25°C for 10 h. The reaction mixture was filtered through a celite pad. The pad was washed with MeOH (8 mL x 2) and the

bioRxiv preprint doi: https://doi.org/10.1101/2023.05.15.540828; this version posted July 23, 2023. The copyright holder for this preprint (which was not certified by peer review) is the author/funder, who has granted bioRxiv a license to display the preprint in perpetuity. It is made available under aCC-BY 4.0 International license.

combined filtrate concentrated in vacuo. The residue was purified by flash silica gel chromatography (eluent of 0–8%, MeOH/CH_2Cl_2) to yield intermediate **y**.

(R)-N-(5-((3-cyano-7-(cyclopropylamino)pyrazolo[1,5-a]pyrimidin-5-yl)amino)-2-(3-(methylamino)piperidin-1-yl)phenyl)propionamide ***(1h).*** Intermediate **y** was synthesized from tert-butyl (*R*)-methyl(piperidin-3-yl)carbamate and *N*-(2-fluoro-5-nitrophenyl)propionamide by Procedure A. To a solution of 5-chloro-7-(cyclopropylamino)pyrazolo[1,5-a]pyrimidine-3-carbonitrile[6] (100 mg, 0.43 mmol) and intermediate **y** (170mg, 0.43 mmol) in dioxane (3 mL) was added Cs_2CO_3 (418 mg, 1.28 mmol), BINAP (40 mg, 0.06 mmol) and $Pd(OAc)_2$ (14.0 mg, 0.06 mmol) at 25°C. The mixture was degassed and purged with N_2 and then heated in a microwave reactor at 130°C for 0.5 h. The reaction mixture was concentrated in vacuo and the residue was purified by flash silica gel chromatography (eluent of 0–4%, MeOH/CH_2Cl_2). To the product in CH_2Cl_2 (5 mL) was added TFA (7 mL), and the mixture was stirred at 25°C for 2 h. The reaction mixture was concentrated in vacuo and the residue was purified by prep-HPLC (column: Xtimate C18 150*40 mm*10 μm; mobile phase: [water (HCO_2H)-MeCN]; B%: 15–45%, 10 min). Compound **1h** (66.3 mg, 11.3%) was obtained as a white solid. ^{1}H NMR (400 MHz, DMSO-d_6) δ 9.65 (s, 1H), 9.33 (br s, 1H), 8.44 (s, 1H), 8.33 (s, 1H), 8.19 (s, 1H), 8.04 (d, J = 2.4 Hz, 1H), 7.82 (d, J = 7.2 Hz, 1H), 7.09 (d, J = 8.4 Hz, 1H), 6.03 (s, 1H), 3.13 (br s, 1H), 3.05 (d, J = 10.4 Hz, 1H), 2.89 - 2.80 (m, 2H), 2.60-2.58 (m, 2H), 2.52-2.51 (m, 1H), 2.48-2.44 (m, 4H), 1.92-1.91 (m, 1H), 1.75 (s, 2H), 1.62-1.60 (m, 1H), 1.12 (t, J = 7.6 Hz, 3H), 0.80-0.79 (m, 2H), 0.72-0.70 (m, 2H). ^{13}C NMR (101 MHz, DMSO-d_6) δ 172.04, 165.85, 156.77, 150.78, 148.07, 144.88, 137.77, 136.07, 132.78, 119.97, 114.74, 76.13, 54.06, 52.95, 38.69, 30.66, 29.41, 23.17, 9.79, 6.39. HPLC R_t = 3.656 min in 8 min chromatography, purity 99.6%. LCMS R_t = 1.925 min in 4 min chromatography, purity 98.0%, MS ESI calcd. for 473.27 $[M+H]^+$ 474.27, found 474.4.

*(S)-N-(5-((3-cyano-7-(cyclopropylamino)pyrazolo[1,5-a]pyrimidin-5-yl)amino)-2-(3-(methylamino)piperidin-1-yl)phenyl)propionamide (**1i**).* Intermediate **y** was synthesized from tert-butyl (*S*)-methyl(piperidin-3-yl)carbamate and *N*-(2-fluoro-5-nitrophenyl)propionamide by Procedure A. To a solution of 5-chloro-7-(cyclopropylamino)pyrazolo[1,5-a]pyrimidine-3-carbonitrile[6] (112 mg, 0.48 mmol) and intermediate **y** (200 mg, 0.53 mmol) in dioxane (3 mL) was added Cs_2CO_3 (502 mg, 1.53 mmol), BINAP (48 mg, 0.07 mmol) and $Pd(OAc)_2$ (16.8 mg, 0.07 mmol) at 25°C. The mixture was degassed and purged with N_2 and heated in a microwave reactor at 130°C for 0.5 h. The reaction mixture was concentrated in vacuo and the residue was purified by flash silica gel chromatography (eluent of 0–4%, MeOH/CH_2Cl_2). To the product in CH_2Cl_2 (5 mL) was added TFA (7 mL), and the mixture was stirred at 25°C for 2 h. The reaction

bioRxiv preprint doi: https://doi.org/10.1101/2023.05.15.540828; this version posted July 23, 2023. The copyright holder for this preprint (which was not certified by peer review) is the author/funder, who has granted bioRxiv a license to display the preprint in perpetuity. It is made available under aCC-BY 4.0 International license.

mixture was concentrated in vacuo and the residue was purified by prep-HPLC (column: Xtimate C18 150*40 mm*10 μm; mobile phase: [water (HCO_2H)-MeCN]; B%: 0–38%, 36min). Compound **1i** (115 mg, 37.0%) was obtained as a yellow solid. ^{1}H NMR (400 MHz, DMSO-d_6) δ 9.65 (s, 1H), 9.09 (s, 1H), 8.43-8.36 (m, 1H), 8.34 (s, 1H), 8.20 (s, 1H), 8.07-8.01 (m, 1H), 7.89-7.78 (m, 1H), 7.12 (d, J = 8.8 Hz, 1H), 6.03 (s, 1H), 3.24 (s, 1H), 3.12-3.05 (m, 1H), 2.93-2.84 (m, 1H), 2.83-2.75 (m, 1H), 2.68 - 2.54 (m, 5H), 2.48-2.41 (m, 2H), 1.95-1.60 (m, 4H), 1.13 (t, J = 7.6 Hz, 3H), 0.84-0.66 (m, 4H). ^{13}C NMR (101 MHz, DMSO-d_6) δ 172.16, 165.58, 156.97, 150.97, 148.26, 145.06, 137.96, 136.25, 132.97, 120.21, 115.33, 114.91, 76.32, 54.47, 53.83, 53.02, 31.24, 29.65, 23.36, 21.77, 9.95, 6.57. HPLC R_t = 3.612 min in 8 min chromatography, purity 99.6%. LCMS R_t = 1.567 min in 4 min chromatography, purity 100.0%, MS ESI calcd. for 473.3 $[M+H]^+$ 474.3, found 474.5.

*(R)-N-(5-((3-cyano-7-(cyclopropylamino)pyrazolo[1,5-a]pyrimidin-5-yl)amino)-2-(3-(methylamino)piperidin-1-yl)phenyl)acetamide (**2b**).* Intermediate **y** was synthesized from tert-butyl (R)-methyl(piperidin-3-yl)carbamate and N-(2-fluoro-5-nitrophenyl)acetamide by Procedure A. To a solution of 5-chloro-7-(cyclopropylamino)pyrazolo[1,5-a]pyrimidine-3-carbonitrile[6] (112 mg, 0.48 mmol) and intermediate **y** (200 mg, 0.55 mmol) in dioxane (3 mL) was added Cs_2CO_3 (541 mg, 1.65 mmol), BINAP (51 mg, 0.08 mmol) and $Pd(OAc)_2$ (17.9 mg, 0.08 mmol) at 25°C. The mixture was degassed and purged with N_2 and heated in a microwave reactor at 130°C for 0.5 h. The reaction mixture was concentrated in vacuo and the residue was purified by flash silica gel chromatography (eluent of 0–32%, EtOAc/petroleum ether) to give the product. To the product in CH_2Cl_2 (5 mL) was added TFA (7 mL), and the mixture was stirred at 25°C for 2 h. The reaction mixture was concentrated in vacuo and the residue was purified by prep-HPLC (column: Phenomenex C18 75*30 mm*3 μm; mobile phase: [water (HCO_2H)-MeCN]; B%: 2–32%, 24 min). Compound **2b** (32.8 mg, 27.4%) was obtained as a white solid. ^{1}H NMR (400 MHz, DMSO-d_6) δ 9.63 (s, 1H), 9.41 (s, 1H), 8.41 (s, 1H), 8.32 (s, 1H), 8.16 (s, 1H), 7.99 (d, J = 1.6 Hz, 1H), 7.83 (d, J = 6.4 Hz, 1H), 7.10 (d, J = 8.8 Hz, 1H), 6.03 (s, 1H), 3.22 (s, 1H), 3.06 (d, J = 11.2 Hz, 1H), 2.93 (d, J = 8.4 Hz, 1H), 2.84 (d, J = 11.2 Hz, 1H), 2.58 (s, 2H), 2.53 (s, 3H), 2.18 (s, 3H), 1.95 (s, 1H), 1.79 (s, 2H), 1.67-1.56 (m, 1H), 0.80 (d, J = 6.8 Hz, 2H), 0.70 (d, J = 2.8 Hz, 2H). ^{13}C NMR (101 MHz, DMSO-d_6) δ 168.62, 163.65, 156.97, 150.98, 148.26, 145.08, 137.91, 136.26, 133.03, 120.20, 115.42, 114.96, 76.32, 54.08, 53.19, 40.15, 39.99, 39.78, 24.09, 23.36, 6.59. HPLC R_t = 3.321 min in 8 min chromatography, purity 99.9%. LCMS R_t = 1.551 min in 4 min chromatography, purity 99.8%, MS ESI calcd. for 459.25 $[M+H]^+$ 460.25, found 460.4.

bioRxiv preprint doi: https://doi.org/10.1101/2023.05.15.540828; this version posted July 23, 2023. The copyright holder for this preprint (which was not certified by peer review) is the author/funder, who has granted bioRxiv a license to display the preprint in perpetuity. It is made available under aCC-BY 4.0 International license.

*(S)-N-(5-((3-cyano-7-(cyclopropylamino)pyrazolo[1,5-a]pyrimidin-5-yl)amino)-2-(3-(methylamino)piperidin-1-yl)phenyl)acetamide (**2c**).* Intermediate **y** was synthesized from tert-butyl (*S*)-methyl(piperidin-3-yl)carbamate and *N*-(2-fluoro-5-nitrophenyl)acetamide by Procedure A. To a solution of 5-chloro-7-(cyclopropylamino)pyrazolo[1,5-a]pyrimidine-3-carbonitrile[6] (237 mg, 1.02 mmol) and intermediate **y** (460 mg, 1.27 mmol) in dioxane (6 mL) was added Cs_2CO_3 (1.0 g, 1.65 mmol), BINAP (94.8 mg, 0.14 mmol) and $Pd(OAc)_2$ (33.2 mg, 0.14 mmol) at 25°C. The mixture was degassed and purged with N_2 and heated in a microwave reactor at 130°C for 0.5 h. The reaction mixture was concentrated in vacuo and the residue was purified by flash silica gel chromatography (eluent of 0–3%, MeOH/CH_2Cl_2). To the product in CH_2Cl_2 (5 mL) was added TFA (7 mL), and the mixture was stirred at 25°C for 2 h. The reaction mixture was concentrated in vacuo and the residue was purified by prep-HPLC (column: Xtimate C18 100*30 mm*10 μm; mobile phase: [water (HCO_2H)-MeCN]; B%: 30%-50%, 10min). Compound **2c** (58 mg, 27.4%) was obtained as a white solid. ^{1}H NMR (400 MHz, DMSO-d_6) δ 9.64 (s, 1H), 9.38-9.21 (m, 1H), 8.39-8.30 (m, 1H), 8.17 (s, 1H), 7.97 (s, 1H), 7.89-7.77 (m, 1H), 7.10 (d, J = 8.8 Hz, 1H), 6.03 (s, 1H), 3.11-3.03 (m, 2H), 3.02-2.90 (m, 2H), 2.89-2.82 (m, 1H), 2.62-2.53 (m, 5H), 2.20 (s, 3H), 2.06-1.94 (m, 1H), 1.89-1.72 (m, 2H), 1.67-1.58 (m, 1H), 0.84-0.76 (m, 2H), 0.73-0.66 (m, 2H). ^{13}C NMR (101 MHz, DMSO-d_6) δ 168.66, 162.94, 156.95, 150.96, 148.25, 145.07, 137.91, 136.26, 132.85, 120.17, 115.48, 114.94, 113.94, 76.32, 54.13, 53.14, 39.99, 30.59, 24.20, 23.36, 6.58. HPLC R_t = 3.324 min in 8 min chromatography, purity 99.2%. LCMS R_t = 1.549 min in 4 min chromatography, purity 99.6%, MS ESI calcd. for 459.25 $[M+H]^+$ 460.25, found 460.4.

*(R)-N-(5-((3-cyano-7-(cyclopropylamino)pyrazolo[1,5-a]pyrimidin-5-yl)amino)-2-(3-(methylamino)pyrrolidin-1-yl)phenyl)acetamide (**2d**).* Intermediate **y** was synthesized from tert-butyl (*R*)-methyl(pyrrolidin-3-yl)carbamate and *N*-(2-fluoro-5-nitrophenyl)acetamide by Procedure A. To a solution of 5-chloro-7-(cyclopropylamino)pyrazolo[1,5-a]pyrimidine-3-carbonitrile[6] (134 mg, 0.57 mmol) and intermediate **y** (250 mg, 0.72 mmol) in dioxane (3 mL) was added Cs_2CO_3 (0.5 g, 0.82 mmol), BINAP (47.4 mg, 0.07 mmol) and $Pd(OAc)_2$ (16.6 mg, 0.07 mmol) at 25°C. The mixture was degassed and purged with N_2 and heated in a microwave reactor at 130°C for 0.5 h. The reaction mixture was concentrated in vacuo and the residue was purified by prep-HPLC (column: Waters Torus 2-PIC 150*19 mm*5 μm; mobile phase: [Heptane-EtOH (0.1% NH_3/H_2O)]; B%: 10–50%, 5min) to give the product as a yellow solid. To the product in CH_2Cl_2 (5 mL) was added TFA (7 mL), and the mixture was stirred at 25°C for 2 h. The reaction mixture was concentrated in vacuo and the residue was purified by prep-HPLC (column: Xtimate C18 100*30 mm*10 μm; mobile phase: [water (HCO_2H)-MeCN]; B%: 25–45%,

bioRxiv preprint doi: https://doi.org/10.1101/2023.05.15.540828; this version posted July 23, 2023. The copyright holder for this preprint (which was not certified by peer review) is the author/funder, who has granted bioRxiv a license to display the preprint in perpetuity. It is made available under aCC-BY 4.0 International license.

10 min). Compound **2d** (20 mg, 30.2%) was obtained as a white solid. ^{1}H NMR (400 MHz, MeOD-d_4) δ 9.56 (s, 1H), 9.30 (s, 1H), 8.46-8.28 (m, 2H), 8.16 (s, 1H), 7.93-7.60 (m, 2H), 7.02 (d, J = 8.4 Hz, 1H), 5.99 (s, 1H), 3.55-3.50 (m, 1H), 3.34-3.09 (m, 4H), 2.95-2.84 (m, 1H), 2.61-2.51 (m, 4H), 2.26-2.06 (m, 4H), 1.9-1.86 (m, 1H), 0.86-0.76 (m, 2H), 0.75-0.66 (m, 2H). ^{13}C NMR (101 MHz, DMSO-d_6) δ 168.49, 157.01, 151.02, 148.19, 145.00, 134.54, 130.86, 118.11, 116.30, 114.95, 76.17, 57.99, 54.44, 49.20, 39.99, 23.89, 23.32, 6.55. HPLC R_t = 3.063 min in 8 min chromatography, purity 99.8%. LCMS R_t = 1.422 min in 4 min chromatography, purity 99.9%, MS ESI calcd. for 445.23 $[M+H]^+$ 446.23, found 446.4.

*(S)-N-(5-((3-cyano-7-(cyclopropylamino)pyrazolo[1,5-a]pyrimidin-5-yl)amino)-2-(3-(methylamino)pyrrolidin-1-yl)phenyl)acetamide (**2e**).* Intermediate **y** was synthesized from tert-butyl (*S*)-methyl(pyrrolidin-3-yl)carbamate and *N*-(2-fluoro-5-nitrophenyl)acetamide by Procedure A. To a solution of 5-chloro-7-(cyclopropylamino)pyrazolo[1,5-a]pyrimidine-3-carbonitrile[6] (520 mg, 2.23 mmol) and intermediate **y** (930 mg, 2.67 mmol) in dioxane (15 mL) was added Cs_2CO_3 (2.2 g, 6.7 mmol), BINAP (207 mg, 0.31 mmol) and $Pd(OAc)_2$ (72.7 mg, 0.31 mmol) at 25°C. The mixture was degassed and purged with N_2 and heated in a microwave reactor at 130°C for 0.5 h. The reaction mixture was concentrated in vacuo and the residue was purified flash silica gel chromatography (eluent of 0–51%, EtOAc/petroleum ether) to give the product as a gray solid. To the product in CH_2Cl_2 (5 mL) was added TFA (7 mL), and the mixture was stirred at 25°C for 2 h. The reaction mixture was concentrated in vacuo and the residue was purified by prep-HPLC (column: Welch Xtimate C18 150*30 mm*5 μm; mobile phase: [water (HCO_2H)-MeCN]; B%: 0–90%, 14 min). Compound **2e** (30.6 mg, 16.2%) was obtained as a light-yellow solid. ^{1}H NMR (400 MHz, DMSO-d_6) δ 9.59 (s, 1H), 9.42 (s, 1H), 8.41 (s, 1H), 8.33 (s, 1H), 8.18 (s, 1H), 7.86 (s, 1H), 7.76 (s, 1H), 7.03 (d, J = 8.8 Hz, 1H), 6.00 (s, 1H), 3.56 (s, 1H), 3.30 (d, J = 4.4 Hz, 1H), 3.21 - 3.16 (m, 1H), 3.16 - 3.11 (m, 1H), 2.82 (q, J = 8.0 Hz, 1H), 2.57 (s, 1H), 2.52-2.51 (m, 3H), 2.26-2.17 (m, 1H), 2.14 (s, 3H), 1.97 (s, 1H), 0.84-0.76 (m, 2H), 0.72-0.66 (m, 2H). ^{13}C NMR (101 MHz, DMSO-d_6) δ 168.51, 165.64, 157.00, 151.01, 148.19, 145.00, 134.62, 131.13, 118.19, 116.20, 115.48, 114.95, 76.16, 76.04, 57.88, 54.30, 49.20, 31.64, 28.59, 23.90, 23.32, 6.55. HPLC R_t = 3.080 min in 8 min chromatography, purity 99.4%. LCMS R_t = 1.420 min in 4 min chromatography, purity 99.7%, MS ESI calcd. for 445.23 $[M+H]^+$ 446.23, found 446.4.

*(S)-N-(5-((3-cyano-7-(cyclopropylamino)pyrazolo[1,5-a]pyrimidin-5-yl)amino)-2-(methyl(pyrrolidin-2-ylmethyl)amino)phenyl)acetamide (**2f**).* Intermediate **y** was synthesized from tert-butyl (*S*)-2-((methylamino)methyl)pyrrolidine-1-carboxylate and *N*-(2-fluoro-5-nitrophenyl)acetamide by Procedure A. To a solution of 5-chloro-7-

bioRxiv preprint doi: https://doi.org/10.1101/2023.05.15.540828; this version posted July 23, 2023. The copyright holder for this preprint (which was not certified by peer review) is the author/funder, who has granted bioRxiv a license to display the preprint in perpetuity. It is made available under aCC-BY 4.0 International license.

(cyclopropylamino)pyrazolo[1,5-a]pyrimidine-3-carbonitrile[6] (52.0 mg, 0.220 mmol) and intermediate **y** (100 mg, 0.280 mmol) in dioxane (2 mL) was added Cs_2CO_3 (209 mg, 0.64 mmol), BINAP (20 mg, 0.03 mmol) and $Pd(OAc)_2$ (7.0 mg, 0.03 mmol) at 25°C. The mixture was degassed and purged with N_2 and heated in a microwave reactor at 130°C for 0.5 h. The reaction mixture was concentrated in vacuo and the residue was purified flash silica gel chromatography (eluent of 0–2%, MeOH/CH_2Cl_2) to give the product as a brown solid. To the product in CH_2Cl_2 (5 mL) was added TFA (7 mL), and the mixture was stirred at 25°C for 2 h. The reaction mixture was concentrated in vacuo and the residue was purified by prep-HPLC (column: Xtimate C18 150*40 mm*10 μm; mobile phase: [water (NH_4HCO_3)-MeCN]; B%: 22–62%, 25 min). Compound **2f** (25.0 mg, 30.3%) was obtained as a yellow solid. ^{1}H NMR (400 MHz, DMSO-d_6) δ 10.76-10.36 (m, 1H), 9.61 (s, 1H), 8.37-8.30 (m, 2H), 8.16 (s, 1H), 7.89-7.77 (m, 1H), 7.17 (d, J = 8.8 Hz, 1H), 6.05 (s, 1H), 3.48-3.39 (m, 1H), 3.36-3.33 (m, 2H), 3.01-2.91 (m, 1H), 2.85-2.74 (m, 1H), 2.66 (s, 3H), 2.61-2.54 (m, 1H), 2.14 (s, 3H), 1.92-1.58 (m, 3H), 1.30-1.17 (m, 1H), 0.83-0.75 (m, 2H), 0.74-0.67 (m, 2H). ^{13}C NMR (101 MHz, DMSO-d_6) δ 168.17, 156.98, 150.95, 148.20, 145.02, 137.56, 135.98, 132.98, 120.22, 114.90, 76.25, 65.21, 59.77, 51.82, 31.69, 24.21, 23.32, 22.38, 6.55. HPLC R_t = 3.426 min in 8 min chromatography, purity 99.4%. LCMS R_t = 2.058 min in 4 min chromatography, purity 95.5%, MS ESI calcd. for 445.23 $[M+H]^+$ 446.23, found 460.3.

*N-(5-((3-cyano-7-(cyclopropylamino)pyrazolo[1,5-a]pyrimidin-5-yl)amino)-2-(piperazin-1-yl)phenyl)acetamide (**2g**).* Intermediate **y** was synthesized from tert-butyl piperazine-1-carboxylate and *N*-(2-fluoro-5-nitrophenyl)acetamide by Procedure A. To a solution of 5-chloro-7-(cyclopropylamino)pyrazolo[1,5-a]pyrimidine-3-carbonitrile[6] (302 mg, 1.29 mmol) and intermediate **y** (433 mg, 1.29 mmol) in dioxane (9 mL) was added Cs_2CO_3 (1.25 g, 3.84 mmol), BINAP (120 mg, 0.18 mmol) and $Pd(OAc)_2$ (42.0 mg, 0.18 mmol) at 25°C. The mixture was degassed and purged with N_2 and heated in a microwave reactor at 130°C for 0.5 h. The reaction mixture was concentrated in vacuo and the residue was purified by flash silica gel chromatography (eluent of 30–70%, EtOAc/petroleum ether) to give the product as a brown solid. To the product in CH_2Cl_2 (5 mL) was added TFA (7 mL), and the mixture was stirred at 25°C for 2 h. The reaction mixture was concentrated in vacuo and the residue was purified by prep-HPLC (column: Xtimate C18 100*30 mm*10 μm; mobile phase: [water (HCO_2H)-MeCN]; B%: 5–96%, 10 min]; B%: 4–34%, 10 min). Compound **2g** (178.4 mg, 27.4%) was obtained as a light yellow solid. ^{1}H NMR (400 MHz, DMSO-d_6) δ 9.68 (s, 1H), 8.92 (s, 1H), 8.33 (m, 1H), 8.48-8.31 (m, 1H), 8.12-7.99 (m, 1H), 7.89 (d, J = 6.8 Hz, 1H), 7.15 (d, J = 9.2 Hz, 1H), 6.03 (s, 1H), 3.35-3.22 (m, 4H), 3.02-2.88 (m, 4H), 2.63-2.55 (m, 1H), 2.16 (s, 3H), 0.87-0.76 (m, 2H),

bioRxiv preprint doi: https://doi.org/10.1101/2023.05.15.540828; this version posted July 23, 2023. The copyright holder for this preprint (which was not certified by peer review) is the author/funder, who has granted bioRxiv a license to display the preprint in perpetuity. It is made available under aCC-BY 4.0 International license.

0.73-0.66 (m, 2H). ^{13}C NMR (101 MHz, DMSO-d_6) δ 168.53, 156.91, 150.90, 148.24, 145.06, 136.92, 136.49, 133.12, 120.45, 115.14, 114.90, 112.84, 76.38, 49.29, 43.46, 39.99, 24.25, 23.34, 6.56. HPLC R_t = 1.599 min in 6 min chromatography, purity 95.6%. LCMS R_t = 1.003 min in 4 min chromatography, purity 95.9%, MS ESI calcd. for 431.22 $[M+H]^+$ 432.22, found 432.2.

*(S)-N-(5-((3-cyano-7-(cyclopropylamino)pyrazolo[1,5-a]pyrimidin-5-yl)amino)-2-(3-hydroxypiperidin-1-yl)phenyl)acetamide (**2i**).* Intermediate **y** was synthesized from (*S*)-piperidin-3-ol hydrochloride and *N*-(2-fluoro-5-nitrophenyl)acetamide by Procedure A. To a solution of 5-chloro-7-(cyclopropylamino)pyrazolo[1,5-a]pyrimidine-3-carbonitrile[6] (75 mg, 0.32 mmol) and intermediate **y** (100 mg, 0.40 mmol) in dioxane (3 mL) was added Cs_2CO_3 (388 mg, 1.19 mmol), BINAP (37.2 mg, 0.05 mmol) and $Pd(OAc)_2$ (12.7 mg, 0.05 mmol) at 25°C. The mixture was degassed, purged with N_2, and heated in a microwave reactor at 130°C for 0.5 h. The reaction mixture was concentrated in vacuo and the residue was purified by prep-HPLC (column: Xtimate C18 150*30 mm*5 μm; mobile phase: [water (NH_4HCO_3)-MeCN]; B%: 20–60%, 25 min) to give compound **2i** (25.0 mg, 13.8%) as a white solid. ^{1}H NMR (400 MHz, DMSO-d_6) δ 9.61 (s, 1H), 9.04 (s, 1H), 8.33 (s, 1H), 8.19-8.04 (m, 2H), 7.88-7.83 (m, 1H), 7.08 (d, J = 8.4 Hz, 1H), 6.03 (s, 1H), 5.09-4.87 (m, 1H), 3.80 (s, 1H), 2.86-2.76 (m, 2H), 2.75-2.67 (m, 1H), 2.65-2.54 (m, 2H), 2.13 (s, 3H), 1.95-1.81 (m, 1H), 1.77-1.55 (m, 2H), 1.54-1.42 (m, 1H), 0.83-0.75 (m, 2H), 0.74-0.67 (m, 2H). ^{13}C NMR (101 MHz, DMSO-d_6) δ 168.74, 157.10, 151.04, 148.24, 145.08, 137.49, 136.04, 134.09, 120.57, 115.02, 114.57, 111.52, 76.29, 48.67, 45.67, 28.83, 24.17, 23.38, 6.61. HPLC R_t = 3.771 min in 8 min chromatography, purity 99.0%. LCMS R_t = 2.050 min in 4 min chromatography, purity 98.3%, MS ESI calcd. for 446.22 $[M+H]^+$ 447.22, found 447.3.

*N-(5-((3-cyano-7-(cyclopropylamino)pyrazolo[1,5-a]pyrimidin-5-yl)amino)-2-(methyl(oxetan-3-yl)amino)phenyl)acetamide (**2j**).* Intermediate **y** was synthesized from *N*-methyloxetan-3-amine and *N*-(2-fluoro-5-nitrophenyl)acetamide by Procedure A. To a solution of 5-chloro-7-(cyclopropylamino)pyrazolo[1,5-a]pyrimidine-3-carbonitrile[6] (96.0 mg, 0.410 mmol) and intermediate **y** (120 mg, 0.510 mmol) in dioxane (3 mL) was added Cs_2CO_3 (398 mg, 1.21 mmol), BINAP (38.1 mg, 0.06 mmol) and $Pd(OAc)_2$ (13.3 mg, 0.06 mmol) at 25°C. The mixture was degassed, purged with N_2, and heated in a microwave reactor at 130°C for 0.5 h. The reaction mixture was concentrated in vacuo and the residue was purified by prep-HPLC (column: Xtimate C18 150 * 40 mm * 10 μm; mobile phase: [water (NH_4HCO_3)-MeCN]; B%: 18–58%, 25 min). Compound **2j** (4.70 mg, 5.88 %) was obtained as a yellow solid. ^{1}H NMR (400 MHz, DMSO-d_6) δ 9.65 (s, 1H), 9.06 (s, 1H), 8.34 (s, 1H), 8.19 (s, 1H), 8.10 (s, 1H), 7.86 (d, J = 8.0 Hz, 1H), 6.97 (d, J = 8.8 Hz, 1H), 6.03 (s, 1H), 4.64-4.56 (m, 2H), 4.44-4.37 (m, 2H), 4.38-

bioRxiv preprint doi: https://doi.org/10.1101/2023.05.15.540828; this version posted July 23, 2023. The copyright holder for this preprint (which was not certified by peer review) is the author/funder, who has granted bioRxiv a license to display the preprint in perpetuity. It is made available under aCC-BY 4.0 International license.

4.30 (m, 1H), 2.62-2.54 (m, 1H), 2.46 (s, 3H), 2.18 (s, 3H), 0.85-0.76 (m, 2H), 0.75-0.67 (m, 2H). HPLC R_t = 4.106 min in 8 min chromatography, purity 99.9%. LCMS R_t = 2.487 min in 4 min chromatography, purity 97.9 %, MS ESI calcd. for 432.2, $[M+H]^+$ 433.2, found 433.2.

*(S)-N-(5-((3-cyano-7-(cyclopropylamino)pyrazolo[1,5-a]pyrimidin-5-yl)amino)-2-(methyl(tetrahydrofuran-3-yl)amino)phenyl)acetamide (**2k**).* Intermediate **y** was synthesized from (*S*)-N-methyltetrahydrofuran-3-amine hydrochloride and *N*-(2-fluoro-5-nitrophenyl)acetamide by Procedure A. To a solution of 5-chloro-7-(cyclopropylamino)pyrazolo[1,5-a]pyrimidine-3-carbonitrile[6] (84.3 mg, 0.361 mmol) and intermediate **y** (90.0 mg, 0.361 mmol) in dioxane (2 mL) was added Cs_2CO_3 (470 mg, 1.44 mmol), BINAP (33.7 mg, 0.054 mmol), and $Pd(OAc)_2$ (12.2 mg, 0.054 mmol) 25°C. The mixture was degassed and purged with N_2 three times, and then heated in a microwave reactor at 120°C for 2 h. The mixture was filtered and concentrated to give a residue that was purified by prep-HPLC purification (column: Phenomenex luna C18 150*25 mm*10 μm; mobile phase: [water (HCO_2H)-MeCN]; B%: 30–60%, 10 min) to give product **2k** (19.3 mg, 11.6% yield) as a white solid. ^{1}H NMR (400 MHz, DMSO-d_6) δ 9.68 (s, 1H), 9.06 (s, 1H), 8.35 (s, 1H), 8.24-8.15 (m, 2H), 7.99-7.88 (m, 1H), 7.30 (d, J = 8.8 Hz, 1H), 6.06 (s, 1H), 3.89-3.75 (m, 1H), 3.71-3.62 (m, 3H), 3.57-3.48 (m, 1H), 2.60-2.52 (m, 1H), 2.53 (s, 3H), 2.14 (s, 3H), 2.00-1.88 (m, 1H), 1.86-1.74 (m, 1H), 0.86-0.78 (m, 2H), 0.76-0.68 (m, 2H). ^{13}C NMR (101 MHz, DMSO-d_6) δ 171.96, 155.87, 149.91, 149.11, 145.60, 139.08, 138.85, 129.13, 119.45, 117.37, 114.13, 78.81, 77.86, 39.99, 39.00, 23.50, 6.58. LCMS: R_t = 0.393 min in 0.8 min chromatography, purity 100.0%, MS ESI calcd. for $C_{23}H_{27}N_8O_2$ $[M+H]^+$ 447.22, found 447.1. HPLC: R_t = 1.850 min in 4 min chromatography, purity 97.4%.

*(R)-N-(5-((3-cyano-7-(cyclopropylamino)pyrazolo[1,5-a]pyrimidin-5-yl)amino)-2-(methyl(tetrahydrofuran-3-yl)amino)phenyl)acetamide (**2l**).* Intermediate **y** was synthesized from (*R*)-N-methyltetrahydrofuran-3-amine hydrochloride and *N*-(2-fluoro-5-nitrophenyl)acetamide by Procedure A. To a solution of 5-chloro-7-(cyclopropylamino)pyrazolo[1,5-a]pyrimidine-3-carbonitrile[6] (98 mg, 0.421 mmol) and intermediate **y** (105 mg, 0.421 mmol) in dioxane (5 mL) was added Cs_2CO_3 (411 mg, 1.26 mmol), BINAP (39.3 mg, 0.063 mmol), and $Pd(OAc)_2$ (14.2 mg, 0.063 mmol) 25°C. The mixture was degassed and purged with N_2 three times, and then heated in a microwave reactor at 120°C for 2 h. The reaction mixture was filtered and concentrated under reduced pressure to give a residue that was purified by prep-TLC (SiO_2, CH_2Cl_2/MeOH = 20/1), and the crude product was purified by prep-HPLC (column: Phenomenex Luna C18 150*25 mm*10 μm; mobile phase: [water (HCO_2H)-MeCN]; B%: 29–59%, 8 min). Compound **2l** (18.2 mg, 9.71% yield) was obtained as a white solid. ^{1}H NMR (400 MHz, DMSO-d_6) δ 9.67 (s, 1H), 8.98 (s, 1H), 8.34 (s, 1H), 8.17 (d, J = 12.8 Hz, 2H), 7.92 (br d, J = 5.2 Hz,

bioRxiv preprint doi: https://doi.org/10.1101/2023.05.15.540828; this version posted July 23, 2023. The copyright holder for this preprint (which was not certified by peer review) is the author/funder, who has granted bioRxiv a license to display the preprint in perpetuity. It is made available under aCC-BY 4.0 International license.

1H), 7.29 (d, *J* = 8.8 Hz, 1H), 6.05 (s, 1H), 3.88 - 3.79 (m, 1H), 3.71-3.62 (m, 3H), 3.56-3.47 (m, 1H), 2.62-2.53 (m, 1H), 2.52 (s, 3H), 2.14 (s, 3H), 1.99-1.86 (m, 1H), 1.84-1.76 (m, 1H), 0.83-0.77 (m, 2H), 0.73-0.68 (m, 2H). ^{13}C NMR (101 MHz, DMSO-d_6) δ 172.48, 156.90, 150.87, 148.20, 145.05, 138.50, 137.18, 134.98, 123.04, 114.87, 76.44, 70.96, 67.04, 63.59, 41.65, 30.73, 23.31, 6.53. LCMS R_t = 0.395 min in 0.8 min chromatography, purity 44.5%, MS ESI calcd. for 446.50 $[M+H]^+$ 447.50, found 447.1. HPLC: Rt = 1.011 min in 4 min chromatography, purity 96.7%.

*(R)-N-(5-((3-cyano-7-(cyclopropylamino)pyrazolo[1,5-a]pyrimidin-5-yl)amino)-2-((tetrahydro-2H-pyran-3-yl)amino)phenyl)acetamide (**2m**).* Intermediate **y** was synthesized from (*R*)-tetrahydro-2H-pyran-3-amine hydrochloride and *N*-(2-fluoro-5-nitrophenyl)acetamide by Procedure A. To a solution of 5-chloro-7-(cyclopropylamino)pyrazolo[1,5-a]pyrimidine-3-carbonitrile[6] (220 mg, 0.943 mmol) and intermediate **y** (235 mg, 0.943 mmol) in dioxane (6 mL) was added Cs_2CO_3 (915 mg, 2,83 mmol), BINAP (87.6 mg, 0.13 mmol), and $Pd(OAc)_2$ (30.2 mg, 0.13 mmol) 25°C. The mixture was degassed and purged with N_2 three times, and then heated in a microwave reactor at 120°C for 2 h. The mixture was filtered and concentrated to give a residue that was purified by prep-HPLC purification (column: Phenomenex luna C18 150*25 mm*10 µm; mobile phase: [water (HCO_2H)-MeCN]; B%: 26–56%, 10 min, and column: Phenomenex C18 150*25 mm*10 µm; mobile phase: [water (NH_4HCO_3)-MeCN]; B%: 22%-52%, 14 min) to give compound **2m** (10 mg, 22.40 µmol, 2.38% yield) as an off-white solid. ^{1}H NMR (400 MHz, DMSO-d_6) δ 9.33 (s, 1H), 9.19 (s, 1H), 8.29 (s, 1H), 8.09 (s, 1H), 7.45 (s, 1H), 7.39 (s, 1H), 6.73 (d, *J* = 8.8 Hz, 1H), 5.90 (s, 1H), 4.54 (d, *J* = 8.0 Hz, 1H), 3.89-3.82 (m, 1H), 3.75-3.67 (m, 1H), 3.42-3.38 (m, 2H), 3.27-3.11 (m, 1H), 2.59-2.52 (m, 1H), 2.06 (s, 3H), 2.01-1.93 (m, 1H), 1.75-1.67 (m, 1H), 1.63-1.45 (m, 2H), 0.82-0.74 (m, 2H), 0.72-0.65 (m, 2H). HPLC: R_t = 1.670 min in 4 min chromatography, purity 97.6%. LCMS R_t = 0.365 min in 0.8 min chromatography, purity 99.1%, MS ESI calcd. for 446.22 $[M+H]^+$ 447.22, found 447.2.

*N-(5-((3-cyano-7-(cyclopropylamino)pyrazolo[1,5-a]pyrimidin-5-yl)amino)-2-(methyl(oxetan-3-ylmethyl)amino)phenyl)acetamide (**2n**).* Intermediate **y** was synthesized from *N*-methyl-1-(oxetan-3-yl)methanamine hydrochloride and *N*-(2-fluoro-5-nitrophenyl)acetamide by Procedure A. To a solution of 5-chloro-7-(cyclopropylamino)pyrazolo[1,5-a]pyrimidine-3-carbonitrile[6] (293 mg, 1.26 mmol) and intermediate **y** (313 mg, 1.26 mmol) in dioxane (10 mL) was added Cs_2CO_3 (1.64 g, 5.02 mmol), BINAP (117 mg, 0.188 mmol), and $Pd(OAc)_2$ (42.2 mg, 0.188 mmol) at 25°C. The mixture was degassed, purged with N_2, and then heated in a microwave reactor at 120 °C for 2 hours. The reaction mixture was diluted with CH_2Cl_2/MeOH (10/1, 30 mL), then filtered, and the filtrate was concentrated to give a crude product that

bioRxiv preprint doi: https://doi.org/10.1101/2023.05.15.540828; this version posted July 23, 2023. The copyright holder for this preprint (which was not certified by peer review) is the author/funder, who has granted bioRxiv a license to display the preprint in perpetuity. It is made available under aCC-BY 4.0 International license.

purified by flash silica gel chromatography (Eluent of 30–80% EtOAc/petroleum ether). The crude product was further purified by prep-HPLC (column: Phenomenex luna C18 150*25 mm*10 μm; mobile phase: [water (HCO_2H)-MeCN]; B%: 22–52%, 10 min) to give Compound **2n** (150.6 mg, 32.9%) as a light-yellow solid. ^{1}H NMR (400 MHz, DMSO-d_6) δ 9.56 (s, 1H), 8.93 (s, 1H), 8.33 (s, 1H), 8.17 (s, 1H), 8.10 (s, 1H), 7.88 (d, J = 7.2 Hz, 1H), 7.24 (d, J = 8.8 Hz, 1H), 6.04 (s, 1H), 4.53 (t, J = 7.2 Hz, 2H), 4.22 (t, J = 6.0 Hz, 2H), 3.15-3.09 (m, 2H), 3.08-3.01 (m, 1H), 2.56 (s, 3H), 2.55-2.51 (m, 1H), 2.12 (s, 3H), 0.84-0.76 (m, 2H), 0.75-0.66 (m, 2H). ^{13}C NMR (101 MHz, DMSO-d_6) δ 168.25, 156.93, 150.89, 148.20, 145.01, 136.87, 136.41, 134.17, 122.04, 114.96, 114.85, 111.72, 76.34, 74.77, 59.67, 42.84, 32.92, 24.24, 23.30, 6.52. HPLC R_t = 2.093 min in 4 min chromatography, purity 96.6%. LCMS R_t = 1.136 min in 3 min chromatography, purity 100%, MS ESI calcd. for 446.22 $[M+H]^+$ 447.22, found 447.2.

bioRxiv preprint doi: https://doi.org/10.1101/2023.05.15.540828; this version posted July 23, 2023. The copyright holder for this preprint (which was not certified by peer review) is the author/funder, who has granted bioRxiv a license to display the preprint in perpetuity. It is made available under aCC-BY 4.0 International license.

Ancillary Information

Supporting Information: SMARTCyp prediction of P450 metabolism of SGC-CK2-1 (**1a**), inhibition of **2h** metabolism by 1-ABT, dose ranging study of EA tolerability in mice by i.p. dosing, and NMR spectra (PDF).

Corresponding Author:

Timothy M. Willson – *Structural Genomics Consortium, UNC Eshelman School of Pharmacy, University of North Carolina at Chapel Hill, Chapel Hill, NC 27599, United States; Rapidly Emerging Antiviral Drug Development Initiative (READDI), Chapel Hill, NC 27599, United States;* orchid.org/0000-0003-4181-8223 ; Email: tim.willson@unc.edu

Authors:

Xuan Yang – *Structural Genomics Consortium, UNC Eshelman School of Pharmacy, University of North Carolina at Chapel Hill, Chapel Hill, NC 27599, United States; Rapidly Emerging Antiviral Drug Development Initiative (READDI), Chapel Hill, NC 27599, United States;* orchid.org/0000-0001-6818-158X

Han Wee Ong – *Structural Genomics Consortium, UNC Eshelman School of Pharmacy, University of North Carolina at Chapel Hill, Chapel Hill, NC 27599, United States; Rapidly Emerging Antiviral Drug Development Initiative (READDI), Chapel Hill, NC 27599, United States;* orchid.org/ 0000-0003-3232-2373

Rebekah J. Dickmander – *Department of Microbiology & Immunology, University of North Carolina at Chapel Hill, Chapel Hill, NC 27599, United States; Department of Chemistry, University of North Carolina at Chapel Hill, Chapel Hill, NC 27599, United States; Rapidly Emerging Antiviral Drug Development Initiative (READDI), Chapel Hill, NC 27599, United States; Department of Microbiology & Immunology, University of North Carolina at Chapel Hill, Chapel Hill, NC 27599, United States; Lineberger Comprehensive Cancer Center, University of North Carolina at Chapel Hill, Chapel Hill, NC 27599, United States;* orchid.org/0000-0002-5367-6587

Jeffery L. Smith – *Structural Genomics Consortium, UNC Eshelman School of Pharmacy, University of North Carolina at Chapel Hill, Chapel Hill, NC 27599, United States;* orchid.org/0000-0003-2189-0420

Jason W. Brown – *Takeda San Diego, San Diego, CA 92121, United States*

bioRxiv preprint doi: https://doi.org/10.1101/2023.05.15.540828; this version posted July 23, 2023. The copyright holder for this preprint (which was not certified by peer review) is the author/funder, who has granted bioRxiv a license to display the preprint in perpetuity. It is made available under aCC-BY 4.0 International license.

William Tao – *Takeda San Diego, San Diego, CA 92121, United States*

Edcon Chang – *Takeda San Diego, San Diego, CA 92121, United States;* orchid.org/0000-0001-9534-0291

Nathaniel J. Moorman – *Department of Microbiology & Immunology, University of North Carolina at Chapel Hill, Chapel Hill, NC 27599, United States; Rapidly Emerging Antiviral Drug Development Initiative (READDI), Chapel Hill, NC 27599, United States; Department of Microbiology & Immunology, University of North Carolina at Chapel Hill, Chapel Hill, NC 27599, United States; Lineberger Comprehensive Cancer Center, University of North Carolina at Chapel Hill, Chapel Hill, NC 27599, United States;* orchid.org/0000-0003-4952-6858

Alison D. Axtman – *Structural Genomics Consortium, UNC Eshelman School of Pharmacy, University of North Carolina at Chapel Hill, Chapel Hill, NC 27599, United States; Rapidly Emerging Antiviral Drug Development Initiative (READDI), Chapel Hill, NC 27599, United States;* orchid.org/0000-0003-4779-9932

Author Contributions

T.M.W, A.D.A., and N.J.M conceived of the study. X.Y., H.W.O., J.W.B, W.T., E.C., and A.D.A designed experiments and compounds. R.J.D. and J.L.S. performed biological studies. T.M.W wrote the manuscript. All authors read and approved the manuscript.

Notes:

The authors declare no competing financial interest.

Funding Sources:

The Structural Genomics Consortium (SGC) is a registered charity (no: 1097737) that receives funds from Bayer AG, Boehringer Ingelheim, Bristol Myers Squibb, Genentech, Genome Canada through Ontario Genomics Institute [OGI-196], EU/EFPIA/OICR/McGill/KTH/Diamond Innovative Medicines Initiative 2 Joint Undertaking [EUbOPEN grant 875510], Janssen, Merck KGaA (aka EMD in Canada and US), Pfizer and Takeda. Research reported in this publication was supported in part by the NC Biotech Center Institutional Support Grant 2018-IDG-1030, by the NIH Illuminating the Druggable Genome 1U24DK116204-01, and Department of Defense ALSRP award AL190107. This project was supported by the Rapidly Emerging Antiviral Drug Development Initiative (READDI) at the University of North Carolina at Chapel Hill with funding from the North Carolina Coronavirus State and Local Fiscal Recovery Funds program,

bioRxiv preprint doi: https://doi.org/10.1101/2023.05.15.540828; this version posted July 23, 2023. The copyright holder for this preprint (which was not certified by peer review) is the author/funder, who has granted bioRxiv a license to display the preprint in perpetuity. It is made available under aCC-BY 4.0 International license.

appropriated by the North Carolina General Assembly. Additional funding was provided by a grant from Millennium Pharmaceuticals (Takeda).

Acknowledgement:

Constructs for NanoBRET measurements of CSNK2A1 and CSNK2A2, were provided by Promega Corporation (Madison, WI). We thank K. Saikatendu Singh (Takeda, San Diego, CA) for facilitating collaborative interactions and constructive criticism throughout the project. WuXi AppTec (Shanghai, China) provided chemical synthesis support. Analiza, Inc (Cleveland, OH) performed kinetic solubility and mouse liver microsome studies. Pharmaron (Beijing, China) provided in vitro and in vivo pharmacokinetic assay support.

Abbreviations Used:

CSNK2A, Casein Kinase 2a; PZP, 3-cyano-7-cyclopropylamino-pyrazolo[1,5-a]pyrimidine; GST, glutathione S-transferase; MHV, mouse hepatitis virus; MLM, mouse liver microsome; i.v., intravenous; i.p., intraperitoneal; C_{max}, maximum concentration; AUC, area under the curve; CL_{int}, intrinsic clearance; EA, ethacrynic acid; 1-ABT, 1-aminobenzotriazole.

bioRxiv preprint doi: https://doi.org/10.1101/2023.05.15.540828; this version posted July 23, 2023. The copyright holder for this preprint (which was not certified by peer review) is the author/funder, who has granted bioRxiv a license to display the preprint in perpetuity. It is made available under aCC-BY 4.0 International license.

References

1. Li, G.; Hilgenfeld, R.; Whitley, R.; De Clercq, E., Therapeutic Strategies for COVID-19: Progress and Lessons Learned. *Nat Rev Drug Discov* **2023**, 1-27.
2. Kumar, N.; Sharma, S.; Kumar, R.; Tripathi, B. N.; Barua, S.; Ly, H.; Rouse, B. T., Host-Directed Antiviral Therapy. *Clin Microbiol Rev* **2020,** *33* (3), e00168-19.
3. Garcia-Carceles, J.; Caballero, E.; Gil, C.; Martinez, A., Kinase Inhibitors as Underexplored Antiviral Agents. *J Med Chem* **2022,** *65* (2), 935-954.
4. Gordon, D. E.; Jang, G. M.; Bouhaddou, M.; Xu, J.; Obernier, K.; White, K. M.; O'Meara, M. J.; Rezelj, V. V.; Guo, J. Z.; Swaney, D. L.; Tummino, T. A.; Huttenhain, R.; Kaake, R. M.; Richards, A. L.; Tutuncuoglu, B.; Foussard, H.; Batra, J.; Haas, K.; Modak, M.; Kim, M.; Haas, P.; Polacco, B. J.; Braberg, H.; Fabius, J. M.; Eckhardt, M.; Soucheray, M.; Bennett, M. J.; Cakir, M.; McGregor, M. J.; Li, Q.; Meyer, B.; Roesch, F.; Vallet, T.; Mac Kain, A.; Miorin, L.; Moreno, E.; Naing, Z. Z. C.; Zhou, Y.; Peng, S.; Shi, Y.; Zhang, Z.; Shen, W.; Kirby, I. T.; Melnyk, J. E.; Chorba, J. S.; Lou, K.; Dai, S. A.; Barrio-Hernandez, I.; Memon, D.; Hernandez-Armenta, C.; Lyu, J.; Mathy, C. J. P.; Perica, T.; Pilla, K. B.; Ganesan, S. J.; Saltzberg, D. J.; Rakesh, R.; Liu, X.; Rosenthal, S. B.; Calviello, L.; Venkataramanan, S.; Liboy-Lugo, J.; Lin, Y.; Huang, X. P.; Liu, Y.; Wankowicz, S. A.; Bohn, M.; Safari, M.; Ugur, F. S.; Koh, C.; Savar, N. S.; Tran, Q. D.; Shengjuler, D.; Fletcher, S. J.; O'Neal, M. C.; Cai, Y.; Chang, J. C. J.; Broadhurst, D. J.; Klippsten, S.; Sharp, P. P.; Wenzell, N. A.; Kuzuoglu-Ozturk, D.; Wang, H. Y.; Trenker, R.; Young, J. M.; Cavero, D. A.; Hiatt, J.; Roth, T. L.; Rathore, U.; Subramanian, A.; Noack, J.; Hubert, M.; Stroud, R. M.; Frankel, A. D.; Rosenberg, O. S.; Verba, K. A.; Agard, D. A.; Ott, M.; Emerman, M.; Jura, N.; von Zastrow, M.; Verdin, E.; Ashworth, A.; Schwartz, O.; d'Enfert, C.; Mukherjee, S.; Jacobson, M.; Malik, H. S.; Fujimori, D. G.; Ideker, T.; Craik, C. S.; Floor, S. N.; Fraser, J. S.; Gross, J. D.; Sali, A.; Roth, B. L.; Ruggero, D.; Taunton, J.; Kortemme, T.; Beltrao, P.; Vignuzzi, M.; Garcia-Sastre, A.; Shokat, K. M.; Shoichet, B. K.; Krogan, N. J., A SARS-CoV-2 Protein Interaction Map Reveals Targets for Drug Repurposing. *Nature* **2020,** *583* (7816), 459-468.
5. Ramon, A. C.; Perez, G. V.; Caballero, E.; Rosales, M.; Aguilar, D.; Vazquez-Blomquist, D.; Ramos, Y.; Rodriguez-Ulloa, A.; Falcon, V.; Rodriguez-Molto, M. P.; Yang, K.; Perera, Y.; Perea, S. E., Targeting of Protein Kinase CK2 Elicits Antiviral Activity on Bovine Coronavirus Infection. *Viruses* **2022,** *14* (3), 552.
6. Yang, X.; Dickmander, R. J.; Bayati, A.; Taft-Benz, S. A.; Smith, J. L.; Wells, C. I.; Madden, E. A.; Brown, J. W.; Lenarcic, E. M.; Yount, B. L., Jr.; Chang, E.; Axtman, A. D.; Baric, R. S.; Heise, M. T.; McPherson, P. S.; Moorman, N. J.; Willson, T. M., Host Kinase CSNK2 is a Target for Inhibition of Pathogenic SARS-like β-Coronaviruses. *ACS Chem Biol* **2022,** *17* (7), 1937-1950.
7. Dowling, J. E.; Chuaqui, C.; Pontz, T. W.; Lyne, P. D.; Larsen, N. A.; Block, M. H.; Chen, H.; Su, N.; Wu, A.; Russell, D.; Pollard, H.; Lee, J. W.; Peng, B.; Thakur, K.; Ye, Q.; Zhang, T.; Brassil, P.; Racicot, V.; Bao, L.; Denz, C. R.; Cooke, E., Potent and Selective Inhibitors of CK2 Kinase Identified through Structure-Guided Hybridization. *ACS Med Chem Lett* **2012,** *3* (4), 278-83.
8. Wells, C. I.; Drewry, D. H.; Pickett, J. E.; Tjaden, A.; Kramer, A.; Muller, S.; Gyenis, L.; Menyhart, D.; Litchfield, D. W.; Knapp, S.; Axtman, A. D., Development of a Potent and Selective Chemical Probe for the Pleiotropic Kinase CK2. *Cell Chem Biol* **2021,** *28* (4), 546-558 e10.
9. Dowling, J. E.; Alimzhanov, M.; Bao, L.; Block, M. H.; Chuaqui, C.; Cooke, E. L.; Denz, C. R.; Hird, A.; Huang, S.; Larsen, N. A.; Peng, B.; Pontz, T. W.; Rivard-Costa, C.; Saeh, J. C.; Thakur, K.; Ye, Q.; Zhang, T.; Lyne, P. D., Structure and Property Based

bioRxiv preprint doi: https://doi.org/10.1101/2023.05.15.540828; this version posted July 23, 2023. The copyright holder for this preprint (which was not certified by peer review) is the author/funder, who has granted bioRxiv a license to display the preprint in perpetuity. It is made available under aCC-BY 4.0 International license.

Design of Pyrazolo[1,5-a]pyrimidine Inhibitors of CK2 Kinase with Activity in Vivo. *ACS Med Chem Lett* **2013,** *4* (8), 800-805.
10. Dowling, J. E.; Alimzhanov, M.; Bao, L.; Chuaqui, C.; Denz, C. R.; Jenkins, E.; Larsen, N. A.; Lyne, P. D.; Pontz, T.; Ye, Q.; Holdgate, G. A.; Snow, L.; O'Connell, N.; Ferguson, A. D., Potent and Selective CK2 Kinase Inhibitors with Effects on Wnt Pathway Signaling in Vivo. *ACS Med Chem Lett* **2016,** *7* (3), 300-305.
11. Dinnon, K. H., 3rd; Leist, S. R.; Schafer, A.; Edwards, C. E.; Martinez, D. R.; Montgomery, S. A.; West, A.; Yount, B. L., Jr.; Hou, Y. J.; Adams, L. E.; Gully, K. L.; Brown, A. J.; Huang, E.; Bryant, M. D.; Choong, I. C.; Glenn, J. S.; Gralinski, L. E.; Sheahan, T. P.; Baric, R. S., A Mouse-adapted Model of SARS-CoV-2 to Test COVID-19 Countermeasures. *Nature* **2020,** *586* (7830), 560-566.
12. Leist, S. R.; Dinnon, K. H., 3rd; Schafer, A.; Tse, L. V.; Okuda, K.; Hou, Y. J.; West, A.; Edwards, C. E.; Sanders, W.; Fritch, E. J.; Gully, K. L.; Scobey, T.; Brown, A. J.; Sheahan, T. P.; Moorman, N. J.; Boucher, R. C.; Gralinski, L. E.; Montgomery, S. A.; Baric, R. S., A Mouse-Adapted SARS-CoV-2 Induces Acute Lung Injury and Mortality in Standard Laboratory Mice. *Cell* **2020,** *183* (4), 1070-1085 e12.
13. Rydberg, P.; Gloriam, D. E.; Olsen, L., The SMARTCyp Cytochrome P450 Metabolism Prediction Server. *Bioinformatics* **2010,** *26* (23), 2988-2989.
14. Rydberg, P.; Gloriam, D. E.; Zaretzki, J.; Breneman, C.; Olsen, L., SMARTCyp: A 2D Method for Prediction of Cytochrome P450-Mediated Drug Metabolism. *ACS Med Chem Lett* **2010,** *1* (3), 96-100.
15. Tyzack, J. D.; Kirchmair, J., Computational Methods and Tools to Predict Cytochrome P450 Metabolism for Drug Discovery. *Chem Biol Drug Des* **2019,** *93* (4), 377-386.
16. Lewis, D. F.; Dickins, M., Baseline Lipophilicity Relationships in Human Cytochromes P450 Associated with Drug Metabolism. *Drug Metab Rev* **2003,** *35* (1), 1-18.
17. Di, L.; Keefer, C.; Scott, D. O.; Strelevitz, T. J.; Chang, G.; Bi, Y. A.; Lai, Y.; Duckworth, J.; Fenner, K.; Troutman, M. D.; Obach, R. S., Mechanistic Insights from Comparing Intrinsic Clearance Values Between Human Liver Microsomes and Hepatocytes to Guide Drug Design. *Eur J Med Chem* **2012,** *57*, 441-448.
18. Potega, A., Glutathione-Mediated Conjugation of Anticancer Drugs: An Overview of Reaction Mechanisms and Biological Significance for Drug Detoxification and Bioactivation. *Molecules* **2022,** *27* (16), 5252.
19. MacFaul, P. A.; Morley, A. D.; Crawford, J. J., A Simple In Vitro Assay for Assessing the Reactivity of Nitrile Containing Compounds. *Bioorg Med Chem Lett* **2009,** *19* (4), 1136-8.
20. Oakley, A., Glutathione Transferases: a Structural Perspective. *Drug Metab Rev* **2011,** *43* (2), 138-51.
21. Allocati, N.; Masulli, M.; Di Ilio, C.; Federici, L., Glutathione Transferases: Substrates, Inihibitors and Pro-drugs in Cancer and Neurodegenerative Diseases. *Oncogenesis* **2018,** *7* (1), 8.
22. Ploemen, J. H.; van Ommen, B.; Bogaards, J. J.; van Bladeren, P. J., Ethacrynic Acid and its Glutathione Conjugate as Inhibitors of Glutathione S-transferases. *Xenobiotica* **1993,** *23* (8), 913-923.
23. Townsend, D. M.; Tew, K. D., The Role of Glutathione-S-transferase in Anti-cancer Drug Resistance. *Oncogene* **2003,** *22* (47), 7369-7375.
24. Kim, Y.; Gast, S. M.; Endo, T.; Lu, D.; Carson, D.; Schmidt-Wolf, I. G., In Vivo Efficacy of the Diuretic Agent Ethacrynic Acid Against Multiple Myeloma. *Leuk Res* **2012,** *36* (5), 598-600.
25. Liu, B.; Huang, X.; Hu, Y.; Chen, T.; Peng, B.; Gao, N.; Jin, Z.; Jia, T.; Zhang, N.; Wang, Z.; Jin, G., Ethacrynic Acid Improves the Antitumor Effects of Irreversible Epidermal Growth Factor Receptor Tyrosine Kinase Inhibitors in Breast Cancer. *Oncotarget* **2016,** *7* (36), 58038-58050.

bioRxiv preprint doi: https://doi.org/10.1101/2023.05.15.540828; this version posted July 23, 2023. The copyright holder for this preprint (which was not certified by peer review) is the author/funder, who has granted bioRxiv a license to display the preprint in perpetuity. It is made available under aCC-BY 4.0 International license.

26. Schmidt, M.; Kim, Y.; Gast, S. M.; Endo, T.; Lu, D.; Carson, D.; Schmidt-Wolf, I. G., Increased In Vivo Efficacy of Lenalidomide and Thalidomide by Addition of Ethacrynic Acid. *In Vivo* **2011,** *25* (3), 325-333.
27. de Montellano, P. R. O., 1-Aminobenzotriazole: A Mechanism-Based Cytochrome P450 Inhibitor and Probe of Cytochrome P450 Biology. *Med Chem (Los Angeles)* **2018,** *8* (3), 038-065.
28. Salvi, M.; Borgo, C.; Pinna, L. A.; Ruzzene, M., Targeting CK2 in Cancer: a Valuable Strategy or a Waste of Time? *Cell Death Discov* **2021,** *7* (1), 325.
29. Pack, M.; Gotz, C.; Wrublewsky, S.; Montenarh, M., SGC-CK2-1 Is an Efficient Inducer of Insulin Production and Secretion in Pancreatic beta-Cells. *Pharmaceutics* **2021,** *14* (1), 19.
30. Boewe, A. S.; Wemmert, S.; Kulas, P.; Schick, B.; Gotz, C.; Wrublewsky, S.; Montenarh, M.; Menger, M. D.; Laschke, M. W.; Ampofo, E., Inhibition of CK2 Reduces NG2 Expression in Juvenile Angiofibroma. *Biomedicines* **2022,** *10* (5), 966.
31. Mishra, S.; Kinoshita, C.; Axtman, A. D.; Young, J. E., Evaluation of a Selective Chemical Probe Validates That CK2 Mediates Neuroinflammation in a Human Induced Pluripotent Stem Cell-Derived Mircroglial Model. *Front Mol Neurosci* **2022,** *15*, 824956.
32. Al Shoyaib, A.; Archie, S. R.; Karamyan, V. T., Intraperitoneal Route of Drug Administration: Should it Be Used in Experimental Animal Studies? *Pharm Res* **2019,** *37* (1), 12.
33. Cannon, P. J.; Heinemann, H. O.; Stason, W. B.; Laragh, J. H., Ethacrynic Acid: Effectiveness and Mode of Diuretic Action in Man. *Circulation* **1965,** *31*, 5-18.

ACS Medicinal Chemistry Letters

pubs.acs.org/acsmedchemlett

Letter

Discovery of a Potent and Selective Naphthyridine-Based Chemical Probe for Casein Kinase 2

Zachary W. Davis-Gilbert, Andreas Krämer, James E. Dunford, Stefanie Howell, Filiz Senbabaoglu, Carrow I. Wells, Frances M. Bashore, Tammy M. Havener, Jeffery L. Smith, Mohammad A. Hossain, Udo Oppermann, David H. Drewry, and Alison D. Axtman*

Cite This: *ACS Med. Chem. Lett.* 2023, 14, 432−441

Read Online

ACCESS | Metrics & More | Article Recommendations | Supporting Information

ABSTRACT: Naphthyridine-based inhibitors were synthesized to yield a potent and cell-active inhibitor of casein kinase 2 (CK2). Compound **2** selectively inhibits CK2α and CK2α' when profiled broadly, thereby making it an exquisitely selective chemical probe for CK2. A negative control that is structurally related but lacks a key hinge-binding nitrogen (**7**) was designed on the basis of structural studies. Compound **7** does not bind CK2α or CK2α' in cells and demonstrates excellent kinome-wide selectivity. Differential anticancer activity was observed when compound **2** was profiled alongside a structurally distinct CK2 chemical probe: SGC-CK2-1. This naphthyridine-based chemical probe (**2**) represents one of the best available small molecule tools with which to interrogate biology mediated by CK2.

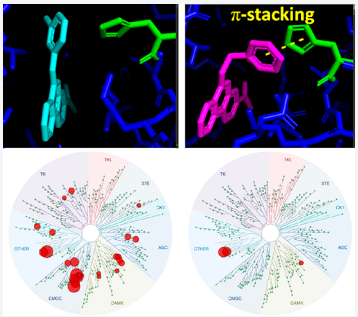

KEYWORDS: *Casein kinase 2, CK2, CSNK2, Protein kinase, Naphthyridine, Chemical probe*

Downloaded via Alison Axtman on August 25, 2023 at 00:54:28 (UTC).
See https://pubs.acs.org/sharingguidelines for options on how to legitimately share published articles.

Casein kinase 2 (CK2, CSNK2) is a highly conserved and ubiquitously expressed serine/threonine kinase for which more than 300 substrates have been identified, and correspondingly, many diverse functions and roles in disease have been ascribed to CK2.[1−5] Examples of indications for which CK2 inhibition has been investigated as therapeutically beneficial include cancer, SARS-CoV-2, and neuroinflammation.[6−10] Since the two catalytic subunits of CK2, CK2α (encoded by the CSNK2A1 gene) and CK2α' (encoded by the CSNK2A2 gene), have >80% identity, small molecule inhibitors bind to both.[11,12] As confirmed via Western blot analyses, inhibitor binding to the two catalytic subunits in cells results in inhibition of the heterotetrameric holoenzyme, which includes a dimer of noncatalytic subunits (CK2β).[11−13]

Recent efforts have identified potent and selective tool molecules that enable the dissection of complex signaling pathways mediated by CK2: IC19, IC20, and SGC-CK2-1 (Figure 1).[11,12] Naphthyridine-based CK2 inhibitors were first described in 2010.[14,15] The most widely used and advanced compound from this series, CX-4945 (silmitasertib), has been evaluated clinically for several oncology indications and recently for SARS-CoV-2.[6,16] Silmitasertib received orphan drug status in the United States for the treatment of advanced cholangiocarcinoma.[9,10] CX-4945 inhibits a number of kinases in addition to CK2, thereby raising the possibility that its success in cancer models may be due, at least in part, to polypharmacology.[11,16] Efforts aimed at narrowing the inhibition profile of CX-4945 have resulted in several naphthyridine analogues, including CX-5011, CX-5279, and

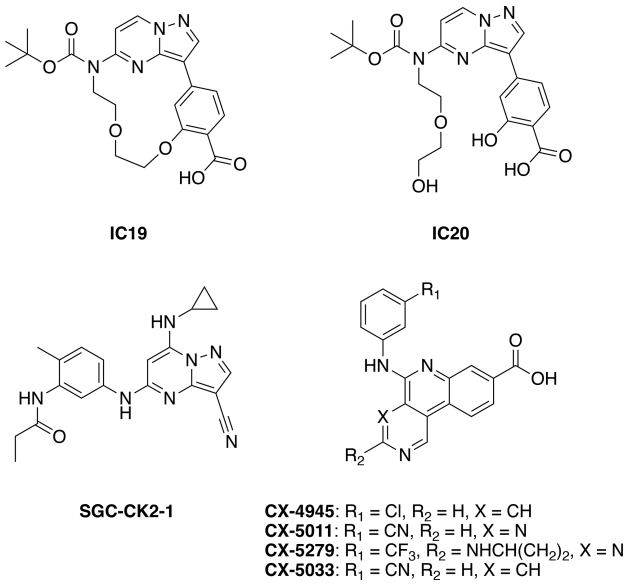

Figure 1. Structures of literature-reported potent CK2 inhibitors.

Received: December 20, 2022
Accepted: March 7, 2023
Published: March 14, 2023

© 2023 The Authors. Published by American Chemical Society

Table 1. Potency and Selectivity Data for Naphthyridine Analogues

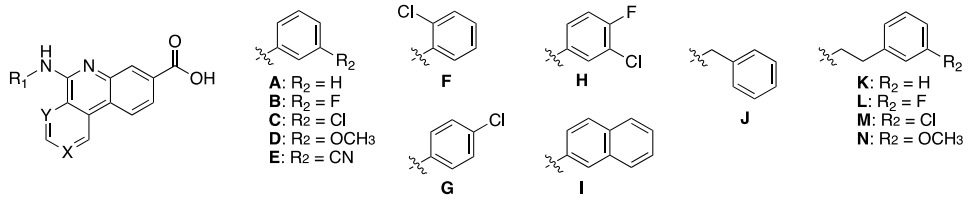

				NanoBRET data		selectivity data		solubility data
compound	X	Y	R_1	CK2α IC_{50} (nM)	CK2α' IC_{50} (nM)	S_{10}(1 μM) score[a]	# kinases with PoC < 10[b]	kinetic solubility (μM)
2	N	N	J	920	200	0.007	3	210.8
8	N	N	N	570	93	0.017	7	151.7
9	N	N	M	830	140	0.02	8	109.1
10	N	N	L	930	270	0.022	9	147.0
11	N	N	I	21	6.0	0.025	10	54.3[c]
12	N	N	G	240	25	0.032	13	209.1
13	N	N	B	350	51	0.042	17	192.0
14	N	N	H	110	19			49.1
15	N	N	F	300	42			121.8[c]
16	N	N	A	740	63			168.2
17	N	N	K	550	110			146.4
CX-5011	N	N	E	350	66			66.7
18	N	CH	M	230	17	0.035	14	184.0
19	N	CH	G	430	130	0.05	20	25.3
CX-5033	N	CH	E	4300	1900	0.079	32	131.7
20	N	CH	I	100	22			32.8
21	N	CH	J	1100	450			202.4
22	N	CH	L	300	62			187.7
23	N	CH	B	680	180			236.7
24	N	CH	N	150	19			180.4
25	N	CH	A	1400	420			184.1
26	N	CH	H	220	43			148.4
27	N	CH	K	260	34			171.4
28	N	CH	D	1200	340			190.4
CX-4945	N	CH	C	240	180	0.069	28	277.1
7	CH	N	J	>10 000	>10 000	0	0	80.4
SGC-CK2-1	NA	NA	NA	36	19	0.007	3	3.7

[a]S_{10}(1 μM): percentage of screened kinases with PoC < 10 at 1 μM. [b]PoC: percent of control values determined at 1 μM via DiscoverX *scan*MAX profiling. [c]Insoluble residue noted during solubility assessment.

CX-5033 (Figure 1), that demonstrate improved selectivity when compared with CX-4945.[11,17]

The clinical promise of the naphthyridine scaffold, demonstrated by the advancement of silmitasertib to Phase II clinical trials in addition to its acceptable human oral bioavailability, motivated further exploration of this chemotype. Despite reports of multiple exemplified naphthyridine analogues with nanomolar biochemical potency for CK2 and antiproliferative activity, a chemical probe with kinome-wide selectivity has not been described on the basis of this core.[16,17] Such a compound would represent an orthogonal tool that would aid in deciphering the complex biological roles of CK2. We hypothesized that synthesizing and characterizing naphthyridine analogues would allow for discovery of a potent and selective tool in this chemical class.

To complement the data that has been collected for published analogues and to expand knowledge around this chemotype, we prepared a series of naphthyridines. We chose to explore the R_1 position in addition to the presence or absence of the nitrogens in the fused ring system. As shown in Table 1, either a pyridine or pyrimidine was appended to the quinoline core to form the tricyclic system found in CX-4945/CX-5033 or CX-5011/CX-5279, respectively. Published crystal structures of naphthyridines CX-4945, CX-5011, and CX-5279 (PDB codes: 3NGA, 3PE2, 3R0T) confirm a pyridine or pyrimidine nitrogen within the tricyclic system engages in a key hydrogen bond with the CK2α hinge region. In addition, the carboxylic acid is involved in a water-mediated hydrogen-bond network. In contrast, the pendant aryl ring at position R_1 that we modified is solvent-exposed, and the CK2α ATP pocket is not space-limited at this position. Accordingly, we appended at the R_1 position substituted phenyl rings or naphthalene either directly via an anilino linkage or using a short alkyl chain. We aimed to explore whether CK2 potency in cells and/or kinome-wide selectivity could be improved through modification of this group. In addition, several analogues (**2**, **8**, **9**, **10**, **17**, **18**, **21**, **22**, **24**, **27**) were designed to reduce the planarity of the resultant molecule in an attempt to improve solubility.

These compounds were evaluated in the CK2α and CK2α' NanoBRET assays to gauge their ability to engage the target kinase CK2 in cells (Table 1). Most CK2 NanoBRET assays were run in triplicate (Figures 2, 3, S2, and S3). The NanoBRET data revealed that molecules from this series

https://doi.org/10.1021/acsmedchemlett.2c00530
ACS Med. Chem. Lett. 2023, 14, 432−441

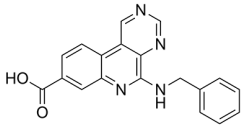

2

S_{10}(1 μM) = 0.007
3 kinases <10 PoC at 1 μM
S_{35}(1 μM) = 0.032
13 kinases <35 PoC at 1 μM

Kinase	DiscoverX PoC value	Assay format	IC_{50} value (nM)
CK2α	0.1	Enzymatic and NB	3.0 and 920
CK2α′	0.2	Enzymatic and NB	<1.0 and 200
DAPK3	6.5	Enzymatic	1500
HIPK1	10	Enzymatic	1800
DAPK2	11	Enzymatic	1500
HIPK3	16	Enzymatic	900
MYLK4	20	Enzymatic	>10000
PIK3CG	23	Enzymatic	5300
PIK3C2G	25	Enzymatic	4500
DYRK1A	28	Enzymatic	760
HIPK2	30	Enzymatic	600
DRAK2	30	Enzymatic	1800
YSK4	34	Enzymatic	3700

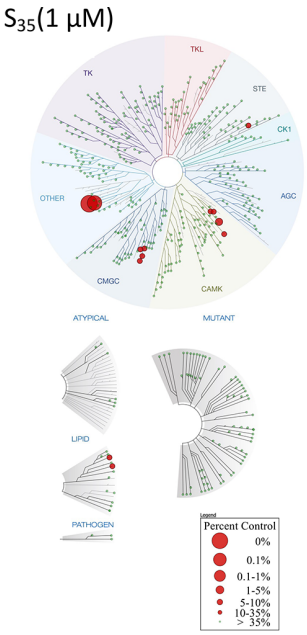

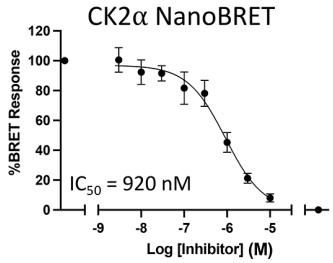

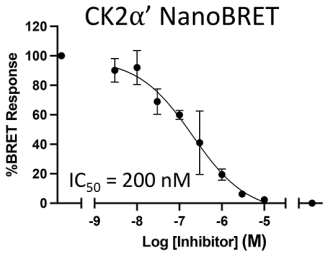

Figure 2. Structure, potency, and selectivity data related to CK2 chemical probe **2**. Kinome tree shows kinases that bind with PoC < 35 when compound **2** was screened at 1 μM. Assay format used to generate data in the last column of the nested table is listed in the preceding column. CK2 NanoBRET assays were run in triplicate (n = 3), and error bars represent standard deviation (SD). PoC = percent of control; NB = NanoBRET.

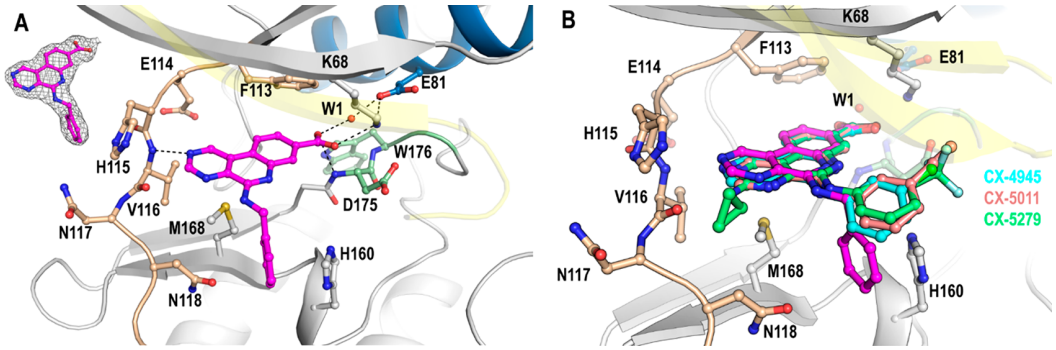

Figure 3. (A) Crystal structures of human CK2α in complex with compound **2** (pink) in cartoon (CK2α) and stick (compound **2**) representation. The hinge region is colored in wheat, the αC helix is in blue, the DWG motif is in green, and the water molecule is shown as a red sphere. The P-loop in yellow was made transparent for better view of the interactions. Hydrogen bonds are indicated as black dashed lines. The insert on the upper left corner is the electron density map ($2F_o-F_c$) of the bound ligand contoured at 1σ. (B) Overlay of compound **2** with published naphthyridine analogues (PDB codes: 3NGA, 3PE2, 3R0T) in the same color scheme as panel A.

engaged CK2α′ and CK2α with IC_{50} values of generally less than 1 μM. Excluding CX-4945, a pronounced 2.3−13-fold bias was observed when comparing IC_{50} values for CK2α′ with those for CK2α, with compounds being more potent against CK2α′. Previously reported CK2 NanoBRET IC_{50} values for CX-4945 align with this trend (7.6-fold bias).[11] Compound **18** demonstrated the most significant difference in IC_{50} values. A more modest 1.9-fold bias for CK2α′ versus CK2α was observed for SGC-CK2-1 and was consistent in the pyrazolopyrimidine series from which it was selected.[11] Compound **11** was the most potent compound in both CK2 NanoBRET assays (IC_{50} < 22 nM), while CX-5033 was weakest in these assays (IC_{50} > 1800 nM).

The kinetic solubility of our naphthyridine analogues was next evaluated (Table 1). While none of our analogues improved on the value obtained for CX-4945, all demonstrated good aqueous solubility (>20 μM). For **2**, **8**, **12**, **13**, **16**, **18**, **21**, **22**, **23**, **24**, **25**, **27**, and **28**, the measured solubility was reported as greater than 75% of the dose concentration, and thus, the actual solubility is estimated to be higher than Table 1 reflects. An insoluble residue was noted for analogues **11** and **15**, and the lowest solubility values (25−50 μM) were recorded for **14**, **19**, and **20**. The series of analogues (**2**, **8**, **9**, **10**, **17**, **18**, **21**, **22**, **24**, **27**) designed to be less planar had good aqueous solubility (all > 100 μM). Of note, all naphthyridine analogues were more soluble than SGC-CK2-1 when evaluated side by side.

Given the published off-targets of CX-4945, the selectivity of these CK2-targeting compounds was important to assess, especially against the highly homologous CMGC kinases from

https://doi.org/10.1021/acsmedchemlett.2c00530
ACS Med. Chem. Lett. 2023, 14, 432−441

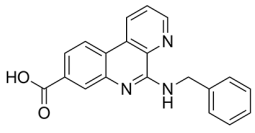

7

Kinase	DiscoverX PoC value	Assay format	IC_{50} value (nM)
PIP5K1C	15	Enzymatic	>10000
CK2α	80	NB	>10000
CK2α′	67	NB	>10000

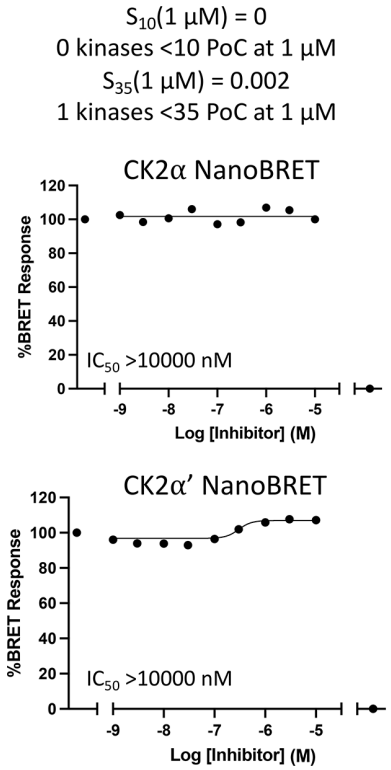

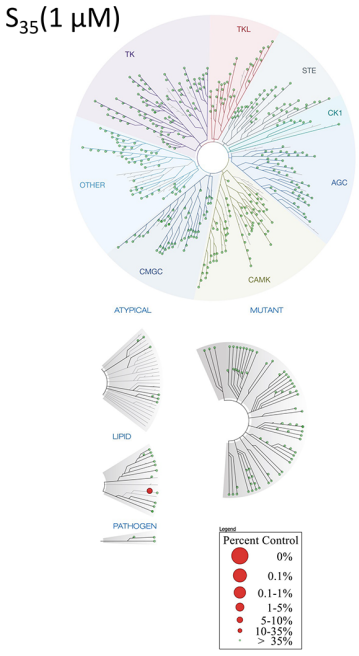

Figure 4. Structure, potency, and selectivity data related to CK2 negative control 7. Kinome tree shows kinases that bind with PoC < 35 when compound 7 was screened at 1 μM. Assay format used to generate data in the last column of the nested table is listed in the preceding column. CK2 NanoBRET assays were run in singlicate (n = 1). PoC = percent of control; NB = NanoBRET.

the DYRK and HIPK subfamilies, which share many key active site residues with CKα and CK2α'. Enzymatic activity assays were carried out at a single concentration (1 μM) of inhibitor to generate percent of control (PoC) values (Table S1). Several compounds, including compounds **2**, **8**, **9**, and **21**, lacked activity against DYRKs and HIPKs, while a few others, including compounds **10**, **17**, **18**, and **24**, demonstrated potent inhibition of just one kinase in the 8-member panel. This result reinforced the idea that selectivity can be imparted in the naphthyridine scaffold. Most compounds (11 in total), however, potently inhibited more than half of the kinases in this enzymatic panel. While it is not a direct comparison, CX-4945 exhibits a PoC < 10 for all of these same kinases in Table S1 when profiled in the DiscoverX *scan*MAX panel at 1 μM (minus DYRK3 since it is not included in the *scan*MAX panel).[11] In our limited DYRK and HIPK subfamily panel, more kinases preferred naphthyridine analogues with Y = CH versus Y = N (Table 1), which rendered them generally less selective.

We considered both the CK2 NanoBRET potency and the small panel enzymatic results to select some analogues for broader selectivity evaluation using DiscoverX *scan*MAX profiling. This kinome-wide profiling was executed at a single inhibitor concentration (1 μM). DiscoverX *scan*MAX data previously generated for CX-4945 at 1 μM is included in Table 1 and shows it has an S_{10} = 0.069 and that it potently binds to nearly 7% of the wild-type human kinases in the panel.[11] Previously published kinome-wide selectivity data collected at 1 μM for SGC-CK2-1 is also included, which supports its utility as a CK2-selective chemical probe.[11] Compound **14** was chosen on the basis of its potency for CK2α and CK2α' in the corresponding NanoBRET assays (Table 1). Compounds **2**, **8**, **9**, **10**, and **18** were also profiled on the basis of their potent inhibition of either 0 or 1 kinase in the enzymatic panel (Table S1). Finally, compounds **12**, **13**, **19**, and CX-5033 were selected as potent inhibitors of HIPK2 with or without CK2 affinity. Exemplars with Y = CH and Y = N (Table 1) were included to determine if the selectivity trend in Table S1 was maintained when more kinases were sampled. The kinome-wide profiling data summarized in the S_{10}(1 μM) column of Table 1 supports the trend of overall selectivity improvements for the Y = N versus Y = CH compounds. Specific examples include compounds **9** versus **18** and **12** versus **19** where the analogue bearing Y = N demonstrated a better selectivity score. Except for CX-5033, all compounds demonstrated an improved selectivity score when compared with CX-4945. Compound **2** emerged as the most promising compound when considering broad selectivity [S_{10}(1 μM) = 0.007]. No

https://doi.org/10.1021/acsmedchemlett.2c00530
ACS Med. Chem. Lett. 2023, 14, 432−441

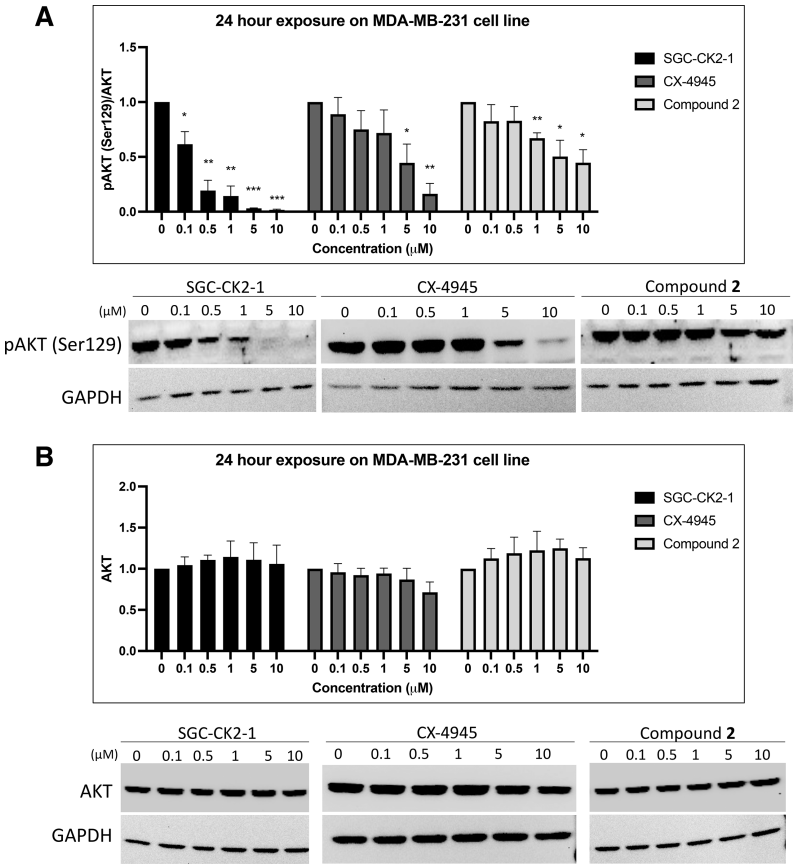

Figure 5. (A) Western blot analyses of pAKT in MDA-MB-231 cells after 24 h treatment with SGC-CK2-1, CX-4945, or compound **2**. Representative blot and quantification of phospho-AKT (Ser129) normalized to AKT, $n = 3$. SGC-CK2-1 p-values: 0.1 μM = 0.0287, 0.5 μM = 0.0045, 1 μM = 0.0038, 5 μM < 0.0001, 10 μM < 0.0001. CX-4945 p-values: 5 μM = 0.0303, 10 μM = 0.0043. Compound **2** p-values: 1 μM = 0.0072, 5 μM = 0.0286, 10 μM = 0.0149. (B) Western blot analyses of AKT in MDA-MB-231 cells after 24 h treatment with SGC-CK2-1, CX-4945, or compound **2**. Representative blot and quantification of total AKT, $n = 3$. Error bars represent SEM. P-values were generated using a parametric unpaired t test with Welch's correction by comparing each treatment condition to the untreated control. None of the concentrations in panel (B) were significantly different than the untreated control.

additional screening was executed to determine the selectivity of compound **2** versus nonkinase targets.

A deeper dive into the DiscoverX *scan*MAX data generated for compound **2** revealed 13 kinases with PoC < 35, including CK2α and CK2α' (Figure 2). Enzymatic assays were employed as an orthogonal method to validate the *scan*MAX binding data for these 13 kinases. Potent inhibition of CK2α and CK2α' was observed ($IC_{50} \leq 3$ nM). Furthermore, the exquisite selectivity of compound **2** was confirmed, with a useful 200-fold window between the inhibition of CK2α and HIPK2, the next most potently inhibited kinase ($IC_{50} = 600$ nM). This compound demonstrates a 4.6-fold bias for binding CK2α' versus CK2α in the corresponding NanoBRET assays (Table 1) and a similar trend in CK2 enzymatic assays (Figure 2).

Structural studies were employed to rationalize the selectivity of compound **2** for CK2. A cocrystal structure of compound **2** bound to CK2α was solved (Figure 3A, Table S4). This structure confirmed a key hydrogen bond between the nitrogen at the "X" position in Table 1 and a backbone NH between H115 and V116. Additional hydrogen bonds were noted between the carboxylic acid and K68, a water mediated with E81 on the αC helix, and a backbone NH adjacent to D175 from the DWG motif. This binding mode was compared with those previously solved for CX-4945, CX-5011, and CX-5279 (Figure 3B). The main difference observed was the orientation of the pendant aryl ring in the front pocket. Compound **2**, which is shown in pink in panel B, can form an additional π-stacking interaction with H160 that is absent in previously solved structures. The methylene spacer present in compound **2**, but not in the other scaffolds where the aryl ring is directly attached, positions the aryl ring so that it can adopt this favorable conformation. It is likely that the ATP binding sites of other kinases do not accommodate this ring in the same way, thereby precluding their binding to compound **2** with high affinity and imparting the selectivity we observe. Many more kinases tolerate binding of naphthyridine analogues with the aryl ring directly attached, which is exemplified by compounds **11**, **12**, **13**, **19**, CX-5033, and CX-4945 in Table 1 that all bind 10 or more kinases with PoC < 10. While the single methylene unit seems to provide the most optimal ability to π-stack, compounds **8**, **9**, **10**, and **18** in Table 1 demonstrate that the incorporation of two methylene groups between the core and pendant aryl ring also imparts selectivity versus those analogues with the aryl ring directly attached.

Consideration of the naphthyridine cocrystal structures (Figure 3) aided in the design of an appropriate negative control compound to be used alongside compound **2** in a

https://doi.org/10.1021/acsmedchemlett.2c00530
ACS Med. Chem. Lett. 2023, 14, 432−441

chemical probe set. To synthesize a structurally related compound that lacked an ability to bind to CK2, we specifically targeted the hinge-binding nitrogen. Compound **7** was prepared with the "X" position in Table 1 replaced by a carbon. The resulting compound was evaluated in the CK2α and CK2α' NanoBRET assays, where it was found to not bind either kinase at concentrations up to 10 μM (Table 1 and Figure 4). When profiled in the DiscoverX *scan*MAX panel at 1 μM, a single kinase (PIP5K1C) was bound with a PoC < 35. Enzymatic follow-up, however, demonstrated that this binding in the DiscoverX panel did not result in PIP5K1C inhibition. Thus, modification of the hinge-binding atom on compound **2** resulted in a negative control (**7**) that lacks CK2 and kinome-wide binding. No additional screening was executed to determine the selectivity of compound **7** versus nonkinase targets.

Noting the discrepancy between enzymatic and NanoBRET potency for these naphthyridines, we sought methods via which we could assess cellular permeability. We did this using two parallel approaches: the NanoBRET assay in permeabilized cells and a parallel artificial membrane permeability assay (PAMPA). All compounds in Table 1 were analyzed using the NanoBRET assay, while only a subset was subjected to PAMPA evaluation. As shown in Table S3 and Figures S4 and S5, all CK2-active compounds, including chemical probe **2**, demonstrated improved cellular target engagement for CK2α and CK2α' when the cells were permeabilized. For most compounds, a more dramatic boost in potency was noted for CK2α' when compared with CK2α. Since permeabilizing cells also reduces the concentration of ATP, we suggest that the higher affinity (K_m) of CK2α' for ATP (reported by commercial vendors) results in a more dramatic shift when cells are permeabilized because there is less ATP competition for binding to the same site as our inhibitors. Interestingly, a very pronounced shift (140−760-fold) in IC_{50} values was noted for CX-5033. A less pronounced fold-change in IC_{50} values was observed for SGC-CK2-1 (<5-fold), which was similar to several naphthyridine analogues (**11**, **12**, **13**, **15**, **16**, **20**, **24**). The PAMPA results (Table S2) support the conclusion that, via this method, compound **2** and negative control **7** are more permeable than CX-4945. The PAMPA effective permeability (P_e) values generated for compounds **2** and **7** correlate with human fraction absorbed (%FA) greater than 80% and good permeability.[18] Unfortunately, the low solubility of SGC-CK2-1 in assay media precluded analogous data generation for this compound. Since we cannot discern the impact of reduced ATP concentration on cellular target engagement when cells are permeabilized, we cannot conclude that the shift in IC_{50} values is because the naphthyridine analogues have poor cellular permeability. The PAMPA data indicate that our chemical probe set compounds are cell-permeable.

With a potent and selective compound in hand, we evaluated the impact on downstream signaling in response to compound **2**. In a previous report, CX-4945 was found to reduce viability, induce cell cycle arrest and apoptosis, and hamper migratory capacity of MDA-MB-231 cells, a triple negative breast cancer cell line with elevated CK2 expression.[19] This result motivated examination of the response of MDA-MB-231 cells to treatment with compound **2**. An orthogonal CK2 probe known to inhibit downstream signaling mediated by CK2, SGC-CK2-1 (Figure 1), was included in these experiments in addition to CX-4945. As shown in Figure 5, a 24 h exposure of MDA-MB-231 cells to SGC-CK2-1, CX-4945, or compound **2** resulted in dose-dependent inhibition of AKT phosphorylation with no impact on total AKT expression. The concentration at which AKT phosphorylation is inhibited by each compound corresponds with the trend in their respective IC_{50} values in the CK2 NanoBRET assays: 19−36 nM for SGC-CK2-1, 180−240 nM for CX-4945, and 200−920 nM for compound **2**. The rank order in efficiency of inhibiting AKT phosphorylation is as follows: SGC-CK2-1 > CX-4945 > compound **2**. This result confirmed that CK2 inhibition by compound **2** disrupts CK2-mediated downstream signaling.

Whether inhibition of CK2 impacts cell survival and is a suitable anticancer target is a topic that has recently garnered much attention.[11,20,21] In our preliminary experiments, neither compound **2** nor SGC-CK2-1 exhibited significant cytotoxicity when MDA-MB-231 cells were treated for 48 h up to a concentration of 10 μM (Figure S6). Compounds **7**, CX-5011, and CX-4945 similarly did not exhibit cytotoxicity in our study (Figure S6). There are several possible explanations for the discrepancy between our observed lack of impact of naphthyridine compounds on viability and their published effect on cell growth.[19] It has been reported that when treated with micromolar concentrations (2−10 μM) of CX-4945 for 24−72 h, MDA-MB-231 cell growth is inhibited. The authors point out that they rely on a WST-1 assay for readout and this indirectly measures cell growth on the basis of metabolic activity in the cells.[19] CK2 regulates cell metabolism, which is a process that can be inhibited without an associated impact on cell growth.[1,22] Another potential explanation is that MDA-MB-231 cells are moderately sensitive to the promotion of CK2-independent cytoplasmic vacuolization, called methuosis, at micromolar concentrations of CX-4945 and CX-5011.[23−25] Metabolic-based viability assay (MTT) results generated in parallel support the idea that this vacuolization impacts cell metabolism.[23] Similarly, methuosis is reported to drive metabolic failure.[26] In contrast to an assay dependent on mitochondrial enzymes (WST-1), we opted to employ a luciferase-based assay (CellTiter-Glo2) that requires ATP in order to generate the luminescent species. Our assay results are more aligned with one that reported IC_{50} values for CX-4945 and CX-5011 of 6.4 and 9.8 μM, respectively, when MDA-MB-231 cells were treated for 4 days in dose−response, and Alamar blue was used to readout cell viability.[17] Taken together, we suggest that the time course of treatment, as well as the method of assessment, can impact observed viability results.

Historically, CK2 has been recognized as an essential mediator in hematological malignancies.[10,27] Multiple myeloma cells have been reported to rely on elevated CK2 for survival. Accordingly, when CX-4945 was profiled against a panel of 13 multiple myeloma cell lines, low micromolar antiproliferative activity was measured via a CellTiter-Glo viability assay.[28] CX-4945 has been explored clinically for relapsed or refractory multiple myeloma.[10] Apoptosis was induced much more effectively in multiple myeloma cells from patients when treated with orthogonal CK2 inhibitors (TBB, a TBB derivative, or CGP029482) than in nonmalignant control cells.[29,30] This data motivated our preliminary examination of the effect of compound **2** versus published naphthyridines (CX-4945, CX-5011, and CX-5033) and SGC-CK2-1 at a single concentration of 1 μM on a panel of multiple myeloma cell lines treated for 5 days. Because it was designed in the later stage, negative control **7** was not included in this preliminary study. It is best practice to employ a chemical probe and its

https://doi.org/10.1021/acsmedchemlett.2c00530
ACS Med. Chem. Lett. 2023, 14, 432−441

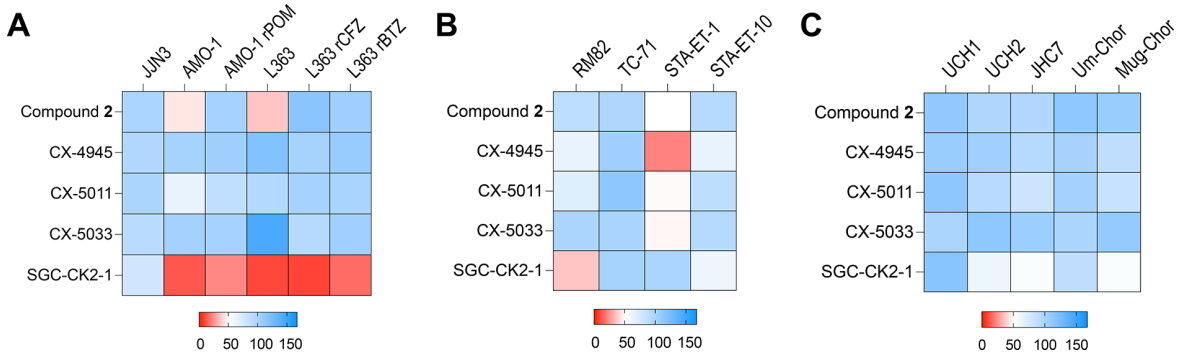

Figure 6. Analysis of impact of naphthyridine analogues and SGC-CK2-1 on viability of (A) multiple myeloma, (B) Ewings sarcoma, and (C) chordoma cell lines when dosed at 1 μM. Scale bar shows the color gradient that corresponds with percent viability.

negative control side-by-side in biological experiments. The responses of JJN3, AMO-1 (parental and pomalidomide-resistant), and L363 (parental, carfilzomib-resistant, and bortezomib-resistant) multiple myeloma cell lines to treatment were analyzed via a metabolic-based viability assay using resazurin (akin to the WST-1 assay). As shown in Figure 6A, our preliminary data demonstrates that JJN3 cells were not responsive to treatment with any compound. The viability of the AMO-1 and L363 parental lines was reduced by treatment with compound **2** but not by treatment with the other naphthyridine analogues. We observed 44% viability of AMO-1 and 36% viability of L363 cells, respectively, following treatment with 1 μM of compound **2**. The viability of the AMO-1 and L363 drug-resistant lines was not impacted by treatment with any naphthyridine analogue. Interestingly, the viability of all AMO-1 and L363 cell lines tested was significantly compromised by treatment with 1 μM of SGC-CK2-1, which resulted in 9−22% viability of the AMO-1 and L363 cells and 77% viability of the JJN3 cells. This suggests a chemotype-specific response and/or reflects the enhanced CK2 affinity of SGC-CK2-1 versus compound **2**. SGC-CK2-1 is nearly 11-fold more active than compound **2** in the CK2α' NanoBRET assay and nearly 26-fold more active than compound **2** in the CK2α NanoBRET assay.[11] Our preliminary viability data aligns with literature reports of multiple myeloma survival being impaired via CK2 inhibition.

Less has been published about the role of CK2 in rare cancers that occur in bones, such as Ewings sarcoma, and in the soft tissue around bones, known as chordoma, which is a rare, slow growing cancer of tissue inside the spine. The *EWS* gene, which encodes a ubiquitously expressed RNA-binding protein of the same name, has been identified as a target of tumor-specific translocations in Ewings sarcoma family tumors. A putative CK2 phosphorylation site (Ser325) on an EWS protein isoform has been reported.[31,32] Literature links between CK2 and chordoma are tenuous. Validated, repurposed chemotherapeutic drugs have been the focus of most cell-based therapeutic screens related to chordoma.[33,34] As an exception, one compound, 5-iodotubericin, that inhibits CK2 in addition to other kinases, has demonstrated dose-responsive inhibition of UCH1 chordoma cells.[35] Motivated to explore whether CK2 inhibition is a therapeutic avenue for these rare cancers, we examined the impact of the same panel of CK2 inhibitors, dosed at 1 μM, on the viability of four Ewings sarcoma and five chordoma cell lines following 5 days of treatment. The preliminary data in Figure 6B demonstrates that most Ewings cell lines were nonresponsive to treatment with naphthyridine analogues. The exception to this was the STA-ET-1 cells, which were modestly impacted by treatment with these compounds. CX-4945 elicited the most robust response of Ewings cell lines for compounds in this structural series and resulted in 21% viability of the STA-ET-1 cells and 63% viability of both the RM82 and STA-ET-10 cells. SGC-CK2-1, in contrast, only significantly impacted RM82 cells (36% viability) versus other Ewings cell lines evaluated. When considering the preliminary chordoma cell line data in Figure 6C, a limited impact on viability was noted. The exception to this trend was observed for SGC-CK2-1, which showed the sensitivity of UCH2, JHC7, and Mug-Chor cells to treatment and resulted in 60%, 53%, and 53% viability, respectively. As was observed in the multiple myeloma cell lines, a chemotype-specific response was observed for SGC-CK2-1 versus naphthyridine-based compounds in chordoma cell lines.

Viability data for naphthyridine compounds CX-4945 and CX-5011 has been published. Multiple studies have demonstrated single or double-digit micromolar viability IC_{50} values after dosing diverse cancer cell lines for 2−4 days.[17,23,36,37] Importantly, a change in the time course of treatment (24 versus 72 h) resulted in notably different impacts on cell viability in HepG2 cells.[23] When CX-4945 was profiled against 43 diverse cancer cell lines, their responses were variable. While leukemia and colon cells demonstrated greater sensitivity, the 11 included breast cancer cell lines displayed the widest range of sensitivities to CX-4945. The authors identified a correlation between sensitivity to CX-4945 and expression levels of the CK2α catalytic subunit in these breast cancer cell lines.[37] These results suggest that for our multiple myeloma, chordoma, and Ewings sarcoma studies, 1 μM of naphthyridine analogues may not have been high enough to see a robust response and/or that, especially in the Ewings sarcoma cell lines, CK2α expression may be lower.

We have described the design, synthesis, and biological evaluation of a series of naphthyridines as inhibitors of CK2. Compound **2** emerged as our most optimal probe candidate. Comparison of cocrystal structures solved for compound **2** versus other naphthyridines revealed a key interaction that may drive its CK2 selectivity and informed design of a structurally related negative control compound (**7**). Inhibition of downstream signaling without an associated impact on viability was observed when MDA-MB-231 breast cancer cells were treated with compound **2**. In contrast, the viability of specific multiple myeloma cell lines was differentially compromised because of treatment with 1 μM of compound **2**, which may be related to different genomic lesions occurring in myeloma, now

https://doi.org/10.1021/acsmedchemlett.2c00530
ACS Med. Chem. Lett. 2023, 14, 432−441

recognized as significant oncogenic drivers in this cancer.[38] Ewings sarcoma and chordoma cell lines were generally not responsive to treatment with compound **2**. Like SGC-CK2-1, compound **2** does not seem to be a broadly antiproliferative agent.[11] This finding supports the concept that CK2 inhibition is a possible personalized treatment strategy for specific cancers, including multiple myeloma, and deserves further study. We recommend compound **2** as a CK2 chemical probe to be employed alongside an orthogonal CK2 chemical probe on the basis of a different chemotype, such as SGC-CK2-1, in cell-based studies aimed at interrogating CK2-mediated biology. As no pharmacokinetic data has been generated for compounds **2** and **7**, we only advise use of our chemical probe set in cellular studies.

■ ASSOCIATED CONTENT

Supporting Information

The Supporting Information is available free of charge at https://pubs.acs.org/doi/10.1021/acsmedchemlett.2c00530.

Supplemental figures (NanoBRET and cell viability assay curves); tables (enzymatic profiling, PAMPA, permeabilized NanoBRET assay, and X-ray crystallographic data); and experimental details, including synthetic schemes and characterization of key compounds, protocols related to selectivity screening and biological assays, and crystallographic details (PDF)

Accession Codes

The PDB accession code for the X-ray cocrystal structure of CK2α + compound **2** is 8BGC.

■ AUTHOR INFORMATION

Corresponding Author

Alison D. Axtman − *Structural Genomics Consortium, UNC Eshelman School of Pharmacy, University of North Carolina at Chapel Hill, Chapel Hill, North Carolina 27599, United States;* orcid.org/0000-0003-4779-9932; Email: alison.axtman@unc.edu

Authors

Zachary W. Davis-Gilbert − *Structural Genomics Consortium, UNC Eshelman School of Pharmacy, University of North Carolina at Chapel Hill, Chapel Hill, North Carolina 27599, United States*

Andreas Krämer − *Institute of Pharmaceutical Chemistry, Goethe University Frankfurt, Frankfurt 60438, Germany; Structural Genomics Consortium, Buchmann Institute for Life Sciences, Goethe University Frankfurt, Frankfurt 60438, Germany; Frankfurt Cancer Institute, Frankfurt 60596, Germany*

James E. Dunford − *Botnar Research Centre, Nuffield Department of Orthopaedics, Rheumatology and Musculoskeletal Sciences, University of Oxford, Oxford OX3 7LD, United Kingdom;* orcid.org/0000-0002-9932-4042

Stefanie Howell − *Structural Genomics Consortium, UNC Eshelman School of Pharmacy, University of North Carolina at Chapel Hill, Chapel Hill, North Carolina 27599, United States*

Filiz Senbabaoglu − *Botnar Research Centre, Nuffield Department of Orthopaedics, Rheumatology and Musculoskeletal Sciences, University of Oxford, Oxford OX3 7LD, United Kingdom*

Carrow I. Wells − *Structural Genomics Consortium, UNC Eshelman School of Pharmacy, University of North Carolina at Chapel Hill, Chapel Hill, North Carolina 27599, United States;* orcid.org/0000-0003-4799-6792

Frances M. Bashore − *Structural Genomics Consortium, UNC Eshelman School of Pharmacy, University of North Carolina at Chapel Hill, Chapel Hill, North Carolina 27599, United States;* orcid.org/0000-0003-4241-9873

Tammy M. Havener − *Structural Genomics Consortium, UNC Eshelman School of Pharmacy, University of North Carolina at Chapel Hill, Chapel Hill, North Carolina 27599, United States;* orcid.org/0000-0002-4613-0498

Jeffery L. Smith − *Structural Genomics Consortium, UNC Eshelman School of Pharmacy, University of North Carolina at Chapel Hill, Chapel Hill, North Carolina 27599, United States*

Mohammad A. Hossain − *Structural Genomics Consortium, UNC Eshelman School of Pharmacy, University of North Carolina at Chapel Hill, Chapel Hill, North Carolina 27599, United States;* orcid.org/0000-0001-8684-8755

Udo Oppermann − *Botnar Research Centre, Nuffield Department of Orthopaedics, Rheumatology and Musculoskeletal Sciences, University of Oxford, Oxford OX3 7LD, United Kingdom; Oxford Translational Myeloma Centre, University of Oxford, Oxford OX3 7LD, United Kingdom*

David H. Drewry − *Structural Genomics Consortium, UNC Eshelman School of Pharmacy, University of North Carolina at Chapel Hill, Chapel Hill, North Carolina 27599, United States; UNC Lineberger Comprehensive Cancer Center, School of Medicine, University of North Carolina at Chapel Hill, Chapel Hill, North Carolina 27599, United States;* orcid.org/0000-0001-5973-5798

Complete contact information is available at: https://pubs.acs.org/10.1021/acsmedchemlett.2c00530

Notes

The authors declare no competing financial interest.

■ ACKNOWLEDGMENTS

Promega kindly provided constructs for NanoBRET measurements of CK2α and CK2α'. The kinome trees in Figures 2 and 4 and the Table of Contents graphic were prepared using the TREE*spot* kinase interaction mapping software at http://treespot.discoverx.com. We thank the Mark Foundation for Cancer Research and the Chordoma Foundation for supporting our efforts related to the rare cancer chordoma. ChemSpace provided synthetic support for our program. We acknowledge the Department of Chemistry Mass Spectrometry Core Laboratory at the University of North Carolina for assisting with mass spectrometry analyses. Furthermore, we thank the beamline scientists at the Swiss Light Source (PSI) for their great support during data collection. The Structural Genomics Consortium (SGC) is a registered charity (number 1097737) that receives funds from Bayer AG, Boehringer Ingelheim, the Canada Foundation for Innovation, Eshelman Institute for Innovation, Genentech, Genome Canada through Ontario Genomics Institute [OGI-196], EU/EFPIA/OICR/McGill/KTH/Diamond, Innovative Medicines Initiative 2 Joint Undertaking [EUbOPEN grant 875510], Janssen, Merck KGaA (a.k.a., EMD in Canada and USA), Pfizer, the São Paulo Research Foundation-FAPESP, and Takeda.

https://doi.org/10.1021/acsmedchemlett.2c00530
ACS Med. Chem. Lett. 2023, 14, 432−441

Research in the Oxford laboratory (U.O.) was supported by Cancer Research UK, the LEAN program grant of the Leducq Foundation, Oxford NIHR Biomedical Research Centre, the Oxford Translational Myeloma Centre, and the BMS-Mt Sinai-Oxford Myeloma Single Cell Consortium. J.E.D. is supported by the Oxford NIHR Biomedical Research Centre. Research reported in this publication was supported in part by DoD ALSRP award AL190107, NC Biotechnology Center Institutional Support Grant 2018-IDG-1030, and NIH U24DK116204.

■ ABBREVIATIONS

IC_{50}, half-maximal inhibitory concentration; K_m, Michaelis constant; NanoBRET, bioluminescence resonance energy transfer using NanoLuciferase; PoC, percent of control

■ REFERENCES

(1) Meggio, F.; Pinna, L. A. One-thousand-and-one substrates of protein kinase CK2? *FASEB J.* **2003**, *17* (3), 349−368.
(2) Salvi, M.; Sarno, S.; Cesaro, L.; Nakamura, H.; Pinna, L. A. Extraordinary pleiotropy of protein kinase CK2 revealed by weblogo phosphoproteome analysis. *Biochim. Biophys. Acta* **2009**, *1793* (5), 847−859.
(3) Rabalski, A. J.; Gyenis, L.; Litchfield, D. W. Molecular pathways: Emergence of protein kinase CK2 (CSNK2) as a potential target to inhibit survival and DNA damage response and repair pathways in cancer cells. *Clin. Cancer Res.* **2016**, *22* (12), 2840−2847.
(4) Nuñez de Villavicencio-Diaz, T.; Rabalski, A. J.; Litchfield, D. W. Protein kinase CK2: Intricate relationships within regulatory cellular networks. *Pharmaceuticals* **2017**, *10* (1), 27.
(5) Ahmed, K.; Gerber, D. A.; Cochet, C. Joining the cell survival squad: An emerging role for protein kinase CK2. *Trends Cell Biol.* **2002**, *12* (5), 226−230.
(6) Bouhaddou, M.; Memon, D.; Meyer, B.; White, K. M.; Rezelj, V. V.; Correa Marrero, M.; Polacco, B. J.; Melnyk, J. E.; Ulferts, S.; Kaake, R. M.; Batra, J.; Richards, A. L.; Stevenson, E.; Gordon, D. E.; Rojc, A.; Obernier, K.; Fabius, J. M.; Soucheray, M.; Miorin, L.; Moreno, E.; Koh, C.; Tran, Q. D.; Hardy, A.; Robinot, R.; Vallet, T.; Nilsson-Payant, B. E.; Hernandez-Armenta, C.; Dunham, A.; Weigang, S.; Knerr, J.; Modak, M.; Quintero, D.; Zhou, Y.; Dugourd, A.; Valdeolivas, A.; Patil, T.; Li, Q.; Hüttenhain, R.; Cakir, M.; Muralidharan, M.; Kim, M.; Jang, G.; Tutuncuoglu, B.; Hiatt, J.; Guo, J. Z.; Xu, J.; Bouhaddou, S.; Mathy, C. J. P.; Gaulton, A.; Manners, E. J.; Félix, E.; Shi, Y.; Goff, M.; Lim, J. K.; McBride, T.; O'Neal, M. C.; Cai, Y.; Chang, J. C. J.; Broadhurst, D. J.; Klippsten, S.; De wit, E.; Leach, A. R.; Kortemme, T.; Shoichet, B.; Ott, M.; Saez-Rodriguez, J.; tenOever, B. R.; Mullins, R. D.; Fischer, E. R.; Kochs, G.; Grosse, R.; García-Sastre, A.; Vignuzzi, M.; Johnson, J. R.; Shokat, K. M.; Swaney, D. L.; Beltrao, P.; Krogan, N. J. The global phosphorylation landscape of SARS-CoV-2 infection. *Cell* **2020**, *182* (3), 685−712.e19.
(7) Yang, X.; Dickmander, R. J.; Bayati, A.; Taft-Benz, S. A.; Smith, J. L.; Wells, C. I.; Madden, E. A.; Brown, J. W.; Lenarcic, E. M.; Yount, B. L.; Chang, E.; Axtman, A. D.; Baric, R. S.; Heise, M. T.; McPherson, P. S.; Moorman, N. J.; Willson, T. M. Host kinase CSNK2 is a target for inhibition of pathogenic SARS-like β-coronaviruses. *ACS Chem. Biol.* **2022**, *17*, 1937−1950.
(8) Mishra, S.; Kinoshita, C.; Axtman, A. D.; Young, J. E. Evaluation of a selective chemical probe validates that CK2 mediates neuroinflammation in an hiPSC-derived microglial model. *Front Mol. Neurosci* **2022**, *15*, 824956.
(9) Zakharia, K.; Miyabe, K.; Wang, Y.; Wu, D.; Moser, C. D.; Borad, M. J.; Roberts, L. R. Preclinical in vitro and in vivo evidence of an antitumor effect of CX-4945, a casein kinase II inhibitor, in cholangiocarcinoma. *Transl Oncol* **2019**, *12* (1), 143−153.
(10) Chon, H. J.; Bae, K. J.; Lee, Y.; Kim, J. The casein kinase 2 inhibitor, CX-4945, as an anti-cancer drug in treatment of human hematological malignancies. *Front Pharmacol* **2015**, *6*, 70.
(11) Wells, C. I.; Drewry, D. H.; Pickett, J. E.; Tjaden, A.; Krämer, A.; Müller, S.; Gyenis, L.; Menyhart, D.; Litchfield, D. W.; Knapp, S.; Axtman, A. D. Development of a potent and selective chemical probe for the pleiotropic kinase CK2. *Cell Chem. Biol.* **2021**, *28*, 546−558.e10.
(12) Krämer, A.; Kurz, C. G.; Berger, B.-T.; Celik, I. E.; Tjaden, A.; Greco, F. A.; Knapp, S.; Hanke, T. Optimization of pyrazolo[1,5-a]pyrimidines lead to the identification of a highly selective casein kinase 2 inhibitor. *Eur. J. Med. Chem.* **2020**, *208*, 112770.
(13) Raaf, J.; Bischoff, N.; Klopffleisch, K.; Brunstein, E.; Olsen, B. B.; Vilk, G.; Litchfield, D. W.; Issinger, O.-G.; Niefind, K. Interaction between CK2α and CK2β, the subunits of protein kinase CK2: Thermodynamic contributions of key residues on the CK2α surface. *Biochemistry* **2011**, *50* (4), 512−522.
(14) Siddiqui-Jain, A.; Drygin, D.; Streiner, N.; Chua, P.; Pierre, F.; O'Brien, S. E.; Bliesath, J.; Omori, M.; Huser, N.; Ho, C.; Proffitt, C.; Schwaebe, M. K.; Ryckman, D. M.; Rice, W. G.; Anderes, K. CX-4945, an orally bioavailable selective inhibitor of protein kinase CK2, inhibits prosurvival and angiogenic signaling and exhibits antitumor efficacy. *Cancer Res.* **2010**, *70* (24), 10288−10298.
(15) Gowda, C.; Sachdev, M.; Muthusami, S.; Kapadia, M.; Petrovic-Dovat, L.; Hartman, M.; Ding, Y.; Song, C.; Payne, J. L.; Tan, B. H.; Dovat, S. Casein kinase II (CK2) as a therapeutic target for hematological malignancies. *Curr. Pharm. Des* **2016**, *23* (1), 95−107.
(16) Pierre, F.; Chua, P. C.; O'Brien, S. E.; Siddiqui-Jain, A.; Bourbon, P.; Haddach, M.; Michaux, J.; Nagasawa, J.; Schwaebe, M. K.; Stefan, E.; Vialettes, A.; Whitten, J. P.; Chen, T. K.; Darjania, L.; Stansfield, R.; Anderes, K.; Bliesath, J.; Drygin, D.; Ho, C.; Omori, M.; Proffitt, C.; Streiner, N.; Trent, K.; Rice, W. G.; Ryckman, D. M. Discovery and SAR of 5-(3-chlorophenylamino)benzo[c][2,6]-naphthyridine-8-carboxylic acid (CX-4945), the first clinical stage inhibitor of protein kinase CK2 for the treatment of cancer. *J. Med. Chem.* **2011**, *54* (2), 635−654.
(17) Battistutta, R.; Cozza, G.; Pierre, F.; Papinutto, E.; Lolli, G.; Sarno, S.; O'Brien, S. E.; Siddiqui-Jain, A.; Haddach, M.; Anderes, K.; Ryckman, D. M.; Meggio, F.; Pinna, L. A. Unprecedented selectivity and structural determinants of a new class of protein kinase CK2 inhibitors in clinical trials for the treatment of cancer. *Biochemistry* **2011**, *50* (39), 8478−8488.
(18) Drewry, D. H.; Annor-Gyamfi, J. K.; Wells, C. I.; Pickett, J. E.; Dederer, V.; Preuss, F.; Mathea, S.; Axtman, A. D. Identification of pyrimidine-based lead compounds for understudied kinases implicated in driving neurodegeneration. *J. Med. Chem.* **2022**, *65* (2), 1313−1328.
(19) Gray, G. K.; McFarland, B. C.; Rowse, A. L.; Gibson, S. A.; Benveniste, E. N. Therapeutic CK2 inhibition attenuates diverse prosurvival signaling cascades and decreases cell viability in human breast cancer cells. *Oncotarget* **2014**, *5* (15), 6484−6496.
(20) Salvi, M.; Borgo, C.; Pinna, L. A.; Ruzzene, M. Targeting CK2 in cancer: a valuable strategy or a waste of time? *Cell Death Discov* **2021**, *7* (1), 325.
(21) Licciardello, M. P.; Workman, P. A New Chemical Probe Challenges the Broad Cancer Essentiality of CK2. *Trends Pharmacol. Sci.* **2021**, *42* (5), 313−315.
(22) Al Quobaili, F.; Montenarh, M. CK2 and the regulation of the carbohydrate metabolism. *Metab., Clin. Exp.* **2012**, *61* (11), 1512−1517.
(23) D'Amore, C.; Moro, E.; Borgo, C.; Itami, K.; Hirota, T.; Pinna, L. A.; Salvi, M. Janus" efficacy of CX-5011: CK2 inhibition and methuosis induction by independent mechanisms. *Biochim Biophys Acta - Mol. Cell Res.* **2020**, *1867* (11), 118807.
(24) D'Amore, C.; Borgo, C.; Sarno, S.; Salvi, M. Role of CK2 inhibitor CX-4945 in anti-cancer combination therapy − potential clinical relevance. *Cell Oncol* **2020**, *43* (6), 1003−1016.
(25) Lertsuwan, J.; Lertsuwan, K.; Sawasdichai, A.; Tasnawijitwong, N.; Lee, K. Y.; Kitchen, P.; Afford, S.; Gaston, K.; Jayaraman, P. S.;

https://doi.org/10.1021/acsmedchemlett.2c00530
ACS Med. Chem. Lett. 2023, 14, 432−441

Satayavivad, J. CX-4945 induces methuosis in cholangiocarcinoma cell lines by a CK2-independent mechanism. *Cancers* **2018**, *10* (9), 283.
(26) Li, Z.; Mbah, N. E.; Overmeyer, J. H.; Sarver, J. G.; George, S.; Trabbic, C. J.; Erhardt, P. W.; Maltese, W. A. The JNK signaling pathway plays a key role in methuosis (non-apoptotic cell death) induced by MOMIPP in glioblastoma. *BMC Cancer* **2019**, *19* (1), 77.
(27) Manni, S.; Carrino, M.; Piazza, F. Role of protein kinases CK1α and CK2 in multiple myeloma: regulation of pivotal survival and stress-managing pathways. *J. Hematol Oncol* **2017**, *10* (1), 157.
(28) Ho, C.; Rice, R.; Drygin, D.; Bliesath, J.; Streiner, N.; Siddiqui-Jain, A.; Proffitt, C.; O'Brien, S.; Anderes, K. CX-4945, a selective and orally bioavailable inhibitor of protein kinase CK2 inhibits PI3K/Akt, JAK-STAT and NF-κB signaling and induces apoptosis in multiple myeloma dells. *Blood* **2010**, *116* (21), 787−787.
(29) Piazza, F. A.; Ruzzene, M.; Gurrieri, C.; Montini, B.; Bonanni, L.; Chioetto, G.; Di Maira, G.; Barbon, F.; Cabrelle, A.; Zambello, R.; Adami, F.; Trentin, L.; Pinna, L. A.; Semenzato, G. Multiple myeloma cell survival relies on high activity of protein kinase CK2. *Blood* **2006**, *108* (5), 1698−1707.
(30) Piazza, F. A.; Gurrieri, C.; Trentin, L.; Semenzato, G. Towards a new age in the treatment of multiple myeloma. *Ann. Hematol* **2007**, *86* (3), 159−172.
(31) Kovar, H.; Jug, G.; Hattinger, C.; Spahn, L.; Aryee, D. N. T.; Ambros, P. F.; Zoubek, A.; Gadner, H. The EWS protein is dispensable for Ewing tumor growth. *Cancer Res.* **2001**, *61* (16), 5992−5997.
(32) Paronetto, M. P. Ewing sarcoma protein: A key player in human cancer. *Int. J. Cell Biol.* **2013**, *2013*, 642853.
(33) Bayrak, O. F.; Aydemir, E.; Gulluoglu, S.; Sahin, F.; Sevli, S.; Yalvac, M. E.; Acar, H.; Ozen, M. The effects of chemotherapeutic agents on differentiated chordoma cells. *J. Neurosurg Spine* **2011**, *15* (6), 620−624.
(34) Xia, M.; Huang, R.; Sakamuru, S.; Alcorta, D.; Cho, M. H.; Lee, D. H.; Park, D. M.; Kelley, M. J.; Sommer, J.; Austin, C. P. Identification of repurposed small molecule drugs for chordoma therapy. *Cancer Biol. Ther* **2013**, *14* (7), 638−647.
(35) Ricci-Vitiani, L.; Runci, D.; D'Alessandris, Q. G.; Cenci, T.; Martini, M.; Bianchi, F.; Maira, G.; Stancato, L.; De Maria, R.; Larocca, L. M.; Pallini, R. Chemotherapy of skull base chordoma tailored on responsiveness of patient-derived tumor cells to rapamycin. *Neoplasia* **2013**, *15* (7), 773−782.
(36) Zanin, S.; Borgo, C.; Girardi, C.; O'Brien, S. E.; Miyata, Y.; Pinna, L. A.; Donella-Deana, A.; Ruzzene, M. Effects of the CK2 inhibitors CX-4945 and CX-5011 on drug-resistant cells. *PLoS One* **2012**, *7* (11), No. e49193.
(37) Siddiqui-Jain, A.; Drygin, D.; Streiner, N.; Chua, P.; Pierre, F.; O'Brien, S. E.; Bliesath, J.; Omori, M.; Huser, N.; Ho, C.; et al. CX-4945, an orally bioavailable selective inhibitor of protein kinase CK2, inhibits prosurvival and angiogenic signaling and exhibits antitumor efficacy. *Cancer Res.* **2010**, *70* (24), 10288−10298.
(38) Kumar, S. K.; Rajkumar, V.; Kyle, R. A.; van Duin, M.; Sonneveld, P.; Mateos, M.-V.; Gay, F.; Anderson, K. C. Multiple myeloma. *Nat. Rev. Dis Primers* **2017**, *3* (1), 17046.

Recommended by ACS

Discovery of *N*-(4-(Aminomethyl)phenyl)-5-methylpyrimidin-2-amine Derivatives as Potent and Selective JAK2 Inhibitors

Yang Tian, Tao Yang, *et al.*
AUGUST 01, 2023
ACS MEDICINAL CHEMISTRY LETTERS
READ

Discovery of 1*H*-Imidazo[4,5-*b*]pyridine Derivatives as Potent and Selective BET Inhibitors for the Management of Neuropathic Pain

Xuetao Chen, Zhengyu Jiang, *et al.*
JUNE 29, 2023
JOURNAL OF MEDICINAL CHEMISTRY
READ

Synthesis and Development of Highly Selective Pyrrolo[2,3-*d*]pyrimidine CSF1R Inhibitors Targeting the Autoinhibited Form

Thomas Ihle Aarhus, Eirik Sundby, *et al.*
MAY 16, 2023
JOURNAL OF MEDICINAL CHEMISTRY
READ

Discovery of Novel *N*-(5-(Pyridin-3-yl)-1*H*-indazol-3-yl)benzamide Derivatives as Potent Cyclin-Dependent Kinase 7 Inhibitors for the Treatment of Autosomal Dominant Po...

Bowen Yang, Tongchao Liu, *et al.*
NOVEMBER 17, 2022
JOURNAL OF MEDICINAL CHEMISTRY
READ

Get More Suggestions >

https://doi.org/10.1021/acsmedchemlett.2c00530
ACS Med. Chem. Lett. 2023, 14, 432−441

frontiers | Frontiers in Molecular Neuroscience

ORIGINAL RESEARCH
published: 14 June 2022
doi: 10.3389/fnmol.2022.824956

Evaluation of a Selective Chemical Probe Validates That CK2 Mediates Neuroinflammation in a Human Induced Pluripotent Stem Cell-Derived Mircroglial Model

Swati Mishra[1,2], Chizuru Kinoshita[1,2], Alison D. Axtman[3] and Jessica E. Young[1,2]**

[1] Department of Laboratory Medicine and Pathology, Seattle, WA, United States, [2] Institute for Stem Cell and Regenerative Medicine, University of Washington, Seattle, WA, United States, [3] Division of Chemical Biology and Medicinal Chemistry, UNC Eshelman School of Pharmacy, University of North Carolina at Chapel Hill, Chapel Hill, NC, United States

OPEN ACCESS

Edited by:
Javier Egea,
Princess University Hospital, Spain

Reviewed by:
Jerome Mertens,
University of Innsbruck, Austria
Mauro Salvi,
University of Padua, Italy
Jun Xu,
Capital Medical University, China

***Correspondence:**
Alison D. Axtman
alison.axtman@unc.edu
Jessica E. Young
jeyoung@uw.edu

Specialty section:
This article was submitted to Brain Disease Mechanisms, a section of the journal Frontiers in Molecular Neuroscience

Received: 29 November 2021
Accepted: 20 May 2022
Published: 14 June 2022

Citation:
Mishra S, Kinoshita C, Axtman AD and Young JE (2022) Evaluation of a Selective Chemical Probe Validates That CK2 Mediates Neuroinflammation in a Human Induced Pluripotent Stem Cell-Derived Mircroglial Model. Front. Mol. Neurosci. 15:824956. doi: 10.3389/fnmol.2022.824956

Novel treatments for neurodegenerative disorders are in high demand. It is imperative that new protein targets be identified to address this need. Characterization and validation of nascent targets can be accomplished very effectively using highly specific and potent chemical probes. Human induced pluripotent stem cells (hiPSCs) provide a relevant platform for testing new compounds in disease relevant cell types. However, many recent studies utilizing this platform have focused on neuronal cells. In this study, we used hiPSC-derived microglia-like cells (MGLs) to perform side-by-side testing of a selective chemical probe, SGC-CK2-1, compared with an advanced clinical candidate, CX-4945, both targeting casein kinase 2 (CK2), one of the first kinases shown to be dysregulated in Alzheimer's disease (AD). CK2 can mediate neuroinflammation in AD, however, its role in microglia, the innate immune cells of the central nervous system (CNS), has not been defined. We analyzed available RNA-seq data to determine the microglial expression of kinases inhibited by SGC-CK2-1 and CX-4945 with a reported role in mediating inflammation in glial cells. As proof-of-concept for using hiPSC-MGLs as a potential screening platform, we used both wild-type (WT) MGLs and MGLs harboring a mutation in presenilin-1 (PSEN1), which is causative for early-onset, familial AD (FAD). We stimulated these MGLs with pro-inflammatory lipopolysaccharides (LPS) derived from *E. coli* and observed strong inhibition of the expression and secretion of proinflammatory cytokines by simultaneous treatment with SGC-CK2-1. A direct comparison shows that SGC-CK2-1 was more effective at suppression of proinflammatory cytokines than CX-4945. Together, these results validate a selective chemical probe, SGC-CK2-1, in human microglia as a tool to reduce neuroinflammation.

Keywords: Alzheimer's disease, hiPSC models, casein kinase 2, neuroinflammation, chemical probe, SGC-CK2-1

INTRODUCTION

Many neurodegenerative disorders that affect aging populations, such as Alzheimer's disease (AD), have few effective treatments (Krahn et al., 2020). AD is characterized by accumulations of amyloid beta (Aβ) peptides in extracellular plaques, intracellular accumulations of hyperphosphorylated tau protein in neurofibrillary tangles (NFTs), synaptic loss, and neuroinflammation. Human induced pluripotent stem cell models have been increasingly utilized to study AD because brain-relevant cell types can be studied *in vitro* and used to profile molecules that may modify these disease phenotypes. Indeed, hiPSC-derived cells have been employed in several screens of small molecules hypothesized to impact AD processes, however, the majority of these experiments have been performed in neuronal cells and largely focused on the effects of compounds on Aβ and tau (Brownjohn et al., 2017; Kondo et al., 2017; van der Kant et al., 2019; Cheng et al., 2021).

One issue to consider when testing small molecules is that most commercially available compounds are suboptimal and have many off-target effects. Therefore, efforts are underway to develop high-quality small molecules to enable interrogation of biological pathways. These molecules, known as chemical probes, need to meet certain criteria relating to on-target potency, selectivity, and cell-based activity (Arrowsmith et al., 2015). Wells et al. (2021) recently developed a chemical probe for the human protein kinase CK2, which has been implicated in the phosphorylation of hundreds of cellular proteins. CK2 is a ubiquitously expressed and evolutionarily conserved pleiotropic serine/threonine kinase that regulates many essential and divergent signaling pathways (Meggio and Pinna, 2003). Previously, the CK2 chemical probe, SGC-CK2-1, outperformed all published inhibitors in terms of kinome-wide selectivity, demonstrated potent inhibition of CK2, and proved active in cells, making it a strong candidate for further studies investigating disease-specific pathways (Wells et al., 2021).

Recent evidence supports that CK2 plays essential functions in the mammalian brain (Perez et al., 2011; Castello et al., 2017; Borgo et al., 2021). Research in this area has been partially motivated by the finding that expression of CK2 is much greater in the mammalian brain when compared to other tissues (Blanquet, 2000; Castello et al., 2017). As such, CK2 has been characterized as an emerging target for neurological, psychiatric, and neurodegenerative diseases (Perez et al., 2011; Castello et al., 2017; Borgo et al., 2021). CK2 was one of the first kinases shown to be aberrant in AD (Iimoto et al., 1990). Additional recent studies have supported this finding and shown that CK2 regulates pathways involved in protein aggregation and neuroinflammation. For example, tau protein is a substrate of CK2 and hyperphosphorylation of tau by CK2 has been suggested to contribute to its resultant accumulation in NFTs (Avila et al., 1994; Rosenberger et al., 2016; Zhang et al., 2018).

In addition to the canonical pathological hallmarks of senile plaques and NFTs, neuroinflammation is apparent in AD pathology and is mediated largely through microglia, the innate immune cells of the central nervous system (Wyss-Coray and Rogers, 2012). When microglia are activated in AD they can release pro-inflammatory cytokines, such as IL-6 and IL-1β, which can exacerbate other pathologies (Hansen et al., 2018). In late stages of AD, chronic inflammation induced by microglia contributes to progressive neuronal cell death (Ransohoff and El Khoury, 2015). Dampening this chronic inflammatory response holds great potential as a disease modifying therapy for AD. CK2 may play a role in AD-specific neuroinflammation based on the findings that CK2 immunoreactive astrocytes are increased in AD vs. non-demented controls and they surround Aβ deposits (Rosenberger et al., 2016). However, little is known about how inhibiting CK2 affects microglia-mediated pathways of neuroinflammation.

Due to the role of microglia in mediating AD-related neuroinflammation and potential function of CK2 inhibition in curbing chronic neuroinflammation, we mined the current literature and publicly available RNA-seq databases to analyze neuroinflammatory-related kinases in microglia that can be inhibited by two CK2 inhibitors: SGC-CK2-1 and commercially available inhibitor, CX4945. Based on the divergent inhibitory profiles of these two compounds, we hypothesized that the selective chemical probe SGC-CK2-1 may represent a tool that can be used to specifically explore the modulation of CK2-dependent expression of proinflammatory cytokines induced in human microglia by treatment with LPS. Literature reports also suggested that inhibition of CK2 *via* SGC-CK2-1 would reduce expression of cytokine release in LPS-stimulated human microglia. hiPSC-derived MGLs respond strongly to LPS treatment and LPS was found to induce CK2 activity in murine macrophage cells (Lodie et al., 1997; Abud et al., 2017). To test our hypothesis, we differentiated MGLs from an hiPSC line engineered to harbor two copies of a penetrant FAD mutation in PSEN1, PS1ΔE9, and its isogenic WT control cell line (Woodruff et al., 2013). These cell lines have previously been shown to have gene dose-dependent effects of the ΔE9 mutation in hiPSC-derived neurons (Woodruff et al., 2013). We investigated the effect of SGC-CK2-1 vs. CX-4945 on pro-inflammatory cytokine expression in LPS-stimulated human microglia derived from hiPSCs. We examined mRNA and protein for IL-6 and IL1-β, two pro-inflammatory cytokines that are increased in AD patients and, when increased, correlate with cognitive impairments associated with AD (Forlenza et al., 2009; Huang and Sheng, 2010; Swardfager et al., 2010; Brosseron et al., 2014; Scarabino et al., 2020; Lyra et al., 2021).

MATERIALS AND METHODS

Cell Lines

An hiPSC cell line homozygous for the point mutation in the PSEN1 gene known to cause FAD, "ΔE9/ΔE9", and its isogenic control hiPSC cell line "WT/WT," were generated as described previously (Woodruff et al., 2013).

Differentiation of Human Induced Pluripotent Stem Cells Into Microglia Like Cells

WT/WT and ΔE9/ΔE9 hiPSCs were differentiated into MGLs using a previously described protocol (McQuade et al., 2018). Briefly, hiPSCs were differentiated into hematopoietic progenitor cells (HPCs) using the STEMdiff™ Hematopoietic Kit (#05310, Stem cell Technologies). HPCs were either frozen using Bambanker HRM freezing media (#BBH01; Bulldog Bio) or further differentiated into MGLs. HPCs were cultured in microglia differentiation medium comprised of DMEM/F12 (#11039047; Thermo Fisher Scientific), B27 (#17504-044; Thermo Fisher Scientific), N2 (#17502-048; Thermo Fisher Scientific), insulin-transferrin-selenite (#41400045; Thermo Fisher Scientific), non-essential amino acids (#11140050; Thermo Fisher Scientific), Glutamax (#35050061; Thermo Fisher Scientific), human insulin (#I2643-25 mg; Sigma) and monothioglycerol (#M1753; Sigma) supplemented with 25 ng/ml human M-CSF (#PHC9501; Thermo Fisher Scientific), 50 ng/ml TGF-β1 (#130-108-969; Miltenyl), and 100 ng/ml IL-34 (#200-34; Peprotech). After 24 days in this medium, two additional cytokines, 100 ng/ml CD200 (#C311; NovoProtein), and 100 ng/ml CX3CL1 (#300-31; PeproTech), were added to the medium described above to mature MGLs. MGLs were cultured in this new medium for an additional week and then harvested for experiments.

Drug Treatments

MGLs generated from WT/WT and ΔE9/ΔE9 hiPSCs were plated into a 48-well plate coated with poly-L-lysine (# P6282; Sigma) at a cell density of 200,000 cells/well. After 24 h, MGLs were treated with either DMSO (#D8418; Sigma) or lipopolysaccharides (LPS, 100 ng/ml) (#4391; Sigma) with or without a casein kinase inhibitor, CX-4945 (#A8330; ApexBio Technology; 0.5 μM) or SGC-CK2-1 (Axtman lab; 10 nM), and cultured for 24 h. At the end of 24 h, RNA, protein, and condidtioned medium were harvested from the MGLs.

Toxicity Analysis

MGLs generated from WT hiPSCs were plated as described above. Increasing doses of either SGC-CK2-1 (10–100 μM) or CX-4945 (500–100 μM) were applied to the cells for 24 h. Cell toxicity was analyzed by calculating the percent live cells using Trypan Blue.

Reverse Transcriptase-Polymerase Chain Reaction (RT-PCR)

For mRNA expression analysis, RNA was extracted using Trizol (#15596018; Thermo Fisher Scientific) and first strand cDNA synthesis was performed using the iScript cDNA Synthesis kit (#1708890; Bio-Rad). Quantitative RT-PCR (qRT-PCR) was performed with SYBR Green Master Mix (#A46012; Thermo Fisher Scientific). Results were quantified using the Delta-Delta Ct method (Livak and Schmittgen, 2001). qRT-PCR was performed with the following primers—IL-6 forward primer 5′ TGCAATAACCACCCCTGACC 3′ and reverse primer 5′ TGCGCAGAATGAGATGAGTTG 3′; IL-1β forward primer 5′ TTTGAGTCTGCCCAGTTCCC 3′ and reverse primer 5′ TCAGTTATATCCTGGCCGCC 3′; RPL13 forward primer 5′AGCCTACAAGAAAGTTTGCCTAT 3′ and reverse primer 5′ TCTTCTTCCGGTAGTGGATCTTGGC 3′; CYC1 forward primer 5′ CCTGGAGGAGAAGAGGAAAGAGA 3′ and reverse primer 5′ TTGAGGACCTCTGTGTATTTGTCAA 3′. IL-6 and IL-1β values were normalized to the geometric mean of the housekeeping genes, RPL13 and CYC1. qRT-PCR results were calculated using the $2^{-\Delta\Delta CT}$ method and presented as fold change from DMSO following the procedure described by Rao et al. (2013).

Enzyme-Linked Immunosorbent Assays

To measure IL-6 and IL-1β secretion, ELISAs were performed for both cytokines using manufacturer's instructions (IL-6: ab178013, abcam; IL-1β: ab214025, abcam). Briefly, MGLs were plated onto poly-l-lysine coated 96 well plates, treated with DMSO, LPS, SGC-CK2-1, CX-4945, SGC-CK2-1+LPS and CX-4945+LPS for 24 h and media was harvested at the end of 24 h. Colorimetric assays were performed using ELISA kits described above and optical density was measured using Perkin Elmer/Wallac Envision 2100 Multilabel Reader.

Western Blot Analysis

Western blot analysis was performed under denaturing conditions using 4–15% gradient polyacrylamide gels (Bio-Rad, #4561084). Proteins were electroblotted onto PVDF membrane (Bio-Rad, #1620177), fixed with 0.4% paraformaldehyde for 30 min and blocked in a blocking buffer containing 5% nonfat dry milk before incubating at 4°C overnight with primary antibody [AKT (pan) (40D4) antibody, Cell Signaling #2920, 1:1,000 dilution, AKT1 (phospho S129) antibody (EPR6150), abcam #133458, 1:1,000 dilution = 1.8 μg/ml] and β-actin (clone AC-15) (Millipore Sigma A5441), 1:7,500 dilution, diluted in 5% bovine serum albumin and 0.2% NaN_3. Membranes were washed in phosphate-buffered saline with 0.05% Tween 20 (PBST) and incubated with appropriate horseradish peroxidase-conjugated secondary antibody (1:7500; GE Healthcare, #NA931V, #NA934V) diluted in the blocking buffer. After rinses with PBST, membranes were developed with Clarity Max ECL Western Blotting Substrate (Bio-Rad, #1705062) and exposed to CL-XPosure Film (Thermo Fisher Scientific, #34091). Quantification of Western blots was performed using ImageJ software.

Statistical Analysis

For all experiments presented in the study, each cell line was differentiated three times and the data represents three biological replicates with 2–3 technical replicates per experiment.

Data points were analyzed for normal distributions and either a one-way ANOVA analysis or a paired *t*-test was performed using GraphPad Prism. Error bars indicate Standard Deviations.

A

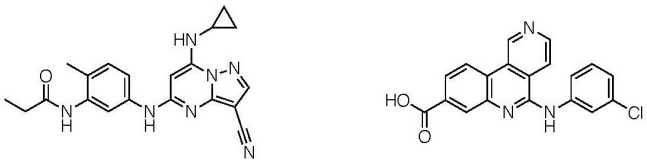

SGC-CK2-1 CX-4945

B

Compound	CK2α PoC at 1 μM	CK2α' PoC at 1 μM	CK2α cellular IC_{50} (nM)	CK2α' cellular IC_{50} (nM)	S_{10} (1 μM)	S_{35} (1 μM)
SGC-CK2-1	0.5	0	36	16	0.007	0.02
CX-4945	0	0.5	340	45	0.069	0.15

FIGURE 1 | Summary of CK2 inhibitor data. **(A)** Structures of SGC-CK2-1 and CX-4945. **(B)** Table of published kinome-wide selectivity scores (S_{10} and S_{35}), CK2α and CK20' binding assay data (PoC at 1 μM), and CK2α and CK2α' cellular target engagement (NanoBRET) IC_{50} values for SGC-CK2-1 and CX-4945.

RESULTS

Selection of Casein Kinase 2 Inhibitors and Dosing Based Upon Published Data

Two CK2 inhibitors (**Figure 1**) were chosen for study based upon literature reports detailing their potent inhibition of this enzyme. These two inhibitors, however, are quite different when considering their potency and kinome-wide selectivity. CX-4945, one of the most employed CK2 inhibitors in published studies and an advanced agent in clinical trials, demonstrates sub-optimal kinome-wide selectivity, significantly inhibiting several kinases with IC_{50} values < 100 nM (Pierre et al., 2011; Wells et al., 2021). The table in **Figure 1B** summarizes the published potency and selectivity data associated with CX-4945 vs. recently disclosed CK2 chemical probe, SGC-CK2-1 (Wells et al., 2021). For reference, the S_{10}(1 μM) selectivity scores reported in **Figure 1B** were calculated by dividing the number of WT human kinases that exhibit percent of control (PoC) < 10 by the total number of WT human kinases that exhibit > 90% inhibition by the total number of WT human kinases after dosing with 1 μM of the given inhibitor and profiling in the DiscoverX *scan*MAX panel. In the same manner, an S_{35}(1 μM) score is representative of the percentage of WT human kinases with PoC < 35 after dosing with 1 μM of the given inhibitor and profiling in the DiscoverX *scan*MAX panel. Accordingly, lower S_{10}(1 μM) or S_{35}(1 μM) values indicate high compound selectivity (Bosc et al., 2017). PoC values reported for various kinases in **Figures 1**–**3** and **Supplementary Table 1** were generated *via* screening at 1 μM in the DiscoverX *scan*MAX panel (Wells et al., 2021). Lower PoC values are indicative of more efficacious binding of the inhibitor to that particular kinase. Doses of CX-4945 and SGC-CK2-1 were selected based on the data in **Figure 1**, considering both the CK2 cellular IC_{50} values as well as the kinome-wide selectivity at 1 μM (**Figures 1**–**3**). In addition, the dosing window used in a previous study that explored the impact of treatment with CX-4945 on cytokine secretion in astrocytes was considered (Rosenberger et al., 2016). Doses above and below the CK2 cellular IC_{50} values for SGC-CK2-1 were probed, offering the ability to inhibit only CK2 and no other kinases. As previously discussed, the kinase next most potently inhibited by SGC-CK2-1 is DYRK2, which has a cellular IC_{50} value = 3,700 nM when evaluated using the same assay format (Wells et al., 2021). Doses of CX-4945 were selected to remain near or below the 1 μM concentration at which the kinome-wide selectivity was profiled, knowing that CK2 would be potently inhibited given the cellular IC_{50} values for this compound. Inhibition of downstream signaling of CK2 in cells has been reported when using our selected doses of each inhibitor (Siddiqui-Jain et al., 2010; Wells et al., 2021).

Summary of Kinases Inhibited by SGC-CK2-1 Implicated in Neuroinflammation

As kinases are known to regulate many signaling pathways and play divergent roles, each kinase inhibited within the S_{35}(1 μM) fraction by CK2 compounds in **Figure 1** was explored in more detail. The table in **Figure 2A** shows all kinases with PoC ≤ 35 in the DiscoverX *scan*MAX panel when SGC-CK2-1 was dosed at 1 μM (Wells et al., 2021). Enzymatic follow-up, carried out at the K_m = ATP for each respective kinase, identified 3 kinases as false positives: DRAK1, PLK4, and MEK5 (Wells et al., 2021). These kinases were not considered further since it was likely that they were artifacts of the binding assay and not inhibited by SGC-CK2-1 (indicated with N/A in **Figure 2A**). To determine the relevance of using hiPSC-derived microglia to test this selective probe, we analyzed RNA-seq data from microglia-like cells generated in monoculture from hiPSCs (GEO accession GSE159108) (Reich et al., 2020). We considered the expression of these S_{35} kinases and expression was categorized as low: (L, < 2,000), medium (M, 2,000–9999), or high (H, > 10,000) based on the bulk RNA-seq values, which were averaged across 5 independent samples. A literature survey was then employed to determine whether a role in neuroinflammation for each of these kinases has been described specifically in glial cells, citing the PubMed source of the data in the table as well. All nine S_{35} kinases were then plotted on a kinome tree (**Figure 2B**). The data in **Figure 2** supports that expression of all kinases

A

Kinase	PoC at 1 μM	Enzymatic IC_{50} (nM)	Expressed in iPSC-derived microglia[1] (PubMed 33613545)	Implicated in neuroinflammation in glia cells	PubMed ID
CSNK2A2	0	2.3	L	Y	26732432
DRAK1	0	>10000	N/A	N/A	N/A
CSNK2A1	0.5	4.2	M	Y	26732432
DYRK2	14	440	M	Y	29155197
PLK4	23	>10000	N/A	N/A	N/A
HIPK2	26	3400	M	N	N/A
MEK5	28	0%I at 1 μM	N/A	N/A	N/A
HIPK1	32	3700	M	N	N/A
HIPK3	34	8100	M	N	N/A

[1]RNA expression; M: medium (2000–9999); L: low (<2000)

B

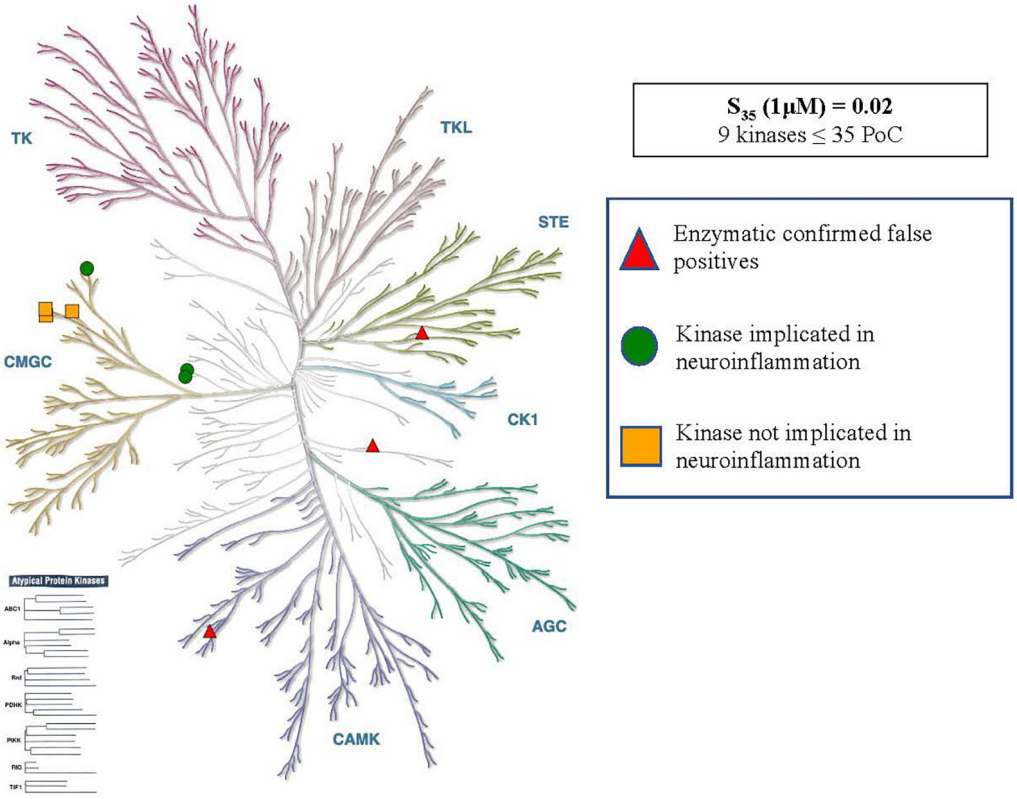

FIGURE 2 | Kinases inhibited by SGC-CK2-1 implicated in neuroinflammation. **(A)** Table of S_{35} kinases, corresponding enzymatic follow-up, expression of inhibited kinases (minus confirmed false positives) in microglia, and reported connections to neuroinflammation in glial cells. **(B)** Visual representation of the distribution of S_{35} kinases around the kinome tree. [1]RNA expression; M, medium (2,000–9,999); L, low (<2,000).

inhibited by SGC-CK2-1 is low to medium in WT hiPSC-derived microglia.

Summary of Kinases Inhibited by CX-4945 Implicated in Neuroinflammation

When considering the inhibitor CX-4945, the situation becomes much more complex. The table in **Figure 3A** shows all WT kinases with PoC < 5 in the DiscoverX *scan*MAX panel when CX-4945 was dosed at 1 μM (Wells et al., 2021). This represents the fraction of kinases most potently inhibited by CX-4945. All 59 WT, non-mutant kinases with PoC ≤ 35 are included in **Supplementary Table 1**. Given the number of kinases with PoC ≤ 35, enzymatic follow-up has not been carried out to confirm or refute inhibition of any of these kinases by CX-4945. Orthogonal profiling in other CX-4945 publications offers validation of inhibition of CLK1–CLK3, DAPK3, DYRK1A, DYRK1B, HIPK3, PIM1, and TBK1 (Pierre et al., 2011; Kim et al., 2014, 2016). The same RNAseq data from hiPSC-derived

A

Kinase	PoC at 1 μM	Expressed in iPSC-derived microglia[1] (PubMed 33613545)	Implicated in neuroinflammation in glia cells	PubMed ID
CSNK2A1	0	M	Y	26732432
DYRK1B	0	L	Y	29751999
HIPK2	0	M	N	N/A
DYRK1A	0.1	M	Y	29850989, 32896600
HIPK1	0.3	M	N	N/A
CSNK2A2	0.5	L	Y	26732432
ERK8	0.9	L	N	N/A
HIPK3	1	M	N	N/A
DRAK2	1.1	L	N	N/A
JAK3(JH1domain-catalytic)	1.5	L	N	N/A
GRK7	1.6	L	N	N/A
CLK1	1.7	M	N	N/A
DAPK3	1.8	L	N	N/A
ULK2	2.2	L	N	N/A
DAPK2	2.7	L	N	N/A
DAPK1	2.8	H	Y	29967321
CDK7	2.9	L	N	N/A
CLK4	2.9	L	N	N/A
GRK3	3.9	M	N	N/A
NEK10	3.9	L	N	N/A

[1]RNA expression; H: high (>10000); M: medium (2000–9999); L: low (<2000)

B

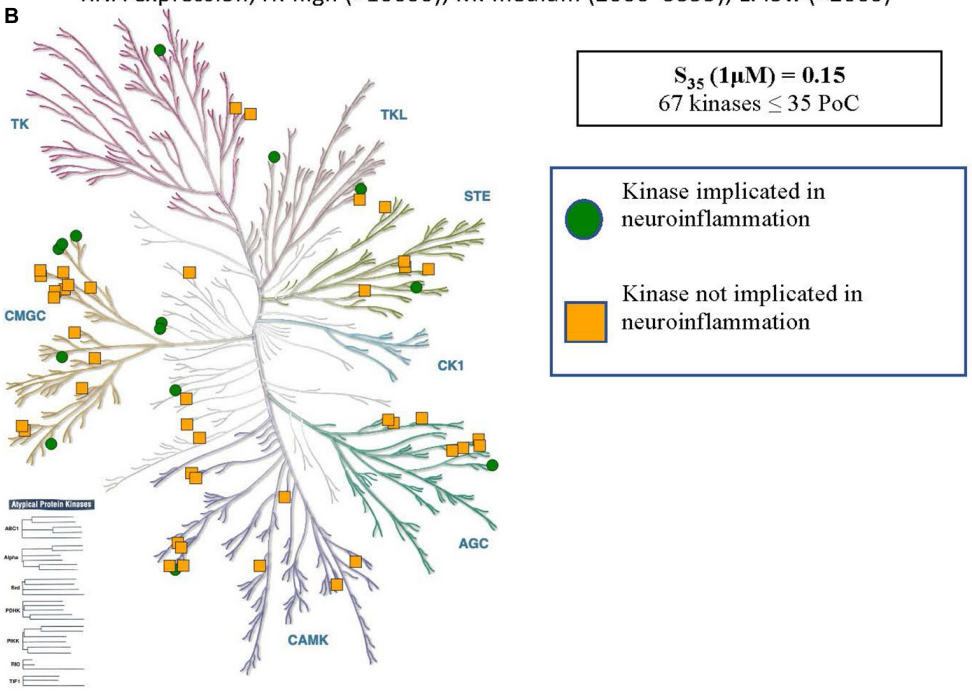

FIGURE 3 | Kinases inhibited by CX-4945 implicated in neuroinflammation. **(A)** Table of S_{35} kinases with PoC < 5, expression of inhibited kinases in microglia, and reported connections to neuroinflammation in glial cells. **(B)** Visual representation of the distribution of all S_{35} kinases around the kinome tree. [1]RNA expression; H, high (>10,000); M, medium (2,000–9,999); L, low (<2,000).

microglia-like cells that were generated in monoculture from GEO accession GSE159108 (Reich et al., 2020) was next consulted to categorize the expression of the 59 WT S_{35} kinases as low (L), medium (M), or high (H) as defined in the previous section. Published connections of these kinases to glia-mediated neuroinflammation and relevant references were also noted

in **Figure 3A** and **Supplementary Table 1**. The tree diagram in **Figure 3B** excludes three lipid kinases and RSK1 (two domains listed in **Supplementary Table 1**) has only been plotted once, showing the distribution of the remaining 56 S_{35} kinases for CX-4945.

Low Nanomolar Doses of SGC-CK2-1 Blunt an Inflammatory Response in Human Induced Pluripotent Stem Cells-Derived Microglial Like Cells Without Associated Toxicity and Suppress Inflammatory Cytokine Expression More Efficiently Than CX-4945

We directly tested whether SGC-CK2-1 could inhibit an inflammatory response more efficiently than CX-4945 using hiPSC-derived MGLs stimulated with LPS. In these experiments we differentiated WT hiPSCs or hiPSCs engineered to harbor two copies of a FAD mutation in PSEN1, PS1ΔE9/ΔE9, into MGLs using published protocols (McQuade et al., 2018). The aim of these experiments was not to draw conclusion about the genetic background of the cells, but to perform a proof-of-concept experiment showing that either WT or AD related cells respond to this type of treatment, which is important for future small molecule screens.

First, we characterized MGLs derived from both of these cell lines and noted no differences in microglial markers in these cells either under baseline or stimulated conditions (**Figures 4A–H**), although the morphology of the cells in both cell lines was altered when treated with LPS (**Figures 4B,F**). Next, we performed a dose-response experiment in WT MGLs and found that SGC-CK2-1 was toxic at concentrations higher than 1 μM (**Supplementary Figure 1A**). Treatment of WT MGLs with LPS significantly induced mRNA expression of pro-inflammatory cytokine genes IL-6 and IL1-β and this expression was significantly reduced at both the 10 and 100 nM concentrations of SGC-CK2-1 (**Supplementary Figure 1B**). Recent literature (D'Amore et al., 2020) suggested an optimal concentration of CX-4945 at 500 nM. This concentration was also not toxic to hiPSC-MGLs, although toxicity was observed at concentrations greater than 1 μM for this compound (**Supplementary Figure 1C**). To confirm that 10 nM SGC-CK2-1 was effectively inhibiting kinase activity in MGLs, we analyzed phosphorylated AKT (Ser 129), a validated substrate of CK2 (Di Maira et al., 2005). We confirmed that CK2 is inhibited by documenting a 50% reduction in a phosphorylated AKT (Ser 129), as compared to total AKT, in microglia cultures treated with 10 nM SGC-CK2-1 (**Supplementary Figure 1D**).

We next wanted to directly compare the efficacy of SGC-CK2-1 with CX-4945. We performed three independent differentiations of both WT and PS1ΔE9/ΔE9 hiPSC to MGLs, stimulated with LPS and treated with 10 nM SGC-CK2-1 (selected based on results in **Supplementary Figures 1A,B**) or 500 nM of CX-4945, which did not show detectable cytotoxicity (**Supplementary Figure 1C**). In both WT and PS1ΔE9/ΔE9 MGLs we observed a significant induction of mRNA expression of IL-6 and IL1-β after LPS treatment (**Figure 5**). In both cell lines, SCG-CK2-1 blunted mRNA induction of these cytokines significantly more than CX-4945. Interestingly, with CX-4945 treatment, mRNA expression of IL1-β in PS1ΔE9/ΔE9 MGLs was not significantly reduced (**Figure 5D**). These results were consistent across the three independent differentiations for each cell line. Since the 50-fold higher dose of CX-4945 could not recapitulate the result observed with 10 nM of SGC-CK2-1, responses to lower concentrations of CX-4945 were not explored. We next analyzed the release of IL-6 and IL-1β by PS1ΔE9/ΔE9 MGLs into the culture medium using an ELISA assay. A significant increase in cytokine protein released into the culture medium in MGLs treated with LPS (**Figures 6A–D**). This increase is ameliorated by treatment with the inhibitors and the reduction by SGC-CK2-1 is more significant than with the commercial molecule CX-4945 (**Figures 6A–D**). Interestingly, at the protein level, we noticed a significant reduction of secreted IL-6 and IL-β in both WT and PS1ΔE9/ΔE9 MGLs, which is somewhat discordant with our mRNA results. However, the timing of mRNA induction and subsequent protein translation, secretion, and/or turn-over is known to vary and to not always be correlative (Liu et al., 2016; Moritz et al., 2019). Thus, it is important to explore orthogonal measurements of both gene and protein expression.

DISCUSSION

Alzheimer's disease is a complex neurodegenerative disorder. The failure of most clinical trials targeting Aβ in AD suggests that it is imperative to look at other pathways in the central nervous system that drive neurodegeneration. One challenge for AD, and other age-related neurodegenerative disorders, is that relevant tissue only becomes available at the end stage of a long and progressive disease. hiPSC models can help to mitigate this challenge as living, relevant human cell types can be generated *in vitro* and recapitulate the genetics and cellular phenotypes of the disorder (Penney et al., 2020). hiPSC-derived cells are emerging as powerful pre-clinical models because potential therapeutics can be screened in human cell types and in a high-throughput manner. Recent studies have used hiPSC-derived neural cells to look at small molecules that modulate Aβ, tau, and synaptic activity (Trudler et al., 2021). However, many of these studies focus on neuron-specific read-outs. Here, we employ hiPSC-derived MGLs to test a specific chemical probe that targets the protein kinase CK2 and look at proinflammatory cytokine expression as a read-out of microglia-mediated neuroinflammation.

With a collection of more than 300 known substrates, it is not surprising that several inflammatory mediators are phosphorylated by CK2. NF-κB, STAT1, STAT3, CREB, CREM, Sp1, and C/EBP are examples of transcription factors regulated by CK2 with a role in inflammation and associated disorders (Bird et al., 1997; Yamaguchi et al., 1998; Filhol et al., 2004; Singh and Ramji, 2008; Drygin et al., 2011). NF-κB regulation by CK2 has been extensively characterized in epithelial, HeLa, and diploid

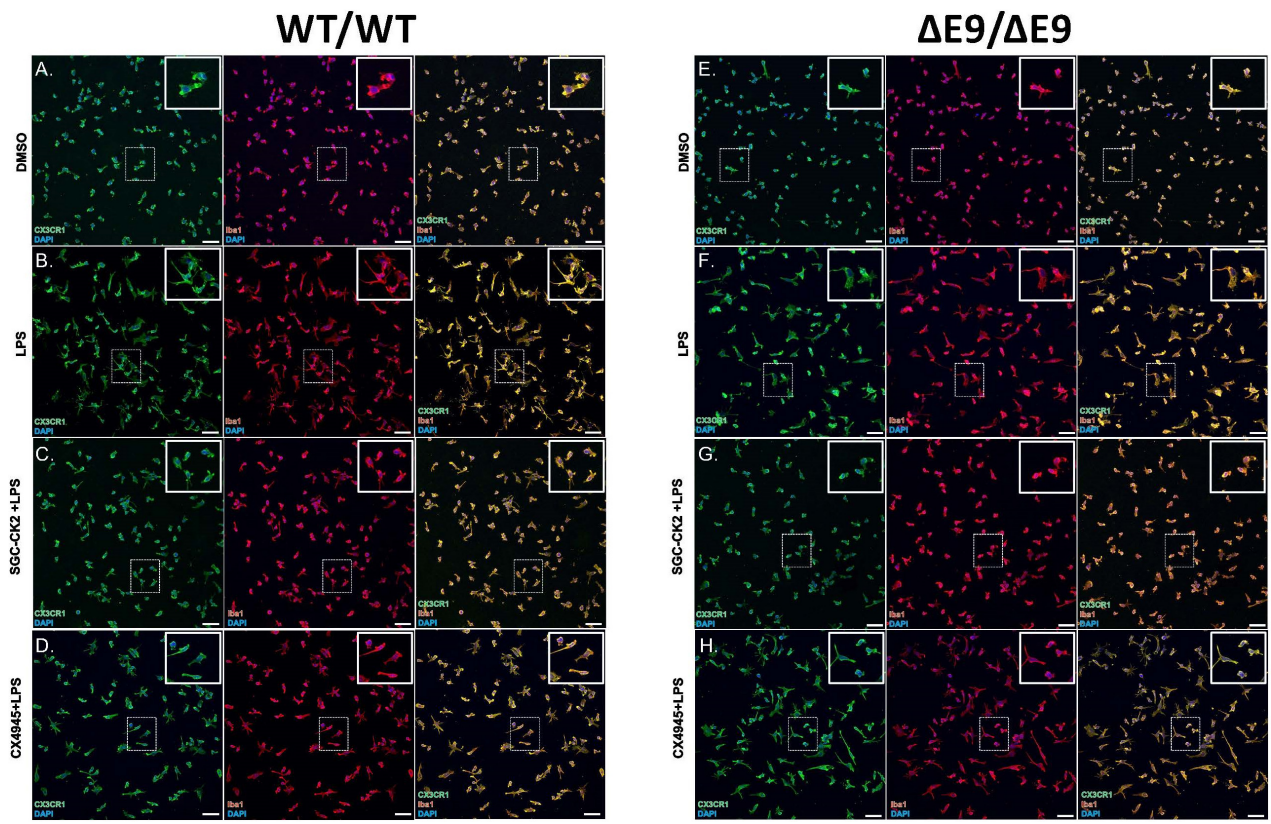

FIGURE 4 | Characterization of DMSO, LPS and drug treated MGLs derived from WT/WT and ΔE9/ΔE9 (FAD) iPSCs. WT **(A–D)** and FAD **(E–H)** MGLs were stimulated with LPS **(B,F)** and simultaneously treated with either SGC-CK2-1 **(C,G)** or CX-4945 **(D,H)** for 24 h and immunocytochemistry was performed. In all conditions, MGLs robustly express microglia specific markers, CX3CR1 and Iba1. Scale bar = 50 μm.

gingival fibroblast cells (Bird et al., 1997; Wang et al., 2000; Parhar et al., 2007; Singh and Ramji, 2008). Furthermore, CK2 activity is stimulated following treatment with proinflammatory agents (LPS) or cytokines (TNF-α, IL-1, TGF-β, or IFN-γ) in a variety of murine and human cell types (Lodie et al., 1997; Rosenberger et al., 2016). These stimuli activate and/or increase the expression of CK2 and/or increase its association with downstream targets or other signaling proteins. Signaling *via* key transcription factors is increased in response, leading to the elevated expression of downstream cytokines and other inflammatory mediators (Singh and Ramji, 2008). The fact that there are multiple CK2 targets that mediate inflammation should increase the efficacy of CK2 inhibitors as anti-inflammatory agents. Unraveling the complex regulation of CK2 signaling and its roles in response to various stimuli that mediate inflammation will be essential if CK2 is to be pursued therapeutically for diseases with an associated inflammatory component, like AD. Also, since CK2 plays a critical role in normal cells, development of targeting strategies that enable specific inhibition of its action in cells responsible for mediating inflammation to drive disease pathology represents an added challenge.

Outside of the brain, CK2 has been shown to contribute to chronic inflammation in non-neuronal cell types including breast cancer, intestinal, renal, immune, and myeloid cells (Yamada et al., 2005; Parhar et al., 2007; Drygin et al., 2011; Koch et al., 2013; Larson et al., 2020). Aberrant CK2 signaling in these cells is associated with inflammatory diseases such as breast cancer, glomerulonephritis, autoimmune encephalomyelitis, atherosclerosis, and T cell lymphoma (Yamaguchi et al., 1998). Additionally, CK2 is known to partially mediate the switch to a more pro-inflammatory state in mouse macrophages (Hagemann et al., 2008; Chen et al., 2017). Inhibition of CK2 decreases secretion of IL-6 in breast cancer cells (Drygin et al., 2011) and mouse macrophages (Glushkova et al., 2018). CK2 is also highly expressed in the brain and CK2 protein levels are reportedly elevated in the AD brain (Rosenberger et al., 2016). Within the AD brain, CK2 localizes to astrocytes associated with cerebral amyloid angiopathy. These astrocytes function during the neuroinflammatory response in AD and CK2 plays a role in this process (Rosenberger et al., 2016). However, whether CK2 mediates a similar inflammatory response in microglia, innate immune cells of the brain derived from a myeloid lineage, is not known.

When considering the narrow kinase inhibition profile of SGC-CK2-1, in addition to CK2, only DYRK2 has an associated neuroinflammatory phenotype described in glial cells (**Figure 2A**). It is worth noting, however, that HIPK family kinases are not very well studied (HIPK1 and HIPK3 are on

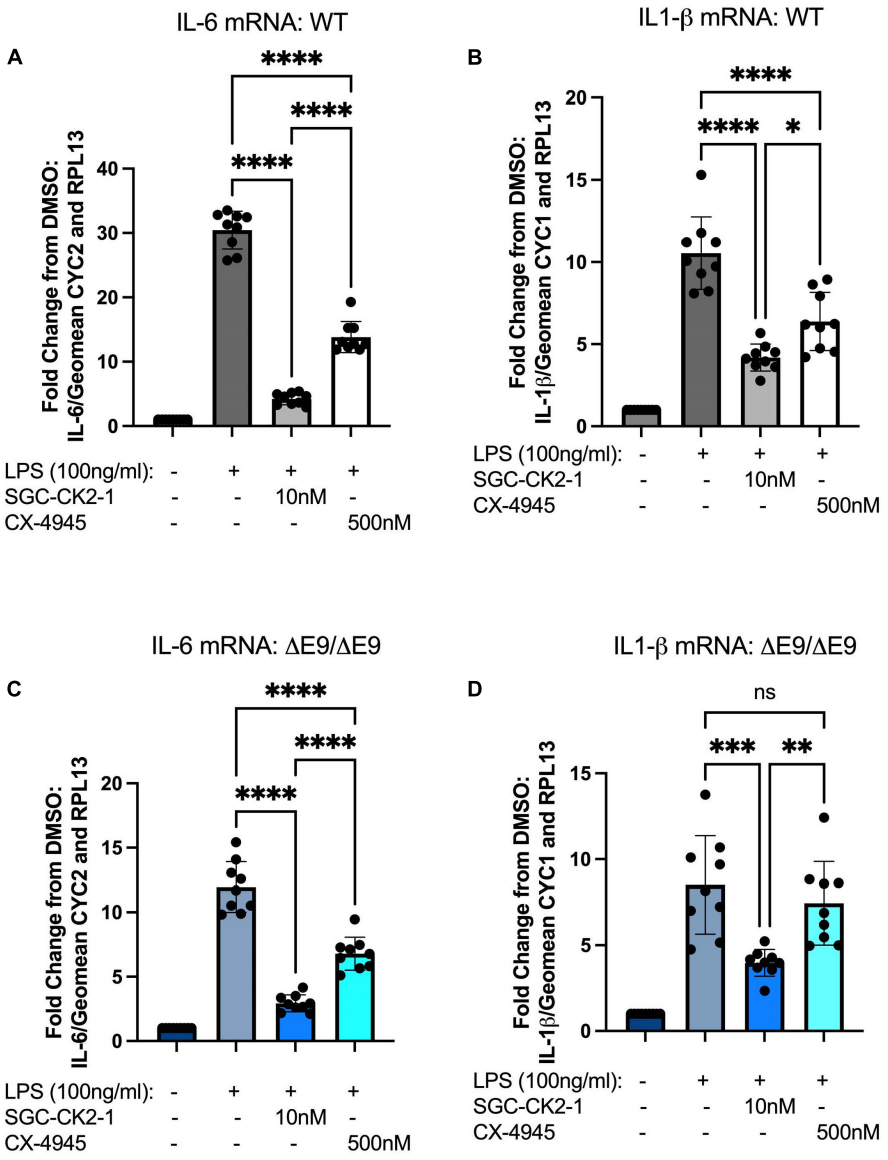

FIGURE 5 | SGC-CK2-1 is more effective at inhibiting mRNA expression of IL-6 and IL1-β in hiPSC-MGLs after LPS stimulation than CX-4945. WT **(A,B)** and FAD **(C,D)** MGLs were stimulated with LPS and simultaneously treated with either SGC-CK2-1 or CX-4945 for 24 h. In all conditions, SGC-CK2-1 was more effective at inhibiting both IL-6 and IL1-β mRNA than CX-4945. These data represent three independent differentiations. ****$p \leq 0.0001$; ***$p = 0.0006$; **$p = 0.0077$; *$p = 0.0293$; ns, not significant by one-way ANOVA analysis. Error bars indicate the mean ± SD.

the NIH-nominated list of understudied kinases defined by the Illuminating the Druggable Genome (IDG) program (Berginski et al., 2020), and it is therefore possible that these kinases could have a role in neuroinflammation that has not yet been characterized. We also acknowledge that pertinent references may have been missed in our literature survey. In terms of CK2- vs. DYRK2-mediated activity, there is a large (100-fold) dosing window that enables inhibition of CK2 without eliciting inhibition of DYRK2 if a proper concentration is selected. Our dose of 10 nM for studies herein was selected to enable inhibition of CK2 without off-target DYRK2 inhibition. The narrow kinome-wide profile of SGC-CK2-1 makes it an ideal candidate molecule to use to interrogate the role of CK2 in neuroinflammation.

With respect to CX-4945, many of the S_{35} kinases with low expression in WT hiPSC-derived microglia correspondingly do not have an associated neuroinflammatory phenotype in glia, while several with medium or high expression have a described role as a mediator of neuroinflammation (**Figure 3A** and **Supplementary Table 1**). This correlation suggests that significant expression of a kinase is one factor that contributes to it having a pronounced role in mediating glial neuroinflammatory processes. As was discussed with respect to the HIPK family and SGC-CK2-1, many kinases inhibited

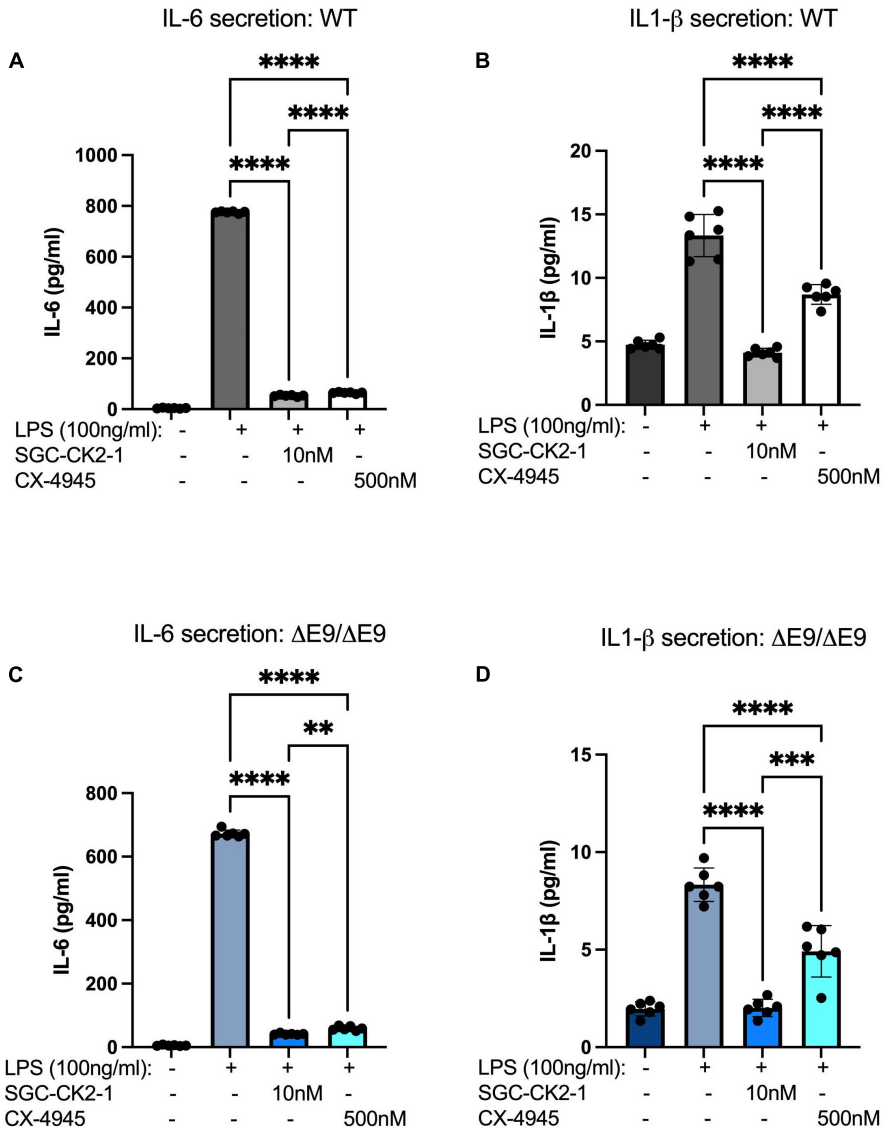

FIGURE 6 | SGC-CK2-1 reduces pro-inflammatory cytokine secretion more effectively than CX-4945. WT **(A,B)** and FAD **(C,D)** MGLs were stimulated with LPS and simultaneously treated with either SGC-CK2-1 or CX-4945 for 24 h. In all conditions, SGC-CK2-1 was more effective at inhibiting both IL-6 and IL1-β cytokine secretion into the culture media than CX-4945. These data represent three independent differentiations. ****$p \leq 0.0001$; ***$p = 0.0006$; **$p = 0.0024$ by one-way ANOVA analysis. Error bars indicate the mean ± SD.

in the S_{35} fraction by CX-4945 are not well studied. In fact, 21 were on the original IDG list of understudied kinases (Berginski et al., 2020). The role of these kinases in mediating neuroinflammation could be delineated if they receive additional attention and high-quality chemical tools are developed to enable their study. As support of this hypothesis, CSNK2A2, CDKL5, DYRK1B, and DYRK2 were the only four IDG kinases on the full list of S_{35} kinases (**Supplementary Table 1**) with an associated neuroinflammatory role described in the literature. In total, thirteen kinases in addition to CK2 that are potently inhibited by CX-4945 have been described as mediators of neuroinflammatory responses in glia. With so many possible off-target kinases responsible for the response observed when treating with CX-4945, one cannot reliably ascribe a phenotype to CK2 when dosing with CX-4945.

Preclinical studies to test small molecules that may be effective against neurodegeneration in AD and other disorders in animal models or transformed cell lines are informative but can miss important human-specific genetics that influence phenotypes and important cell-type specific differences may impact the effects of a particular drug. hiPSCs are a promising model to overcome some of these limitations. hiPSCs are now efficiently differentiated into all cell types of the CNS (Penney et al., 2020) and advances in 3-D modeling using cerebral organoids have enabled using these to test small molecules in a high-throughput manner (Costamagna et al., 2021; Park et al., 2021). However, in

general, many recent studies involving small molecule screening of AD phenotypes using hiPSC models have been performed in neurons (Yahata et al., 2011; Brownjohn et al., 2017; Kondo et al., 2017; van der Kant et al., 2019). Here, we aimed to perform a side-by-side test of a selective and a non-selective kinase inhibitor using hiPSC-derived MGLs and probe a neuroinflammatory response. Our data encompasses both a WT and a familial AD genetic background and shows that the selective inhibitor SGC-CK2-1 efficiently inhibits an LPS-induced inflammatory response in both cell lines with consistent results between independent differentiations. Furthermore, this inhibitor demonstrates a more effective reduction in pro-inflammatory cytokine expression and secretion than CX-4945 (**Figures 5**, **6**). Our study is not powered to directly analyze molecular links between CK2 and PSEN1 mutations. It is certainly plausible that different FAD mutations and genetic variants linked to increased AD risk may modify the inhibitory effects of SGC-CK2-1. However, together our data suggest that this small molecule could be broadly effective across both strongly genetic and sporadic AD cases.

Our study demonstrates the benefits of side-by-side testing of selective vs. non-selective inhibitors in a relevant cell type. Future work that encompasses side-by-side testing in other CNS cell types and assaying for cell-type specific phenotypes (i.e., tau phosphorylation in neurons or cholesterol transport in astrocytes) will certainly be informative. In addition, our study does not have the power to detect intrinsic differences in the inflammatory response based on cell line genotype. Therefore, additional studies aimed at analyzing multiple cell lines with AD mutations or risk variants compared with isogenic wild-type cells will be necessary to understand the biological mechanisms behind the neuroinflammatory response in these cells. Future work can include incorporating humanized cells into mouse models to further test the effects of these compounds in an *in vivo* model.

In general, our work and multiple other studies in the field, have highlighted the utility of hiPSC-derived cells as tools for pre-clinical study *in vitro*, especially related to evaluation of high-quality chemical tools. The hiPSC-derived model is a powerful methodology to simultaneously begin to validate therapeutic hypotheses in a relevant cellular system and identify potential chemical starting points for drug development. Evaluation of chemical probes in hiPSC-derived cellular systems has the potential to illuminate new opportunities for therapeutic intervention for diseases of the CNS and could prove to be transformative.

CONCLUSION

Our study has certain limitations. First, we have performed this as proof-of-concept and used only one cell line that is representative of an autosomal dominant AD background and one cell line that is representative of a wild-type background. The goal of our experiments was to directly test a chemical probe vs. a commercial inhibitor. There are many future studies needed to understand how CK2 inhibition may impact the full range of pathologies present in AD. However, in this work, we show that SGC-CK2-1 is a potent suppressor of the CK2-mediated neuroinflammatory response and outperforms CX-4945 in inhibiting the expression of the proinflammatory cytokines IL-6 and IL-1β. These results could partially be explained by previous work showing that SGC-CK2-1 is both more potent and more selective for CK2 than CX-4945 when tested in cancer cell lines, but also provide new data underscoring the power associated with profiling selective probes in an AD-relevant cell type and model.

DATA AVAILABILITY STATEMENT

The original contributions presented in this study are included in the article/**Supplementary Material**, further inquiries can be directed to the corresponding author/s.

AUTHOR CONTRIBUTIONS

SM, ADA, and JY conceived to the project and contributed to the writing and editing of the manuscript. ADA performed the DiscoverX *scan*MAX analysis, analysis of bulk-RNAseq, and generated the kinome trees *via* KinMap (Eid et al., 2017). SM and CK performed all hiPSC-MGLs experiments. SM and JY analyzed the hiPSC-MGLs experiments. All authors contributed to the article and approved the submitted version.

FUNDING

Research reported in this publication was supported in part by Department of Defense grant AL190107 and NIH grants U24DK116204 and U54AG065187 to ADA. JY is funded by grants from the NIH: R01AG062148, K01AG059841, and U54AG065187.

SUPPLEMENTARY MATERIAL

The Supplementary Material for this article can be found online at: https://www.frontiersin.org/articles/10.3389/fnmol.2022.824956/full#supplementary-material

REFERENCES

Abud, E. M., Ramirez, R. N., Martinez, E. S., Healy, L. M., Nguyen, C. H. H., Newman, S. A., et al. (2017). iPSC-derived human microglia-like cells to study neurological diseases. *Neuron* 94, 278–293 e9. doi: 10.1016/j.neuron.2017.03.042

Arrowsmith, C. H., Audia, J. E., Austin, C., Baell, J., Bennett, J., Blagg, J., et al. (2015). The promise and peril of chemical probes. *Nat. Chem. Biol.* 11, 536–541.

Avila, J., Ulloa, L., González, J., Moreno, F., and Díaz-Nido, J. (1994). Phosphorylation of microtubule-associated proteins by protein kinase CK2 in neuritogenesis. *Cell Mol. Biol. Res.* 40, 573–579.

Berginski, M. E., Moret, N., Liu, C., Goldfarb, D., Sorger, P. K., and Gomez, S. M. (2020). The Dark Kinase Knowledgebase: an online compendium of knowledge and experimental results of understudied kinases. *Nucleic Acids Res.* 49, D529–D535. doi: 10.1093/nar/gkaa853

Bird, T. A., Schooley, K., Dower, S. K., Hagen, H., and Virca, G. D. (1997). Activation of nuclear transcription factor NF-kappaB by interleukin-1 is accompanied by casein kinase II-mediated phosphorylation of the p65 subunit. *J. Biol. Chem.* 272, 32606–32612. doi: 10.1074/jbc.272.51.32606

Blanquet, P. R. (2000). Casein kinase 2 as a potentially important enzyme in the nervous system. *Prog. Neurobiol.* 60, 211–246. doi: 10.1016/s0301-0082(99)00026-x

Borgo, C., D'Amore, C., Sarno, S., Salvi, M., and Ruzzene, M. (2021). Protein kinase CK2: a potential therapeutic target for diverse human diseases. *Signal Transduct. Target. Ther.* 6:183. doi: 10.1038/s41392-021-00567-7

Bosc, N., Meyer, C., and Bonnet, P. (2017). The use of novel selectivity metrics in kinase research. *BMC Bioinformatics* 18:17. doi: 10.1186/s12859-016-1413-y

Brosseron, F., Krauthausen, M., Kummer, M., and Heneka, M. T. (2014). Body fluid cytokine levels in mild cognitive impairment and Alzheimer's disease: a comparative overview. *Mol. Neurobiol.* 50, 534–544. doi: 10.1007/s12035-014-8657-1

Brownjohn, P. W., Smith, J., Portelius, E., Serneels, L., Kvartsberg, H., De Strooper, B., et al. (2017). Phenotypic screening identifies modulators of amyloid precursor protein processing in human stem cell models of Alzheimer's disease. *Stem Cell Rep.* 8, 870–882. doi: 10.1016/j.stemcr.2017.02.006

Castello, J., Ragnauth, A., Friedman, E., and Rebholz, H. (2017). CK2—an emerging target for neurological and psychiatric disorders. *Pharmaceuticals* 10:7. doi: 10.3390/ph10010007

Chen, Y., Liu, W., Wang, Y., Zhang, L., Wei, J., Zhang, X., et al. (2017). Casein kinase 2 interacting protein-1 regulates M1 and M2 inflammatory macrophage polarization. *Cell Signal* 33, 107–121. doi: 10.1016/j.cellsig.2017.02.015

Cheng, C., Reis, S. A., Adams, E. T., Fass, D. M., Angus, S. P., Stuhlmiller, T. J., et al. (2021). High-content image-based analysis and proteomic profiling identifies Tau phosphorylation inhibitors in a human iPSC-derived glutamatergic neuronal model of tauopathy. *Sci. Rep.* 11:17029. doi: 10.1038/s41598-021-96227-5

Costamagna, G., Comi, G. P., and Corti, S. (2021). Advancing drug discovery for neurological disorders using iPSC-derived neural organoids. *Int. J. Mol. Sci.* 22:2659. doi: 10.3390/ijms22052659

D'Amore, C., Borgo, C., Sarno, S., and Salvi, M. (2020). Role of CK2 inhibitor CX-4945 in anti-cancer combination therapy - potential clinical relevance. *Cell Oncol. (Dordr)* 43, 1003–1016. doi: 10.1007/s13402-020-00566-w

Di Maira, G., Salvi, M., Arrigoni, G., Marin, O., Sarno, S., Brustolon, F., et al. (2005). Protein kinase CK2 phosphorylates and upregulates Akt/PKB. *Cell Death Differ.* 12, 668–677. doi: 10.1038/sj.cdd.4401604

Drygin, D., Ho, C. B., Omori, M., Bliesath, J., Proffitt, C., Rice, R., et al. (2011). Protein kinase CK2 modulates IL-6 expression in inflammatory breast cancer. *Biochem. Biophys. Res. Commun.* 415, 163–167. doi: 10.1016/j.bbrc.2011.10.046

Eid, S., Turk, S., Volkamer, A., Rippmann, F., and Fulle, S. (2017). KinMap: a web-based tool for interactive navigation through human kinome data. *BMC Bioinformatics* 18:16. doi: 10.1186/s12859-016-1433-7

Filhol, O., Martiel, J. L., and Cochet, C. (2004). Protein kinase CK2: a new view of an old molecular complex. *EMBO Rep.* 5, 351–355. doi: 10.1038/sj.embor.7400115

Forlenza, O. V., Diniz, B. S., Talib, L. L., Mendonca, V. A., Ojopi, E. B., Gattaz, W. F., et al. (2009). Increased serum IL-1beta level in Alzheimer's disease and mild cognitive impairment. *Dement. Geriatr. Cogn. Disord.* 28, 507–512. doi: 10.1159/000255051

Glushkova, O. V., Parfenyuk, S. B., Novoselova, T. V., Khrenov, M. O., Lunin, S. M., and Novoselova, E. G. (2018). The role of p38 and CK2 protein kinases in the response of RAW 264.7 macrophages to lipopolysaccharide. *Biochemistry (Mosc)* 83, 746–754. doi: 10.1134/S0006297918060123

Hagemann, T., Lawrence, T., McNeish, I., Charles, K. A., Kulbe, H., Thompson, R. G., et al. (2008). "Re-educating" tumor-associated macrophages by targeting NF-kappaB. *J. Exp. Med.* 205, 1261–1268. doi: 10.1084/jem.20080108

Hansen, D. V., Hanson, J. E., and Sheng, M. (2018). Microglia in Alzheimer's disease. *J. Cell Biol.* 217, 459–472.

Huang, Z. B., and Sheng, G. Q. (2010). Interleukin-1beta with learning and memory. *Neurosci. Bull.* 26, 455–468.

Iimoto, D. S., Masliah, E., DeTeresa, R., Terry, R. D., and Saitoh, T. (1990). Aberrant casein kinase II in Alzheimer's disease. *Brain Res.* 507, 273–280. doi: 10.1016/0006-8993(90)90282-g

Kim, H., Choi, K., Kang, H., Lee, S.-Y., Chi, S.-W., Lee, M.-S., et al. (2014). Identification of a novel function of CX-4945 as a splicing regulator. *PLoS One* 9:e94978. doi: 10.1371/journal.pone.0094978

Kim, H., Lee, K.-S., Kim, A.-K., Choi, M., Choi, K., Kang, M., et al. (2016). A chemical with proven clinical safety rescues Down-syndrome-related phenotypes in through DYRK1A inhibition. *Dis. Model. Mech.* 9, 839–848. doi: 10.1242/dmm.025668

Koch, S., Capaldo, C. T., Hilgarth, R. S., Fournier, B., Parkos, C. A., and Nusrat, A. (2013). Protein kinase CK2 is a critical regulator of epithelial homeostasis in chronic intestinal inflammation. *Mucosal Immunol.* 6, 136–145. doi: 10.1038/mi.2012.57

Kondo, T., Imamura, K., Funayama, M., Tsukita, K., Miyake, M., Ohta, A., et al. (2017). iPSC-based compound screening and in vitro trials identify a synergistic anti-amyloid beta combination for Alzheimer's disease. *Cell Rep.* 21, 2304–2312. doi: 10.1016/j.celrep.2017.10.109

Krahn, A. I., Wells, C., Drewry, D. H., Beitel, L. K., Durcan, T. M., and Axtman, A. D. (2020). Defining the neural kinome: strategies and opportunities for small molecule drug discovery to target neurodegenerative diseases. *ACS Chem. Neurosci.* 11, 1871–1886. doi: 10.1021/acschemneuro.0c00176

Larson, S. R., Bortell, N., Illies, A., Crisler, W. J., Matsuda, J. L., and Lenz, L. L. (2020). Myeloid cell CK2 regulates inflammation and resistance to bacterial infection. *Front. Immunol.* 11:590266. doi: 10.3389/fimmu.2020.590266

Liu, Y., Beyer, A., and Aebersold, R. (2016). On the dependency of cellular protein levels on mRNA abundance. *Cell* 165, 535–550. doi: 10.1016/j.cell.2016.03.014

Livak, K. J., and Schmittgen, T. D. (2001). Analysis of relative gene expression data using real-time quantitative PCR and the $2^{-\Delta\Delta C_T}$ Method. *Methods* 25, 402–408. doi: 10.1006/meth.2001.1262

Lodie, T. A., Savedra, R. Jr., Golenbock, D. T., Van Beveren, C. P., Maki, R. A., and Fenton, M. J. (1997). Stimulation of macrophages by lipopolysaccharide alters the phosphorylation state, conformation, and function of PU.1 via activation of casein kinase II. *J. Immunol. (Baltimore, Md : 1950)* 158, 1848–1856.

Lyra, E. S. N. M., Goncalves, R. A., Pascoal, T. A., Lima-Filho, R. A. S., Resende, E. P. F., Vieira, E. L. M., et al. (2021). Pro-inflammatory interleukin-6 signaling links cognitive impairments and peripheral metabolic alterations in Alzheimer's disease. *Transl. Psychiatry* 11:251. doi: 10.1038/s41398-021-01349-z

McQuade, A., Coburn, M., Tu, C. H., Hasselmann, J., Davtyan, H., and Blurton-Jones, M. (2018). Development and validation of a simplified method to generate human microglia from pluripotent stem cells. *Mol. Neurodegener.* 13:67. doi: 10.1186/s13024-018-0297-x

Meggio, F., and Pinna, L. A. (2003). One-thousand-and-one substrates of protein kinase CK2? *FASEB J.* 17, 349–368. doi: 10.1096/fj.02-0473rev

Moritz, C. P., Muhlhaus, T., Tenzer, S., Schulenborg, T., and Friauf, E. (2019). Poor transcript-protein correlation in the brain: negatively correlating gene products reveal neuronal polarity as a potential cause. *J. Neurochem.* 149, 582–604. doi: 10.1111/jnc.14664

Parhar, K., Morse, J., and Salh, B. (2007). The role of protein kinase CK2 in intestinal epithelial cell inflammatory signaling. *Int. J. Colorectal. Dis.* 22, 601–609. doi: 10.1007/s00384-006-0193-7

Park, J. C., Jang, S. Y., Lee, D., Lee, J., Kang, U., Chang, H., et al. (2021). A logical network-based drug-screening platform for Alzheimer's disease representing pathological features of human brain organoids. *Nat. Commun.* 12:280. doi: 10.1038/s41467-020-20440-5

Penney, J., Ralvenius, W. T., and Tsai, L. H. (2020). Modeling Alzheimer's disease with iPSC-derived brain cells. *Mol. Psychiatry* 25, 148–167. doi: 10.1038/s41380-019-0468-3

Perez, D. I., Gil, C., and Martinez, A. (2011). Protein kinases CK1 and CK2 as new targets for neurodegenerative diseases. *Med. Res. Rev.* 31, 924–954. doi: 10.1002/med.20207

Pierre, F., Chua, P. C., O'Brien, S. E., Siddiqui-Jain, A., Bourbon, P., Haddach, M., et al. (2011). Discovery and SAR of 5-(3-chlorophenylamino)benzo[c][2,6]naphthyridine-8-carboxylic acid (CX-4945),

the first clinical stage inhibitor of protein kinase CK2 for the treatment of cancer. *J. Med. Chem.* 54, 635–654. doi: 10.1021/jm101251q

Ransohoff, R. M., and El Khoury, J. (2015). Microglia in health and disease. *Cold Spring Harb. Perspect. Biol.* 8:a020560.

Rao, X., Huang, X., Zhou, Z., and Lin, X. (2013). An improvement of the 2ˆ(-delta delta CT) method for quantitative real-time polymerase chain reaction data analysis. *Biostat. Bioinform. Biomath.* 3, 71–85.

Reich, M., Paris, I., Ebeling, M., Dahm, N., Schweitzer, C., Reinhardt, D., et al. (2020). Alzheimer's risk gene TREM2 determines functional properties of new type of human iPSC-derived Microglia. *Front. Immunol.* 11:617860. doi: 10.3389/fimmu.2020.617860

Rosenberger, A. F. N., Morrema, T. H. J., Gerritsen, W. H., van Haastert, E. S., Snkhchyan, H., Hilhorst, R., et al. (2016). Increased occurrence of protein kinase CK2 in astrocytes in Alzheimer's disease pathology. *J. Neuroinflamm.* 13:4. doi: 10.1186/s12974-015-0470-x

Scarabino, D., Peconi, M., Broggio, E., Gambina, G., Maggi, E., Armeli, F., et al. (2020). Relationship between proinflammatory cytokines (Il-1beta. Il-18) and leukocyte telomere length in mild cognitive impairment and Alzheimer's disease. *Exp. Gerontol.* 136:110945. doi: 10.1016/j.exger.2020.110945

Siddiqui-Jain, A., Drygin, D., Streiner, N., Chua, P., Pierre, F., O'Brien, S. E., et al. (2010). CX-4945, an orally bioavailable selective inhibitor of protein kinase CK2, inhibits prosurvival and angiogenic signaling and exhibits antitumor efficacy. *Cancer Res.* 70, 10288–10298. doi: 10.1158/0008-5472.CAN-10-1893

Singh, N. N., and Ramji, D. P. (2008). Protein kinase CK2, an important regulator of the inflammatory response? *J. Mol. Med. (Berl)* 86, 887–897. doi: 10.1007/s00109-008-0352-0

Swardfager, W., Lanctot, K., Rothenburg, L., Wong, A., Cappell, J., and Herrmann, N. (2010). A meta-analysis of cytokines in Alzheimer's disease. *Biol. Psychiatry* 68, 930–941.

Trudler, D., Ghatak, S., and Lipton, S. A. (2021). Emerging hiPSC models for drug discovery in neurodegenerative diseases. *Int. J. Mol. Sci.* 22:8196. doi: 10.3390/ijms22158196

van der Kant, R., Langness, V. F., Herrera, C. M., Williams, D. A., Fong, L. K., Leestemaker, Y., et al. (2019). Cholesterol metabolism is a druggable axis that independently regulates tau and amyloid-beta in iPSC-derived Alzheimer's disease neurons. *Cell Stem Cell* 24, 363–375 e9. doi: 10.1016/j.stem.2018.12.013

Wang, D., Westerheide, S. D., Hanson, J. L., and Baldwin, A. S. Jr. (2000). Tumor necrosis factor alpha-induced phosphorylation of RelA/p65 on Ser529 is controlled by casein kinase II. *J. Biol. Chem.* 275, 32592–32597. doi: 10.1074/jbc.M001358200

Wells, C. I., Drewry, D. H., Pickett, J. E., Tjaden, A., Kramer, A., Muller, S., et al. (2021). Development of a potent and selective chemical probe for the pleiotropic kinase CK2. *Cell Chem. Biol.* 28, 546–558 e10. doi: 10.1016/j.chembiol.2020.12.013

Woodruff, G., Young, J. E., Martinez, F. J., Buen, F., Gore, A., Kinaga, J., et al. (2013). The presenilin-1 DeltaE9 mutation results in reduced gamma-secretase activity, but not total loss of PS1 function, in isogenic human stem cells. *Cell Rep.* 5, 974–985. doi: 10.1016/j.celrep.2013.10.018

Wyss-Coray, T., and Rogers, J. (2012). Inflammation in Alzheimer disease-a brief review of the basic science and clinical literature. *Cold Spring Harb. Perspect. Med.* 2:a006346. doi: 10.1101/cshperspect.a006346

Yahata, N., Asai, M., Kitaoka, S., Takahashi, K., Asaka, I., Hioki, H., et al. (2011). Anti-Abeta drug screening platform using human iPS cell-derived neurons for the treatment of Alzheimer's disease. *PLoS One* 6:e25788. doi: 10.1371/journal.pone.0025788

Yamada, M., Katsuma, S., Adachi, T., Hirasawa, A., Shiojima, S., Kadowaki, T., et al. (2005). Inhibition of protein kinase CK2 prevents the progression of glomerulonephritis. *Proc. Natl. Acad. Sci. U.S.A.* 102, 7736–7741. doi: 10.1073/pnas.0409818102

Yamaguchi, Y., Wada, T., Suzuki, F., Takagi, T., Hasegawa, J., and Handa, H. (1998). Casein kinase II interacts with the bZIP domains of several transcription factors. *Nucleic Acids Res.* 26, 3854–3861. doi: 10.1093/nar/26.16.3854

Zhang, Q., Xia, Y., Wang, Y., Shentu, Y., Zeng, K., Mahaman, Y. A. R., et al. (2018). CK2 Phosphorylating I2PP2A/SET mediates tau pathology and cognitive impairment. *Front. Mol. Neurosci.* 11:146. doi: 10.3389/fnmol.2018.00146

Conflict of Interest: The authors declare that the research was conducted in the absence of any commercial or financial relationships that could be construed as a potential conflict of interest.

Publisher's Note: All claims expressed in this article are solely those of the authors and do not necessarily represent those of their affiliated organizations, or those of the publisher, the editors and the reviewers. Any product that may be evaluated in this article, or claim that may be made by its manufacturer, is not guaranteed or endorsed by the publisher.

Copyright © 2022 Mishra, Kinoshita, Axtman and Young. This is an open-access article distributed under the terms of the Creative Commons Attribution License (CC BY). The use, distribution or reproduction in other forums is permitted, provided the original author(s) and the copyright owner(s) are credited and that the original publication in this journal is cited, in accordance with accepted academic practice. No use, distribution or reproduction is permitted which does not comply with these terms.

bioRxiv preprint doi: https://doi.org/10.1101/2023.03.22.533562; this version posted March 24, 2023. The copyright holder for this preprint (which was not certified by peer review) is the author/funder. All rights reserved. No reuse allowed without permission.

Homozygous ALS-linked mutations in TARDBP/TDP-43 lead to progressive synaptic dysfunction in human iPSC-derived motor neurons

Sarah Lépine[1,2], Angela Nauleau-Javaudin[1,3], Eric Deneault[4], Carol X.-Q. Chen[1], Narges Abdian[1], Anna Krystina Franco-Flores[1], Ghazal Haghi[1], María José Castellanos-Montiel[1], Gilles Maussion[1], Mathilde Chaineau[1,*], and Thomas M. Durcan[1,*]

[1]Early Drug Discovery Unit (EDDU), The Neuro-Montreal Neurological Institute and Hospital, Department of Neurology and Neurosurgery, McGill University, Montreal, QC, H3A 1A1, Canada
[2]Faculty of Medicine and Health Sciences, McGill University Montreal, QC, H3G 2M1, Canada
[3]Faculty of Medicine, Université de Montréal, Montreal, QC, H3C 3J7, Canada
[4]Centre for Oncology, Radiopharmaceuticals and Research; Biologic and Radiopharmaceutical Drugs Directorate, Health Products and Food Branch, Health Canada, Ottawa, ON, K1A 0K9, Canada

*Correspondence: thomas.durcan@mcgill.ca; mathilde.chaineau@mcgill.ca

bioRxiv preprint doi: https://doi.org/10.1101/2023.03.22.533562; this version posted March 24, 2023. The copyright holder for this preprint (which was not certified by peer review) is the author/funder. All rights reserved. No reuse allowed without permission.

Summary

Cytoplasmic mislocalization and aggregation of the RNA-binding protein TDP-43 is a pathological hallmark of the motor neuron (MN) disease amyotrophic lateral sclerosis (ALS). Furthermore, while mutations in the *TARDBP* gene (encoding TDP-43) have been associated with ALS, the pathogenic consequences of these mutations remain poorly understood. Using CRISPR/Cas9, we engineered two homozygous knock-in iPSC lines carrying mutations in *TARDBP* encoding TDP-43^{A382T} and TDP-43^{G348C}, two common yet understudied ALS TDP-43 variants. MNs differentiated from knock-in iPSCs had normal viability and displayed no significant changes in TDP-43 subcellular localization, phosphorylation, solubility, or aggregation compared with isogenic control MNs. However, our results highlight synaptic impairments in both TDP-43^{A382T} and TDP-43^{G348C} MN cultures, as reflected in synapse abnormalities and alterations in spontaneous neuronal activity. Collectively, our findings argue that MN dysfunction precedes the occurrence of TDP-43 pathology and neurodegeneration in ALS, and further implicates synaptic and excitability defects in the pathobiology of this disease.

Highlights

- MNs differentiated from knock-in iPSCs do not display a neurodegenerative phenotype.
- Mutant MNs do not show TDP-43 pathology.
- TDP-43 variants lead to a progressive decline in spontaneous neuronal activity.
- Functional impairments are accompanied by abnormal synaptic marker expression.

eTOC blurb

Using CRISPR/Cas9-edited iPSCs, Lépine et al. demonstrate that ALS TDP-43 variants (TDP-43^{A382T} and TDP43^{G348C}) lead to alterations in spontaneous neuronal activity and synaptic

bioRxiv preprint doi: https://doi.org/10.1101/2023.03.22.533562; this version posted March 24, 2023. The copyright holder for this preprint (which was not certified by peer review) is the author/funder. All rights reserved. No reuse allowed without permission.

abnormalities in the absence of TDP-43 mislocalization, aggregation, or neurodegeneration. These findings imply that TDP-43 pathology is not required to induce MN dysfunction and support the presence of early synaptic impairments prior to MN loss in ALS.

Keywords: TDP-43; TARDBP; amyotrophic lateral sclerosis; CRISPR/Cas9; gene editing; induced pluripotent stem cells; disease modeling; motor neuron; synapse; multielectrode array

bioRxiv preprint doi: https://doi.org/10.1101/2023.03.22.533562; this version posted March 24, 2023. The copyright holder for this preprint (which was not certified by peer review) is the author/funder. All rights reserved. No reuse allowed without permission.

Introduction

Amyotrophic lateral sclerosis (ALS) is a neurodegenerative disorder characterized by the progressive loss of motor neurons (MNs) in the brain and the spinal cord, resulting in weakness and paralysis that is usually fatal within two to four years after onset (Moura et al., 2015). While about 10% of ALS cases follow a pattern of inheritance (termed familial ALS (fALS)), the majority of cases occur in the absence of a clear family history (sporadic ALS (sALS)). Overall, it is estimated that 15-20% of cases have a known genetic cause (Kenna et al., 2013). The *TARDBP* gene (encoding TDP-43) is among the most commonly mutated ALS-associated genes after *C9ORF72*, *SOD1* and *FUS*, with nearly 40 missense mutations identified in patients to date (ALSoD database; https://alsod.ac.uk/). At the neuropathological level, the cytoplasmic mislocalization and aggregation of TDP-43 is a signature feature of ALS. These pathological changes, known as TDP-43 pathology, are observed in post-mortem tissues of >95% of patients (Arai et al., 2006; Mackenzie et al., 2007; Neumann et al., 2006), suggesting that convergent mechanisms of TDP-43 dysfunction are involved in both familial and sporadic disease. Thus, identifying the mechanisms through which TDP-43 dysregulation contributes to disease pathogenesis is of foremost importance in developing new therapeutics for ALS.

TDP-43 is a DNA/RNA binding protein involved in several steps of RNA processing including transcription, splicing, RNA transport, and translation (Alami et al., 2014; Buratti and Baralle, 2001; Coyne et al., 2014; Ou et al., 1995). Early efforts to decipher the pathological roles of TDP-43 in ALS have primarily focused on overexpression and loss-of-function models and demonstrated that TDP-43 levels must be tightly regulated for it to exert its normal cellular functions. Indeed, genetic ablation of *TARDBP* is lethal during embryogenesis (Kraemer et al., 2010; Sephton et al., 2010), and acute TDP-43 depletion (i.e., via conditional knockout or RNA interference) leads to neurodegeneration and ALS-like manifestations in mice (Iguchi et al., 2013; Wu et al., 2012; Yang et al., 2014). Similarly, overexpression of ALS-associated TDP-43

bioRxiv preprint doi: https://doi.org/10.1101/2023.03.22.533562; this version posted March 24, 2023. The copyright holder for this preprint (which was not certified by peer review) is the author/funder. All rights reserved. No reuse allowed without permission.

variants, or even the wild-type protein, exerts deleterious effects across species, including motor deficits, shortened lifespan, and MN loss (Armstrong and Drapeau, 2013; Estes et al., 2011; Kabashi et al., 2010; Mitchell et al., 2015; Shan et al., 2010). Given the potential confounding effects of overexpression strategies, discerning the pathological contributions of *TARDBP* mutations has been challenging.

Progress in induced pluripotent stem cell (iPSC) and gene editing technologies now offer an unprecedented opportunity to model ALS with human disease-relevant cells. Our group and others have established robust workflows for quality control, gene editing, and differentiation of iPSCs into several cell types, including MNs (Chen et al., 2021; Deneault et al., 2022; Du et al., 2015). In recent years, a number of iPSC-derived models have been generated to assess the effects of *TARDBP* mutations expressed at endogenous levels *in vitro* (reviewed in (Hawrot et al., 2020)). Although both gain- and loss-of-function mechanisms have been proposed, the pathogenic properties of ALS TDP-43 variants remain poorly understood. In particular, the pathologic manifestations of the TDP-43^{A382T} and TDP-43^{G348C} variants - the first and third most frequent ALS variants of TDP-43, respectively (ALSoD database; https://alsod.ac.uk/) - have not yet been fully characterized in a human model system.

To address this gap, we utilized CRISPR/Cas9 to generate two homozygous knock-in iPSC lines carrying point mutations in *TARDBP* coding for TDP-43^{A382T} or TDP-43^{G348C}. We found that these mutations did not cause overt neurodegeneration nor TDP-43 aggregation or cytoplasmic mislocalization. Furthermore, mutant MNs did not recapitulate other biochemical hallmarks of pathologically altered TDP-43, including phosphorylation, C-terminal cleavage, and accumulation of detergent-insoluble species. Despite the apparent absence of TDP-43 pathology, our results highlight synaptic abnormalities and decreased neuronal activity in mutant MNs, pointing to synaptic dysfunction as an early event in ALS pathogenesis.

bioRxiv preprint doi: https://doi.org/10.1101/2023.03.22.533562; this version posted March 24, 2023. The copyright holder for this preprint (which was not certified by peer review) is the author/funder. All rights reserved. No reuse allowed without permission.

Results

Generation of *TARDBP* knock-in iPSCs lines using CRIPSR/Cas9

The vast majority of *TARDBP* mutations cluster in exon 6 of the gene, which encodes the protein's C-terminal domain. Using CRISPR/Cas9 technology, we edited a well characterized healthy control iPSC line (i.e., AIW002-02) (Chen et al., 2021) to generate two homozygous knock-in *TARDBP* iPSC lines expressing TDP-43^{A382T} or TDP-43^{G348C} (**Table S1**). Gene editing was performed by nucleofection of (i) the Cas9 nuclease, (ii) the single guide RNA (sgRNA) targeting the edit site of *TARDBP* (exon 6), and (iii) the single-stranded donor oligonucleotide (ssODN) carrying the mutation and the homology arms to enable integration into the genome via homology-directed repair (**Figure 1A; Table S2**). Successful introduction of the mutations and homozygosity of the iPSC lines were confirmed by digital droplet PCR (ddPCR) and Sanger sequencing (**Figures 1B, S1A and S1B; Table S3**). The pluripotency of gene-edited iPSCs was verified by performing immunocytochemistry for pluripotency-associated markers Nanog, TRA-1-60, SSEA-4, and Oct-3/4 (**Figure S2B**). Genome stability testing confirmed that *TARDBP* knock-in iPSC lines maintained normal karyotypes and chromosome copy numbers (**Figures S2C and S2D**). Isogeneity with the parental control iPSC line was verified using short-tandem repeat (STR) profiling (**Figure S2E**).

TARDBP mutations do not impair normal differentiation of iPSCs into MNs

The two knock-in iPSC lines (TDP-43^{A382T} and TDP-43^{G348C}) and the AIW002-02 parental isogenic control line were differentiated into MNs using a previously published protocol that mimics MN differentiation during development (Deneault et al., 2022) (**Figure 1C**). Cells were harvested at multiple timepoints to characterize the differentiation process and validate their identity. iPSCs were initially induced into neuroepithelial progenitors (NEPs) via dual-SMAD

bioRxiv preprint doi: https://doi.org/10.1101/2023.03.22.533562; this version posted March 24, 2023. The copyright holder for this preprint (which was not certified by peer review) is the author/funder. All rights reserved. No reuse allowed without permission.

signaling inhibition, followed by specification into MN progenitor cells (MNPCs). MNPCs showed immunoreactivity for progenitor markers OLIG2, PAX6, and Nestin without significant differences between mutant and isogenic control cultures (**Figure S3A-S3D**). MNPCs were then cryopreserved or plated for final differentiation into MNs (**Video 1**). After two- and four-weeks post-plating of MNPCs, immunocytochemical analyses revealed a similar proportion of $HB9^{+}$ and $ISL1/2^{+}$ MNs as well as comparable expression of cholinergic markers ChAT and VAChT among mutant and isogenic control cultures (**Figure 1E-1I**). Quantitative PCR (qPCR) analysis examining longitudinal transcript levels of developmental markers confirmed that mutant and isogenic control cultures downregulated MNPC markers and upregulated MN markers as they differentiated into MNs (**Figure 1D**). Additionally, differentiating MNs upregulated *FOXP1* and downregulated *LHX3* (**Figure 1D**), consistent with limb-innervating lateral motor column (LMC) MN identity (Amoroso et al., 2013). LMC MNs ($FOXP1^{+}$/$LHX3^{-}$) are most susceptible to neurodegeneration in the majority of ALS patients, where disease typically first manifests by focal weakness in distal limb muscles (Masrori and Van Damme, 2020). Lastly, immunostaining with two neuronal markers (NF-H and βIII-tubulin) revealed that TDP-43 MN cultures formed a dense axonal network with similar morphological features relative to control conditions, including comparable total axonal area and branching (**Figure 2A-2F**). Overall, these results indicate that $TDP\text{-}43^{A382T}$ and $TDP\text{-}43^{G348C}$ do not impair the normal differentiation of iPSCs into MNs.

TDP-43 MN cultures maintain viability

Neurodegeneration is a core feature of ALS. For this reason, we examined whether MNs derived from *TARDBP* knock-in iPSCs were more vulnerable to cell death. We analyzed the viability of MNs differentiated for 2, 4 and 6 weeks using an ATP-based luminescent viability assay (**Figure 2G**). TDP-43 MN cultures survived at comparable levels to the isogenic control under basal conditions. Given that neurotrophic factors (NFs) are known to promote cell survival, we

bioRxiv preprint doi: https://doi.org/10.1101/2023.03.22.533562; this version posted March 24, 2023. The copyright holder for this preprint (which was not certified by peer review) is the author/funder. All rights reserved. No reuse allowed without permission.

hypothesized that withdrawal of NF supplementation from the differentiation medium might reveal a specific vulnerability of ALS MNs, as reported by another group with *C9ORF72* iPSC-derived MNs (Shi et al., 2019). The overall survival of MN cultures decreased by approximately 40% at 6-weeks post-plating when cells were differentiated in medium without NFs compared with complete medium, highlighting the importance of NF supplementation for long-term culture of iPSC-derived MNs. However, viability remained comparable between the mutant and control cell lines.

Next, we tested the hypothesis that TDP-43 MNs might be more vulnerable when challenged with a cellular stressor, such as glutamate. Glutamate excitotoxicity has been proposed to play a role in the pathogenesis of ALS (Blasco et al., 2014; Rothstein et al., 1992, 1995). Thus, we analyzed the viability of MN cultures treated with glutamate for 24 hours (**Figure 2H**). As expected, glutamate treatment induced MN death, as shown by a significant decrease in viability compared with vehicle-treated cultures. When comparing the survival of glutamate-treated TDP-43 MNs and isogenic control, we observed a trend towards reduced viability in both TDP-43^{A382T} and TDP-43^{G348C} MNs indicative of a potentially enhanced susceptibility to glutamate, although this effect did not reach statistical significance. Taken together, these results indicate that TDP-43 MNs did not display a neurodegenerative phenotype up to the latest timepoint investigated.

Mutant MNs do not accumulate insoluble or phosphorylated TDP-43

TDP-43 aggregates constitute the pathological hallmark of ALS, with a biochemical signature that consists of detergent-insoluble phosphorylated TDP-43 as well as C-terminal fragments of the protein (Arai et al., 2006; Mackenzie et al., 2007; Neumann et al., 2006). To assess TDP-43 levels and solubility, we performed protein fractionation of mutant and control MN cultures into total, soluble, and insoluble fractions (**Figure 3A**). Western blot analysis of total lysates showed similar TDP-43 levels between mutant and isogenic control MNs (**Figures 3G and 3H**).

bioRxiv preprint doi: https://doi.org/10.1101/2023.03.22.533562; this version posted March 24, 2023. The copyright holder for this preprint (which was not certified by peer review) is the author/funder. All rights reserved. No reuse allowed without permission.

Accordingly, *TARDBP* transcripts levels were also unchanged between mutant and control samples at all tested timepoints (**Figure S4A**), indicating that the mutations do not cause impairments in the autoregulatory function of TDP-43, where TDP-43 regulate levels of its own *TARDBP* transcript via a negative feedback loop (Ayala et al., 2011). When analyzing the soluble (RIPA) and insoluble (urea) protein fractions, mutant and control lysates showed comparable levels of soluble and insoluble TDP-43 (**Figures 3B-3D**), indicating a similar solubility of TDP-43^{A382T} and TDP-43^{G348C} to the wild-type protein. The C-terminal fragment of 35 kDa (CTF-35) was markedly enriched in insoluble fractions, although no differences in insoluble CTF-35 levels were observed mutant and control MNs (**Figure 3E**). Additionally, the CTF-35/TDP-43 ratio did not significantly differ (**Figure 3F**), indicating that the TDP-43 variants do not display enhanced C-terminal cleavage compared with control.

Next, we analyzed the phosphorylation state of TDP-43 using an antibody targeting phosphorylated TDP-43 (pTDP-43) (Ser409/410). Using western blotting, we found similar levels of total pTDP-43 in unfractionated lysates of mutant and control MNs (**Figures 3I and 3J**). Immunostaining showed abundant punctate pTDP-43 in the cytoplasm, with no notable differences in the abundance of pTDP-43^{+} puncta between mutant and control MNs (**Figure S4B**).

TDP-43^{A382T} and TDP-43^{G348C} do not exhibit changes in nucleocytoplasmic localization

Another prominent feature of TDP-43 pathology is mislocalization of TDP-43 in the cytoplasm. Thus, we performed nuclear/cytosolic protein fractionation experiments to quantify the distribution of TDP-43 (**Figures 4A and 4B**). Western blot analysis indicated no significant differences in TDP-43 levels in nuclear and cytosolic fractions of TDP-43 MNs compared with control (**Figures 4C and 4D**). CTF-35 was mainly recovered in cytosolic fractions, at similar

bioRxiv preprint doi: https://doi.org/10.1101/2023.03.22.533562; this version posted March 24, 2023. The copyright holder for this preprint (which was not certified by peer review) is the author/funder. All rights reserved. No reuse allowed without permission.

levels between samples (**Figure 4E**). The CTF-35/TDP-43 ratio was also comparable, confirming the absence of increased C-terminal cleavage in TDP-43 MNs compared with control (**Figure 4F**).

To further assess TDP-43 subcellular localization, we performed immunocytochemistry (**Figures 4G**). TDP-43 was predominantly nuclear with some signal detected in the cytoplasm. Immunocytochemical analyses revealed comparable nuclear-to-cytosolic ratios and TDP-43/Hoechst correlation coefficients between TDP-43 MNs and control, indicating similar nucleocytoplasmic localization (**Figures 4H and 4I**). These observations were recapitulated with a second TDP-43 antibody targeting the protein's N-terminus (rather than its C-terminus) (**Figures S5A-S5C**). Compared with C-terminal immunostaining, N-terminal immunostaining showed a more prominent cytosolic signal and TDP-43^{+} puncta could be observed, as previously described (Weskamp et al., 2020). However, it is worthy noting that TDP-43^{+} puncta were not detected more frequently in mutant MNs compared with control and did not co-localize with pTDP-43^{+} puncta, in line with recent findings (Ratti et al., 2020). As such, we hypothesize that TDP-43^{+} puncta may represent RNA granules rather than proper aggregates. Taken together, these results indicate that mutant MNs do not exhibit TDP-43 pathology as observed in post-mortem tissues.

Progressive decline in spontaneous neuronal activity in TDP-43 MNs

To assess the activity and functionality of MNs, we performed electrophysiological profiling of MN cultures using multielectrode array (MEA) over a span of 8 weeks post-plating. We observed progressive alteration of spontaneous neuronal activity in TDP-43^{A382T} and TDP-43^{G348C} MNs with prolonged time in culture, as shown by a significant decline in mean firing rate compared with isogenic control MNs 5 weeks post-plating (**Figure 5B**). Additionally, we noted fewer active

bioRxiv preprint doi: https://doi.org/10.1101/2023.03.22.533562; this version posted March 24, 2023. The copyright holder for this preprint (which was not certified by peer review) is the author/funder. All rights reserved. No reuse allowed without permission.

electrodes in TDP-43 MN cultures compared with control cultures despite a similar distribution of cells over the electrodes (**Figure 5A and 5C; Video 2**), indicating that they are more electrophysiologically silent. Among active electrodes, however, the burst frequency, number of spikes per burst, and burst duration remained unchanged between TDP-43 and control MN cultures (**Figure S5A, S5B and S5C**). Treatment with the sodium-channel blocker tetrodotoxin (TTX) abolished neuronal activity, thereby confirming that the recorded signals are due to action potentials and not artifacts (**Figure 5D**).

TDP-43 MNs exhibit abnormal pre- and postsynaptic puncta

To further study the mechanisms underlying altered neuronal activity, we examined whether TDP-43 MNs would display changes in synapse number and morphology. We performed co-immunostaining for presynaptic (synapsin I) and postsynaptic (PSD95) compartments in MN cultures differentiated for 6 weeks (**Figure 6A**) and analyzed mean puncta count, size, and signal intensity. We found no significant change in the number of synapsin I^+ puncta between TDP-43 MNs and control (**Figure 6B**). However, the average size of synapsin I^+ puncta was increased in TDP-43^{A382T} MNs, but not TDP-43^{G348C} MNs, compared with control (**Figure 6C**). We also observed a significant decrease in synapsin I^+ puncta mean intensity in TDP-43^{G348C} MNs compared with TDP-43^{A382T} and control MNs (**Figure 6D**). When analyzing PSD95 immunostaining, the number of $PSD95^+$ puncta was significantly decreased in TDP-43^{A382T} MNs and we observed a trend towards fewer $PSD95^+$ puncta in TDP-43^{G348C} compared with control (**Figure 6E**). Both TDP-43^{A382T} MNs and TDP-43^{G348C} MNs displayed significantly larger $PSD95^+$ puncta sizes than control MNs (**Figure 6F**). The mean intensity of $PSD95^+$ puncta was not significantly different between TDP-43 MNs and control, although a trend towards decreased $PSD95^+$ puncta intensity was observed in TDP-43^{G348C} MNs (**Figure 6G**). We also analyzed the colocalization of both synapsin I and PSD95 markers. We found no significant change in the

bioRxiv preprint doi: https://doi.org/10.1101/2023.03.22.533562; this version posted March 24, 2023. The copyright holder for this preprint (which was not certified by peer review) is the author/funder. All rights reserved. No reuse allowed without permission.

number of synapsin I^{+}/PSD95^{+} puncta between TDP-43 MNs and control (**Figure 6H**). However, the size of synapsin I^{+}/PSD95^{+} puncta was significantly larger in TDP-43^{A382T} MNs, but not TDP-43^{G348C} MNs, compared with control (**Figure 6I**). Based on these observations, we conclude that TDP-43 MNs exhibit synaptic defects.

TDP-43 variants perturb the expression of synaptic proteins post-transcriptionally

Earlier MEA experiments implied that alterations in activity manifest after prolonged time in culture, leading us to analyze protein levels of presynaptic (synapsin I, synaptophysin) and postsynaptic (PSD95) markers at several timepoints (**Figure 7A**). Western blot analysis indicated increased levels of PSD95 at 2 weeks post-plating in both TDP-43 MN cultures compared with control, but those levels were not significantly different at other timepoints (**Figure 7B**). We observed comparable levels of synaptophysin between samples at all timepoints (**Figure 7D**). Levels of synapsin I, however, were significantly depleted at 6-weeks post-plating, coinciding with the observed decline in mean firing rate (**Figure 7C**). We next sought to determine whether dysregulation of synaptic marker expression occurs at the transcriptional level (**Figure 7E-7G**). Despite the prominent decrease in synapsin I protein at 6-weeks post-plating, *SYN1* transcript levels, however, remained unchanged between TDP-43 and control MNs at this timepoint (**Figure 7F**). These results imply that TDP-43 variants perturb the expression of synapsin I post-transcriptionally. In summary, we find that impairments in spontaneous neuronal activity are reflected by abnormal synaptic marker expression.

Discussion

The detection of TDP-43 pathology in almost all ALS cases, along with the identification of disease-causing mutations in the *TARDBP* gene, underscores a central role of TDP-43 dysregulation in ALS pathobiology. Yet, the mechanisms by which *TARDBP* mutations

bioRxiv preprint doi: https://doi.org/10.1101/2023.03.22.533562; this version posted March 24, 2023. The copyright holder for this preprint (which was not certified by peer review) is the author/funder. All rights reserved. No reuse allowed without permission.

contribute to MN dysfunction and neurodegeneration remains poorly understood. In this study, we harnessed iPSC and CRIPSR/Cas9 gene editing technologies to study the impact of *TARDBP* mutations in a more physiological context. Due to our lack of TDP-43 patient samples, we edited a healthy control iPSC line to generate two homozygous knock-in iPSC lines with *TARDBP* mutations encoding the TDP-43^{A382T} and TDP-43^{G348C} variants, respectively, thereby allowing the comparison of cellular phenotypes between gene-edited cells and their parental cell line. This isogenic experimental design (where cell lines share the same genetic information except for the mutation of interest) is critical to eliminate variability due to genetic background, reprogramming, and differentiation efficiencies, which can affect the reproducibility of experiments in iPSC studies (Kilpinen et al., 2017; Rouhani et al., 2014). One limitation of this study, however, is that since the mutant iPSC lines were not derived from patient cells, they may lack ALS genetic modifiers naturally present in patients' genotypes, which could be important contributors to the disease phenotypes.

With these edited lines, we tested the hypothesis that MNs differentiated from the *TARDBP* knock-in iPSCs would manifest features of ALS *in vitro* when cultured for a prolonged period. We found that TDP-43 MNs did not exhibit a cell death phenotype up to 6 weeks of maturation, the latest timepoint investigated. These observations are consistent with earlier reports in which differences in viability between MN cultures derived from *TARDBP* mutant and control iPSC lines were not detected under basal culture conditions (Devlin et al., 2015; Egawa et al., 2012; Krach et al., 2022; Seminary et al., 2018; Zhang et al., 2013). Some noted enhanced stress-induced neuronal death following treatment with compounds such as sodium arsenite, staurosporine, MG-132 or LY294002 (a selective PI3K inhibitor) (Bilican et al., 2012; Egawa et al., 2012; Sun et al., 2018; Zhang et al., 2013), suggesting some inherent vulnerability conferred by the mutations. Our work showed only trends towards increased susceptibility of mutant MNs to glutamate toxicity. The absence of overt MN loss may reflect the immaturity of MNs at the

bioRxiv preprint doi: https://doi.org/10.1101/2023.03.22.533562; this version posted March 24, 2023. The copyright holder for this preprint (which was not certified by peer review) is the author/funder. All rights reserved. No reuse allowed without permission.

timepoints examined. In future studies, overcoming the challenges associated with long-term culture of MNs in monolayers (i.e., cell clumping and detachment) or use of three-dimensional culture models (i.e., spheroids, organoids) (Castellanos-Montiel et al., 2023; de Majo et al., 2023; Pereira et al., 2021) may enable neurodegeneration to be observed after several months of culture, without the need for exogenous treatments with stressors to elicit a phenotype. Alternatively, transcription factor-mediated transdifferentiation towards specific neurons, avoiding intermediate proliferative pluripotent stem cell stage, may help retaining specific age-related and epigenetic features involved in neurodegenerative disorders (Mollinari et al., 2018).

As aging is a strong risk factor for ALS, enhancing the maturation of MN cultures may also accelerate the manifestation of end-stage disease features, such as TDP-43 pathology. Here, we show that mutant MNs did not robustly display cytoplasmic mislocalization, aggregation, or accumulation of insoluble TDP-43 under basal conditions, in line with most recent reports of iPSC-derived MNs carrying *TARBDP* mutations (Bossolasco et al., 2018; Dafinca et al., 2020; Imaizumi et al., 2022; Klim et al., 2019; Krach et al., 2022; Kreiter et al., 2018; Ratti et al., 2020; Wang et al., 2013). Some studies, in contrast, found that mutant MNs recapitulate partial aspects of TDP-43 pathology *in vitro* (Bilican et al., 2012; Egawa et al., 2012; Fazal et al., 2021; Fujimori et al., 2018; Smith et al., 2021; Sun et al., 2018), sometimes reporting enhanced cytoplasmic distribution of TDP-43 (albeit without nuclear depletion), increased levels of insoluble TDP-43 and lower molecular weight species and/or, in few instances, detection of "preinclusion-like aggregates" by immunocytochemistry or electron microscopy. These discrepancies, together with the absence of overt neurodegeneration, suggest that iPSC-derived MNs may model early stages of ALS.

One prominent finding of the present study is the progressive decline in spontaneous neuronal activity in TDP-43^{A382T} and TDP-43^{G348C} MNs after several weeks in culture. Although we noted abnormal pre- and postsynaptic puncta, we found no significant changes in the number of

bioRxiv preprint doi: https://doi.org/10.1101/2023.03.22.533562; this version posted March 24, 2023. The copyright holder for this preprint (which was not certified by peer review) is the author/funder. All rights reserved. No reuse allowed without permission.

synapsin I^+/$PSD95^+$ puncta between TDP-43 MNs and control, indicating that altered neuronal activity is not due to a failure of synaptogenesis nor synaptic loss. These results suggest that functional alterations in synaptic activity may arise before the physical disruption of synapses in ALS. Indeed, previous studies of animal models and ALS patients have implicated excitability defects in this disease (Martínez-Silva et al., 2018; Vucic et al., 2008). Additionally, neuronal hypoexcitability, sometimes preceded by transient early hyperexcitability, has been described in iPSC-derived neurons with mutations in *TARDBP* (Dafinca et al., 2020; Devlin et al., 2015; Zhang et al., 2013). A possible progression from initial hyper- to hypoexcitability is also supported by studies in ALS mouse models (Delestrée et al., 2014; Fuchs et al., 2013) and iPSC-derived models carrying mutations in *C9ORF72* (Dafinca et al., 2020; Devlin et al., 2015; Sareen et al., 2013; Zhao et al., 2020), *SOD1* (Kim et al., 2020; Naujock et al., 2016; Wainger et al., 2014) and *FUS* (Guo et al., 2017; Naujock et al., 2016), depending on the timepoint examined.

Accumulating evidence suggests that TDP-43 is involved in synaptic functions, both at central and neuromuscular synapses (reviewed in (Gulino, 2023; Lépine et al., 2022; Ling, 2018)). Pathologically altered TDP-43 has been shown to perturb the expression of synaptic genes in ALS mouse models and patients (Brown et al., 2022; Ma et al., 2022; Mishra et al., 2007; Polymenidou et al., 2011). Here, we found that synapsin I protein levels, but not *SYN1* transcript levels, were depleted in TDP-43^{A382T} and TDP-43^{G348C} MNs after 6 weeks post-plating, which was coincident with the decline in neuronal activity. These results imply that differences in synapsin I levels result from a post-transcriptional mechanism, such as impairments in mRNA transport, translation and/or mRNA sequestration by TDP-43, as described by several groups (Alami et al., 2014; Altman et al., 2021; Coyne et al., 2017; Zuo et al., 2021). Further research will be required to elucidate the molecular mechanisms by which *TARDBP* mutations lead to

bioRxiv preprint doi: https://doi.org/10.1101/2023.03.22.533562; this version posted March 24, 2023. The copyright holder for this preprint (which was not certified by peer review) is the author/funder. All rights reserved. No reuse allowed without permission.

decreased synapsin I expression, potentially contributing to functional defects (Baldelli et al., 2007; Rosahl et al., 1995).

Overall, our findings indicate that TDP-43 pathology is not required to induce MN dysfunction and support the presence of early synaptic impairments prior to MN loss in ALS. As the synapse emerges as a promising therapeutic target for ALS, neuronal activity and synapse integrity may serve as disease-relevant phenotypic readouts for drug discovery.

bioRxiv preprint doi: https://doi.org/10.1101/2023.03.22.533562; this version posted March 24, 2023. The copyright holder for this preprint (which was not certified by peer review) is the author/funder. All rights reserved. No reuse allowed without permission.

Experimental Procedures

See further details in the Supplemental Experimental Procedures.

Resource Availabilities

Corresponding author. Further information and requests should be directed to the lead contact, Thomas M. Durcan (thomas.durcan@mcgill.ca).

Materials availability. Cell lines generated in this study will be made available on request, under the open science framework of the Neuro, and through a cost recovery model.

Data and code availability. Derived data supporting the findings of this study are available from the lead contact upon request.

iPSC lines and culture

The use of human cells in this study was approved by McGill University Health Center Research Ethics Board (DURCAN_iPSC / 2019-5374). To knock-in selected mutations, we used the previously characterized control cell line AIW002-02, reprogrammed from peripheral blood mononuclear cells (PBMCs) of a 37-year-old Caucasian male, as previously described (Chen et al., 2021). A summary of the iPSC lines used can be found in **Table S1**. iPSCs were maintained on dishes coated with Matrigel (Corning Millipore) in mTeSR1 (StemCell Technologies) and passaged at 80% confluence using Gentle Cell Dissociation Reagent (StemCell Technologies). Cultures were routinely tested for mycoplasma using the MycoAlert Mycoplasma Detection kit (Lonza).

bioRxiv preprint doi: https://doi.org/10.1101/2023.03.22.533562; this version posted March 24, 2023. The copyright holder for this preprint (which was not certified by peer review) is the author/funder. All rights reserved. No reuse allowed without permission.

CRISPR/Cas9 genome editing and validation

To genetically edit *TARDBP*, CRISPR reagents were transfected into iPSCs using the P3 Primary Cell 4D Nucleofector™ X Kit S (Lonza), as previously described (Deneault et al., 2022). Briefly, iPSCs at 50% confluency were dissociated with Accutase (StemCell Technologies) and 500,000 cells were resuspended in 25 µL of Cas9: sgRNA ribonucleoprotein (RNP)-ssODN-buffer mix, consisting of 1 μL of Cas9 protein (stock 61 μM), 3 μL of sgRNA (stock 100 μM), and 1 μL of ssODNs (stock 100 μM) in 20 μL of nucleofection buffer P3. The reaction mixture was then electroporated using the CA137 program in a Nucleofector 4D device. The sequences of the sgRNAs and ssODNs used are provided in **Table S2**.

After limiting dilution, gene-edited clones were identified by ddPCR (QX200™ Droplet Reader, Bio-Rad). The detection of the modified nucleotide by ddPCR was based on a TaqMan® assay including two PCR primers and two DNA probes fused with different fluorophores (FAM and HEX), with one probe specific to the original allele and the other probe to the edited allele. Locked Nucleic Acid (LNA®) probes were designed following the manufacturer's criteria. Sequence integrity of successful clones was assessed using Sanger sequencing. The sequences of the primers and probes used for ddPCR, and Sanger sequencing are provided in **Table S3**.

Statistical tests

Biological replicates were defined as independent differentiations unless otherwise specified. Statistical analyses were performed with the GraphPad Prism 9.3.0 software. Data distribution was assumed to be normal although this was not formally tested. Differences between multiple groups were analyzed using one-way or two-way analysis of variance (ANOVA) tests. Means

bioRxiv preprint doi: https://doi.org/10.1101/2023.03.22.533562; this version posted March 24, 2023. The copyright holder for this preprint (which was not certified by peer review) is the author/funder. All rights reserved. No reuse allowed without permission.

and standard errors of the mean were used for data presentation. Significance was defined as $p<0.05$.

Acknowledgements

We acknowledge Dr. Vincent Soubannier for training and guidance on microscopy image acquisition and analysis, Ghislaine Deyab for guidance on MEA data analysis, Shuming Li for programming the macro for visualization of MEA data, and Dr. Mark R. Aurousseau for his contribution to the development of the glutamate assay. We are also grateful to Dr. Gary A.B. Armstrong for creative discussions and his advice and to Dr. Lenore K. Beitel for proofreading the manuscript. SL was supported by the Faculty of Medicine and Health Sciences of McGill University. TMD acknowledges support from the Canada First Research Excellence Fund, awarded through the Healthy Brains, Healthy Lives initiative at McGill University, the CQDM FACs program, and the US Department of Defense ALS Research Program support. All figures and schematics were created with BioRender.com.

Author contributions

SL, MC, and TMD conceived the project. SL, MC, GM, and TMD designed experiments. ED designed and performed editing of the *TARDBP* knock-in iPSC lines. CXQC and NA performed iPSC characterization and quality control. SL, AKFF, GH, and MJCM performed inductions of iPSCs to MNPCs. MC and GH developed the glutamate viability assay. SL performed experiments, with support from ANJ and AKFF. SL performed data analysis. SL prepared the original draft of the manuscript. SL, MC, and TMD reviewed and edited the manuscript. TMD supervised all aspects of the study. All authors reviewed and commented on the manuscript.

bioRxiv preprint doi: https://doi.org/10.1101/2023.03.22.533562; this version posted March 24, 2023. The copyright holder for this preprint (which was not certified by peer review) is the author/funder. All rights reserved. No reuse allowed without permission.

Declaration of interests

The authors declare no competing interests.

References

Alami, N.H., Smith, R.B., Carrasco, M.A., Williams, L.A., Winborn, C.S., Han, S.S.W., Kiskinis, E., Winborn, B., Freibaum, B.D., Kanagaraj, A., et al. (2014). Axonal transport of TDP-43 mRNA granules is impaired by ALS-causing mutations. Neuron *81*, 536–543. https://doi.org/10.1016/j.neuron.2013.12.018.

Altman, T., Ionescu, A., Ibraheem, A., Priesmann, D., Gradus-Pery, T., Farberov, L., Alexandra, G., Shelestovich, N., Dafinca, R., Shomron, N., et al. (2021). Axonal TDP-43 condensates drive neuromuscular junction disruption through inhibition of local synthesis of nuclear encoded mitochondrial proteins. Nat. Commun. *12*, 6914. https://doi.org/10.1038/s41467-021-27221-8.

Amoroso, M.W., Croft, G.F., Williams, D.J., O'Keeffe, S., Carrasco, M.A., Davis, A.R., Roybon, L., Oakley, D.H., Maniatis, T., Henderson, C.E., et al. (2013). Accelerated high-yield generation of limb-innervating motor neurons from human stem cells. J. Neurosci. *33*, 574–586. https://doi.org/10.1523/JNEUROSCI.0906-12.2013.

Arai, T., Hasegawa, M., Akiyama, H., Ikeda, K., Nonaka, T., Mori, H., Mann, D., Tsuchiya, K., Yoshida, M., Hashizume, Y., et al. (2006). TDP-43 is a component of ubiquitin-positive tau-negative inclusions in frontotemporal lobar degeneration and amyotrophic lateral sclerosis. Biochem. Biophys. Res. Commun. *351*, 602–611. https://doi.org/10.1016/j.bbrc.2006.10.093.

Armstrong, G.A.B., and Drapeau, P. (2013). Calcium channel agonists protect against neuromuscular dysfunction in a genetic model of TDP-43 mutation in ALS. J. Neurosci. *33*, 1741–1752. https://doi.org/10.1523/JNEUROSCI.4003-12.2013.

Ayala, Y.M., De Conti, L., Avendaño-Vázquez, S.E., Dhir, A., Romano, M., D'Ambrogio, A., Tollervey, J., Ule, J., Baralle, M., Buratti, E., et al. (2011). TDP-43 regulates its mRNA levels through a negative feedback loop. EMBO J. *30*, 277–288. https://doi.org/10.1038/emboj.2010.310.

Baldelli, P., Fassio, A., Valtorta, F., and Benfenati, F. (2007). Lack of synapsin I reduces the readily releasable pool of synaptic vesicles at central inhibitory synapses. J. Neurosci. *27*, 13520–13531. https://doi.org/10.1523/JNEUROSCI.3151-07.2007.

Bilican, B., Serio, A., Barmada, S.J., Nishimura, A.L., Sullivan, G.J., Carrasco, M., Phatnani, H.P., Puddifoot, C.A., Story, D., Fletcher, J., et al. (2012). Mutant induced pluripotent stem cell lines recapitulate aspects of TDP-43 proteinopathies and reveal cell-specific vulnerability. Proc. Natl. Acad. Sci. U. S. A. *109*, 5803–5808. https://doi.org/10.1073/pnas.1202922109.

Blasco, H., Mavel, S., Corcia, P., and Gordon, P.H. (2014). The glutamate hypothesis in ALS: Pathophysiology and drug development. Curr. Med. Chem. *21*, 3551–3575. https://doi.org/10.2174/0929867321666140916120118.

Bossolasco, P., Sassone, F., Gumina, V., Peverelli, S., Garzo, M., and Silani, V. (2018). Motor

bioRxiv preprint doi: https://doi.org/10.1101/2023.03.22.533562; this version posted March 24, 2023. The copyright holder for this preprint (which was not certified by peer review) is the author/funder. All rights reserved. No reuse allowed without permission.

neuron differentiation of iPSCs obtained from peripheral blood of a mutant TARDBP ALS patient. Stem Cell Res. *30*, 61–68. https://doi.org/10.1016/j.scr.2018.05.009.

Brown, A., Wilkins, O.G., Keuss, M.J., Hill, S.E., Zanovello, M., Lee, W.C., Bampton, A., Lee, F.C.Y., Masino, L., Qi, Y.A., et al. (2022). TDP-43 loss and ALS-risk SNPs drive mis-splicing and depletion of UNC13A. Nature *603*, 131–137. https://doi.org/10.1038/s41586-022-04436-3.

Buratti, E., and Baralle, F.E. (2001). Characterization and functional implications of the RNA binding properties of nuclear factor TDP-43, a novel splicing regulator of CFTR exon 9. J. Biol. Chem. *276*, 36337–36343. https://doi.org/10.1074/jbc.M104236200.

Castellanos-Montiel, M.J., Chaineau, M., Franco-Flores, A.K., Haghi, G., Carrillo-Valenzuela, D., Reintsch, W.E., Chen, C.X.-Q., and Durcan, T.M. (2023). An optimized workflow to generate and characterize iPSC-derived motor neuron (MN) spheroids. Cells *12*, 545. https://doi.org/10.3390/cells12040545.

Chen, C.X.Q., Abdian, N., Maussion, G., Thomas, R.A., Demirova, I., Cai, E., Tabatabaei, M., Beitel, L.K., Karamchandani, J., Fon, E.A., et al. (2021). A multistep workflow to evaluate newly generated iPSCs and their ability to generate different cell types. Methods Protoc. *4*, 50. https://doi.org/10.3390/mps4030050.

Coyne, A.N., Siddegowda, B.B., Estes, P.S., Johannesmeyer, J., Kovalik, T., Daniel, S.G., Pearson, A., Bowser, R., and Zarnescu, D.C. (2014). FUTSCH/MAP1B mRNA is a translational target of TDP-43 and is neuroprotective in a Drosophila model of amyotrophic lateral sclerosis. J. Neurosci. *34*, 15962–15974. https://doi.org/10.1523/JNEUROSCI.2526-14.2014.

Coyne, A.N., Lorenzini, I., Chou, C.-C., Torvund, M., Rogers, R.S., Starr, A., Zaepfel, B.L., Levy, J., Johannesmeyer, J., Schwartz, J.C., et al. (2017). Post-transcriptional inhibition of Hsc70-4/HSPA8 expression leads to synaptic vesicle cycling defects in multiple models of ALS. Cell Rep. *21*, 110–125. https://doi.org/10.1016/j.celrep.2017.09.028.

Dafinca, R., Barbagallo, P., Farrimond, L., Candalija, A., Scaber, J., Ababneh, N.A., Sathyaprakash, C., Vowles, J., Cowley, S.A., and Talbot, K. (2020). Impairment of mitochondrial calcium buffering links mutations in C9ORF72 and TARDBP in iPS-derived motor neurons from patients with ALS/FTD. Stem Cell Reports *14*, 892–908. https://doi.org/10.1016/j.stemcr.2020.03.023.

Delestrée, N., Manuel, M., Iglesias, C., Elbasiouny, S.M., Heckman, C.J., and Zytnicki, D. (2014). Adult spinal motoneurones are not hyperexcitable in a mouse model of inherited amyotrophic lateral sclerosis. J. Physiol. *592*, 1687–1703. https://doi.org/10.1113/jphysiol.2013.265843.

Deneault, E., Chaineau, M., Nicouleau, M., Castellanos Montiel, M.J., Franco Flores, A.K., Haghi, G., Chen, C.X.Q., Abdian, N., Shlaifer, I., Beitel, L.K., et al. (2022). A streamlined CRISPR workflow to introduce mutations and generate isogenic iPSCs for modeling amyotrophic lateral sclerosis. Methods *203*, 297–310. https://doi.org/10.1016/j.ymeth.2021.09.002.

Devlin, A.-C., Burr, K., Borooah, S., Foster, J.D., Cleary, E.M., Geti, I., Vallier, L., Shaw, C.E., Chandran, S., and Miles, G.B. (2015). Human iPSC-derived motoneurons harbouring TARDBP or C9ORF72 ALS mutations are dysfunctional despite maintaining viability. Nat. Commun. *6*, 5999. https://doi.org/10.1038/ncomms6999.

Du, Z.W., Chen, H., Liu, H., Lu, J., Qian, K., Huang, C.T.L., Zhong, X., Fan, F., and Zhang, S.C. (2015). Generation and expansion of highly pure motor neuron progenitors from human pluripotent stem cells. Nat. Commun. *6*, 6626. https://doi.org/10.1038/ncomms7626.

bioRxiv preprint doi: https://doi.org/10.1101/2023.03.22.533562; this version posted March 24, 2023. The copyright holder for this preprint (which was not certified by peer review) is the author/funder. All rights reserved. No reuse allowed without permission.

Egawa, N., Kitaoka, S., Tsukita, K., Naitoh, M., Takahashi, K., Yamamoto, T., Adachi, F., Kondo, T., Okita, K., Asaka, I., et al. (2012). Drug screening for ALS using patient-specific induced pluripotent stem cells. Sci. Transl. Med. *4*, 145ra104. https://doi.org/10.1126/scitranslmed.3004052.

Estes, P.S., Boehringer, A., Zwick, R., Tang, J.E., Grigsby, B., and Zarnescu, D.C. (2011). Wild-type and A315T mutant TDP-43 exert differential neurotoxicity in a Drosophila model of ALS. Hum. Mol. Genet. *20*, 2308–2321. https://doi.org/10.1093/hmg/ddr124.

Fazal, R., Boeynaems, S., Swijsen, A., De Decker, M., Fumagalli, L., Moisse, M., Vanneste, J., Guo, W., Boon, R., Vercruysse, T., et al. (2021). HDAC6 inhibition restores TDP-43 pathology and axonal transport defects in human motor neurons with TARDBP mutations. EMBO J. *40*, 1–24. https://doi.org/10.15252/embj.2020106177.

Fuchs, A., Kutterer, S., Mühling, T., Duda, J., Schütz, B., Liss, B., Keller, B.U., and Roeper, J. (2013). Selective mitochondrial Ca 2+ uptake deficit in disease endstage vulnerable motoneurons of the SOD1 G93A mouse model of amyotrophic lateral sclerosis. J. Physiol. *591*, 2723–2745. https://doi.org/10.1113/jphysiol.2012.247981.

Fujimori, K., Ishikawa, M., Otomo, A., Atsuta, N., Nakamura, R., Akiyama, T., Hadano, S., Aoki, M., Saya, H., Sobue, G., et al. (2018). Modeling sporadic ALS in iPSC-derived motor neurons identifies a potential therapeutic agent. Nat. Med. *24*, 1579–1589. https://doi.org/10.1038/s41591-018-0140-5.

Gulino, R. (2023). Synaptic dysfunction and plasticity in amyotrophic lateral sclerosis. Int. J. Mol. Sci. *24*, 4613. https://doi.org/10.3390/ijms24054613.

Guo, W., Naujock, M., Fumagalli, L., Vandoorne, T., Baatsen, P., Boon, R., Ordovás, L., Patel, A., Welters, M., Vanwelden, T., et al. (2017). HDAC6 inhibition reverses axonal transport defects in motor neurons derived from FUS-ALS patients. Nat. Commun. *8*, 861. https://doi.org/10.1038/s41467-017-00911-y.

Hawrot, J., Imhof, S., and Wainger, B.J. (2020). Modeling cell-autonomous motor neuron phenotypes in ALS using iPSCs. Neurobiol. Dis. *134*, 104680. https://doi.org/10.1016/j.nbd.2019.104680.

Iguchi, Y., Katsuno, M., Niwa, J., Takagi, S., Ishigaki, S., Ikenaka, K., Kawai, K., Watanabe, H., Yamanaka, K., Takahashi, R., et al. (2013). Loss of TDP-43 causes age-dependent progressive motor neuron degeneration. Brain *136*, 1371–1382. https://doi.org/10.1093/brain/awt029.

Imaizumi, K., Ideno, H., Sato, T., Morimoto, S., and Okano, H. (2022). Pathogenic mutation of TDP-43 impairs RNA processing in a cell type-specific manner: Implications for the pathogenesis of ALS/FTLD. ENeuro *9*, 1–12. https://doi.org/10.1523/ENEURO.0061-22.2022.

Kabashi, E., Lin, L., Tradewell, M.L., Dion, P.A., Bercier, V., Bourgouin, P., Rochefort, D., Bel Hadj, S., Durham, H.D., Velde, C. Vande, et al. (2010). Gain and loss of function of ALS-related mutations of TARDBP (TDP-43) cause motor deficits in vivo. Hum. Mol. Genet. *19*, 671–683. https://doi.org/10.1093/hmg/ddp534.

Kenna, K.P., McLaughlin, R.L., Byrne, S., Elamin, M., Heverin, M., Kenny, E.M., Cormican, P., Morris, D.W., Donaghy, C.G., Bradley, D.G., et al. (2013). Delineating the genetic heterogeneity of ALS using targeted high-throughput sequencing. J. Med. Genet. *50*, 776–783. https://doi.org/10.1136/jmedgenet-2013-101795.

Kilpinen, H., Goncalves, A., Leha, A., Afzal, V., Alasoo, K., Ashford, S., Bala, S., Bensaddek, D.,

bioRxiv preprint doi: https://doi.org/10.1101/2023.03.22.533562; this version posted March 24, 2023. The copyright holder for this preprint (which was not certified by peer review) is the author/funder. All rights reserved. No reuse allowed without permission.

Casale, F.P., Culley, O.J., et al. (2017). Common genetic variation drives molecular heterogeneity in human iPSCs. Nature *546*, 370–375. https://doi.org/10.1038/nature22403.

Kim, B.W., Ryu, J., Jeong, Y.E., Kim, J., and Martin, L.J. (2020). Human motor neurons with SOD1-G93A mutation generated from CRISPR/Cas9 gene-edited iPSCs develop pathological features of amyotrophic lateral sclerosis. Front. Cell. Neurosci. *14*, 1–16. https://doi.org/10.3389/fncel.2020.604171.

Klim, J.R., Williams, L.A., Limone, F., Guerra San Juan, I., Davis-Dusenbery, B.N., Mordes, D.A., Burberry, A., Steinbaugh, M.J., Gamage, K.K., Kirchner, R., et al. (2019). ALS-implicated protein TDP-43 sustains levels of STMN2, a mediator of motor neuron growth and repair. Nat. Neurosci. *22*, 167–179. https://doi.org/10.1038/s41593-018-0300-4.

Krach, F., Wheeler, E.C., Regensburger, M., Boerstler, T., Wend, H., Vu, A.Q., Wang, R., Reischl, S., Boldt, K., Batra, R., et al. (2022). Aberrant NOVA1 function disrupts alternative splicing in early stages of amyotrophic lateral sclerosis. Acta Neuropathol. *144*, 413–435. https://doi.org/10.1007/s00401-022-02450-3.

Kraemer, B.C., Schuck, T., Wheeler, J.M., Robinson, L.C., Trojanowski, J.Q., Lee, V.M.Y., and Schellenberg, G.D. (2010). Loss of murine TDP-43 disrupts motor function and plays an essential role in embryogenesis. Acta Neuropathol. *119*, 409–419. https://doi.org/10.1007/s00401-010-0659-0.

Kreiter, N., Pal, A., Lojewski, X., Corcia, P., Naujock, M., Reinhardt, P., Sterneckert, J., Petri, S., Wegner, F., Storch, A., et al. (2018). Age-dependent neurodegeneration and organelle transport deficiencies in mutant TDP43 patient-derived neurons are independent of TDP43 aggregation. Neurobiol. Dis. *115*, 167–181. https://doi.org/10.1016/j.nbd.2018.03.010.

Lépine, S., Castellanos-Montiel, M.J., and Durcan, T.M. (2022). TDP-43 dysregulation and neuromuscular junction disruption in amyotrophic lateral sclerosis. Transl. Neurodegener. *11*, 1–24. https://doi.org/10.1186/s40035-022-00331-z.

Ling, S.-C. (2018). Synaptic paths to neurodegeneration: The emerging role of TDP-43 and FUS in synaptic functions. Neural Plast. *2018*, 1–13. https://doi.org/10.1155/2018/8413496.

Ma, X.R., Prudencio, M., Koike, Y., Vatsavayai, S.C., Kim, G., Harbinski, F., Briner, A., Rodriguez, C.M., Guo, C., Akiyama, T., et al. (2022). TDP-43 represses cryptic exon inclusion in the FTD–ALS gene UNC13A. Nature *603*, 124–130. https://doi.org/10.1038/s41586-022-04424-7.

Mackenzie, I.R.A., Bigio, E.H., Ince, P.G., Geser, F., Neumann, M., Cairns, N.J., Kwong, L.K., Forman, M.S., Ravits, J., Stewart, H., et al. (2007). Pathological TDP-43 distinguishes sporadic amyotrophic lateral sclerosis from amyotrophic lateral sclerosis with SOD1 mutations. Ann. Neurol. *61*, 427–434. https://doi.org/10.1002/ana.21147.

de Majo, M., Koontz, M., Marsan, E., Salinas, N., Ramsey, A., Kuo, Y.-M., Seo, K., Li, H., Dräger, N., Leng, K., et al. (2023). Granulin loss of function in human mature brain organoids implicates astrocytes in TDP-43 pathology. Stem Cell Reports *13*, 1–15. https://doi.org/10.1016/j.stemcr.2023.01.012.

Martínez-Silva, M. de L., Imhoff-Manuel, R.D., Sharma, A., Heckman, C., Shneider, N.A., Roselli, F., Zytnicki, D., and Manuel, M. (2018). Hypoexcitability precedes denervation in the large fast-contracting motor units in two unrelated mouse models of ALS. Elife *7*, e30955. https://doi.org/10.7554/eLife.30955.

bioRxiv preprint doi: https://doi.org/10.1101/2023.03.22.533562; this version posted March 24, 2023. The copyright holder for this preprint (which was not certified by peer review) is the author/funder. All rights reserved. No reuse allowed without permission.

Masrori, P., and Van Damme, P. (2020). Amyotrophic lateral sclerosis: a clinical review. Eur. J. Neurol. *27*, 1918–1929. https://doi.org/10.1111/ene.14393.

Mishra, M., Paunesku, T., Woloschak, G.E., Siddique, T., Zhu, L., Lin, S., Greco, K., and Bigio, E.H. (2007). Gene expression analysis of frontotemporal lobar degeneration of the motor neuron disease type with ubiquitinated inclusions. Acta Neuropathol. *114*, 81–94. https://doi.org/10.1007/s00401-007-0240-7.

Mitchell, J.C., Constable, R., So, E., Vance, C., Scotter, E., Glover, L., Hortobagyi, T., Arnold, E.S., Ling, S.-C., McAlonis, M., et al. (2015). Wild type human TDP-43 potentiates ALS-linked mutant TDP-43 driven progressive motor and cortical neuron degeneration with pathological features of ALS. Acta Neuropathol. Commun. *3*, 36. https://doi.org/10.1186/s40478-015-0212-4.

Mollinari, C., Zhao, J., Lupacchini, L., Garaci, E., Merlo, D., and Pei, G. (2018). Transdifferentiation: a new promise for neurodegenerative diseases. Cell Death Dis. *9*, 830. https://doi.org/10.1038/s41419-018-0891-4.

Moura, M.C., Novaes, M.R.C.G., Eduardo, E.J., Zago, Y.S.S.P., Freitas, R.D.N.B., and Casulari, L.A. (2015). Prognostic factors in amyotrophic lateral sclerosis: A population-based study. PLoS One *10*, e0141500. https://doi.org/10.1371/journal.pone.0141500.

Naujock, M., Stanslowsky, N., Bufler, S., Naumann, M., Reinhardt, P., Sterneckert, J., Kefalakes, E., Kassebaum, C., Bursch, F., Lojewski, X., et al. (2016). 4-Aminopyridine induced activity rescues hypoexcitable motor neurons from amyotrophic lateral sclerosis patient-derived induced pluripotent stem cells. Stem Cells *34*, 1563–1575. https://doi.org/10.1002/stem.2354.

Neumann, M., Sampathu, D.M., Kwong, L.K., Truax, A.C., Micsenyi, M.C., Chou, T.T., Bruce, J., Schuck, T., Grossman, M., Clark, C.M., et al. (2006). Ubiquitinated TDP-43 in frontotemporal lobar degeneration and amyotrophic lateral sclerosis. Science (80-.). *314*, 130–133. https://doi.org/10.1126/science.1134108.

Ou, S.H., Wu, F., Harrich, D., García-Martínez, L.F., and Gaynor, R.B. (1995). Cloning and characterization of a novel cellular protein, TDP-43, that binds to human immunodeficiency virus type 1 TAR DNA sequence motifs. J. Virol. *69*, 3584–3596. https://doi.org/10.1128/jvi.69.6.3584-3596.1995.

Pereira, J.D., DuBreuil, D.M., Devlin, A.-C., Held, A., Sapir, Y., Berezovski, E., Hawrot, J., Dorfman, K., Chander, V., and Wainger, B.J. (2021). Human sensorimotor organoids derived from healthy and amyotrophic lateral sclerosis stem cells form neuromuscular junctions. Nat. Commun. *12*, 4744. https://doi.org/10.1038/s41467-021-24776-4.

Polymenidou, M., Lagier-Tourenne, C., Hutt, K.R., Huelga, S.C., Moran, J., Liang, T.Y., Ling, S.-C., Sun, E., Wancewicz, E., Mazur, C., et al. (2011). Long pre-mRNA depletion and RNA missplicing contribute to neuronal vulnerability from loss of TDP-43. Nat. Neurosci. *14*, 459–468. https://doi.org/10.1038/nn.2779.

Ratti, A., Gumina, V., Lenzi, P., Bossolasco, P., Fulceri, F., Volpe, C., Bardelli, D., Pregnolato, F., Maraschi, A., Fornai, F., et al. (2020). Chronic stress induces formation of stress granules and pathological TDP-43 aggregates in human ALS fibroblasts and iPSC-motoneurons. Neurobiol. Dis. *145*, 105051. https://doi.org/10.1016/j.nbd.2020.105051.

Rosahl, T.W., Spillane, D., Missler, M., Herz, J., Selig, D.K., Wolff, J.R., Hammer, R.E., Malenka, R.C., and Südhof, T.C. (1995). Essential functions of synapsins I and II in synaptic vesicle regulation. Nature *375*, 488–493. https://doi.org/10.1038/375488a0.

bioRxiv preprint doi: https://doi.org/10.1101/2023.03.22.533562; this version posted March 24, 2023. The copyright holder for this preprint (which was not certified by peer review) is the author/funder. All rights reserved. No reuse allowed without permission.

Rothstein, J.D., Martin, L.J., and Kuncl, R.W. (1992). Decreased glutamate transport by the brain and spinal cord in amyotrophic lateral sclerosis. N. Engl. J. Med. *326*, 1464–1468. https://doi.org/10.1056/NEJM199205283262204.

Rothstein, J.D., Van Kammen, M., Levey, A.I., Martin, L.J., and Kuncl, R.W. (1995). Selective loss of glial glutamate transporter GLT-1 in amyotrophic lateral sclerosis. Ann. Neurol. *38*, 73–84. https://doi.org/10.1002/ana.410380114.

Rouhani, F., Kumasaka, N., de Brito, M.C., Bradley, A., Vallier, L., and Gaffney, D. (2014). Genetic background drives transcriptional variation in human induced pluripotent stem cells. PLoS Genet. *10*, e1004432. https://doi.org/10.1371/journal.pgen.1004432.

Sareen, D., O'Rourke, J.G., Meera, P., Muhammad, A.K.M.G., Grant, S., Simpkinson, M., Bell, S., Carmona, S., Ornelas, L., Sahabian, A., et al. (2013). Targeting RNA foci in iPSC-derived motor neurons from ALS patients with a C9ORF72 repeat expansion. Sci. Transl. Med. *5*, 208ra149. https://doi.org/10.1126/scitranslmed.3007529.

Seminary, E.R., Sison, S.L., and Ebert, A.D. (2018). Modeling protein aggregation and the heat shock response in ALS iPSC-derived motor neurons. Front. Neurosci. *12*, 1–15. https://doi.org/10.3389/fnins.2018.00086.

Sephton, C.F., Good, S.K., Atkin, S., Dewey, C.M., Mayer, P., Herz, J., and Yu, G. (2010). TDP-43 is a developmentally regulated protein essential for early embryonic development. J. Biol. Chem. *285*, 6826–6834. https://doi.org/10.1074/jbc.M109.061846.

Shan, X., Chiang, P.-M., Price, D.L., and Wong, P.C. (2010). Altered distributions of Gemini of coiled bodies and mitochondria in motor neurons of TDP-43 transgenic mice. Proc. Natl. Acad. Sci. *107*, 16325–16330. https://doi.org/10.1073/pnas.1003459107.

Shi, Y., Hung, S.T., Rocha, G., Lin, S., Linares, G.R., Staats, K.A., Seah, C., Wang, Y., Chickering, M., Lai, J., et al. (2019). Identification and therapeutic rescue of autophagosome and glutamate receptor defects in C9ORF72 and sporadic ALS neurons. JCI Insight *4*, 1–21. https://doi.org/10.1172/jci.insight.127736.

Smith, A.S.T., Chun, C., Hesson, J., Mathieu, J., Valdmanis, P.N., Mack, D.L., Choi, B.O., Kim, D.H., and Bothwell, M. (2021). Human induced pluripotent stem cell-derived TDP-43 mutant neurons exhibit consistent functional phenotypes across multiple gene edited lines despite transcriptomic and splicing discrepancies. Front. Cell Dev. Biol. *9*, 1–18. https://doi.org/10.3389/fcell.2021.728707.

Sun, X., Song, J., Huang, H., Chen, H., and Qian, K. (2018). Modeling hallmark pathology using motor neurons derived from the family and sporadic amyotrophic lateral sclerosis patient-specific iPS cells. Stem Cell Res. Ther. *9*, 315. https://doi.org/10.1186/s13287-018-1048-1.

Vucic, S., Nicholson, G.A., and Kiernan, M.C. (2008). Cortical hyperexcitability may precede the onset of familial amyotrophic lateral sclerosis. Brain *131*, 1540–1550. https://doi.org/10.1093/brain/awn071.

Wainger, B.J., Kiskinis, E., Mellin, C., Wiskow, O., Han, S.S.W., Sandoe, J., Perez, N.P., Williams, L.A., Lee, S., Boulting, G., et al. (2014). Intrinsic membrane hyperexcitability of amyotrophic lateral sclerosis patient-derived motor neurons. Cell Rep. *7*, 1–11. https://doi.org/10.1016/j.celrep.2014.03.019.

Wang, W., Li, L., Lin, W.-L., Dickson, D.W., Petrucelli, L., Zhang, T., and Wang, X. (2013). The ALS disease-associated mutant TDP-43 impairs mitochondrial dynamics and function in motor

bioRxiv preprint doi: https://doi.org/10.1101/2023.03.22.533562; this version posted March 24, 2023. The copyright holder for this preprint (which was not certified by peer review) is the author/funder. All rights reserved. No reuse allowed without permission.

neurons. Hum. Mol. Genet. *22*, 4706–4719. https://doi.org/10.1093/hmg/ddt319.

Weskamp, K., Tank, E.M., Miguez, R., McBride, J.P., Gómez, N.B., White, M., Lin, Z., Gonzalez, C.M., Serio, A., Sreedharan, J., et al. (2020). Shortened TDP43 isoforms upregulated by neuronal hyperactivity drive TDP43 pathology in ALS. J. Clin. Invest. *130*, 1139–1155. https://doi.org/10.1172/JCI130988.

Wu, L.-S., Cheng, W.-C., and Shen, C.-K.J. (2012). Targeted depletion of TDP-43 expression in the spinal cord motor neurons leads to the development of amyotrophic lateral sclerosis-like phenotypes in mice. J. Biol. Chem. *287*, 27335–27344. https://doi.org/10.1074/jbc.M112.359000.

Yang, C., Wang, H., Qiao, T., Yang, B., Aliaga, L., Qiu, L., Tan, W., Salameh, J., McKenna-Yasek, D.M., Smith, T., et al. (2014). Partial loss of TDP-43 function causes phenotypes of amyotrophic lateral sclerosis. Proc. Natl. Acad. Sci. *111*, E1121–E1129. https://doi.org/10.1073/pnas.1322641111.

Zhang, Z., Almeida, S., Lu, Y., Nishimura, A.L., Peng, L., Sun, D., Wu, B., Karydas, A.M., Tartaglia, M.C., Fong, J.C., et al. (2013). Downregulation of microRNA-9 in iPSC-derived neurons of FTD/ALS patients with TDP-43 mutations. PLoS One *8*, e76055. https://doi.org/10.1371/journal.pone.0076055.

Zhao, C., Devlin, A., Chouhan, A.K., Selvaraj, B.T., Stavrou, M., Burr, K., Brivio, V., He, X., Mehta, A.R., Story, D., et al. (2020). Mutant C9orf72 human iPSC-derived astrocytes cause non-cell autonomous motor neuron pathophysiology. Glia *68*, 1046–1064. https://doi.org/10.1002/glia.23761.

Zuo, X., Zhou, J., Li, Y., Wu, K., Chen, Z., Luo, Z., Zhang, X., Liang, Y., Esteban, M.A., Zhou, Y., et al. (2021). TDP-43 aggregation induced by oxidative stress causes global mitochondrial imbalance in ALS. Nat. Struct. Mol. Biol. *28*, 132–142. https://doi.org/10.1038/s41594-020-00537-7.

bioRxiv preprint doi: https://doi.org/10.1101/2023.03.22.533562; this version posted March 24, 2023. The copyright holder for this preprint (which was not certified by peer review) is the author/funder. All rights reserved. No reuse allowed without permission.

Figures

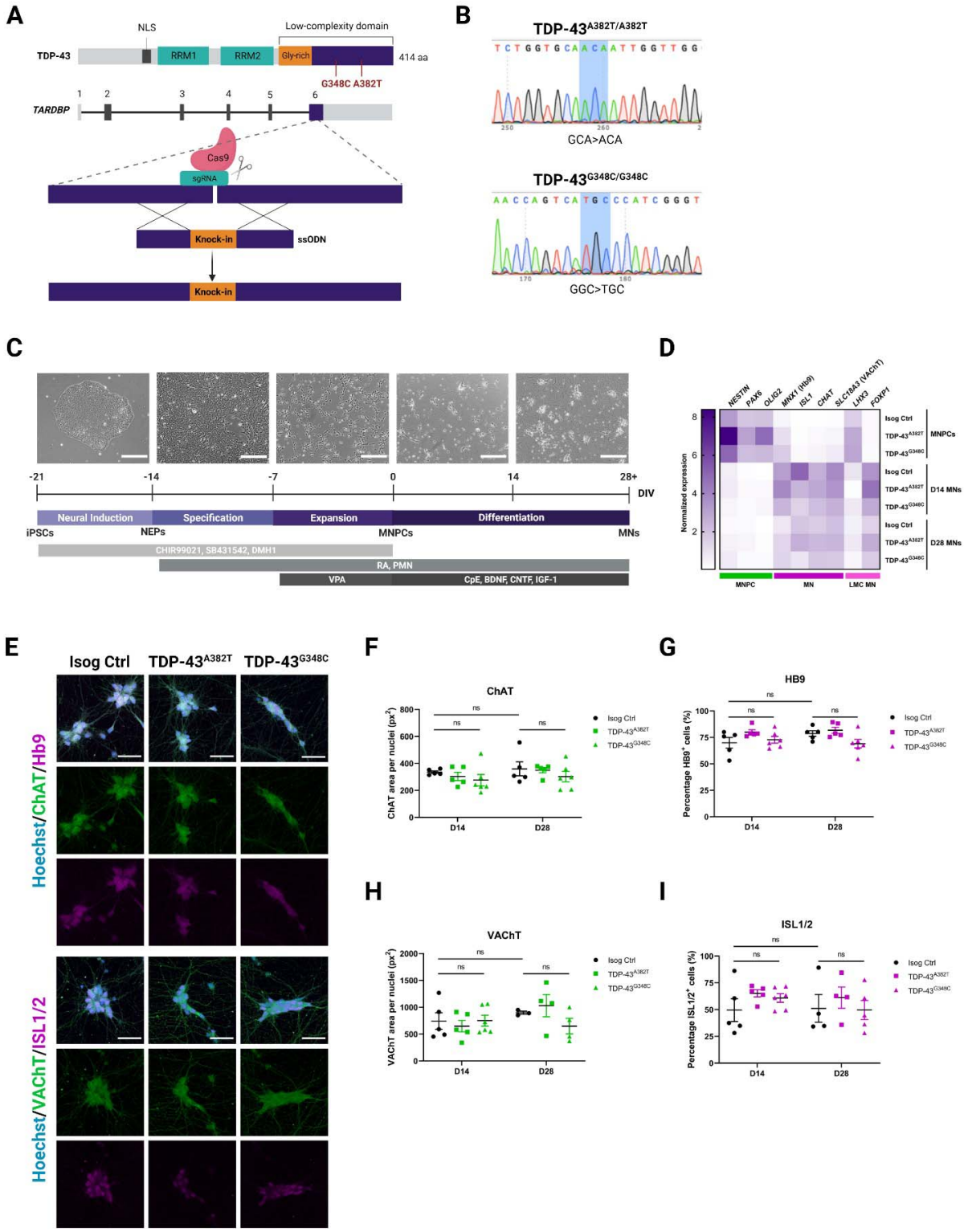

Figure 1. Generation of *TARDBP* knock-in iPSC lines and differentiation into MNs.

bioRxiv preprint doi: https://doi.org/10.1101/2023.03.22.533562; this version posted March 24, 2023. The copyright holder for this preprint (which was not certified by peer review) is the author/funder. All rights reserved. No reuse allowed without permission.

(A) Schematic representation of CRISPR/Cas9-mediated genome editing via homology-directed repair.

(B) iPSC lines genotyping using Sanger sequencing.

(C) Schematic representation of the protocol for sequential differentiation of iPSCs into neuroepithelial progenitors (NEPs), MNPCs, and MNs with representative phase-contrast images of cells along differentiation. Scale bar, 250 µm. For time-lapse movie depicting maturation of MNPCs into MNs, see Video 1.

(D) qPCR heatmap showing normalized transcripts levels of MNPC (green), MN (purple), and LMC (pink) markers during differentiation of MNPCs into MNs. Mean plotted. n=3 independent experiments.

(E-I) Representative images (E) and quantification (F-I) of MNs differentiated for 2 weeks (D14) and 4 weeks (D28) subjected to immunocytochemistry for the common MN markers Hb9, ISL1/2, ChAT and VAChT. Scale bar, 50 µm. Data shown as mean ± SEM. n=5 independent experiments.

See also Figures S1 to S3.

bioRxiv preprint doi: https://doi.org/10.1101/2023.03.22.533562; this version posted March 24, 2023. The copyright holder for this preprint (which was not certified by peer review) is the author/funder. All rights reserved. No reuse allowed without permission.

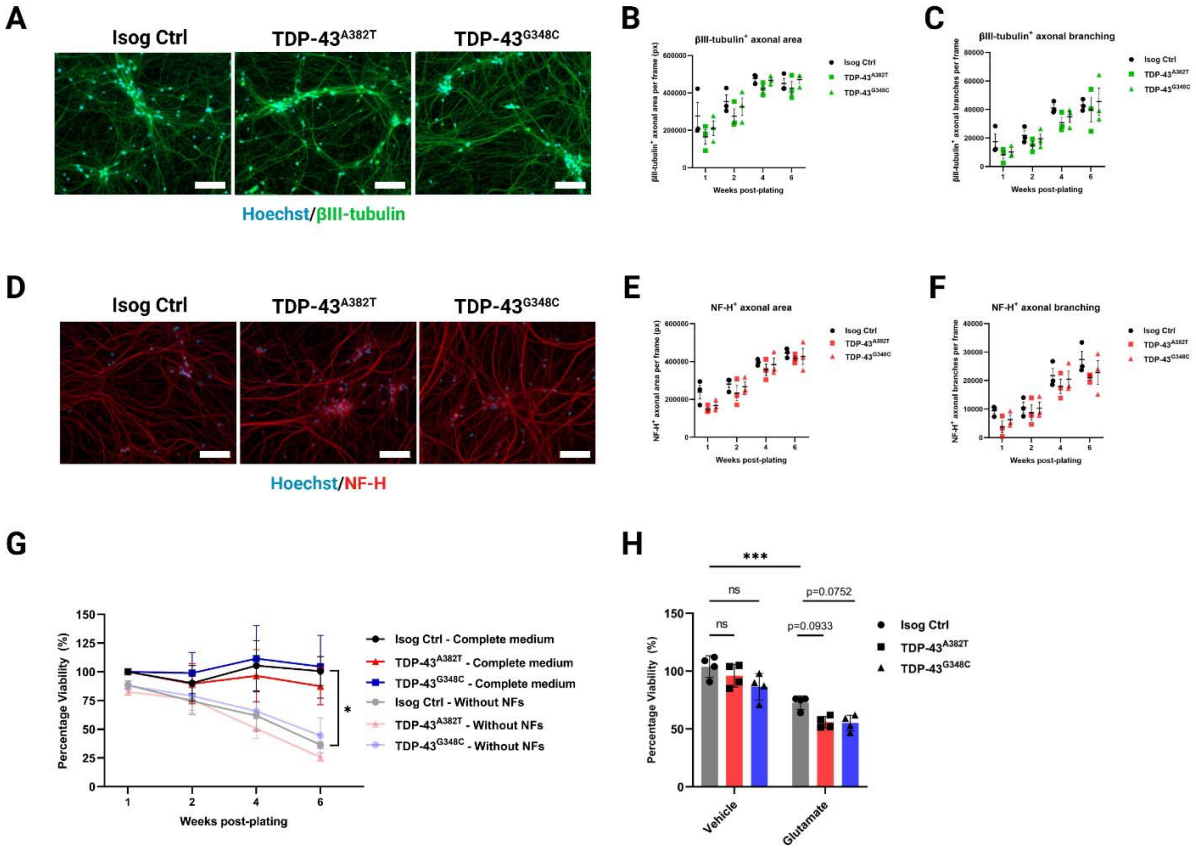

Figure 2. TDP-43 MN cultures form a normal axonal network and maintain viability.

(A,D) Representative images of MNs differentiated for 6 weeks subjected to immunocytochemistry for neuronal markers βIII-tubulin (A) and NF-H (D). Scale bar, 100 μm.

(B,C) Quantification of total area (B) and number of branches (C) of βIII-tubulin^{+} axons. n=3 independent experiments.

(E,F) Quantification of total area (E) and number of branches (F) of NF-H^{+} axons. n=3 independent experiments.

(G) Viability of MN cultures differentiated with and without neurotrophic factor (NF) supplementation over a span of 6 weeks post-plating. n=4 independent experiments.

(H) Effect of glutamate treatment (0.1 mM glutamate, 24 h) on viability of MNs differentiated for 6 weeks. n=4 independent experiments.

bioRxiv preprint doi: https://doi.org/10.1101/2023.03.22.533562; this version posted March 24, 2023. The copyright holder for this preprint (which was not certified by peer review) is the author/funder. All rights reserved. No reuse allowed without permission.

All data shown as mean ± SEM. *p<0.05, **p<0.01, ***p<0.001.

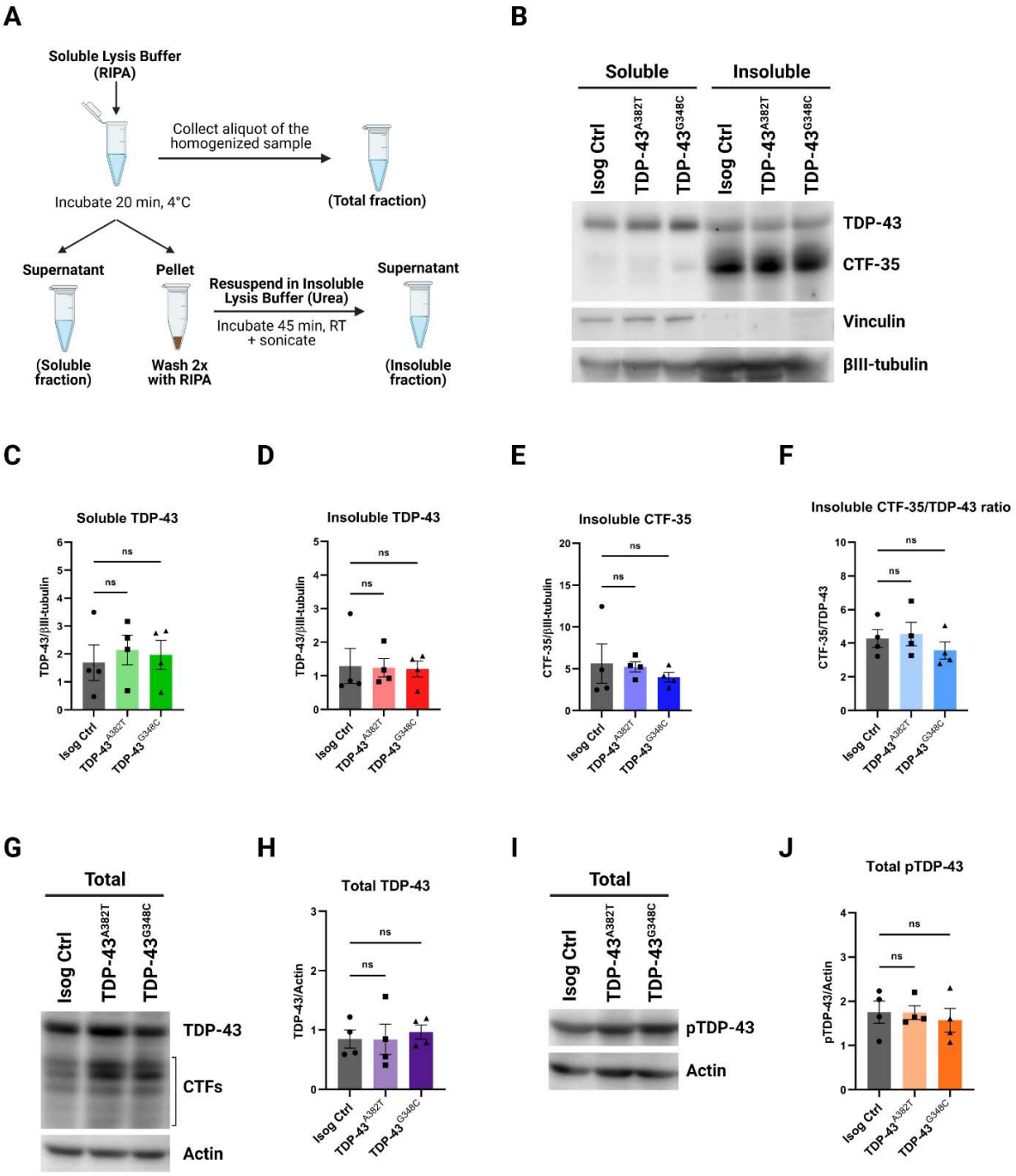

Figure 3. Quantification of TDP-43 levels in total, soluble, and insoluble protein fractions.

(A) Schematics representing the fractionation workflow into total (unfractionated), soluble (RIPA), and insoluble (urea) protein fractions.

bioRxiv preprint doi: https://doi.org/10.1101/2023.03.22.533562; this version posted March 24, 2023. The copyright holder for this preprint (which was not certified by peer review) is the author/funder. All rights reserved. No reuse allowed without permission.

(B-F) Immunoblot (B) and quantification of TDP-43 (C, D) and C-terminal fragment of 35 kDa (CTF-35) (E, F) levels in soluble and insoluble fractions. Vinculin (soluble) and βIII-tubulin were used as fractionation and loading controls, respectively.

(G-J) Immunoblot (G, I) and quantification of total levels of TDP-43 (H) and phosphorylated TDP-43 (Ser409/410) (J) in unfractionated lysates. Actin was used as loading control.

All data shown as mean ± SEM. Extractions were performed in in MNs harvested at 6 weeks post-plating. n=4 independent experiments. See also Figure S4.

bioRxiv preprint doi: https://doi.org/10.1101/2023.03.22.533562; this version posted March 24, 2023. The copyright holder for this preprint (which was not certified by peer review) is the author/funder. All rights reserved. No reuse allowed without permission.

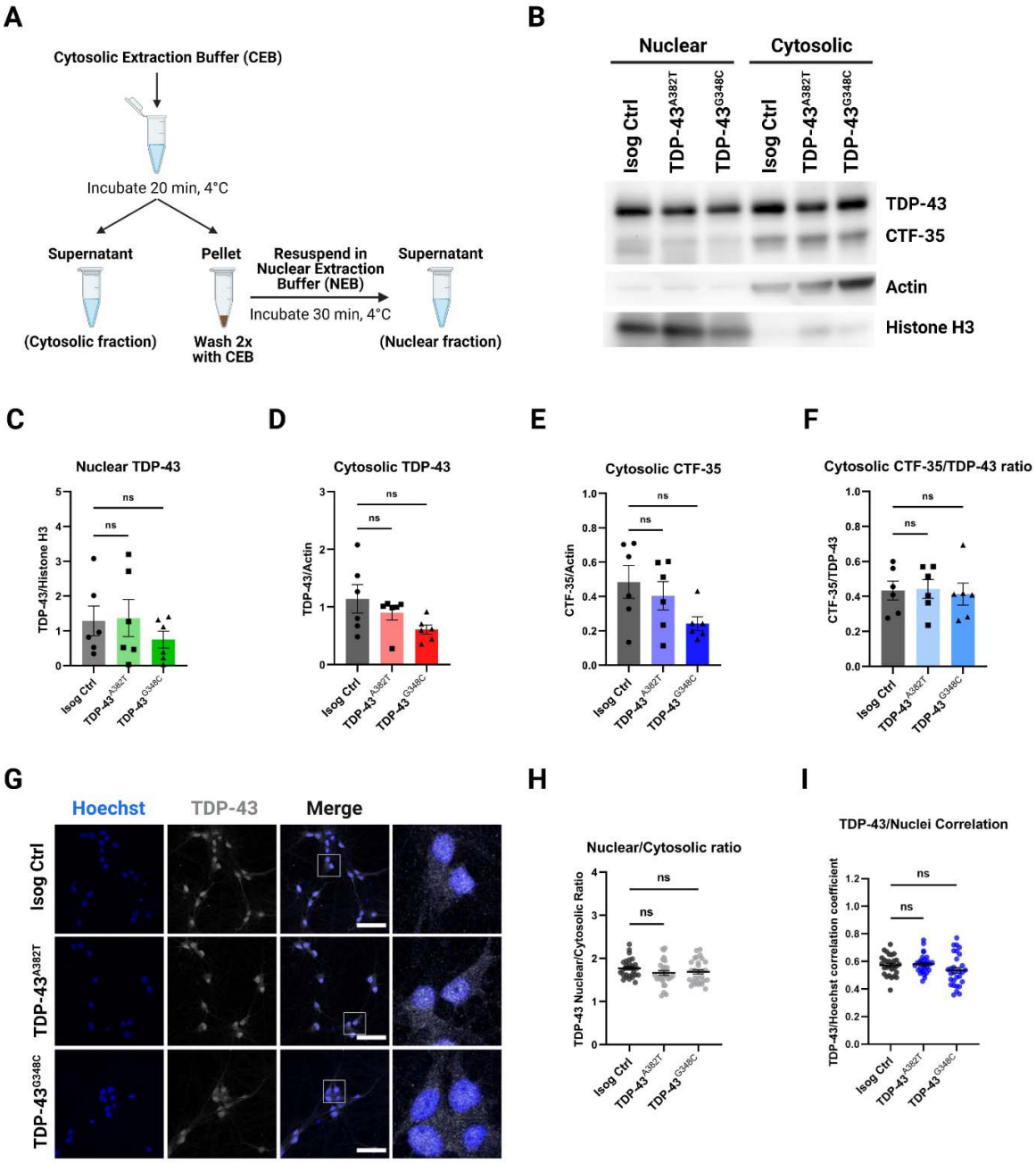

Figure 4. Subcellular distribution of TDP-43 in MNs.

(A) Schematics representing the fractionation workflow into nuclear and cytosolic fractions.

(B-F) Immunoblot of nuclear and cytosolic fractions (B) and quantification of nuclear (C) and cytosolic (D) TDP-43 levels, and cytosolic C-terminal fragment of 35 kDa (CTF-35) levels (E and

bioRxiv preprint doi: https://doi.org/10.1101/2023.03.22.533562; this version posted March 24, 2023. The copyright holder for this preprint (which was not certified by peer review) is the author/funder. All rights reserved. No reuse allowed without permission.

F). Histone H3 (nuclear marker) and actin (cytosolic marker) were used as both loading and fractionation controls. n=6 extractions from 4 independent differentiations. Pooled data from MNs harvested 4- and 6-weeks post-plating.

(G) Representative images of MNs differentiated for 6 weeks subjected to immunocytochemistry for TDP-43 (C-terminal antibody). Scale bar, 50 μm.

(H, I) Quantification of TDP-43 distribution using the nuclear/cytosolic ratio of TDP-43 fluorescence signal intensity (H) and the TDP-43/Hoechst correlation coefficient (I). Individual data points represent per-frame mean values from 5 independent experiments.

All data shown as mean ± SEM. See also Figure S5.

bioRxiv preprint doi: https://doi.org/10.1101/2023.03.22.533562; this version posted March 24, 2023. The copyright holder for this preprint (which was not certified by peer review) is the author/funder. All rights reserved. No reuse allowed without permission.

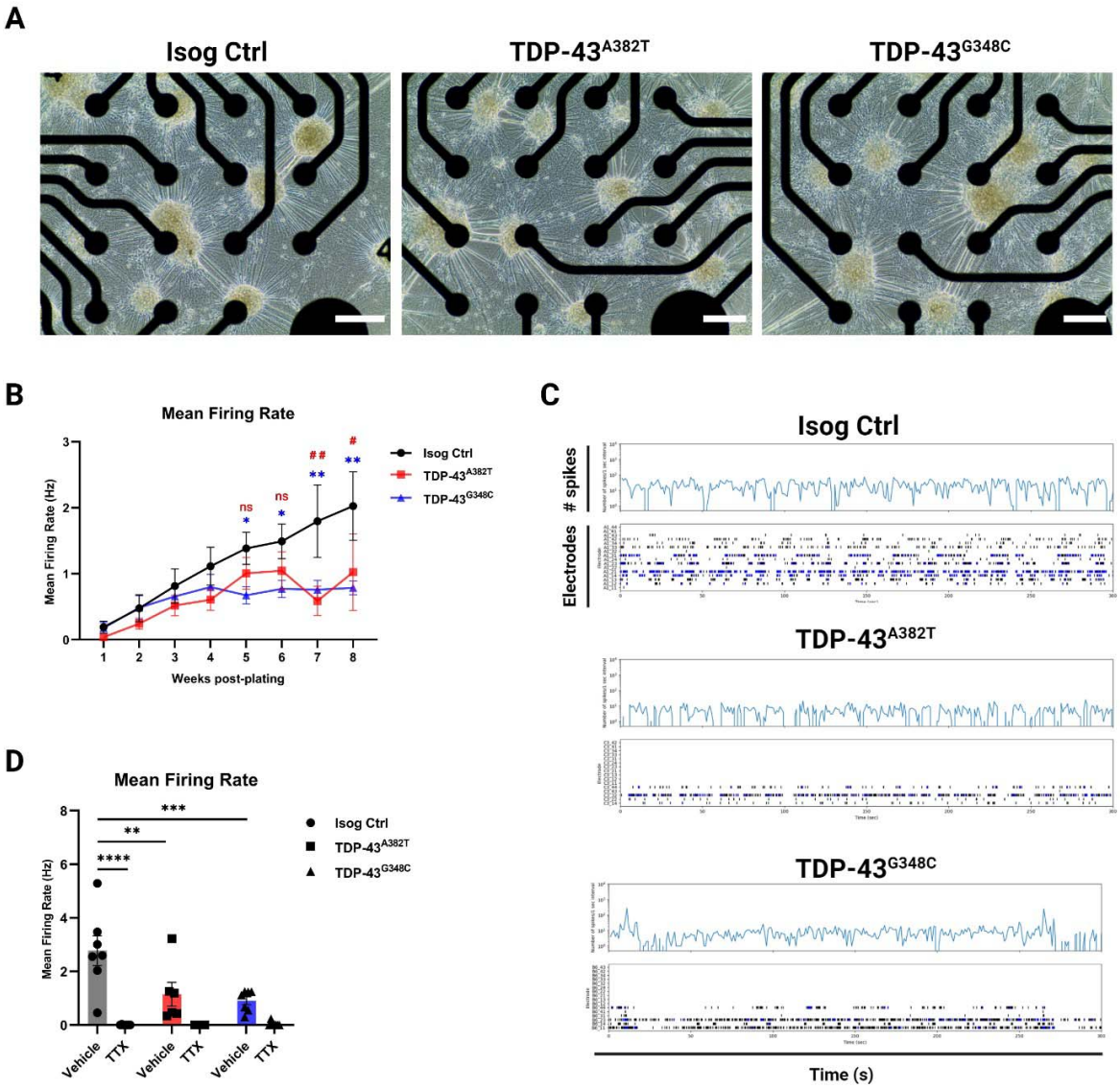

Figure 5. TDP-43 MNs show progressive alterations in spontaneous neuronal activity.

(A) Representative phase-contrast images of MNs differentiated for 6 weeks on 24-well MEA plates. Scale bar, 250 µm**.**

(B) Longitudinal changes in mean firing rate of MNs recorded weekly over a span of 8 weeks post-plating. n=11 independent experiments.

(C) Spontaneous neuronal activity of MN cultures differentiated for 6 weeks recorded for 300s shown as raster plot and spike histogram. Individual spikes are shown in black and bursts are shown in blue.

bioRxiv preprint doi: https://doi.org/10.1101/2023.03.22.533562; this version posted March 24, 2023. The copyright holder for this preprint (which was not certified by peer review) is the author/funder. All rights reserved. No reuse allowed without permission.

(D) Effect of TTX treatment on mean firing rate in MNs differentiated for 6 weeks. n=7 independent experiments.

All data shown as mean ± SEM. *p<0.05, **p<0.01, ***p<0.001, ****p<0.0001. See also Figure S6.

bioRxiv preprint doi: https://doi.org/10.1101/2023.03.22.533562; this version posted March 24, 2023. The copyright holder for this preprint (which was not certified by peer review) is the author/funder. All rights reserved. No reuse allowed without permission.

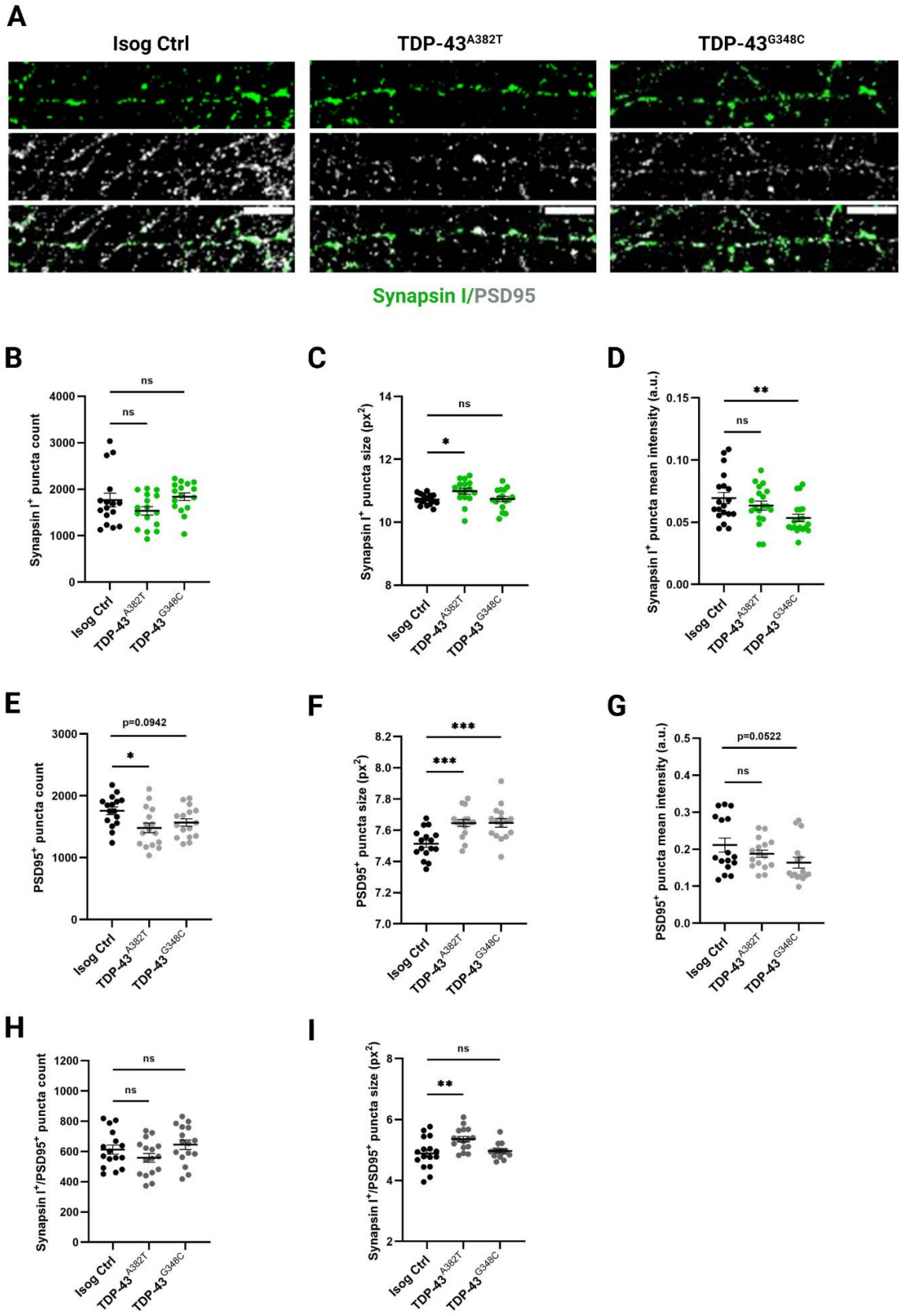

bioRxiv preprint doi: https://doi.org/10.1101/2023.03.22.533562; this version posted March 24, 2023. The copyright holder for this preprint (which was not certified by peer review) is the author/funder. All rights reserved. No reuse allowed without permission.

Figure 6. TDP-43 MNs exhibit synaptic abnormalities.

(A) Representative images of 6 weeks post-plating MN neurites subjected to immunocytochemistry for synapsin I and PSD95. Scale bar, 10 μm.

(B-D) Quantification of the average number (B), size (C), and intensity (D) of synapsin I^+ puncta.

(E-G) Quantification of the average number (E), size (F), and intensity (G) of $PSD95^+$ puncta.

(H,I) Quantification of the average number (H), and size (I) of synapsin I^+/$PSD95^+$ puncta.

Individual points represent per-frame values from 3 independent experiments.

All data shown as mean ± SEM. *p<0.05, **p<0.01, ***p<0.001.

bioRxiv preprint doi: https://doi.org/10.1101/2023.03.22.533562; this version posted March 24, 2023. The copyright holder for this preprint (which was not certified by peer review) is the author/funder. All rights reserved. No reuse allowed without permission.

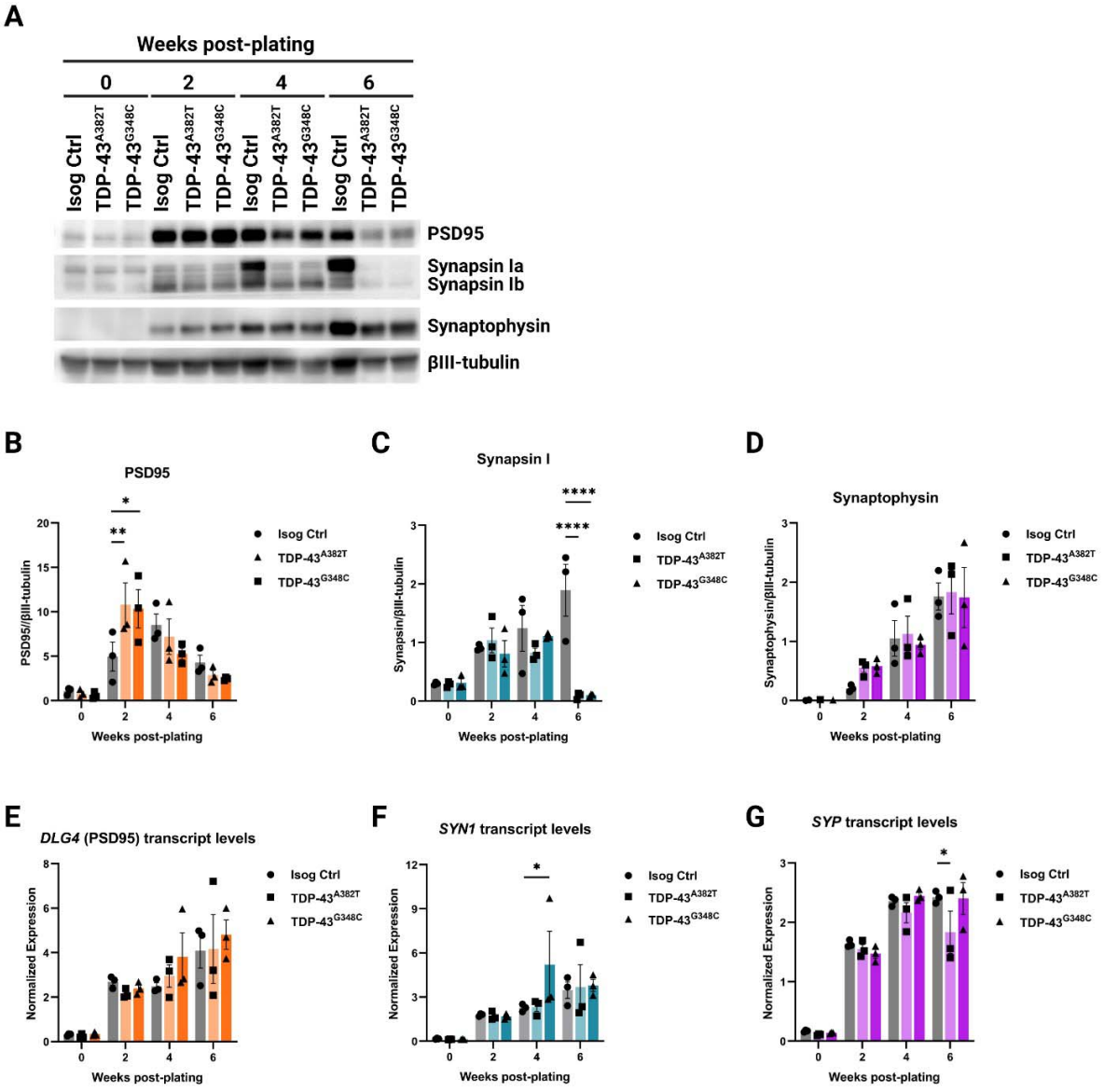

Figure 7. TDP-43 variants lead to decreased synapsin I protein levels but not *SYN1* transcript levels.

(A-D) Immunoblot (A) and quantification of protein levels of PSD95 (B), synapsin I (C), and synaptophysin (D) in MNPCs and MNs harvested after 2, 4, and 6 weeks of differentiation. βIII-tubulin was used as loading control.

(E-G) Longitudinal quantification of relative transcript levels of *DLG4* (encoding PSD95) (E), *SYN1* (F), and *SYP* (G) using qPCR.

bioRxiv preprint doi: https://doi.org/10.1101/2023.03.22.533562; this version posted March 24, 2023. The copyright holder for this preprint (which was not certified by peer review) is the author/funder. All rights reserved. No reuse allowed without permission.

All data shown as mean ± SEM. *p<0.05, **p<0.01, ***p<0.001, ****p<0.0001. n=3 independent experiments.

Videos

bioRxiv preprint doi: https://doi.org/10.1101/2023.03.22.533562; this version posted March 24, 2023. The copyright holder for this preprint (which was not certified by peer review) is the author/funder. All rights reserved. No reuse allowed without permission.

Video 1. Differentiation of MNPCs into MNs. Related to Figure 1. Time-lapse movie depicting the differentiation of MNPCs into MNs during 2 weeks post-plating. Scale bar, 150 μm.

Video 2. Electrophysiological recording of MN cultures using MEA. Related to Figure 5. Movie depicting spontaneous neuronal activity in MNs differentiated for 7 weeks using the AxIS Navigator 1.5.1.12 software (Axion Biosystems). Warmer colors indicate greater changes in local field potentials.

bioRxiv preprint doi: https://doi.org/10.1101/2023.03.22.533562; this version posted March 24, 2023. The copyright holder for this preprint (which was not certified by peer review) is the author/funder. All rights reserved. No reuse allowed without permission.

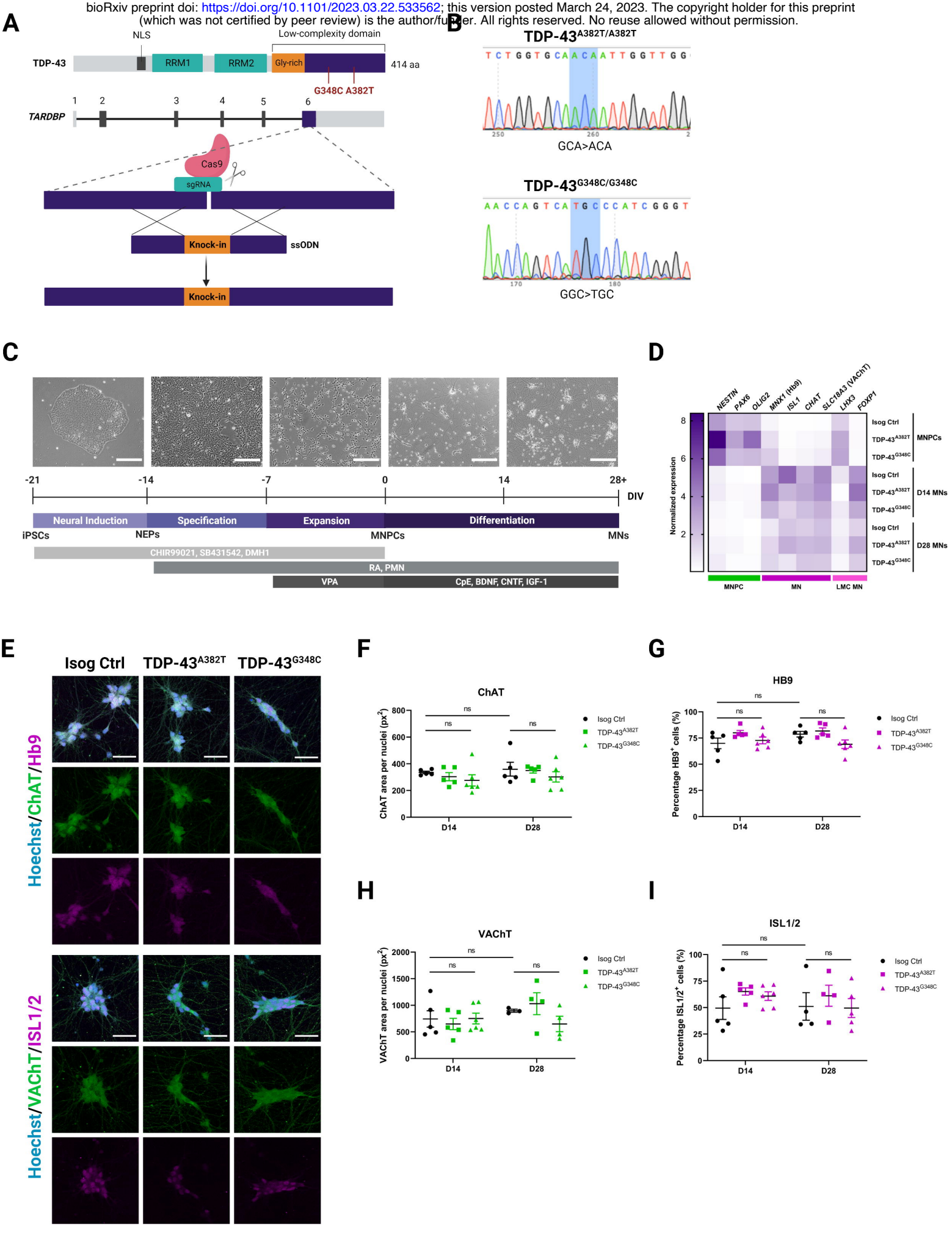

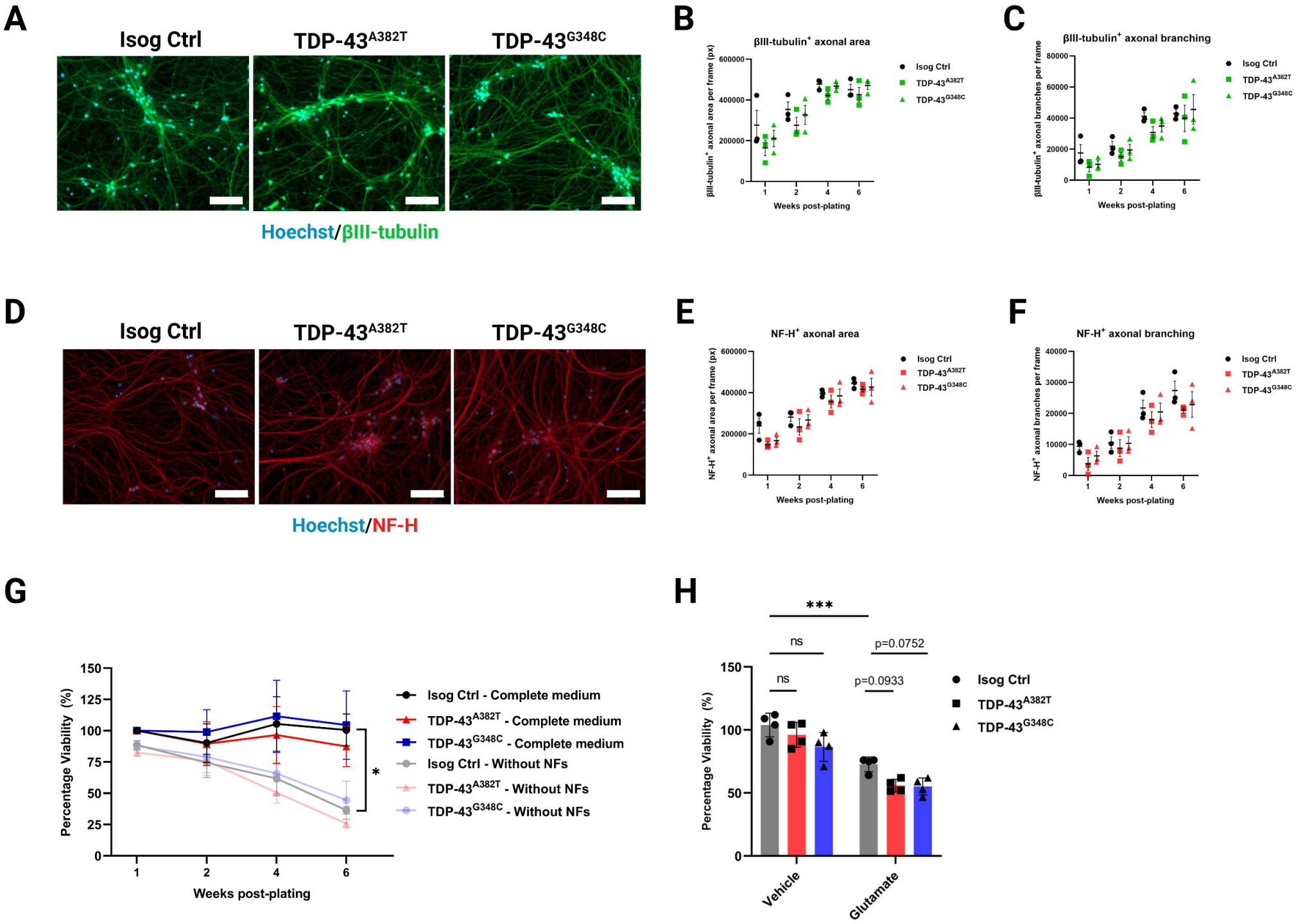
A
Isog Ctrl
TDP-43A382T
TDP-43G348C
Hoechst/βIII-tubulin
B
βIII-tubulin+ axonal area
βIII-tubulin+ axonal area per frame (px)
Weeks post-plating
Isog Ctrl
TDP-43A382T
TDP-43G348C
C
βIII-tubulin+ axonal branching
βIII-tubulin+ axonal branches per frame
Weeks post-plating
D
Isog Ctrl
TDP-43A382T
TDP-43G348C
Hoechst/NF-H
E
NF-H+ axonal area
NF-H+ axonal area per frame (px)
Weeks post-plating
F
NF-H+ axonal branching
NF-H+ axonal branches per frame
Weeks post-plating
G
Percentage Viability (%)
Weeks post-plating
Isog Ctrl - Complete medium
TDP-43A382T - Complete medium
TDP-43G348C - Complete medium
Isog Ctrl - Without NFs
TDP-43A382T - Without NFs
TDP-43G348C - Without NFs
*
H
***
ns
p=0.0752
ns
p=0.0933
Percentage Viability (%)
Vehicle
Glutamate
Isog Ctrl
TDP-43A382T
TDP-43G348C

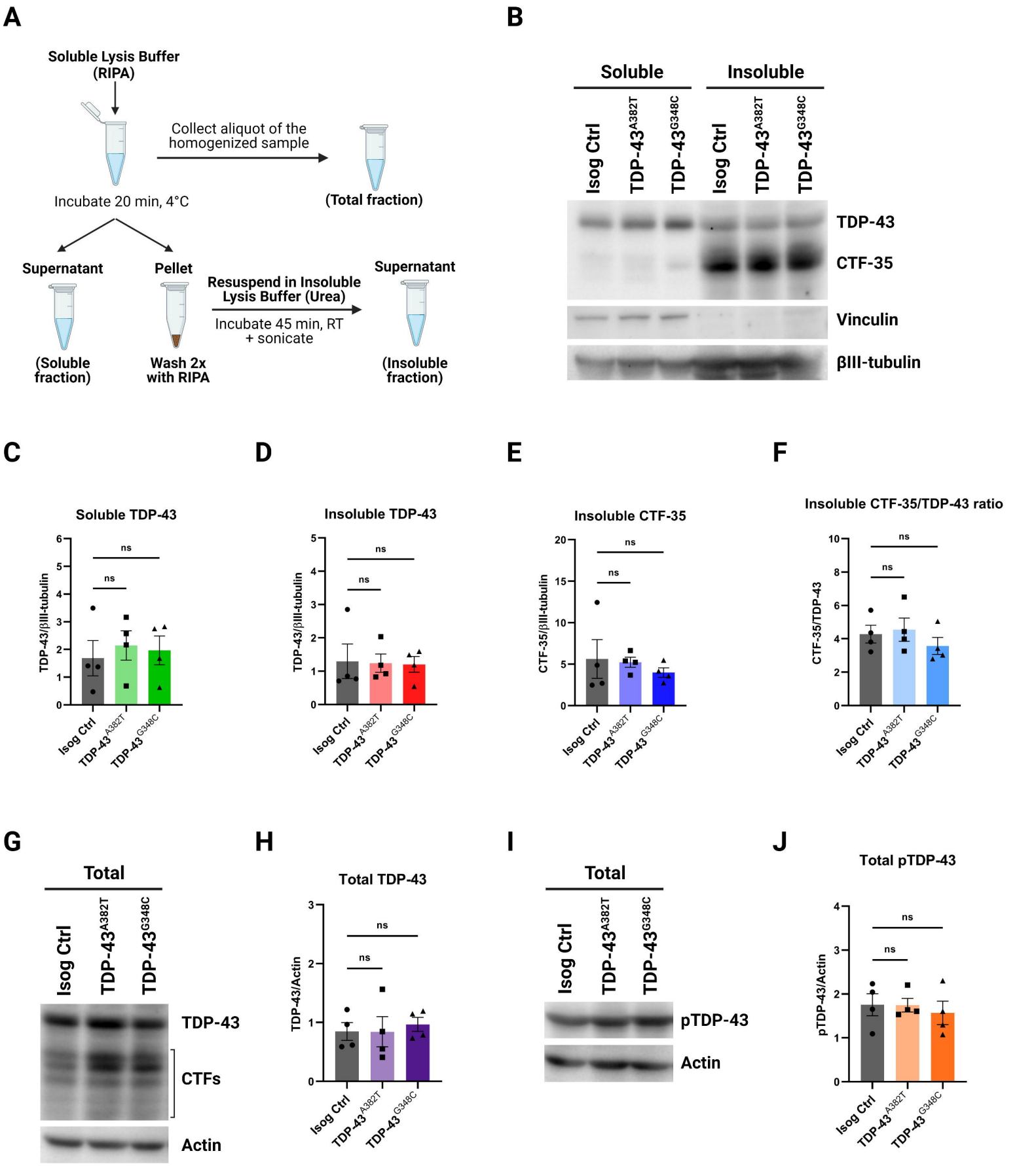
A
Soluble Lysis Buffer (RIPA)
Collect aliquot of the homogenized sample
Incubate 20 min, 4°C
(Total fraction)
Supernatant
Pellet
Resuspend in Insoluble Lysis Buffer (Urea)
Incubate 45 min, RT + sonicate
Supernatant
(Soluble fraction)
Wash 2x with RIPA
(Insoluble fraction)
B
Soluble
Insoluble
Isog Ctrl
TDP-43A382T
TDP-43G348C
TDP-43
CTF-35
Vinculin
βIII-tubulin
C
Soluble TDP-43
TDP-43/βIII-tubulin
D
Insoluble TDP-43
E
Insoluble CTF-35
CTF-35/βIII-tubulin
F
Insoluble CTF-35/TDP-43 ratio
CTF-35/TDP-43
ns
G
Total
TDP-43
CTFs
Actin
H
Total TDP-43
TDP-43/Actin
I
Total
pTDP-43
Actin
J
Total pTDP-43
pTDP-43/Actin

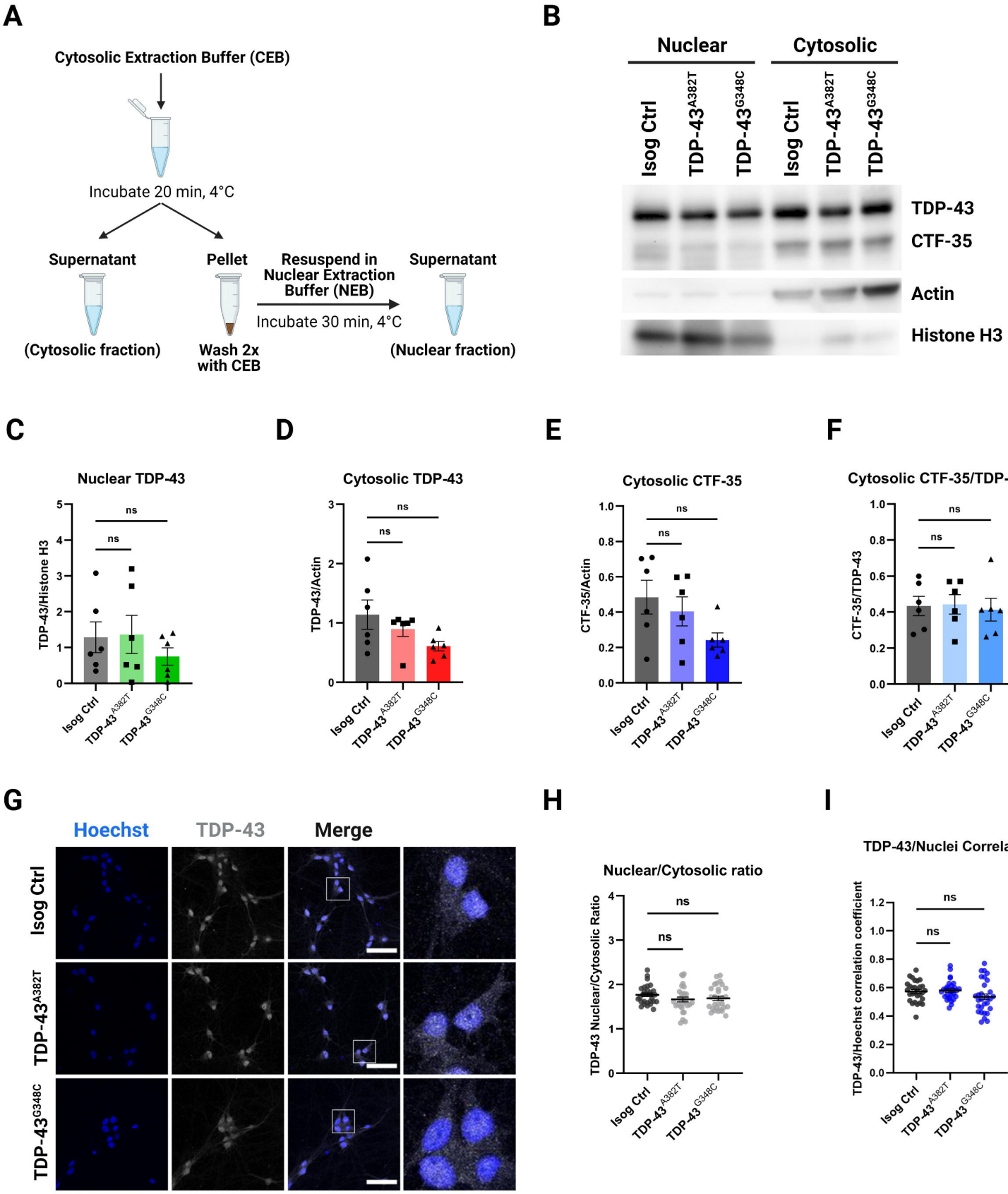
A
Cytosolic Extraction Buffer (CEB)
Incubate 20 min, 4°C
Supernatant
Pellet
Resuspend in Nuclear Extraction Buffer (NEB)
Supernatant
Incubate 30 min, 4°C
(Cytosolic fraction)
Wash 2x with CEB
(Nuclear fraction)
B
Nuclear
Cytosolic
Isog Ctrl
TDP-43A382T
TDP-43G348C
Isog Ctrl
TDP-43A382T
TDP-43G348C
TDP-43
CTF-35
Actin
Histone H3
C
Nuclear TDP-43
TDP-43/Histone H3
ns
ns
Isog Ctrl
TDP-43A382T
TDP-43G348C
D
Cytosolic TDP-43
TDP-43/Actin
ns
ns
Isog Ctrl
TDP-43A382T
TDP-43G348C
E
Cytosolic CTF-35
CTF-35/Actin
ns
ns
Isog Ctrl
TDP-43A382T
TDP-43G348C
F
Cytosolic CTF-35/TDP-43 ratio
CTF-35/TDP-43
ns
ns
Isog Ctrl
TDP-43A382T
TDP-43G348C
G
Hoechst
TDP-43
Merge
Isog Ctrl
TDP-43A382T
TDP-43G348C
H
Nuclear/Cytosolic ratio
TDP-43 Nuclear/Cytosolic Ratio
ns
ns
Isog Ctrl
TDP-43A382T
TDP-43G348C
I
TDP-43/Nuclei Correlation
TDP-43/Hoechst correlation coefficient
ns
ns
Isog Ctrl
TDP-43A382T
TDP-43G348C

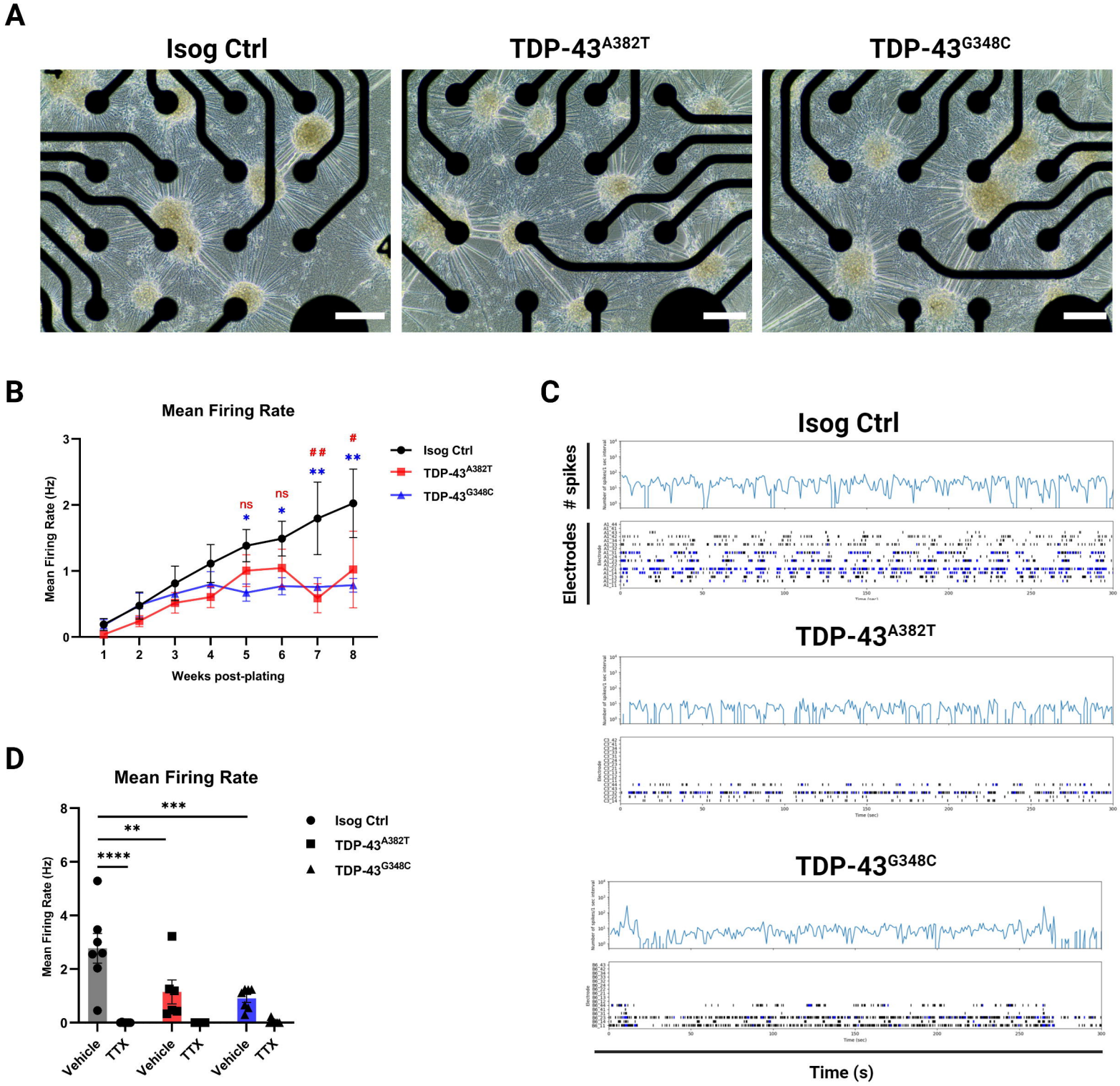
A
Isog Ctrl
TDP-43A382T
TDP-43G348C
B
Mean Firing Rate
Mean Firing Rate (Hz)
Weeks post-plating
Isog Ctrl
TDP-43A382T
TDP-43G348C
ns
*
ns
*
##
**
#
**
C
Isog Ctrl
spikes
Electrodes
TDP-43A382T
TDP-43G348C
Time (s)
D
Mean Firing Rate
Mean Firing Rate (Hz)
***
**
****
Isog Ctrl
TDP-43A382T
TDP-43G348C
Vehicle
TTX
Vehicle
TTX
Vehicle
TTX

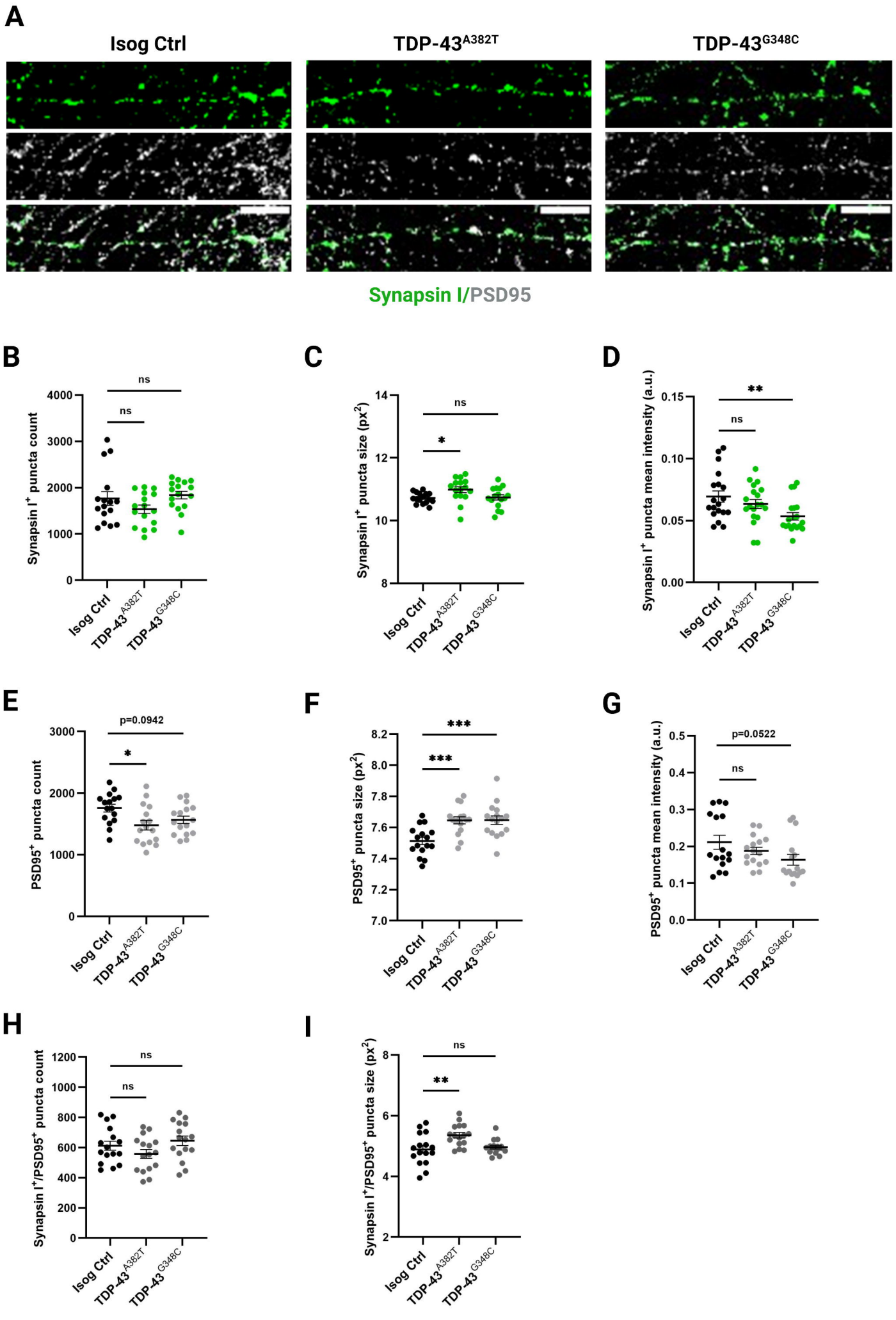
A
Isog Ctrl
TDP-43A382T
TDP-43G348C
Synapsin I/PSD95
B
Synapsin I+ puncta count
ns
ns
C
Synapsin I+ puncta size (px2)
ns
*
D
Synapsin I+ puncta mean intensity (a.u.)
**
ns
E
PSD95+ puncta count
p=0.0942
*
F
PSD95+ puncta size (px2)
***
***
G
PSD95+ puncta mean intensity (a.u.)
p=0.0522
ns
H
Synapsin I+/PSD95+ puncta count
ns
ns
I
Synapsin I+/PSD95+ puncta size (px2)
ns
**
Isog Ctrl
TDP-43A382T
TDP-43G348C

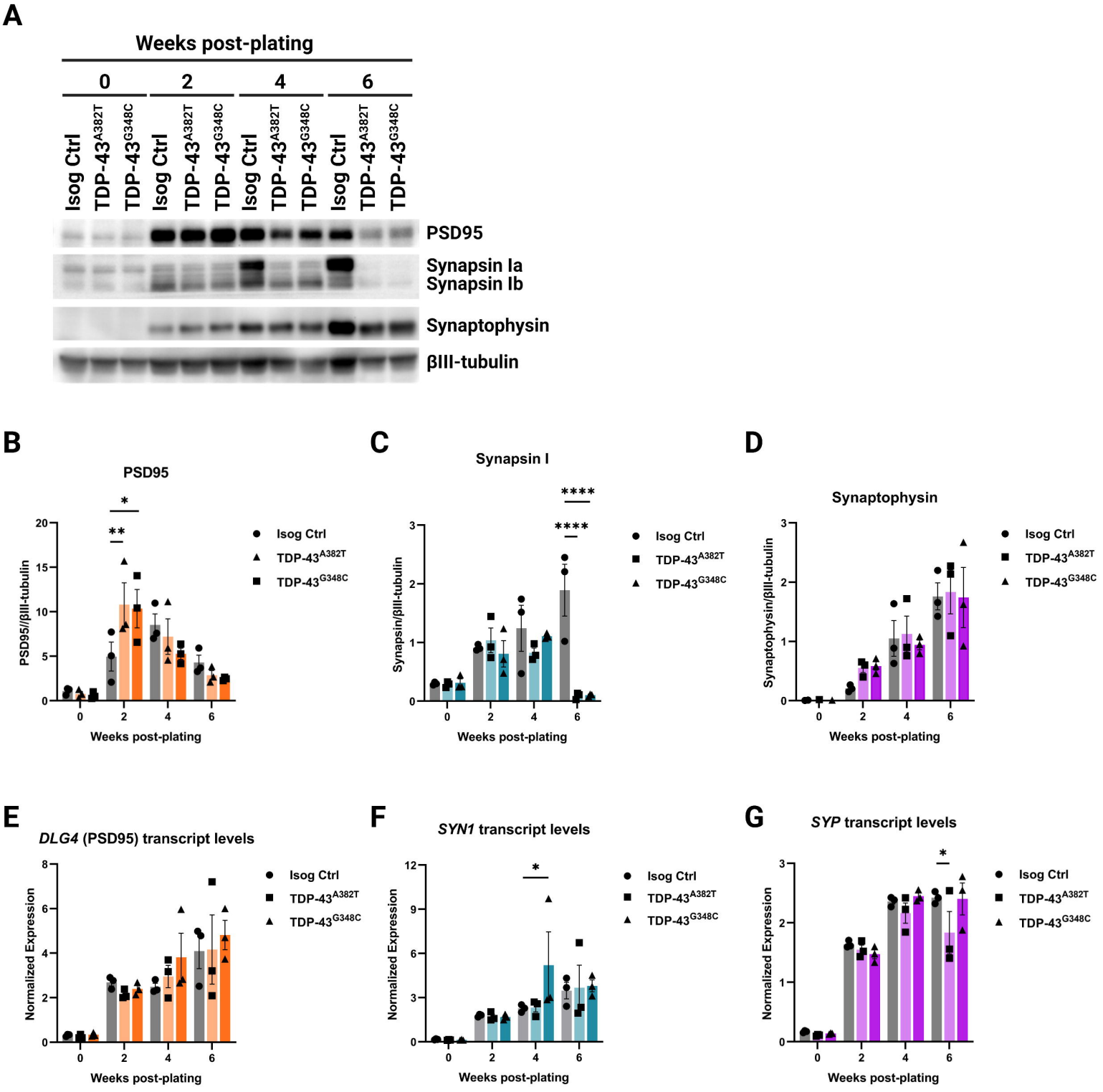
A
Weeks post-plating
0
2
4
6
Isog Ctrl
TDP-43A382T
TDP-43G348C
PSD95
Synapsin Ia
Synapsin Ib
Synaptophysin
βIII-tubulin
B
PSD95
PSD95/βIII-tubulin
Weeks post-plating
C
Synapsin I
Synapsin/βIII-tubulin
D
Synaptophysin
Synaptophysin/βIII-tubulin
E
DLG4 (PSD95) transcript levels
Normalized Expression
F
SYN1 transcript levels
G
SYP transcript levels